THE UNIVERSITY
of EDINBURGH

Pioneer Transcription Factor Interactions and

Chromatin Binding Dynamics

During Zygotic Genome Activation

Julia Auer

Thesis presented for the degree of Doctor of Philosophy

The University of Edinburgh

2023

Declaration

This thesis is entirely my own work, and unless otherwise stated all experiments were done solely by myself. This work has not been submitted for any other degree or professional qualification. The included publication is my own work.

Julia Auer

May 2023

Acknowledgements

And of course, my friends have been invaluable. Hannah, thanks for always being there, even from abroad! Damson, thanks for putting up with my surely endless rants about lab things. Elias, the silver lining of all the PhD roller-coasters was meeting you, thank you for believing in me.

Und zum Schluß: ohne meine Familie hätte ich es wirklich nicht geschafft. Mama und Papa, danke dass ihr einfach immer da seid und an mich glaubt. Liebe Oma Ruth, danke für die vielen aufmunternden Plauder-WhatsApps!

Abstract

Cell fate transitions are regulated by the activity of factors such as pioneer transcription factors (PTFs) to promote new transcriptional programmes. PTFs can bind to closed chromatin, and often interact with other PTFs and chromatin remodelers, to make chromatin accessible for transcription. How PTFs dynamically bind DNA and interact with each other to achieve this has mainly been studied *in vitro*. Zygotic Genome Activation (ZGA) is an excellent model to study the dynamics of PTFs in the context of gene expression *in vivo*, as transcription begins from a previously silent genome. In this thesis I aimed to harness live quantitative microscopy to study the interactions and chromatin binding dynamics of the PTFs Nanog, Pou5f3, and Sox19b required for ZGA in zebrafish. I first verified whether Fluorescence Correlation Spectroscopy (FCS) can be used to examine PTF chromatin-bound diffusion. After optimising the tagging strategy, sample preparation and measurement, as well as the analysis by autocorrelation and curve fitting, I showed that FCS can measure the diffusion of fluorescently-tagged PTFs at ZGA. However, I found no significant difference in diffusion between Nanog-Citrine and mCherry-Pou5f3, or changes to their diffusion as ZGA progresses. This suggests that the short-lived chromatin interactions measured by FCS, which may reflect TF DNA motif search, remain constant for Nanog and Pou5f3 during ZGA.

Next, I wanted to test whether Nanog, Sox19b and Pou5f3 directly interact during ZGA. The spectral proximity of (m)Citrine and mCherry made these an unsuitable fluorophore pair for Fluorescence Cross-Correlation Spectroscopy, but allowed me to use Foerster Resonance Energy Transfer (FRET) assays. I began by showing that mCitrine and mCherry are indeed a good FRET pair. I then moved on to measure FRET by changes to the donor lifetime, as this method is less susceptible to concentration and photobleaching. For this, I used a semi-quantitative lifetime-based measure, Average Arrival Time (AAT), which does not require fitting analysis and therefore performs better in systems with low signal-to-noise ratio. Optimising sample preparation, image acquisition, and data analysis allowed me to detect

interactions between controls in zebrafish embryos: the AAT of mCitrine was slightly but significantly lower in the mCitrine-mCherry tandem fusion, compared to negative controls.

I then showed that Nanog-mCitrine and Sox19b-mCherry may interact at ZGA, however the low resolution of AAT measurements paired with the slight mCitrine AAT shift limited any further investigation. To efficiently probe PTF-PTF interactions by AAT-FRET, an alternative FRET pair in which the donor undergoes a larger lifetime shift would be required.

Overall, I have found that the target-search dynamics of Nanog and Pou5f3 may not differ significantly throughout ZGA, and that Nanog and Sox19b may interact. However my data were significantly limited by the fluorophore choice and the low signal-to-noise ratio. Further optimisations to the experimental setup would help to quantify more reliably how the PTFs behave dynamically to regulate transcriptional onset at ZGA.

Lay Summary

Scientists have studied for decades how individual cells can develop into whole organisms, by dividing and becoming successively more specialised. Each cell contains the instructions to become any cell type, encoded in a molecule called DNA. Transcription factors (TFs) are proteins that ensure the correct instructions are followed to make different cell types. TFs often work together, but how they move to bind the DNA, and interact with each other, to drive a new programme of cell specification is not fully understood.

In my project, I studied TFs that drive a very early event in development called Zygotic Genome Activation (ZGA) in zebrafish. These TFs help the embryo take control of its development, by making sure the embryo's cells start to use their DNA instructions and begin to specialise. I applied different kinds of microscopy to try to follow the movement and interactions of some of these TFs in zebrafish embryos during ZGA. I began by optimising the experiments, from sample preparation to measurement, and analysis, as it is challenging to collect accurate measurements from live zebrafish embryos which develop very quickly. I was able to follow how the TFs search for their binding site on DNA, but did not see any changes during ZGA. I tested whether I can measure interactions between TFs using a new microscopy technique that requires less analysis. I found that some of the factors might interact during ZGA. Further improvements to methods and more specialised equipment would be needed to conclusively follow the behaviour of TFs directing cell fate at ZGA in zebrafish embryos.

Table of Contents

List of Figures

List of Tables

List of Equations

List of Abbreviations

CCD, EMCCD	Charge-coupled device (electron multiplying)
2D/3D	Two-/three-dimensional
AAT	Average arrival time
AccPb	Acceptor photobleaching
ACF, $G(\tau)$	Autocorrelation function
AD	Activation domain
APD	Avalanche photodiode
AU	Airy unit
b.r.	Biological replicate
Bi-FC	Bimolecular fluorescence complementation
blue miR-430 MO	Genetools blue-tagged mir-430 morpholino
bp	Base pairs
BSA	Bovine serum albumin
CCF	Cross-correlation function
Cryo-EM	Cryo-electron microscopy
cv^2	Coefficient of variation
DBD	DNA binding domain
DMEM	Dulbecco's modified eagle medium
DNA	Dioxyribonucleic acid
E3	Embryo medium
EMSA	Electrophoretic mobility shift assay
ESC, mESC	(Mouse) embryonic stem cell
EtBr	Ethidium bromide
FCCS	Fluorescence cross-correlation spectroscopy
FCS	Fluorescence correlation spectroscopy
FLIM	Fluorescence lifetime imaging microscopy
FOV	Field of view
FRAP	Fluorescence recovery after photobleaching
FRET, smFRET, SE-FRET	(Sensitised Emission) (single molecule) Foerster Resonance Energy Transfer
GaAsP	Gallium arsenide phosphide
GFP, (m)eGFP, paGFP	Green fluorescent protein (monomeric) (enhanced) (photoactivatable)
HEPES	4-2-hydroxyethylpiperazine-1-ethanesulfonic acid
HMG	High mobility group DNA binding domain
HOM	Homeodomain DNA binding domain
hpf	Hours post fertilisation
Hz	Hertz
IDR	Intrinsically disordered region
IRF	Instrument response function

LMP agarose	Low melting point agarose
mfD	Minimum fraction of interacting donor
MO	Morpholino
MW	Mean weighted
MZ; MZ*nps*; MZ*nanog*;MZ*spg793*; MZ*sox19b*	Maternal-zygotic; *Nanog, Pou5f3, Sox19b* triple mutant; *Nanog* mutant; *Pou5f3* mutant; *Sox19b* mutant
Mzt	Maternal-to-zygotic transition
N:c ratio	Nuclear-to-cytoplasmic ratio
NA	Numerical aperture
O/n	Overnight
OVE	Observation volume element
PAPA	Proximity-assisted photoactivation
PBS	Phosphate buffered saline
Pen/strep	Penicillin/streptomycin
PFA	Paraformaldehyde
PMT	Photomultiplier tube
Pol II	RNA Polymerase II
PSF	Point spread function
PSN	Pouf53, sox19b, nanog
Px	Pixel
RCCA	Relative cross-correlation amplitude
RFP, mRFP	Red fluorescent protein (monomeric)
RNA, mRNA	(Messenger) ribonucleic acid
ROI	Region of interest
SMT	Single molecule tracking
SNR	Signal-to-noise ratio
SPAD	Single photon avalanche diode
SPIM	Singe plane illumination microscopy
Stdev	Standard deviation
TCSPC	Time-correlated single photon counting
TF, PTF	(Pioneer) Transcription factor
W(R)	Tryptophan (repeat)
WLL	White light laser
WT	Wild-type
ZGA	Zygotic genome activation
κ	Structural parameter of confocal volume
ρ(slow/fast)	Proportion (slow/fast component)
τ	Fluorescence lifetime
τ_D(slow/fast)	Diffusion time (slow/fast component)
τ_{Trip}	Triplet time

1 Introduction

Development of multicellular organisms from a single cell requires the specification of cell types (Waddington, 1942), by the expression of distinct sets of genes with spatial and temporal precision. Controlling the onset of new transcriptional programmes is regulated by an interplay of different factors, including the concentration of specific transcription factors (TFs) and chromatin organisation (Gonzalez-Sandoval and Gasser, 2016). A key example is the reprogramming of differentiated cells such as fibroblasts to become pluripotent stem cells, induced by the expression of master TFs OCT4, KLF4, SOX2, and C-MYC (Takahashi and Yamanaka, 2006).

1.1 Transcription factors

TFs are proteins which regulate transcription through their binding to target DNA sequence motifs at regulatory elements such as promoters and enhancers (Isbel et al., 2022). They then recruit cofactors to modify chromatin and recruit RNA polymerase II (Pol II). TFs families are defined by their DNA binding domain (DBD), which typically recognise 6-12 base pairs (bp) (Bilu and Barkai, 2005). TFs will have a specific binding affinity for different DNA motifs (Grossman et al., 2017). Besides their DBDs, other features allow them to recognise and bind sequences in different ways. For example, TFs of the hormone receptor family, such as the glucocorticoid receptor, respond directly to signalling, while others like basic helix-loop-helix (bHLH) TFs such as TWIST1 require dimerisation (**Table 1.1**,(Auer et al., 2020)).

Table 1.1 Overview of selected TF families and their DNA binding characteristics

taken from (Auer et al., 2020).

TF DNA-binding domains	Structural basis for DNA binding	Examples	References
Helix-turn-helix	This motif consists of four α-helices and an N-terminal flexible arm. The third α-helix forms base-specific contacts with the major groove of the DNA. The N-terminal flexible arm interacts with the minor groove of DNA in a sequence-specific manner. The turn between the first and second helix interacts with the DNA backbone.	PAX genes (e.g. PAX6), POU genes (e.g. OCT4), HOX genes (e.g. HOXA1), DUX genes (e.g. DUX4), SOX genes (e.g. SOX2)	(Gruschus et al., 1997, Holland et al., 2007, Kissinger et al., 1990, Qian et al., 1993)
C2H2-zinc finger	The zinc finger domain contains a β-sheet and an α-helix, stabilised by a zinc ion between them. Three amino acid residues in the α-helix bind a DNA major-groove triplet. Multiple zinc finger domains allow binding of extended DNA sequences.	CTCF, PRDM1, GLI genes (e.g. GLI 1), MTF genes (e.g. MTF-1), ZAS family (e.g. HIVEP1)	(Chen et al., 1999, Elrod-Erickson et al., 1996, Keller and Maniatis, 1992, Klug, 1999, Maekawa et al., 1989, Najafabadi et al., 2015, Pavletich and Pabo, 1991, Pavletich and Pabo, 1993, Radtke et al., 1993)
Basic Helix loop helix	These contain two amphipathic α-helices separated by a linker region (the loop), which can be of variable length. TFs containing this domain can form both homo- and heterodimers via interactions between the hydrophobic residues on the corresponding surfaces of the two helices.	TCF class (e.g. TCF4), MYC family (e.g. c-MYC), MYF genes (e.g. MYOD1), AS-C genes (e.g. MASH-1)	(Cao et al., 2002, Davis et al., 1990, Davis et al., 1987, Krause et al., 1990, Meredith and Johnson, 2000, Murre et al., 1989, Sun and Baltimore, 1991)
Basic leucine zipper	The TFs bind to DNA via basic 'arms' adjacent to the leucine zipper protein dimerization domain. Dimerization, whereby the leucine residue	AP-1 genes (e.g. FOS, JUN, CRE genes e.g. CREB4), C/EBPA, BACH genes (e.g.	(Bohmann et al., 1987, Dang et al., 2008, Ellenberger et al., 1992, Landschulz et al., 1988, O'Shea et al., 1991, Oyake et al., 1996, Petrovick et al.,

	interactions between the right-handed amphipathic α-helices of the two dimerization domains form a coiled-coil dimer, is key to DNA binding and transcriptional regulation. TFs can form homo- or heterodimers.	BACH1), c-MYC, GCN4	1998, Sassone-Corsi et al., 1988)
Nuclear hormone (steroid) receptor	Receptor TFs bear a conserved DNA-binding region and specific hormone-binding region at the C termini. Ligand binding can cause nucleo-cytoplasmic translocation and affect the ability of these TFs to bind DNA. The α-helices of the DNA-binding domain contact DNA half sites. Homo- or heterodimers regulate transcription as co-activating or co-repressing complexes.	Homodimeric: Glucocorticoid Receptor, Mineralcorticoid Receptor, Progesterone Receptor, Estrogen Receptor, Androgen Receptor, Triiodothyronine Receptor Heterodimeric: Retinoic X Receptor, Retinoic Acid Receptor genes (RAR-α,β,γ), Vitamin D Receptor	(Chandra et al., 2008, Giguere et al., 1987, Green et al., 1986, Hollenberg et al., 1985, Lippman et al., 1973, Luisi et al., 1991, Mangelsdorf et al., 1990, Miesfeld et al., 1986, Petkovich et al., 1987)

1.1.1 Searching for binding sites in chromatin

A TF's mode of target-site search, DNA binding kinetics and residence time affect transcription dynamics. DNA binding kinetics are affected by factors such as the relative concentration of TF and target site, and their binding affinity (Levine, 2010). TFs have individual target site search dynamics (i.e. sampling the nucleus to different extents by non-specific binding), which can depend on the chromatin state of the target (Izeddin et al., 2014) (section 1.2). In general, TF diffuse in the nucleus and undergo transient, perhaps electrostatic, interactions with chromatin, to search for their cognate DNA binding sites (**Figure 1.1**A) (Chen et al., 2014b, Elf et al., 2007, Liu et al., 2014a, Slutsky and Mirny, 2004, Voss et al., 2011, Vukojevic et al., 2010).

These transient TF-DNA interactions have been studied by microscopy techniques such as Fluorescence Correlation Spectroscopy (FCS) and Single Molecule Tracking (SMT), which can measure the fraction and speed of diffusing TF molecules. More detail on microscopy techniques used to study TF-chromatin binding dynamics can be found in sections 1.3.2-1.3.3.
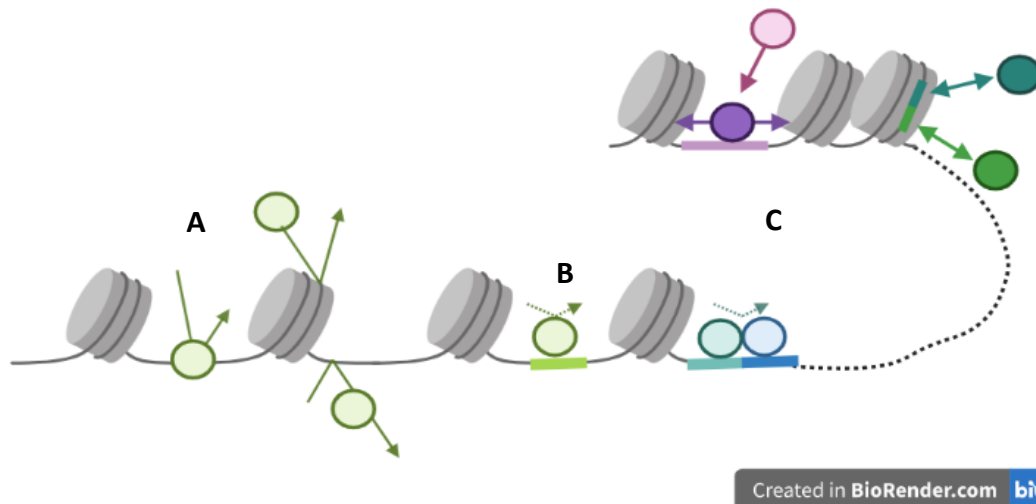
Figure 1.1 Transcription factor DNA binding dynamics and TF-TF interactions.

A) Transcription factors (TFs, light green) diffuse around the nucleus, and transiently bind to DNA by e.g. non-specific electrostatic interactions to search for their binding site in chromatin (Chen et al., 2014b, Elf et al., 2007, Liu et al., 2014a, Slutsky and Mirny, 2004, Voss et al., 2011, Vukojevic et al., 2010). B) TFs bind specifically to their cognate DNA motif, with seconds-range residence times (Chen et al., 2014a, Gebhardt et al., 2013, Mazza et al., 2012, Raccaud et al., 2019). C) TF binding affinity and location are modulated by other TFs (Spitz and Furlong, 2012). TFs may dimerise (Vamosi et al., 2008) or co-bind adjacent motifs (blue) (Boyer et al., 2005), jointly compete with histones by simultaneous transient binding (dark green) (Miller and Widom, 2003, Voss et al., 2011), or bind hierarchically with a master TF followed by a tissue-specific TF (pink) (Mullen et al., 2011, Ravasi et al., 2010).

By contrast, specific binding interactions between the TF and the DNA target site are mediated by recognition of DNA bases by weak dipole interactions, as well as DNA shape (Rohs et al., 2010). Seconds-range TF residence times have been defined by SMT and Fluorescence Recovery After Photobleaching (FRAP) (**Figure 1.1**B) (Chen et al., 2014a, Chen et al., 2022, Gebhardt et al., 2013, Izeddin et al., 2014, Mazza et al., 2012, Raccaud et al., 2019), reviewed in (Auer et al., 2020, Liu and Tjian, 2018). Mutations to the DBD of p65 altering only slow DNA binding dynamics (Callegari et al., 2019) support the notion that cognate site search and binding are independent processes. It is likely that TF-chromatin binding dynamics do not always fall within the discrete categories of slow and fast diffusion, as for example SMT of CTCF and FOXA1 suggested better fitting by a power-law (Garcia et al., 2021). In terms of function, however, transcription seems to scale with TF residence time, rather than occupancy (Callegari et al., 2019, Trojanowski et al., 2022).

1.1.1.1 Transcription Factor interactions

The activity of multiple TFs is integrated in Gene Regulatory Networks (GRNs) to drive cell-type specific transcriptional programmes. The interplay of TFs is therefore a key part of their function (reviewed in (Spitz and Furlong, 2012)). The network of direct and indirect interactions within each cell's complement of TFs tunes gene expression by modulating TF target site search and binding kinetics. A further aspect is the extent to which DNA motif grammar (i.e. the relative position of motifs) facilitates TF interactions in the assembly of TFs at a regulatory element, versus TFs themselves acting as a scaffold, (reviewed in (Spitz and Furlong, 2012)). Models range from the enhanceosome, in which the DNA motif positions dictate TF interactions, or the billboard, where a subset of motifs with less constrained positions is bound, to a more combinatory model of TF interactions and DNA together acting as a scaffold.

This means that overlapping spatiotemporal domains of TF expression can lead to developmental patterning, as studied extensively in *Drosophila* segmentation (Ip et al., 1992, Stanojevic et al., 1991). Yet how TF interactions regulate gene expression

depends on the individual and combinatorial function of TFs, in the context of chromatin (section 1.2). For example, some TFs may act as broadly-expressed facilitators for narrowly-expressed specifiers (Ravasi et al., 2010), or as master TFs recruiting cell-type specific TFs (Mullen et al., 2011).

1.1.1.2 Modes of TF-TF interactions

TFs can dimerise via their activation domain (AD) to form heterodimers, e.g FOS/JUN (Pernus and Langowski, 2015, Vamosi et al., 2008) and RAR/RXR (Reho et al., 2020), or homodimers including FOS (Szaloki et al., 2015) and OLIG2 (Oasa et al., 2020) (**Figure 1.1**C). These examples have been studied by Fluorescence Cross-Correlation Spectroscopy (FCCS) and Foerster Resonance Energy Transfer (FRET) (see sections 1.3.4,1.3.5,1.3.6 for more detail). *In vitro* techniques such as gel shift assays have also been used to show that PAX6 and SOX2 form a complex on the DC5 eye enhancer (Kamachi et al., 2001). Intrinsically disordered regions (IDRs) may also mediate TF interactions with varying degrees of specificity, depending on the ordered nature of the partner's binding domain (reviewed in (Ferrie et al., 2022)). For example, NANOG may oligomerise via its C-terminal IDR (Choi et al., 2022).

While static techniques like ChIP-seq can highlight TF occupancy at adjacent cognate sites (e.g. SOX2, OCT4, and NANOG in embryonic stem cells (ESCs) (Boyer et al., 2005)), co-occupancy does not always translate to direct interactions. TFs may bind sequentially (**Figure 1.1**C), such as SMAD2/3 being recruited by OCT4, MYOD1, or PU.1 (Mullen et al., 2011), and SOX factors recruiting β-catenin (Mukherjee et al., 2022a). A TF such as HMGI may facilitate others' binding by causing DNA architecture to change (Falvo et al., 1995) or increasing chromatin accessibility (Mullen et al., 2011). In other cases, TFs can help each other to bind by each interacting with DNA transiently (**Figure 1.1**C); the high dissociation rate of one TF creates an opportunity for others to bind. This has been described in the assisted loading model, such as the Estrogen Receptor pBox protein binding to the Glucocorticoid Response Element after the Glucocorticoid Receptor bound there transiently to recruit the SWI/SNF (BAF) chromatin remodelling complex (Voss et al.,

2011). Similarly in the collaborative competition model, LexA, TetR and Gcn-4 TFs jointly compete with histones (Miller and Widom, 2003). Finally, cofactors such as p300 or the Mediator complex could bridge TF interactions (Merika et al., 1998, Spitz and Furlong, 2012).

1.1.1.3 Function of TF-TF interactions

TF interactions affect levels and specificity of gene expression by modulating each-others' binding kinetics, for example by changing their affinity for a DNA binding site. The loss of transcriptional activation, but not binding, upon removal of p65's AD, suggests that direct TF interactions may increase transcriptional activation by extending TF residence times (Callegari et al., 2019, Trojanowski et al., 2022). IDR interactions can also facilitate DNA target search and binding, perhaps by local increases in TF concentration, as seen for Bicoid binding to low affinity sites in *Drosophila* embryos (Mir et al., 2017). A TF's motif affinity or binding specificity can further be partner-dependent, such as Hox TFs modulating Extradenticle specificity along the *Drosophila* Anterior-Posterior axis (Slattery et al., 2011). This allows different combinations of TFs to work together at tissue-specific enhancers to ensure correct patterns of gene expression. One example of this is OCT4 partnering with SOX2 in pluripotent cells, then switching to SOX17 to specify endoderm (Aksoy et al., 2013). In *Drosophila*, pMAD binds with Tinman in the dorsal mesoderm, but with Scalloped in the wing imaginal disc (Guss et al., 2001, Lee and Frasch, 2005, Xu et al., 1998). This partner-dependent TF activity can even be harnessed in reprogramming, as co-expression of ATOH1 with GFI1 and POU4F3 turns it into a specifier for inner ear hair cells rather than neuronal cells (Costa et al., 2022).

Expression patterns also involve TFs competing for the same motifs, such as KLF4 and ZFP281 driving opposing mESC states (Hu et al., 2022). In limb bud development, *Shh* expression levels and domains are fine-tuned by the combinatorial action of activating TFs ETS1/GABPA and repressing TFs ETV4/5 on the ZRS enhancer (Lettice et al., 2012).

8

Yet as detailed, interacting TFs need neither have the same activity, nor bind together. Indirect or hierarchical TF interactions often involve a master TF causing changes to chromatin accessibility and recruiting specific TFs (e.g. SMAD2/3 recruited by OCT4, MYOD1, or PU.1 in different cell types (Mullen et al., 2011)), or priming a region for later occupancy by specific TFs (e.g. SOX2 is replaced by SOX4 in pre-B cells (Liber et al., 2010), and FOXA1 replaces FOXD3 in endoderm differentiation from ESCs (Xu et al., 2009)). Early in reprogramming these TFs may also collaborate, as OCT4, SOX2, and KLF4 are enriched at co-bound reprogramming genes in closed chromatin (Soufi et al., 2012). However, these interactions are context-dependent, as SOX2 increases OCT4 chromatin binding in ESCs (Biddle et al., 2019, Chen et al., 2014a), whereas OCT4 may facilitate SOX2 binding only to nucleosomal targets (Li et al., 2019). Thus, TF interactions, such as master TFs facilitating the binding of cell-type specific TFs, can kick-start specification by modulating the chromatin context. Further direct and indirect TF interactions, between cell-type specific combinations, then continue to drive GRNs to achieve differentiation.

1.1.2 TF Chromatin Sensitivity

Although the number of TF molecules in a nucleus has been shown to exceed the number of binding sites by a factor of 10 (MacQuarrie et al., 2011, Simicevic et al., 2013), most binding sites remain unbound (Hansen et al., 2012, Slattery et al., 2014). TF binding specificity must depend on factors in addition to DNA binding affinity and TF concentration (Isbel et al., 2022). Global and local chromatin accessibility will make some binding sites more available for binding (section 1.2) – most TFs preferentially bind to 'open' chromatin (Liu et al., 2017). However, TF sensitivity to chromatin varies not only between TFs, but also for the motifs bound by a TF.

Chromatin sensitivity is the affinity of a TF for a binding site within a nucleosome (Isbel et al., 2022). Only about 4 consecutive bp of DNA wrapped around a nucleosome are solvent-facing, so less than 10% of nucleosomal DNA is accessible

(Matsumoto et al., 2019, Michael and Thoma, 2021). TF binding will therefore be sensitive to nucleosome positioning - most TFs can bind their motif at the entry/exit sites of nucleosomes (Zhu et al., 2018) where nucleosome breathing (spontaneous unwrapping) exposes DNA motifs most (Li et al., 2005, Li and Widom, 2004, Polach and Widom, 1995). Further, TF structure determines how much unwrapping needs to happen to reduce steric hindrance between TF and histones, and the impact of motif position and orientation (Donovan et al., 2023, Tims et al., 2011). Gal4, a zinc finger (znf) protein which contacts DNA in the major groove, binds with higher affinity at sites further outside nucleosome as measured by single molecule FRET (smFRET) and Electrophoretic Mobility Shift Assay (EMSA) (Donovan et al., 2023). Simulations suggest that ordered binding of first SOX2 (contacting the minor groove) then OCT4 (contacting the major groove), to adjacent nucleosomal motifs, is kinetically favoured by taking advantage of nucleosome breathing at entry-exit site (Kulic and Schiessel, 2008, Mondal et al., 2022). Accordingly, fewer TFs can bind at the dyad, or bind periodically to exposed parts of a motif (Michael and Thoma, 2021). This speaks to the importance of factors able to make chromatin accessible for transcription – nucleosome remodelers and pioneer TFs.

1.1.3 Pioneer transcription factors

Pioneer transcription factors (PTFs) can bind their motifs when these are packaged into nucleosomes and can make chromatin more accessible for other TFs either by direct action or by recruiting chromatin remodelers. PTFs regulate changes to transcriptional programmes during differentiation, reprogramming, or in response to environmental signals (Larson et al., 2021, Zaret, 2020). In early mouse embryogenesis, chromatin accessibility increases concomitantly with increasing OCT4 and SOX2 chromatin binding stability (Gao et al., 2018, Ladstatter and Tachibana, 2019, Li et al., 2018, Wu et al., 2016), and OCT4 was shown to increase accessibility in the 8-cell embryo (Lu et al., 2016). Further, chromatin accessibility is sensitive to OCT4 and SOX2 levels, which influences ESC differentiation (Strebinger et al., 2019).

1.1.3.1 Nucleosome engagement

PTFs seem to have unique properties, affected by how they engage with nucleosomal DNA target sites, while avoiding steric hindrance from histones and the other DNA gyre. DBD, motif position, interactions and co-factors all influence PTF-nucleosome interactions. **Figure 1.2**A, taken from (Luzete-Monteiro and Zaret, 2022), outlines modes of nucleosome binding exhibited by known PTFs. For example, the small DBD of homeodomain and forkhead TFs binds in individual DNA grooves, to allow the binding of periodic motifs (Michael and Thoma, 2021, Zhu et al., 2018). PTFs like OCT4, which has two DBDs connected by a flexible linker, can even span across DNA gyres to bind motifs in both simultaneously (Zhu et al., 2018). SOX family TFs prefer binding to the dyad, avoiding clashes as here only one gyre of DNA is wound – and perhaps aiding the DNA distorting activity of SOX factors (Dodonova et al., 2020, Donovan et al., 2019, Michael et al., 2020). Finally, the entry-exit region of nucleosomes is preferred by many PTFs and non-pioneer TFs as nucleosome breathing aids binding – particularly for bHLH and basic leucine-zipper (bZIP) PTFs with larger DBD α -helices (Luzete-Monteiro and Zaret, 2022, Michael and Thoma, 2021). OCT4 can additionally bind at the entry-exit site, showing that PTFs have flexible binding behaviour dependent on motif position and orientation as well as interaction partners. For example, OCT4 and SOX2 can bind nucleosomes both at periodic motifs and the dyad, and OCT4 also binds the entry-exit site (Michael and Thoma, 2021).

Outward facing sequence motifs are commonly preferred - including by GATA3, SOX2, OCT4, p53, and Rap1 - to prevent clashing with histones or the adjacent DNA gyre (Mivelaz et al., 2020, Roberts et al., 2021, Tan and Takada, 2020, Yu and Buck, 2019). Indeed, DBDs with short α-helices help PTFs to easily contact DNA at the outer nucleosome surface (Fernandez Garcia et al., 2019, Luzete-Monteiro and Zaret, 2022). Some PTFs, such as ETX and CREB-bZIP, may further require a specific motif orientation to avoid steric hindrance between its non-DBD domains and the nucleosome (Zhu et al., 2018).

Flexibility in motif binding is advantageous. For example, OCT4 and KLF4 can engage with partial motifs. OCT4 binds a partial motif on nucleosomes with its POU-specific (POU$_s$) DBD, while the second homeodomain DBD (POU$_{HD}$) remains unbound (**Figure 1.2**B) (Michael et al., 2020, Soufi et al., 2015). Accordingly, OCT4 can bind motifs irrespective of their position or orientation (Li et al., 2019). SOX2 and C-MYC are able bind flexibly to degenerate or incomplete motifs by having DBDs which remain disordered when unbound. This may reduce steric clashes between the partially unbound DBD and the nucleosome (Luzete-Monteiro and Zaret, 2022, Michael et al., 2020, Nishimura et al., 2020, Soufi et al., 2015). This suggests that some PTFs may be more effective at binding to nucleosomes than others. Homeodomain PTFs may for example help PTFs with DBDs lacking the aforementioned α-helices (Fernandez Garcia et al., 2019).
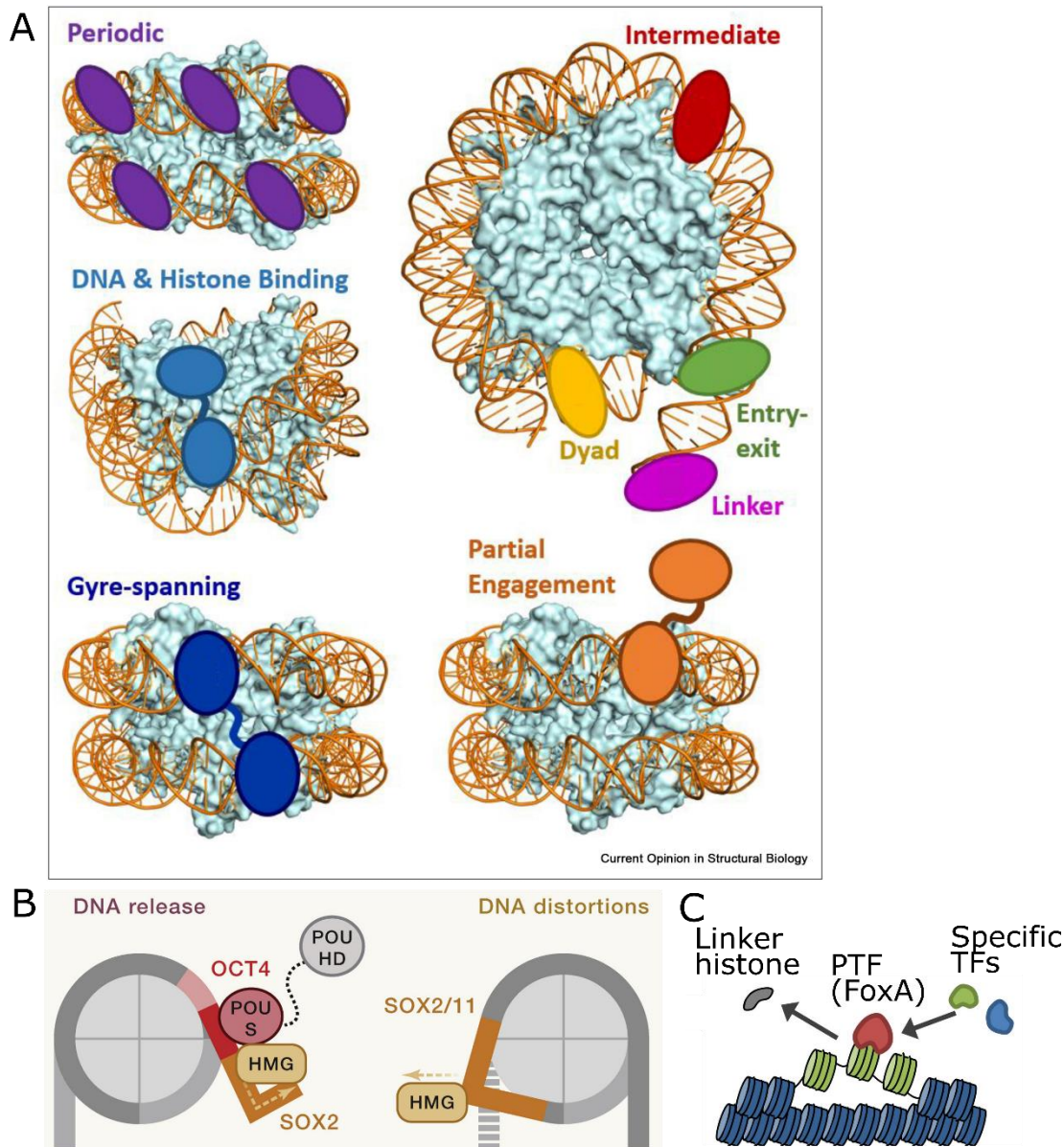
Figure 1.2 PTF nucleosome binding and opening.

A) *The mode of PTF-nucleosome engagement depends on the DNA binding domain (DBD), motif position, and interaction partners (Luzete-Monteiro and Zaret, 2022). Homeodomain and forkhead domain PTFs can bind periodically due to small DBDs, while SOX factors prefer to bind at the dyad perhaps to avoid steric clashes with an adjacent DNA gyre for DNA distortion. Base helix-loop-helix (bHLH) and basic leucine-zipper (bZIP) PTFs - and some TFs - bind at the entry-exit site, where there are fewer clashes with histones/ DNA gyres. (cont. over page)*

Other PTFs (e.g. PU.1) are able to bind linker DNA (Frederick et al., 2023) or contact histones (e.g. OCT4 (Tan and Takada, 2020)). PTFs may also contact multiple motifs, or partial motifs, using one or multiple DBDs. Figure taken from (Luzete-Monteiro and Zaret, 2022). **B)** *PTFs may directly open nucleosomes by stabilising transiently unwrapped states, or by distorting DNA, but often require additional PTFs or chromatin remodelers (Luzete-Monteiro and Zaret, 2022). Figure taken from (Michael and Thoma, 2021).* **C)** *PTFs with a winged-helix domain similar to the linker histone, such as FOXA1 and FOXH1, can displace linker histones decompact nucleosome arrays (Iwafuchi-Doi et al., 2016, Pluta et al., 2022). Figure adapted from (Iwafuchi-Doi et al., 2016).*

1.1.3.2 Opening nucleosomes

PTFs also have very different effects on the nucleosome. Nucleosomes may be destabilised simply by PTFs competing with histones for DNA binding, explaining why increasing the concentration of some PTFs extends their pioneering activity (Hansen and Cohen, 2022, Minderjahn et al., 2020). FOXA1 and FOXH1 can bind nucleosome arrays and displace linker histones, due to their winged-helix domain (**Figure 1.2**C) (Cirillo et al., 1998, Iwafuchi-Doi et al., 2016, Pluta et al., 2022). Binding of other PTFs such as SOX2 have been shown to actively distort DNA (Dodonova et al., 2020, Michael and Thoma, 2021) or stabilise transient unwrapping (Donovan et al., 2019) (**Figure 1.2**B). However, NF-kB unwraps nucleosomes without destabilising these (Stormberg et al., 2021). GAF seems to have a unique pioneering activity, independent of chromatin remodelers, which perhaps relates to its oligomerisation and extremely long - 2 minute - chromatin binding residence time (Tang et al., 2022).

This suggests that PTFs must generally interact with other PTFs, non-pioneer TFs, and/or chromatin remodelers, especially to engage with nucleosome arrays and make chromatin accessible. Removal or inactivation of remodelers reduces PTF binding and accessibility – as shown for OCT4-SOX2 and REST upon BAF removal (Barisic et al., 2019, King and Klose, 2017). Similarly, while PU.1 co-operates with

the PTF CEBPA to bind nucleosomes, it must recruit cBAF to decompact chromatin in an ATP-dependent manner (Frederick et al., 2023).

The loss of chromatin accessibility upon acute removal of OCT4 (Friman et al., 2019) or BAF (Iurlaro et al., 2021, Schick et al., 2021) further suggests that both PTFs and remodelers are required continuously, and act dynamically (Isbel et al., 2022). The study of PTF-nucleosome binding is mostly limited to *in vitro* work, measuring binding dynamics to reconstituted nucleosomes (Soufi et al., 2015) or analysing the bound structure of PTFs with nucleosomes (Dodonova et al., 2020, Michael et al., 2020). This also brings with it a significant trade-off between high resolution, using cryo-EM and crystallography, or kinetic information using SPT and FRET *in vitro*. Thus, studying PTF-nucleosome engagement in the different chromatin contexts found in live cells remains challenging.

1.2 Transcription Factors regulate cell identity, in a chromatin context

1.2.1 Chromatin accessibility

Global and local chromatin organisation are major factors affecting TF-chromatin binding, and thereby transcriptional activation (Mansisidor and Risca, 2022). For example, the incorporation of histone variants into nucleosomes affects the availability of specific sequences for transcription factor binding (section 1.1.2). Less stable H2AZ and H3.3-containing nucleosomesare enriched at the transcription start site (TSS) and are associated with high accessibility (**Figure 1.3**C) (Brahma and Henikoff, 2019, Henikoff, 2008, Henikoff, 2009, Kubik et al., 2015, Xi et al., 2011). Nucleosome spacing and turnover are defined by factors such as linker histone levels (Fan et al., 2005), histone stability (Henikoff, 2008) and nucleosome remodelers (Zilberman et al., 2008).

Chromatin accessibility and transcription also correlate with histone modifications (**Figure 1.3**C,D). Acetylation of histone H3, for example, is associated with nucleosome remodelling to provide access for TFs at active regulatory elements

(Lee et al., 1993). Acetyl and methyl groups are deposited by histone acetyltransferases (HATs) such as p300 (Dyson and Wright, 2016) and histone methyltransferases (HMTs), themselves recruited by TFs (Greer and Shi, 2012). Active promoters and enhancers are acetylated at histone 3, lysine 27 (H3K27ac), lysine 9 (H3K9ac), and lysine 122 (H3K122ac), while H3 lysine 4 is tri-methylated at promoters (H3K4me3) and mono-methylated at enhancers (H3K4me1) (Millan-Zambrano et al., 2022, Pradeepa et al., 2016). Actively transcribed gene bodies are marked by tri-methylation of H3 lysine 36 (H3K36me3) (Millan-Zambrano et al., 2022). The combination of histone modifications is interpreted via proteins such as BRD4, which is a 'reader' of acetylation and recruits the core transcriptional machinery (Jang et al., 2005).
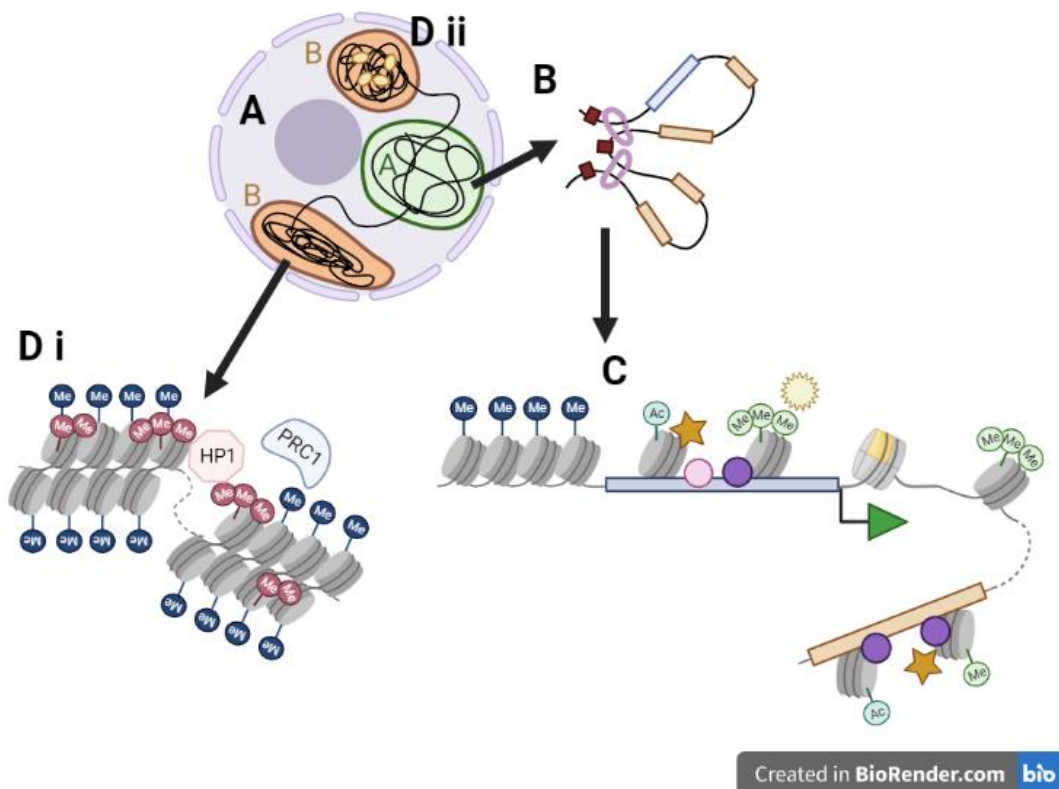
Figure 1.3 Global and local chromatin organisation.

A) Chromatin is organised to into A (green) and B (red) compartments within the nucleus which reflect more permeable, transcriptionally active, euchromatin and impermeable, inactive, heterochromatin domains, respectively (Gonzalez-Sandoval and Gasser, 2016, Klemm et al., 2019, Mansisidor and Risca, 2022). (cont. over page)

B) Regulatory elements can be brought into contact to form topologically associated domains (TADs) by cohesin-mediated loop formation (Bickmore, 2013, Dixon et al., 2012, Kane et al., 2022, Rao et al., 2017), which may allow cell-type specific enhancer-promoter contacts and could mediate transcriptional 'microenvironments' (Boija et al., 2018, Sabari et al., 2018b, Whyte et al., 2013). C) Within TADs, transcription factors (circles) and chromatin remodelers (stars) target gene regulatory elements (promoters in blue and enhancers in orange), to mediate changes in accessibility and deposit histone marks, and the recruitment of core transcriptional machinery for gene expression. Histone variants may also facilitate accessibility, for example H2A.Z and H3.3 at the Transcription Start Site (TSS, green arrow) (Brahma and Henikoff, 2019, Henikoff, 2008, Henikoff, 2009, Kubik et al., 2015, Xi et al., 2011). D) i. Constitutive heterochromatin is most densely packed, marked by H3K9me2 and -me3, cross-linked by Heterochromatin Protein 1 (HP1) (Strom et al., 2021), and DNA is highly methylated. ii. Facultative heterochromatin can change accessibility during development, and may be organised into domains by polycomb repressive complex (PRC1) (Boyle et al., 2020, Illingworth, 2019, McLaughlin et al., 2019, Simon and Kingston, 2013).

1.2.2 Chromatin organisation

Local changes to accessibility happen in a global chromatin context to impact transcription (**Figure 1.3**). While nucleosome density may affect TF search dynamics (Kieffer-Kwon et al., 2017), the increasing number of TFs shown to interact with condensed mitotic chromosomes (e.g. SOX2 (Teves et al., 2016)) suggests that binding is affected by mechanisms in additio to local chromatin accessibility.

This may include the global organisation of chromatin into more or less permeable compartments (Mansisidor and Risca, 2022), and long-range interactions such as enhancer-promoter loops (Bickmore, 2013). The former are also defined as 'A' and 'B' compartments, or transcriptionally active euchromatin and repressed heterochromatin, respectively (**Figure 1.3**A) (Gonzalez-Sandoval and Gasser, 2016,

Klemm et al., 2019)). Heterochromatin can come in different flavours, from very dense constitutive heterochromatin marked by Heterochromatin Protein 1 (HP1) deposited H3K9me2 and -me3 (Strom et al., 2021), to facultative heterochromatin which is more dynamic during development (Williamson et al., 2012) and organised by the repressive polycomb complexes PRC1 and PRC2 (**Figure 1.3**D) (Boyle et al., 2020, Illingworth, 2019, McLaughlin et al., 2019, Simon and Kingston, 2013). Yet while most TFs do not bind in heterochromatin, chromatin compaction need not translate to lower accessibility (Illingworth, 2019, Mieczkowski et al., 2016, Mueller et al., 2017). Global chromatin organisation such as compartments may stabilise cell fate by controlling access for TFs (Soufi et al., 2012) while keeping certain regulatory elements poised for potential later activation.

More locally, topologically associated domains (TADs) formed by cohesin mediated loop extrusion (**Figure 1.3**B) (Dixon et al., 2012, Kane et al., 2022, Rao et al., 2017) increase the probability of transcription-enhancing protein interactions by creating a local enrichment of regulatory elements and TF binding sites (Bickmore, 2013, Morey et al., 2009, Schoenfelder et al., 2010, Sutherland and Bickmore, 2009). Clustering of enhancers, TFs and transcriptional machinery has been observed by microscopy (Liu et al., 2014b, Liu and Tjian, 2018, Sabari et al., 2018a), and is proposed to enhance transcription in so-called 'microenvironments', although their formation, functionality, and relationship to TADs are controversial topics (Boija et al., 2018, Sabari et al., 2018b, Whyte et al., 2013).

Changes in chromatin accessibility and structure have been described through differentiation and in development. For example, nucleosome clutches were shown to change size during ESC differentiation (Gomez-Garcia et al., 2021), and linker histone occupancy increases globally (Perez-Montero et al., 2013). The relationship between chromatin organisation and transcription is particularly obvious during zygotic genome activation (ZGA), when chromatin structure, modifications, and accessibility change globally and locally before widespread transcriptional onset (Liu et al., 2018b, Wu et al., 2016).

1.3 Measuring TF dynamics and interactions by quantitative microscopy

To investigate the activity of TFs in precise developmental transitions, their DNA binding dynamics and interactions must be studied in the context of chromatin, *in vivo*.

Fluorescence microscopy allows fluorophore-tagged molecules to be located in cells and tissues. A fluorophore can absorb a photon to enter the higher energy 'excited' state and, during its return to the lower energy 'ground' state, emits a fluorescent photon. This is visualised in Jablonski diagrams (Jablonski, 1933). Excitation and emission occur at defined wavelengths for each fluorophore. As the emitted photon has less energy, the wavelength of fluorescent light is longer than the excitation wavelength. The difference in excitation/emission wavelengths, termed Stokes Shift, is characteristic to each fluorophore (Stokes, 1852). The cycle of excitation and emission occurs until the fluorophore irreversibly enters a dark triplet state, called photobleaching (Rost, 1991). Though less bright and photostable than organic dyes, fluorescent proteins can be genetically encoded. The basic principle of fluorescence microscopes is to excite fluorophores in the sample using a laser (ideally at the peak of the fluorophore's excitation wavelength spectrum). The emitted photons are then captured using filters set to transmit photons in a given wavelength range given by the fluorophore's emission spectrum. These photons are then collected by detectors which convert the photons to electrons to create an image.

1.3.1 Confocal microscopy

High spatial and temporal resolution are needed to precisely localise and measure the movement of fluorescent molecules. A microscope's resolution is defined as the smallest resolvable distance between two objects. As light spreads out when it travels, the image recorded represents a Point Spread Function (PSF) centred on the object emitting the fluorescence. The pattern of the PSF's lateral intensity

distribution is described by an Airy pattern. The width of the PSF, or full width at half maximum (FWHM), determines the microscope's resolution. Resolution is further limited to the wavelength of light (λ), and is inversely proportional to the numerical aperture (NA) of the microscope's objective lens (Rayleigh criterion). The lateral resolution of a microscope is therefore calculated by $0.6\ \lambda$ /NA. Confocal microscopes use pinholes to improve spatial resolution by focusing the laser beam onto a point in the specimen, and by excluding out-of-focus light emitted from the focal point in the specimen (Minsky, 1988, Petráň et al., 1968). The smaller resultant PSF means that lateral resolution is given by $0.4\ \lambda$ /NA.
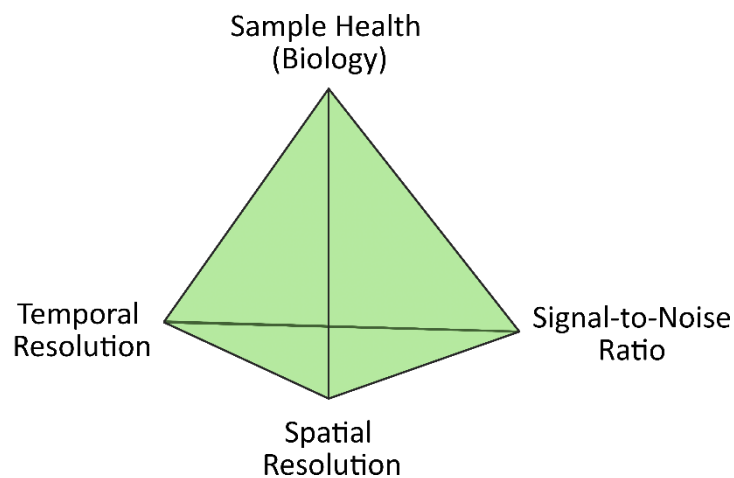
Figure 1.4 Diagram of the 'Pyramid of Frustration' in live microscopy.

Temporal and spatial resolution must be balanced with the signal-to-noise ratio (SNR), as well as the constraints of a live sample which must be protected from photobleaching – for example, the time-frame of cellular processes, and the lowered signal and resolution in thick specimens.

However, spatial and temporal resolution are part of a larger 'pyramid of frustration' encountered particularly in live microscopy (**Figure 1.4**). For example, light scattering becomes a significant problem in thick specimens such as live embryos, leading to lower resolution and signal-to-noise ratio (SNR). Yet the signal cannot be increased by longer illumination schemes with higher laser power, as in addition to the cytotoxic effect of photobleaching, long acquisition times are

constrained by dynamic cellular processes. The SNR can be improved by better optical sectioning using multi-photon microscopy (Denk et al., 1990), or more focused illumination e.g. by narrower beams of light in Single Plane Illumination Microscopy (SPIM) (Huisken et al., 2004), which also increases axial resolution (**Figure 1.5**A).

Improvements to detectors are also needed to attain high photon efficiency – i.e. accurate, high resolution readout - with a low photon budget. Photomultiplier tubes (PMTs) and Avalanche Photodiodes (APDs) or Single Photon Avalanche Diodes (SPADs) use the photoelectric effect to produce electrons from incident photons, and amplify these (Art, 2006). The resultant low noise and short dead-time giving up to <50 picosecond resolution (PicoQuant, 2023) means that PMTs, APDs, and SPADs are commonly used to measure fast processes. However, they suffer from typically low quantum efficiency, and increased gain causes higher dark noise (false detections). Single pixel sampling also limits spatial resolution (Bankhead, 2023). By contrast, charge-coupled devices (CCDs) use an array of metal oxide semiconductors to convert photons to electrons, measuring the accumulated charge at each pixel across the exposure time (Art, 2006, Spring, 2023). CCDs and electron multiplying CCDs (EMCCDs) therefore work better with low signal samples, and provide higher spatial resolution. However the time resolution is limited by collection, readout, and reset of the pixel charge (Bankhead, 2023). The development of hybrid detectors is therefore another key part to overcoming the 'pyramid of frustration' for live quantitative microscopy. For example, the Leica HyD-X detectors have an array of PMT gallium arsenide phosphide (GaAsP) photocathodes coupled to APDs (Becker et al., 2011). This improves sensitivity, but with a reported dead time of <1.5 nanoseconds (ns). Further, cooling detectors lowers dark noise encountered particularly in low-signal samples (Schweikhard, 2020).

1.3.2 Quantitative microscopy techniques to study TF dynamics *in vivo*

While confocal microscopy cannot resolve individual molecules, single photon counting detectors allow quantitative analysis of the signal to study for example the amount, dynamics, and interactions of TFs (**Figure 1.5**B,C). FRAP was first used to study molecule dynamics *in vivo* by photobleaching dye molecules in a region of interest (ROI) and monitoring the rate of fluorescence recovery (Axelrod et al., 1976). Processes such as diffusion and binding cause the exchange of photobleached molecules with intact fluorescent molecules in the ROI. The rate and extent of fluorescence recovery is therefore informative of the binding and/or diffusion dynamics of the labelled molecule. However, FRAP only gives information averaged from a population of molecules, and relies on the assumptions made in the fitting model (Mazza et al., 2012, Mueller et al., 2013, Stasevich et al., 2010). FRAP is better suited to study slow, binding-dominant, processes, rather than fast diffusion (Liu and Tjian, 2018). SMT, by contrast, follows the trajectory of individual molecules. While this makes it a better technique to unpick complex diffusion and binding dynamics, SMT requires sparse labelling e.g. by photo-activatable fluorophores to identify individual molecules, and can be limited by image acquisition times (Liu and Tjian, 2018). SMT has been used to investigate the target-search strategies and cognate site binding of different TFs (Izeddin et al., 2014).

Alternatively, diffusion can be measured by correlating images temporally and/or spatially. Image Correlation Spectroscopy (ICS), and variants such as raster ICS (RICS) (Priest et al., 2019) can be performed with higher fluorophore concentrations, but these are limited to slower diffusion speeds than FCS and SMT. RICS has been used to measure the chromatin binding of the trimeric TF NF-Y (Priest et al., 2021).
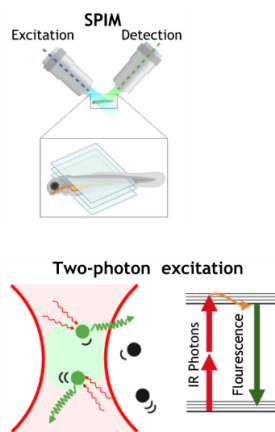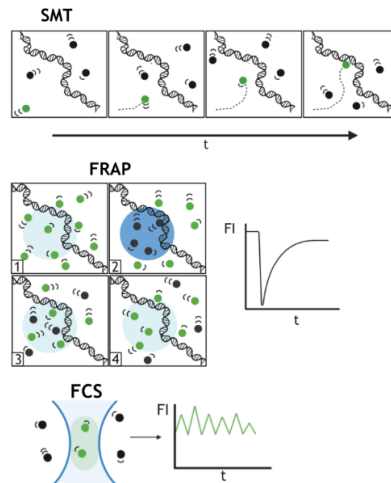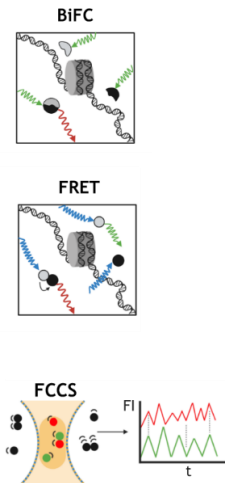
Figure 1.5 Quantitative microscopy methods to study TF behaviour.

A) *Single Plane Illumination Microscopy (SPIM) illuminates the sample with a thin light sheet (0.5-1.5µm) (Huisken et al., 2004), whereas multi-photon microscopy uses two (or more) lower energy (infra-red, IR) photons, reducing out-of-focus excitation (Denk et al., 1990). Both methods improve the SNR for microscopy deeper within a sample.* *B)* *In Single Molecule Tracking (SMT) individual molecules are tracked to measure displacement, and derive diffusion and binding kinetics (Elf et al., 2007). In Fluorescence Recovery After Photobleaching (FRAP) fluorophores in a small section are photobleached, and the fluorescence recovery monitored to derive diffusion and binding kinetics (Axelrod et al., 1976). FCS is explained in Fig. 1.6.* *C)* *In Bimolecular Fluorescence Complementation (BiFC), split fluorophore tags form a complex and emit fluorescence upon interaction (Hu et al., 2002). FCCS and FRET are explained in Figs. 1.7 and 1.8. Adapted from (Auer et al., 2020).*

1.3.3 Fluorescence Correlation Spectroscopy to study chromatin binding dynamics

FCS can be used to study the numbers and diffusion of fluorescently-labelled molecules (Digman and Gratton, 2011, Ehrenberg and Rigler, 1974, Magde et al., 1972, Schwille and Haustein, 2002). Single-photon detectors are used to record the fluctuations in intensity of excited fluorescent molecules within a sub-femtolitre detection volume (observation volume element, OVE) (**Figure 1.6**A). The intensity fluctuation profile ($I(t)$) is compared to itself across different lag-times ($I(t+\tau)$) to create an autocorrelation function (ACF, or $G(\tau)$) (**Equation 1.1**).

Equation 1.1 Autocorrelation equation.

Where I is the fluorescence intensity, t is time, τ is the lag-time

$$G(\tau) = \frac{\langle \delta I(t) \cdot \delta I(t + \tau) \rangle_t}{\langle I(t) \rangle_t^2}$$

This reflects molecule number and dynamics; fast-diffusing molecules will cross the OVE more quickly, leading to fast fluctuations of fluorescence intensity, and so the intensity fluctuation profile will have higher self-similarity at short lag-times. The intensity fluctuations from slow-diffusing molecules will retain high self-similarity at long lag-times. This translates to a right-shift (towards longer lag-times) in ACFs for slower diffusing molecules (**Figure 1.6**B).
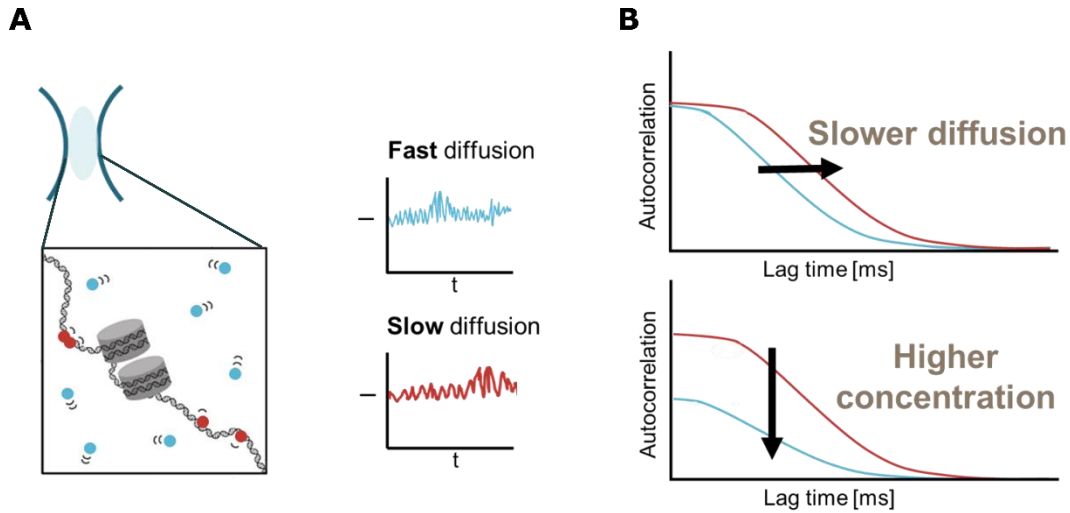
Figure 1.6 Fluorescence Correlation Spectroscopy theory.

 A) *Fluorescently-labelled molecules diffuse into and out of the sub-femtolitre observation volume element (OVE) causing fluctuations in the fluorescence intensity (I) measured over time (t) by single-photon sensitivity detectors. Faster diffusion results in a higher frequency of intensity fluctuations.* **B)** *The fluorescence intensity is compared at different lag times (t+τ) to create an autocorrelation function (ACF) which reflects the speed and concentration of diffusing molecules. Diffusion speed and molecule number are then derived by curve fitting with appropriate models.*

ACFs are then fitted to calculate molecule number and diffusion. To study TF-chromatin binding, ACFs are fit to models with components to reflect freely diffusing and chromatin-bound TF populations (**Equation 1.2**).

Equation 1.2 3D Triplet diffusion model, from Picoquant SymPhoTime software.
Where τ_{Diff} is the speed and ρ is the contribution of diffusing species [i], τ_{Trip} is the triplet state, N is the number of molecules, κ is the OVE structural parameter (length: diameter ratio), and G_{inf} the correlation offset.

$$G(t) = \left[1 + \sum_{j=0}^{n_{Trip}-1} T[j]\left[\exp\left(-\frac{t}{\tau_{Trip}[j]}\right) - 1\right]\right] \sum_{i=0}^{n_{Diff}-1} \frac{\rho[i]}{\left[1 + \left[\frac{t}{\tau_{Diff}[i]}\right]^{\alpha[i]}\right]\left[1 + \frac{\left[\frac{t}{\tau_{Diff}[i]}\right]^{\alpha[i]}}{\kappa^2}\right]^{0.5}} + G_{Inf}$$

An FCS measurement combines information from a population of molecules, such as TFs, which may show a range of diffusive and binding behaviours depending on the chromatin context and binding strength. Fitting models could therefore include multiple components to reflect, for example, free diffusion, anomalous (hindered) diffusion, slow diffusion due to weak electrostatic interactions with chromatin. As with FRAP, the suitability of models to fit population data is difficult to determine, even using mutagenesis to target different putative components. Therefore the most commonly used diffusion model simply has a fast- and slow- component, which correspond to freely-diffusing TF molecules, and chromatin-interacting TF molecules respectively (Mazza et al., 2012).

1.3.3.1 Applications and limitations of FCS to study TF-chromatin binding dynamics

FCS has been used to quantify SOX2 and OCT4 levels and chromatin binding dynamics, to further understand how PTF-chromatin interactions could link to chromatin accessibility (**Table 3.1**). FCS measurements similarly show that OCT4 and SOX2 have more and longer-lasting chromatin interactions in pluripotent cells than in differentiated cells (Lam et al., 2012b, Verneri et al., 2020). FCS has also linked PTF cell-to-cell variability to later cell fate, as OCT4 and SOX2 have longer-lived chromatin binding in cells of the blastocyst that will contribute to the future embryo, whereas CDX2-chromatin interactions are slower in future extraembryonic cells (Kaur et al., 2013). This specification could begin as early as the 4-cell stage, where cells with longer-lived SOX2 chromatin-binding dynamics will later form the inner cell mass (ICM) (White et al., 2016).

But FCS is only suited to study fast dynamics (limited in this by the detector's photon counting resolution alone). Molecules with slow dynamics cannot be studied, as molecules residing within the OVE for a longer time do not create sufficient fluorescence intensity fluctuations within the measurement window for autocorrelation analysis. Further, as slow-moving molecules are more susceptible to photobleaching, they tend to be under-represented. FCS is therefore unable to

detect most specific TF chromatin-binding interactions, which tend to have residence times in the high millisecond or second range (Stasevich et al., 2010). Of note, chromatin itself moves with diffusion times of 100-200 milliseconds (ms), depending on its organisation, when measured by FCS (Wachsmuth et al., 2016). This can convolute the interpretation of fluctuations measured from chromatin-interacting TFs.

Finally, FCS is limited by the requirement for low fluorophore concentrations to detect intensity fluctuations. Sparse labelling techniques are therefore often used, such as ligand titration with HALO- or SNAP- tagged TFs (Chen et al., 2014a) or photo-activateable fluorophores such as paGFP (Kaur et al., 2013). A further challenge for FCS in live 3D samples is depth of focus, which has led to combinations of illumination strategies. For example, SPIM-FCS allowed the comparison of Bicoid chromatin-binding along its concentration gradient in Drosophila embryos (Mir et al., 2017). Similarly, two-photon excitation FCS was used to investigate chromatin association of heat shock factor in polytene nuclei of drosophila salivary glands (Yao et al., 2006).

1.3.4 Quantitative microscopy techniques to study TF interactions

Various techniques are available to study protein-protein interactions, such as *in vitro* biochemical assays based on using a 'bait' protein to detect an interacting 'prey' protein. *In vivo* approaches such as the yeast two-hybrid method tag the proteins of interest with a DBD and a transcription activating domain, to report interaction by transcription of a reporter gene (reviewed in (Ozawa and Umezawa, 2002). But these techniques do not provide spatial or dynamic information on the functional interaction between two proteins. This is the advantage of imaging, although there is often a trade-off between spatial and temporal resolution as well as sensitivity (section 1.3.1). For example, Proximity Ligation Assays visualise interacting proteins *in situ* but require cell fixation and indirect

immunofluorescence (Soderberg et al., 2008), which limits spatial resolution and efficiency.

In vivo fluorescence microscopy can offer high spatial and temporal resolution and is therefore best suited to probe dynamic protein-protein interactions. Three common methods are Bimolecular Fluorescence Complementation (BiFC), FCCS and FRET (**Figure 1.5**). In BiFC, a fluorescent signal is only produced if the two halves of a split fluorophore, tagging the proteins of interest, are reconstituted by the interacting proteins (Hu et al., 2002). This provides low background signal and the potential for high spatial resolution. However, the irreversible reconstitution and delayed fluorescence limit quantification of the interaction kinetics, and non-interacting protein populations cannot be visualised. By contrast, FCCS reports on the dynamics of interacting partners, such as FOS and JUN (Pernus and Langowski, 2015), but spectral bleed-through or cross-talk can lead to overinterpretation of interactions (Bacia and Schwille, 2007, Ng et al., 2018). While FRET cannot report on the diffusion dynamics of interactors, it allows real-time characterisation of stoichiometry, dynamics, and cellular location of protein interactions *in vivo*, including identifying TF interactions (Zhuo and Knox, 2022). smFRET for example showed that the yeast PTF Rap1 loosens nucleosome stacking rather than opening nucleosomes (Mivelaz et al., 2020).

The advantage of imaging techniques is the potential to integrate different spatiotemporal measurements required to understand TF interactions and function. TF diffusion and chromatin binding can be related to oligomerisation and interaction and the local chromatin environment. RICS, FRET, and analysis of fluorescence fluctuations in Number & Brightness (NB), were used together to show NF-Y must trimerise to bind chromatin (Priest et al., 2021). Pair correlation analysis, based on RICS, identifies barriers to diffusion, and was combined with NB to suggest that chromatin compaction affects the diffusion and oligomerisation of HP1-a (Hinde et al., 2011)

.

1.3.5 Fluorescence Cross-Correlation Spectroscopy to study co-diffusion

Pairwise Interactions between freely-diffusing or chromatin-bound molecules can be studied by FCCS (Bacia and Schwille, 2007, Krieger et al., 2014). Two molecules of interest are tagged by spectrally distinct fluorophores and fluorescence intensity fluctuations are simultaneously recorded using two detectors (**Figure 1.7**A). The co-occurrence and co-variance of intensity fluctuations in both channels, analysed by cross-correlation, indicates co-diffusion and therefore interaction between the two molecules (**Equation 1.3**).

Equation 1.3 Cross-correlation equations relative to the A) green B) red channel.

Where I_g, I_r are the green/red fluorescence intensity, t is time, τ is the lag-time.

$$A)\ G_{g-r}(\tau) = \frac{\langle \delta I_g(t) \cdot \delta I_r(t+\tau) \rangle_t}{(I_g(t))(I_r(t))_t} \qquad B)\ G_{r-g}(\tau) = \frac{\langle \delta I_r(t) \cdot \delta I_g(t+\tau) \rangle_t}{(I_r(t))(I_g(t))_t}$$
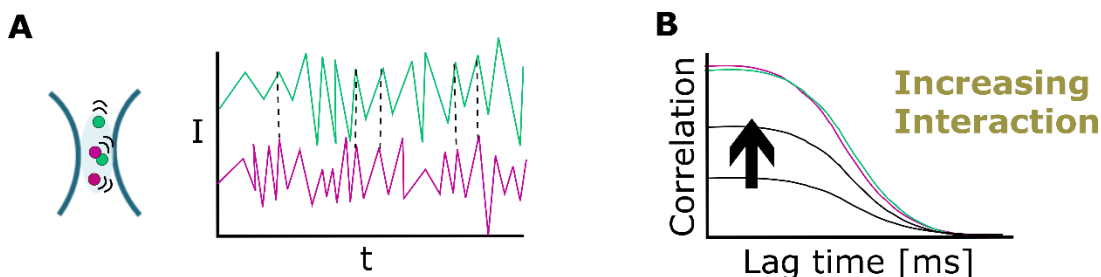
Figure 1.7 Fluorescence Cross-Correlation Spectroscopy theory.

A) Proteins of interest labelled with spectrally distinct fluorophores diffuse through the OVE, causing fluctuations in fluorescence intensity (I) over time (t). Fluorescence intensity traces are compared between channels by cross-correlation. Co-diffusing molecules (interacting) will have more similar traces (dotted line). B) The concentration of interacting molecules is proportional to the y-intercept of the cross-correlation function (CCF).

The amplitude of the cross-correlation function (CCF) is proportional to the extent of interaction (**Figure 1.7**B). Comparison of cross- and auto-correlation curves in the

Relative Cross-Correlation amplitude (RCCA) gives the proportion of co-diffusing (interacting) molecules relative to each channel (**Equation 1.4**).

Equation 1.4 Relative Cross-Correlation Amplitude, relative to the A) green B) red channel.
Where $G_{CC}(0), G_r(0)$, $G_g(0)$ are the y-intercepts of the CCF, red channel ACF, and green channel ACF, respectively.

$$A) \; RCCA(g) = \frac{G_{CC}(0)}{G_r(0)} \qquad B) \; RCCA(r) = \frac{G_{CC}(0)}{G_g(0)}$$

1.3.6 Foerster Resonance Energy Transfer to study interactions

In FRET, changes in the fluorescence of 'donor' and 'acceptor' fluorophores, tagging two molecules of interest, are monitored. An excited donor can transfer energy non-radiatively to an acceptor (**Figure 1.7**A). This quenches the donor, decreasing its fluorescence intensity and lifetime, while the acceptor's fluorescence intensity increases. FRET requires the donor and acceptor to be within 10 nanometres (nm), and that their emission/excitation spectra overlap (Forster, 1946). As the proximity and degree of spectral overlap affect efficiency of energy transfer, FRET can be used to measure the distance and extent of interaction between two molecules (Stryer and Haugland, 1967). However FRET efficiency also depends on other factors, such as the refractive index of the medium between donor and acceptor, and their relative orientation (Jares-Erijman and Jovin, 2003, Knox and van Amerongen, 2002). These can lead to the underestimation of interactions.

Intensity-based FRET assays include calculating the ratio of donor fluorescence intensity in the presence or absence of the acceptor (FRET efficiency), or fluorescence intensity of the acceptor in the presence or absence of the donor, when using a laser wavelength that excites the donor (sensitised emission; SE-FRET) (Bastiaens, 1998, Halavatyi and Terjung, 2017, Jares-Erijman and Jovin, 2003) (**Table 4.1**). Intensity-based FRET is sensitive to photobleaching and the stoichiometry of donor and acceptor. Moreover, in 3D samples, aberrations caused by non-uniform

sample illumination can affect intensity-based measurements (Datta et al., 2020). Good controls are challenging, requiring complex assays and mathematical corrections (reviewed in detail by (Jares-Erijman and Jovin, 2003)). For example, other assays alter the ability of donor or acceptor to FRET, including depleting the donor ground state by oxygen depletion, or photobleaching the acceptor (if this is a fluorophore).
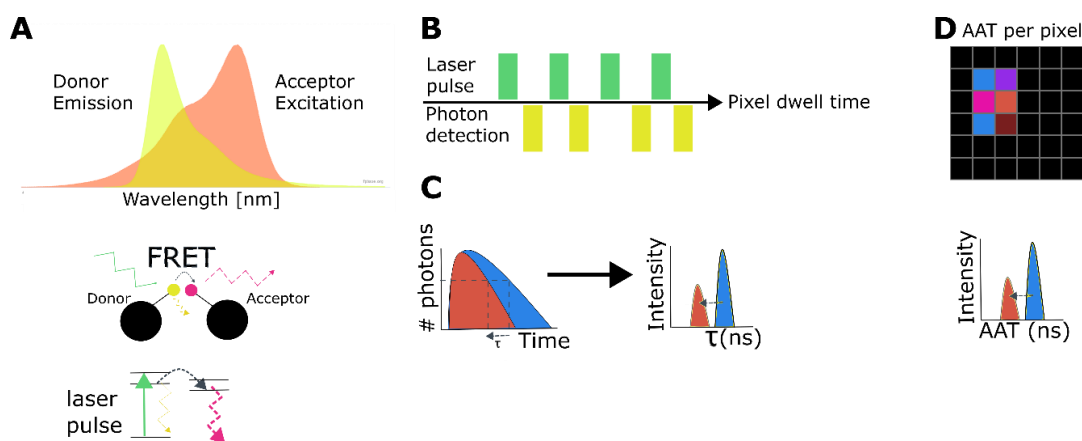
Figure 1.8 Foerster Resonance Energy Transfer and Fluorescence Lifetime.

A) Foerster Resonace Energy Transfer (FRET) is the non-radiative energy transfer between a <10 nm apart donor and acceptor fluorophore pair with overlapping emission and excitation spectra; the donor fluorescence intensity and lifetime (τ) decrease, while the acceptor fluorescence intensity increases. B) τ is measured by timing photon arrival at the detector after each laser pulse. C) In fluorescence lifetime imaging microscopy (FLIM), the exponential decay of individual detected photons over excitation cycles (left, blue) is fitted to derive τ (right, blue). FLIM-FRET measures the reduction in donor τ when in presence of the acceptor (red). D) In Average Arrival Time (AAT) the average time of photon arrival is recorded per pixel. This provides a semi-quantitative way to compare FRETing (red) and non-FRETing conditions (blue) (Roberti, 2020).

1.3.6.1 Measuring interactions by fluorescence lifetime-based FRET

Fluorescence lifetime (τ) is the time spent by a fluorophore in its excited state, between excitation and emission. As the donor is in the excited state for a shorter

time, and emits fewer photons, the donor τ is reduced upon FRET. Lifetime-based FRET assays are a more robust way to quantify FRET, as τ is not susceptible to photobleaching or affected by the relative donor/acceptor stoichiometry, or the scattering of light in 3D samples (Datta et al., 2020). However some fluorophores are sensitive to the cellular environment, so that τ can also be an indicator of chromatin compaction for example (Auduge et al., 2019). Typical Fluorescence Lifetime Imaging Microscopy (FLIM) -FRET assays include comparison of donor τ in the presence vs. absence of the acceptor, and recovery of donor τ upon acceptor photobleaching (AccPb).

Traditional time-domain FLIM calculates τ by fitting the exponential decay of photon arrival times detected relative to each laser pulse by time-correlated single photon counting (TCSPC) detectors (**Figure 1.8**B,C). Modulated lasers and detectors are required to measure FLIM in the frequency domain (Gratton et al., 2003). Again, as a method reporting on an averaged population of molecules, a model with correct assumptions must be chosen – meaning that the fluorescence lifetime characteristics of the donor must be known before comparisons can be made. For example, while it is simplest to use a two-component bi-exponential model to calculate τ and the fraction of FRETing and non-FRETing donor molecules, the donor's characteristic fluorescence decay could itself be multi-exponential, and further convoluted by the detector (Instrument Response Function, IRF) (Xiao, 2021). For accurate τ calculation, TCSPC requires high photon counts and SNR, which depend on the τ precision and dynamic range (Li et al., 2010).

Collecting sufficient photon counts for a high SNR poses a particular challenge for live 3D samples with lower signal. Acquisition times for TCSPC FLIM-FRET would be incompatible with the fast development of zebrafish embryos, for example. Here, recent developments in fit-free FLIM and FLIM-FRET metrics are useful; fewer photons are required for accurate τ calculation, speeding up acquisition and computation times. Deep learning algorithms such as the extreme learning machine (ELM, (Zang, 2022)) can accurately extract τ from mono- and bi-exponential

fluorescence decays. Although ELM reduces computation time, it still relies on decay curves generated using time-tagged or -gated detectors, and donor fluorescence decay characteristics and IRF must still be accounted for. Alternative approaches such as phasor plots (Digman et al., 2008, Jameson, 1984, Leray et al., 2012) avoid these considerations and can effectively filter out background fluorescence, albeit at the cost of some spatial information (Padilla-Parra et al., 2008).

To date, the simplest way to assay lifetime-based FRET is by comparing the per-pixel average arrival time (AAT) of donor photons in the absence vs. presence of the acceptor (**Figure 1.8**D,**Equation 1.5**).

Equation 1.5 Average Arrival Time, AAT, per pixel.

Where AT (Arrival time) is photon detection time – laser pulse time, and N = total no. photons.

$$AAT = \frac{\sum AT}{N}$$

The arrival time of donor photons at the detector is measured relative to the laser pulse, and is affected by the τ. As AAT is therefore τ-related, but requires no extra computation, it can be used for semi-quantitative τ comparisons (Roberti 2020). Further, the extent of donor-acceptor interaction can be estimated using the mfD (minimum fraction of interacting donor), which uses the ratio of donor-alone AAT vs. donor+acceptor AAT (**Equation 1.6**) (Padilla-Parra et al., 2008, Padilla-Parra et al., 2009).

Equation 1.6 Minimum Fraction of Donor Interaction, mfD, per pixel.

Where D is the donor AAT in absence of the acceptor, and DA is the donor AAT in presence of the acceptor.

$$mfD = \frac{1 - \frac{DA}{D}}{(\frac{DA}{2D} - 1)^2}$$

The ease of computation means that on-the-fly maps of AAT and mfD can be generated (Alvarez, 2022, Roberti, 2020). However, as averaging photon arrival times across each pixel limits the AAT resolution (0.1 ns for the Leica Stellaris 8), FRET can only be detected for high FRET efficiency pairs with a large donor τ shift.

1.4 Zygotic Genome Activation

The activation of transcription by maternally deposited TFs from a previously silent genome makes ZGA an excellent model in which to study the mechanism by which the interplay of factors, such as TFs and chromatin state, determine cell-fate transitions. Across species, maternally deposited factors drive the beginning of development. Species load different sets of maternal mRNAs, with variable gene coverage – from ~40% in mouse, to ~70% in zebrafish *(Danio rerio)* and ~75% in *Drosophila*, to drive general cell processes and initial patterning in the embryo (reviewed in (Vastenhouw et al., 2019)). During the Maternal-to-Zygotic Transition (MZT) two tightly controlled processes occur: clearance of certain maternally deposited mRNAs, and the onset of zygotic transcription at ZGA (**Figure 1.9**A, reviewed in (Tadros and Lipshitz, 2009, Vastenhouw et al., 2019)).
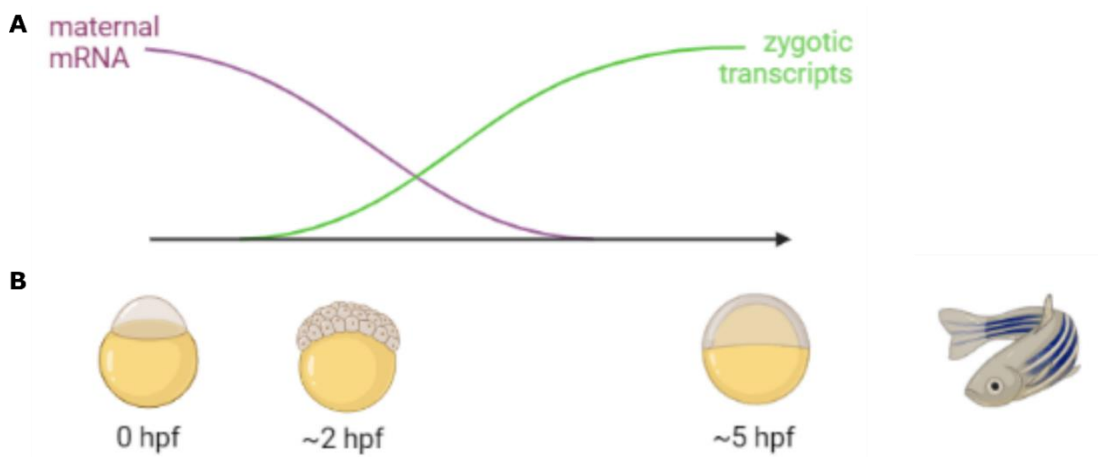
Figure 1.9 Dynamics of maternal mRNA clearance and zygotic transcription at the Maternal-To-Zygotic Transition (MZT*).*

A) *Maternally deposited factors (mRNA and proteins) drive initial development – including the onset of transcription at Zygotic Genome Activation (ZGA). Maternal mRNA expression regulates ZGA by timely increased translation efficiency followed by transcript degradation. Zygotic gene expression increases gradually. **B)** In zebrafish, the first zygotic transcripts are detected approximately 2 hours post fertilisation (hpf), and ZGA ends ~5 hpf (shield stage) before gastrulation begins. (Reviewed in (Vastenhouw et al., 2019).*

Most genes expressed at ZGA (ZGA genes) are developmental regulators such as TFs or micro RNAs (De Renzis et al., 2007, Lee et al., 2013), but the genes themselves are not common between species, and correspond to very different genome coverage (5% for *Xenopus* (Collart et al., 2014, Tan et al., 2013) vs. 20% in mouse (Hamatani et al., 2004) and 25% in zebrafish (Aanes et al., 2011, Harvey et al., 2013, Lee et al., 2013)). While the majority of ZGA genes are already maternally deposited (only 25% ZGA genes in zebrafish are only zygotically expressed (Lee et al., 2013)), in some cases different mRNA isoforms are used to alter their function (Aanes et al., 2013, Atallah and Lott, 2018, Haberle et al., 2014) (reviewed in (Vastenhouw et al., 2019)).

Activation of zygotic transcription at ZGA across species is gradual and stochastic and not, as previously thought, divided into a minor and major 'wave' of transcription (reviewed in (Jukam et al., 2017, Vastenhouw et al., 2019)). Yet ZGA also varies between species in terms of timing (cell cycle number and absolute time) and regulatory factors. In mouse, zygotic transcripts have been detected already at the 1-cell stage (~12 hours post fertilisation, hpf) (Hamatani et al., 2004), compared to cell cycle 6 for zebrafish (~2 hpf) (**Figure 1.9**B) (Heyn et al., 2014, Mathavan et al., 2005), or nuclear cycle 8 for *Drosophila* (~1 hpf) (Lott et al., 2011, Pritchard and Schubiger, 1996).

1.4.1 Maternal control of ZGA

The regulation of timely transcription at ZGA is thought to rely mainly on the balance of maternally deposited repressors and activators, in the context of an increasing nuclear-to-cytoplasmic (n:c) ratio, lengthening cell cycles, and chromatin organisation (**Figure 1.10**, **Figure 1.11**) reviewed in (Onichtchouk and Driever, 2016, Schulz and Harrison, 2019, Tadros and Lipshitz, 2009, Vastenhouw et al., 2019).

Repressive histone and DNA modifications can regulate specific gene activation at ZGA, but other repressive factors act to prevent premature transcriptional onset. While the initially fast, then lengthening, cell cycle was originally thought to time ZGA by permitting transcription to compete with DNA replication, lengthening the

cell cycle was only sufficient to cause premature ZGA in *Xenopus* (Collart et al., 2013, McCleland and O'Farrell, 2008, Zhang et al., 2014a). This suggests that the cell cycle can regulate the transcriptional output (Dalle Nogare et al., 2009, Edgar and Schubiger, 1986, Hadzhiev et al., 2019, Rothe et al., 1992), but is not the only repressive factor (**Figure 1.10**B).

In fact, the main general repressor seem to be maternally loaded histones (Amodeo et al., 2015, Joseph et al., 2017), whose high concentration pre ZGA allows them to out-compete the transcriptional machinery for DNA binding (Joseph et al., 2017, Palfy et al., 2017). Relief of this repression is probably linked with the increasing n:c ratio caused by reductive cell divisions: nuclear histones will be diluted by the increasing DNA content or reduced nuclear import (Joseph et al., 2017, Shindo and Amodeo, 2019) (**Figure 1.10**A). Indeed, increasing the nuclear volume in *Xenopus* causes premature ZGA (Jevtic and Levy, 2015, Jevtic and Levy, 2017).

Maternally deposited transcripts must also be degraded in a specific and time-sensitive manner. This is governed by common mechanisms across species, first by maternal and then by zygotic factors, although the degree of mRNA clearance varies between species: in zebrafish only ~25% is degraded (Aanes et al., 2011, Harvey et al., 2013, Mishima and Tomari, 2016), versus ~ 60% in *Drosophila* (Thomsen et al., 2010). Factors driving mRNA clearance include RNA binding proteins, small non-coding RNAs, RNA modification, and codon use (reviewed in (Vastenhouw et al., 2019)). In zebrafish the micro-RNA miR-430 causes 40% of transcript clearance by translational repression, deadenylation, and transcript decay. It is also one of the first zygotic transcripts (Bazzini et al., 2012, Giraldez et al., 2006). In *Xenopus* the homolog miR-427 also controls degradation by deadenylation (Lund et al., 2009), other micro-RNAs may have evolved independently for this function in *Drosophila* (Benoit et al., 2009, Bushati et al., 2008, Luo et al., 2016).

A further ZGA timing mechanism is to upregulate the expression of activating factors (**Figure 1.10**A). Limited availability of general transcriptional machinery, such as TBP and Pol II subunits maternally deposited as proteins and mRNA, restricts

transcription until further translation ((Veenstra et al., 1999), reviewed in (Vastenhouw et al., 2019, Wu and Vastenhouw, 2020)). Indeed, the translation efficiency of maternal mRNA is regulated to coincide with MZT. In *Drosophila* 50% transcripts are upregulated, and 20% downregulated, at the beginning of MZT (Kronja et al., 2014). Poly(A) tail length has been shown to correlate with translation in embryonic tissues before ZGA (Eichhorn et al., 2016, Subtelny et al., 2014), with factors such as CPEB in zebrafish lengthening (Winata et al., 2018), or Smaug and PUM in *Drosophila* shortening, the poly(A) tail of maternal mRNAs (Eichhorn et al., 2016, Tadros et al., 2007, Vardy and Orr-Weaver, 2007).

Some species also control the stability and function of maternal proteins, in part to prevent premature activation of ZGA. Ubiquitination of OMA-1 and OMA-2 ends its phosphorylation-dependent sequestration the TF TAF-4 in the cytoplasm, which can then enter the nucleus to activate ZGA in *C. elegans* (Guven-Ozkan et al., 2008). Similarly, ubiquitination of the mouse TAB1 kinase allows nuclear relocation of the TF NF-kB (Yang et al., 2017).

Changes to Pol II could further regulate transcriptional activity in zebrafish. Pol II is present at the 8-cell stage, but the transcriptionally active version of Pol II (phosphorylated at serine 5 for transcription initiation, serine 2 for elongation – reviewed in (Bartkowiak and Greenleaf, 2011)) is only detected at ZGA (Vastenhouw et al., 2010). Conversely, in *Drosophila* Pol II activity is regulated by pausing on DNA before ZGA (Chen et al., 2013, Zeitlinger et al., 2007) and the selective localisation of active phosphorylated versions only in transcriptionally active somatic nuclei (Edgar and Schubiger, 1986, Seydoux and Dunn, 1997). Yet in both zebrafish and *Drosophila*, the first transcription events are confined to two nuclear areas that overlap with Pol II foci (Blythe and Wieschaus, 2016, Chan et al., 2019, Chen et al., 2013, Hadzhiev et al., 2019, Hilbert et al., 2021, Hug et al., 2017), indicating that subnuclear localisation of transcriptional machinery – and TFs – may equally regulate onset, perhaps by the formation of permissive 'microenvironments'.
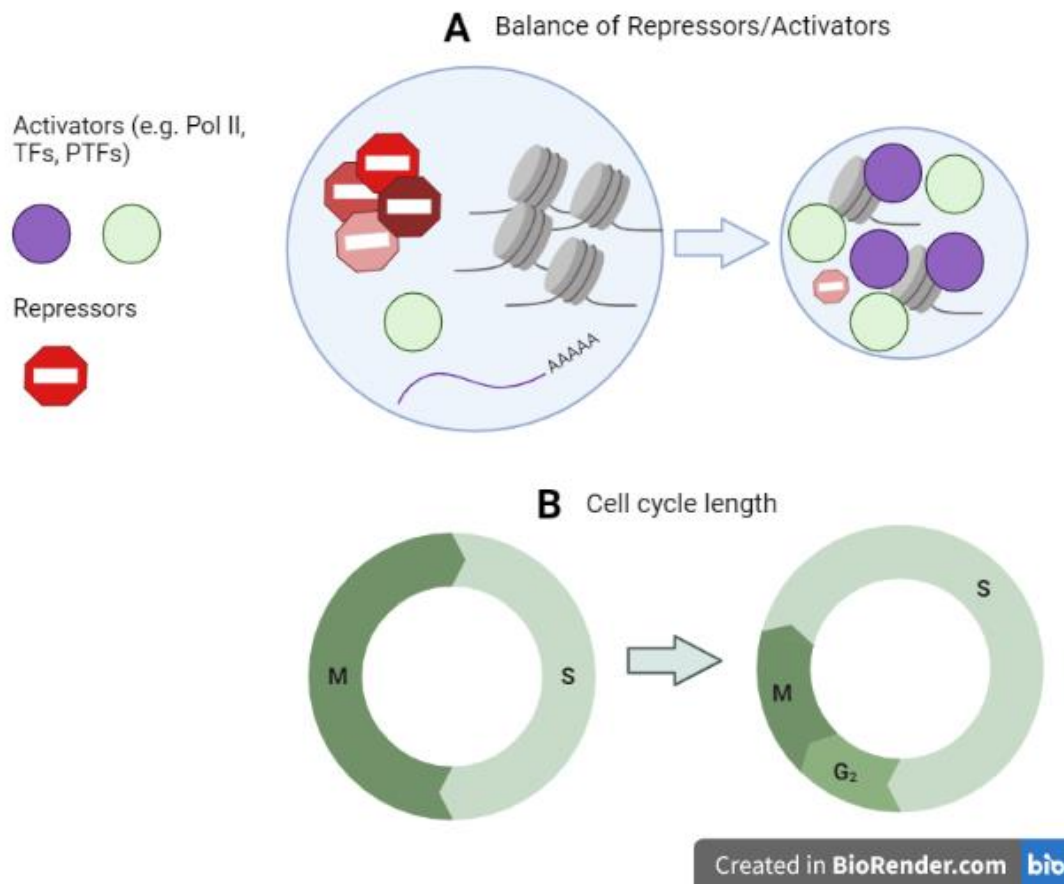
Figure 1.10 Factors regulating Zygotic Genome Activation.

*The onset of transcription is timed by a combination of mechanisms. **A)** The increasing nuclear-to-cytoplasmic ratio, caused by reductive cell divisions, may dilute out specific (red) and general repressors e.g. histones, while translation of maternal mRNA increases the abundance of activators e.g. TFs (purple + green). **B)** Lengthening of the cell cycle, in particular the longer S phase and introduction of G2, creates more time for transcription. (Reviewed in (Schulz and Harrison, 2019, Vastenhouw et al., 2019)).*

TFs are key gene-specific activators required for ZGA, as indicated by their high expression pre ZGA, and motif enrichment in promoters of ZGA genes (Wu and Vastenhouw, 2020). Among the TFs required for ZGA in different species, identified by the defective or deregulated development upon depletion, are: Zelda in *Drosophila* (Harrison et al., 2011, Liang et al., 2008, Nien et al., 2011)*,* Pou5f3/Sox19b/Nanog in zebrafish (Lee et al., 2013, Leichsenring et al., 2013), DUX4

in human (De Iaco et al., 2017, Hendrickson et al., 2017), DUX, DPPA2 and 4, and most recently NR5A2 in mouse (De Iaco et al., 2019, Eckersley-Maslin et al., 2019, Gassler et al., 2022). While the TFs active during ZGA are not conserved between species, they seem to have common properties that make chromatin competent for transcription at ZGA. Most have been suggested to be PTFs as their binding at ZGA gene regulatory elements correlates with increased local chromatin accessibility (Gassler et al., 2022, Harrison et al., 2011, McDaniel et al., 2019, Palfy et al., 2020, Veil et al., 2019).

1.4.2 Changes to chromatin organisation during ZGA

Chromatin is reorganised during ZGA, meaning that the previously dispersed (Ahmed et al., 2010) and mobile (Boskovic et al., 2014) chromatin is compacted to form compartments such as repressive heterochromatin (Ancelin et al., 2016, Laue et al., 2019), and more local accessible domains such as TADs (Hug et al., 2017, Kaaij et al., 2018) (**Figure 1.11**A). This compaction is thought to be mediated in part by the exchange of linker histones (Perez-Montero et al., 2013, Saeki et al., 2005).

While chromatin accessibility decreases globally during ZGA, there are local increases associated with histone modifications (**Figure 1.11**B) (Blythe and Wieschaus, 2016, Liu et al., 2018b, Lu et al., 2016, Wu et al., 2016). Epigenetic marks such as histone modifications and DNA methylation are generally lost upon fertilisation and re-established during ZGA (Guo et al., 2014, Peat et al., 2014). For example, in zebrafish the formation of TADs by cohesin mediated loop extrusion seems to be required for ZGA, and has been linked to active histone marks such as H3K4me1, H3K4me3 and H3K27me3 (Meier et al., 2018). Promoters begin to be marked with H3K4me3 during ZGA, across species including zebrafish (Vastenhouw et al., 2010, Zhang et al., 2014b) and mouse (Dahl et al., 2016, Zhang et al., 2016). Although such histone modifications may not be causative of transcriptional activation, promoter H3K4me3 is often deposited before transcription begins, and was shown to be required for transcription in mice (Dahl et al., 2016, Zhang et al., 2016). Similarly in zebrafish promoters need to be marked with H3K27ac pre ZGA

for transcription of miR-430 (Chan et al., 2019, Sato et al., 2019, Zhang et al., 2018). While enhancer hypermethylation and low promoter methylation can predict activity in zebrafish embryogenesis (Andersen et al., 2012, Kaaij et al., 2016, Liu et al., 2018b), local methylation changes have not been associated with transcriptional activation at ZGA – rather with repression (Kaaij et al., 2016, Potok et al., 2013).
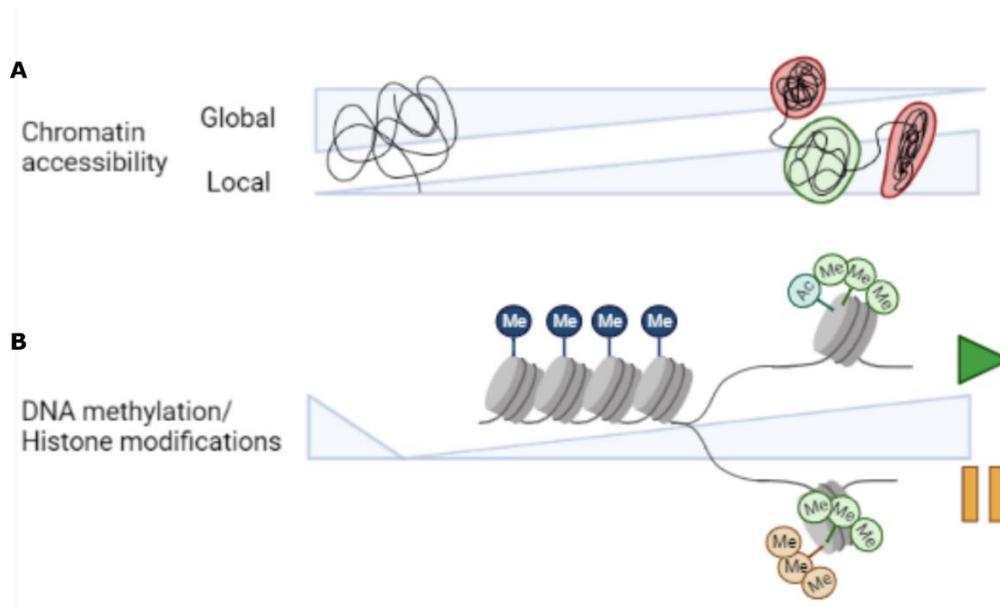
Figure 1.11 Changes to chromatin organisation and accessibility during ZGA.

A) Across most species, chromatin is very accessible after fertilisation, lacking heterochromatin, compartments, and TADs. During ZGA, chromatin is reorganised into differentially accessible compartments. Global accessibility is lost, whereas local accessibility e.g. in TADs increases (Reviewed in (Vastenhouw et al., 2019). B) Epigenetic marks are also lost and re-established for most species after fertilisation. H3K4me3 (green) and H3K27ac (blue) are active histone modifications deposited at regulatory elements before ZGA (Reviewed in (Vastenhouw et al., 2019). The polycomb repressive complex 2 (PRC2) later adds repressive H3K27me3 (orange) to H3K4me3 marked regulatory elements (in Drosophila, PRC2 maintains inherited H3K27me3 (Zenk et al., 2017)). This 'bivalent' mark poises developmental genes for activation or repression post ZGA (Akkers et al., 2009, Vastenhouw et al., 2010).

Repressive H3K27me3 and active H3K4me3 together mark 'bivalent' regulatory elements for later use (Bernstein et al., 2006). H3K27me3 is deposited by PRC2, and recognised by PRC1 (Pasini and Di Croce, 2016, Shen et al., 2008). In *Drosophila*, PRC2 maintains H3K27me3 inherited from the oocyte, to regulate developmental gene expression at ZGA by preventing aberrant H3K27 acetylation (Zenk et al., 2017). In most other species, H3K27me3 seems to be depleted upon fertilisation (not entirely in mice), and regained at developmental genes (Inoue et al., 2017, Liu et al., 2016, Xia et al., 2019). In *Xenopus* and zebrafish, H3K4me3 is deposited at ZGA, while H3K27me3 is deployed later (Akkers et al., 2009, Vastenhouw et al., 2010). In zebrafish, TFs were suggested to recruit PRC1 to regulatory elements pre-ZGA, for later PRC2-mediated H3K27me3 deposition to poise developmental genes also marked with H3K4me3 post ZGA (Hickey et al., 2022).

Finally, in zebrafish the loss of chromatin organisation and epigenetic marks is slightly delayed; compartments and TADs are only transiently lost during ZGA (Kaaij et al., 2018), DNA methylation reaches a minimum at the 64-cell stage, to recover by the 256-cell stage (Potok et al., 2013), and over 50% H3K4me3 marks are lost up to the 16-cell stage, then re-established by the 1000-cell stage (ZGA) (Zhu et al., 2019).

1.4.3   Chromatin organisation and promoter features time transcriptional onset in zebrafish ZGA: the miR-430 locus

In zebrafish, transcriptional onset seems to be differently regulated at the beginning of ZGA (64-cell stage, early ZGA) versus main ZGA (1000-cell stage, when bulk of ZGA genes are transcribed). Genes with higher chromatin accessibility and H3K27ac begin expression earlier (Hadzhiev et al., 2023). While most early ZGA genes lack H3K4me3, deposition of the bivalent H3K4me3 and H3K27ac marks at some early ZGA genes may prime these for later regulation in development. Promoter features also time transcriptional onset: early-expressed znf genes have promoters with a sharp TSS and a TATA box, as well as lower H3K4me3, compared to broad TSS and lack of TATA box in later-expressed znf genes (**Figure 1.12**). miR-430, the earliest

and highest transcribed ZGA gene (Heyn et al., 2014), has the same promoter features as early znf genes. Yet the high expression of miR-430 is due to its uniquely repetitive locus, with 100s of copies leading to high promoter density (Hadzhiev et al., 2023). This in turn leads to the formation of two large transcription bodies per cell in early ZGA, containing the majority of the cell's active Pol II and nascent RNA (Chan et al., 2019, Hadzhiev et al., 2019, Hilbert et al., 2021).
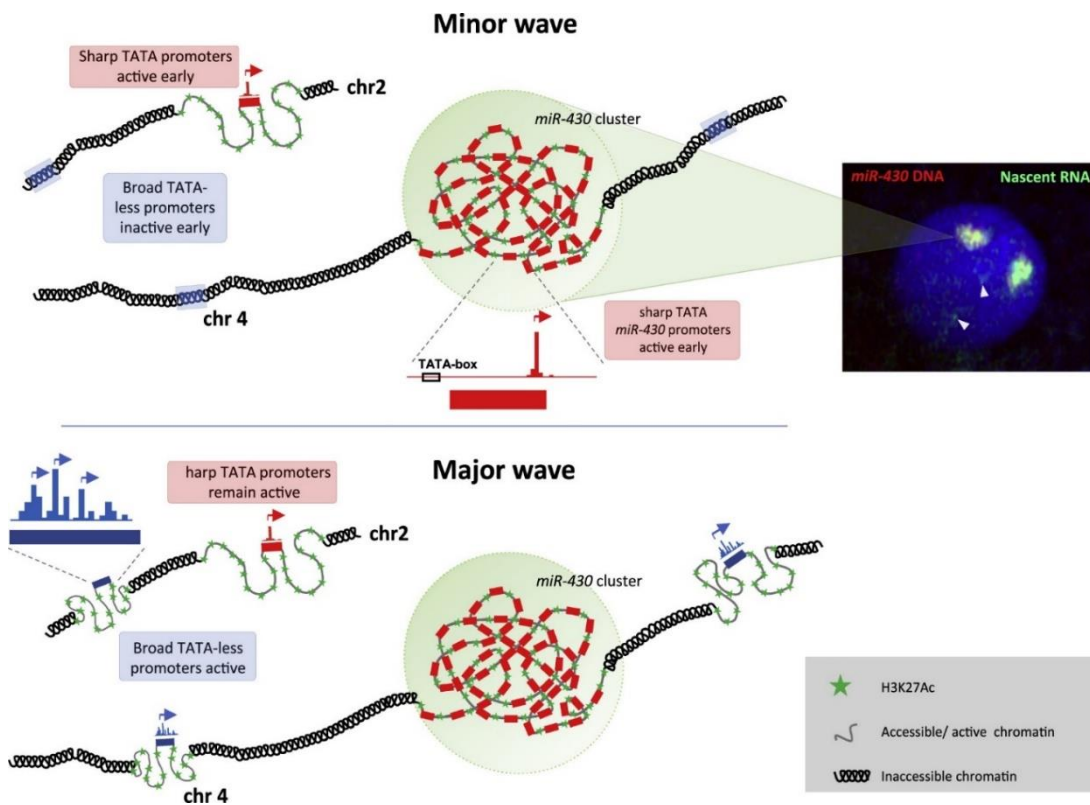
Figure 1.12 Promoter architectures regulating transcriptional onset: the miR-430 locus (taken from (Hadzhiev et al., 2023).

Transcription from the miR-430 cluster begins at the 64-cell stage. miR-430 and zinc finger (znf) genes expressed early in ZGA (here termed "Minor wave") share promoter features including a sharp TSS containing a TATA box. Genes expressed during main ZGA (here termed "Major wave") have a broad TSS, lack a TATA box.

The repetitive nature of the miR-430 locus makes it a useful target to study the regulation of transcription onset at a specific genomic locus *in vivo*: the miR-430 transcription bodies can be visualised using injected fluorescently labelled morpholinos against miR-430 nascent transcripts (Hadzhiev et al., 2019, Sato et al., 2019). High-resolution imaging has shown that chromatin is locally depleted to allow high miR-430 transcription (Hilbert et al., 2021). Interestingly, while Pou5f3, Sox19b, and Nanog are all required for miR-430 transcription, Nanog is required for formation of miR-430 transcription bodies, and may recruit Sox19b and Pol II to these (Kuznetsova et al., 2023).

1.4.4 Zebrafish Pou5f3, Sox19b, Nanog

Pou5f3, Sox19b, and Nanog (PSN) –homologs of the mammalian pluripotency factors OCT4, SOX2, and NANOG - are indispensable for zebrafish ZGA, and their mRNAs are maternally deposited. (Lee et al., 2013, Leichsenring et al., 2013). PSN are defined as PTFs, as their binding at ZGA gene regulatory elements was linked to the enrichment of histone marks such as H3K4me3 and H3K27ac, and increased chromatin accessibility (Leichsenring et al., 2013, Palfy et al., 2020). Recent work in maternal-zygotic triple mutants (MZ*nps*) – which lack maternally deposited PSN mRNA and zygotic expression – confirmed that the PTFs act individually, jointly, and sometimes interchangeably to make chromatin accessible for ZGA, and showed that accessibility is sensitive to PTF dosage (Miao et al., 2022, Veil et al., 2019). While the exact mechanism of PSN pioneer activity for transcriptional activation at ZGA remains to be determined, it involves recruitment of the HAT p300 and the acetylated histone reader Brd4, as ZGA in MZ*nps* is rescued by recruiting acetyltransferase activity using dCas9 (Chan et al., 2019, Miao et al., 2022). The interplay between PSN activity and chromatin organisation at ZGA in particular needs further examination, as cohesin binding sites enriched for active histone marks also overlap PSN binding (Hug et al., 2017, Meier et al., 2018).

PSN may have different roles as ZGA progresses: Pou5f3 and Nanog binding to nucleosomal DNA (High Nucleosome Affinity Regions; HNARs) has been suggested

to destabilise nucleosomes pre ZGA, while PSN act together to maintain accessible sites post ZGA (Veil et al., 2019). PSN mainly bind to the promoter of miR-430, with Pou5f3 and Sox19b distributed more broadly than Nanog (Hadzhiev et al., 2023) and Nanog may recruit Sox19b and Pol II to form the miR-430 transcription body (Kuznetsova et al., 2023). Later, Nanog seems to be required mainly for extraembryonic tissue (Gagnon et al., 2018, Veil et al., 2018), but it could also function by working with Pou5f3 and Sox19b (Perez-Camps et al., 2016), which themselves may cooperate at enhancers to regulate specific genes at ZGA for later dorsoventral patterning (Gao et al., 2022).

In vivo studies of PSN chromatin binding dynamics would provide further insight into the regulation of chromatin accessibility by PTFs for transcription during ZGA.

1.5 Summary and thesis aims

PTFs regulate cell fate transitions by making chromatin accessible to other TFs, either by their nucleosome binding activity, or recruitment of chromatin remodelers. The activity and function of PTF-chromatin binding events and PTF interactions driving cell fate transitions are still being characterised, and ZGA, in which transcription begins from a previously silent genome, is an excellent model in which to do this. Specifically, interactions and chromatin binding dynamics of PTFs required for ZGA can be studied by quantitative microscopy in zebrafish, as they are externally fertilised which aids manipulation and visualisation of embryos.

Thus, the aims of my PhD thesis were:

1) To test whether FCS and FCCS can be used to characterise the individual and joint chromatin-binding dynamics of PSN in live zebrafish embryos undergoing ZGA.

2) To optimise a lifetime-based FRET assay, AAT-FRET, to detect protein interactions in live zebrafish embryos.

3) To test whether interactions between PSN can be detected *in vivo* using AAT-FRET.

2 Materials and Methods

2.1 Molecular biology

2.1.1 Pou5f3/Sox19b/Nanog cloning

2.1.1.1 cDNA cloning in TOPO

Pou5f3/Sox19b/Nanog cDNA sequences were previously synthesised by members of the Papadopoulos lab, by reverse transcription from LiCl purified AB zebrafish RNA using the Promega GoScript Reverse Transcription System kit (Promega, A5000). Primers were used to add overhangs with N-terminal BamHI/BglII and C-terminal EcoRI sites (no stop codon), or N-terminal EcoRI and C-terminal XhoI/SalI sites (with stop codon) (**Table 2.1**). A-overhangs were added by incubating the purified cDNA in a 10 µL reaction with 0.2 µL Taq polymerase, 1 µL 10X PCR buffer (Thermo Scientific, EP0401), and 1 µL 2 millimolar (mM) dATPs, 20 minutes (min) at 72 °C. Inserts were then incubated in 7 µL reactions with 0.5 µL pCR 2.1-TOPO TA vector (Invitrogen, 451641) and 1 µL NaCl for 30 min at room temperature (RT). The reaction was stopped by adding 3 µL ddH$_2$O, and desalted on 47 mm (0.22 µm pore size) membrane filters (Millipore, GSWP04700) in ddH$_2$O. 10 µL reaction product was transformed into 50 µL TOP10 (Invitrogen, C404010) homemade electrocompetent *E.Coli,* using 1350 Volts, 10 micro-Faradays, 600 Ohm electroporation settings (Biorad). Clones were grown overnight (o/n) at 37 °C on Lysogeny Broth (LB) plates with 50 µg/mL Kanamycin (Kan) (IGC technical services) coated with 40 µL 40 µg/µL X-gal for blue-white screening of insert-carrying plasmids. Correct insertion was verified by colony PCR: white colonies were streaked on to fresh LB 'master' plates using a pipette tip and dipped into the colony PCR reaction mix (**Table 2.2**, primers **Table 2.3**, PCR program T**able 2.4**). PCR products were analysed by gel electrophoresis on a 1% agarose gel stained with 1 µg/mL EtBr. Positive colonies were picked from the master plate and grown o/n at 37 °C in 5 mL LB with 10 µg/mL Kan. Plasmid DNA was prepared using the PureLink Quick Plasmid Miniprep Kit (Invitrogen, K210010) and sequenced by Sanger sequencing (IGC technical services, primers in **Table 2.5**).

Table 2.1 RT PCR primers with overhangs

cDNA	Forward primer	Reverse primer
Nanog	*GGATCC*ATGGCGGACTGGAAGATGCCAGTG A (*BamHI*)	*GAATTC*CAGCAAAGTTATTCCTTTAGTTGCCCAC (*EcoRI*)
	*GAATTC*ATGGCGGACTGGAAGATGCCAGTG A (*EcoRI*)	*GTCGAC***TCA**CAGCAAAGTTATTCCTTTAGTTGCCCAC (*SalI,* **Stop**)
Sox19 b	*GGATCC*ATGATGTACAGCATGATGGAGCAC G (*BamHI*)	*GAATTC*GATGTGAGTGAGGGGAACAGTTCCACCA (*EcoRI*)
	*GAATTC*ATGATGTACAGCATGATGGAGCAC G (*EcoRI*)	*CTCGAG***TCA**GATGTGAGTGAGGGGAACAGTTCCACC A (*XhoI,* **Stop**)
Pou5f3	*AGATCT*ATGACGGAGAGAGCGCAGAGCCCA A (*BglII*)	*GAATTC*GCTGGTGAGATGACCCACCAAACCAGGG (*EcoRI*)
	*GAATTC*ATGACGGAGAGAGCGCAGAGCCCA A (*EcoRI*)	*CTCGAG***TCA**GCTGGTGAGATGACCCACCAAACCAGG G (*XhoI,* **Stop**)

Table 2.2 Colony PCR reagents

Reagent	Volume (µL)
2X DreamTaq Green PCR Master Mix (Thermo Scientific, K1081)	5
Forward + Reverse primers, 10µM	0.5+0.5
ddH$_2$0	4
	Total = 10 µL/reaction

Table 2.3 TOPO colony PCR primers

cDNA	Forward primer	Reverse primer	Annealing temp (°C)
Nanog	TCAGGTGAGAGAACCTGTTTTCAAG	CAGGAAACAGCTATGACCATGATTACGC	62
Sox19 b	TACATGAACAGCGCCAGCTCTTACA	"	63
Pou5f3	CCTGGAGAGAGATGTAGTGCGTGTA	"	63

48

Table 2.4 Colony PCR program

Step	Temperature (°c)	Time	Cycles
Initial denature	95	5 min	1
Denature	95	30 seconds (s)	32
Anneal	*Table 2.2	30 s	
Extend	72	60 s	
Final extension	72	5 min	1
Cool down	4	5 min	
Hold	10	hold	

Table 2.5 TOPO Sequencing primers

cDNA	Primers
Nanog	CAGGAAACAGCTATGACCATGATTACGC, TCAGGTGAGAGAACCTGTTTTCAAG, AGTCACGACGTTGTAAAACGACGGCC
Sox19b	CAGGAAACAGCTATGACCATGATTACGC, TACATGAACAGCGCCAGCTCTTACA, AGTCACGACGTTGTAAAACGACGGCC
Pou5f3	CAGGAAACAGCTATGACCATGATTACGC, GGCCAGAAATTAGGGTTCCATGGCG, AGTCACGACGTTGTAAAACGACGGCC

2.1.1.2 WT Pou5f3/Sox19b/Nanog and fluorophore constructs in pCS2+

Pou5f3, Sox19b, Nanog, as well as mCherry and Citrine (already in TOPO with the BamHI-EcoRI or EcoRI-Stop-XhoI overhangs) were then sub-cloned from TOPO into pCS2+ vectors, alone and in different N- or C- terminal combinations (**Figure 2.1**), for *in vitro* transcription. TOPO vectors, and the empty pCS2+ vector, were digested using the relevant restriction enzyme pairs (**Table 2.1**) in 50-100 µL reaction mixes (**Table 2.6**), for 2 hours (h) at 37 °C. Inserts were gel purified from a 0.8% UltraPure Low Melting Point (LMP) Agarose gel (Invitrogen, 16520050) using the Promega Wizard SV Gel and PCR Cleanup System (Promega, A9281) or the QIAquick Gel Extraction Kit (Qiagen, 28704), the plasmid backbone by column purification using

the QIAquick PCR Purification Kit (Qiagen, 28104), and eluted in ~ 30 μL ddH$_2$O. Insert(s) and backbone were ligated using T4 ligase (NEB, M0202S) in a 10 μL reaction mix (**Table 2.7**), incubated for 30 min at RT. Ligation reactions were either desalted and 10 μL transformed into TOP10 E.Coli by electroporation as above, or 5 μL reaction mix was transformed by heat shock into 50 μL DH5α competent *E.Coli* (Invitrogen). Clones were grown overnight (o/n) at 37 °C on LB plates with 50 μg/mL Ampicillin (Amp) (IGC technical services). Correct insertion was verified by colony PCR as previously described (primer combinations in **Table 2.8**, PCR program T**able 2.4**). Plasmid DNA was prepared using the PureLink Quick Plasmid Miniprep Kit (Invitrogen, K210010) and sequenced by Sanger sequencing (IGC technical services, primers **Table 2.5**).

Table 2.6 TOPO digestion reaction mix

Reagent	Volume (μL)
BamHI-HF/ BglII/ EcoRI-HF/ XhoI/ SalI-HF (NEB R3136S/ R0144S/ R3101S/ R0146S/ R3138S)	5+5
10X NEB Cutsmart buffer (NEB, B7204)	10
Plasmid	~ 1 μg
ddH$_2$0	To 100 μL

Table 2.7 pCS2+ Ligation Reaction

Reagent	Volume (μL)
pCS2+ backbone	50-100ng
Insert (s)	3:1 molar ratio to backbone
T4 Ligase	1
10X T4 Ligase buffer	1
ddH$_2$0	To 10 μL

Table 2.8 pCS2+ colony PCR primers

cDNA	Forward primer	Reverse primer	Annealing temp (°C)
Nanog-Citrine	GGACGTCGGAGCAAGCTT GATTTAGGTG	GTGCTGCTTCATGTGGTCGG GGTAG	67
Cit-Nanog	"	TCCTCTCCTGCTGTGGAGGTT AAGT	66

Nanog-mCh	"	GTTCATCACGCGCTCCCAC	61
mCh-Nanog	"	TCCTCTCCTGCTGTGGAGGTT AAGT	66
Sox19b-Citrine	"	GTGCTGCTTCATGTGGTCGG GGTAG	67
Cit- Sox19b	"	CGTAGCCGTCCATCCTCGGG CTGC	67
Sox19b -mCh	"	GTTCATCACGCGCTCCCAC	61
mCh- Sox19b	"	CGTAGCCGTCCATCCTCGGG CTGC	67
Pou5f3-Citrine	"	GTGCTGCTTCATGTGGTCGG GGTAG	67
Cit- Pou5f3	"	GGCCAGAAATTAGGGTTCCA TGGCG	67
Pou5f3-mCh	"	GTTCATCACGCGCTCCCAC	61
mCh- Pou5f3	"	GGCCAGAAATTAGGGTTCCA TGGCG	67
Citrine	"	GTGCTGCTTCATGTGGTCGG GGTAG	67
mCherry	"	GTTCATCACGCGCTCCCAC	61
mCherry-mCitrine	"	GTGCTGCTTCATGTGGTCGG GGTAG	67
Nanog	"	TCCTCTCCTGCTGTGGAGGTT AAGT	66
Sox19b	"	CGTAGCCGTCCATCCTCGGG CTGC	67
Pou5f3	"	GGCCAGAAATTAGGGTTCCA TGGCG	67

Table 2.9 pCS2+ Sequencing primers

pCS2+ construct	Primers
Nanog-Cit	GGACGTCGGAGCAAGCTTGATTTAGGTG, GAATTCCAGCAAAGTTATTCCTTTAGTTGCCCAC, CAGGAAACAGCTATGACCATGATTACGC
Cit-Nanog	GGACGTCGGAGCAAGCTTGATTTAGGTG, TCCTCTCCTGCTGTGGAGGTTAAGT, CAGGAAACAGCTATGACCATGATTACGC
Nanog-mCh	GGACGTCGGAGCAAGCTTGATTTAGGTG, GAATTCAAGGCGCGTATGGTGAG, CAGGAAACAGCTATGACCATGATTACGC
mCh-Nanog	GGACGTCGGAGCAAGCTTGATTTAGGTG, TCCTCTCCTGCTGTGGAGGTTAAGT, CAGGAAACAGCTATGACCATGATTACGC
Sox19b-Cit	GGACGTCGGAGCAAGCTTGATTTAGGTG, TACATGAACAGCGCCAGCTCTTACA, CAGGAAACAGCTATGACCATGATTACGC
Cit- Sox19b	GGACGTCGGAGCAAGCTTGATTTAGGTG, CGTAGCCGTCCATCCTCGGGCTGC, CAGGAAACAGCTATGACCATGATTACGC
Sox19b -mCh	GGACGTCGGAGCAAGCTTGATTTAGGTG, TACATGAACAGCGCCAGCTCTTACA,

51

	CAGGAAACAGCTATGACCATGATTACGC
mCh- Sox19b	GGACGTCGGAGCAAGCTTGATTTAGGTG, CGTAGCCGTCCATCCTCGGGCTGC, CAGGAAACAGCTATGACCATGATTACGC
Pou5f3-Cit	GGACGTCGGAGCAAGCTTGATTTAGGTG, GGCCAGAAATTAGGGTTCCATGGCG, CAGGAAACAGCTATGACCATGATTACGC
Cit- Pou5f3	GGACGTCGGAGCAAGCTTGATTTAGGTG, GCTCGCCGACCACTACCAGC, GGCCAGAAATTAGGGTTCCATGGCG, CAGGAAACAGCTATGACCATGATTACGC
Pou5f3-mCh	N/A
mCh- Pou5f3	GGACGTCGGAGCAAGCTTGATTTAGGTG, CACCCCGCCGACATCCCCGACTACT, GGCCAGAAATTAGGGTTCCATGGCG, CAGGAAACAGCTATGACCATGATTACGC
Citrine	GGACGTCGGAGCAAGCTTGATTTAGGTG, CAGGAAACAGCTATGACCATGATTACGC
mCherry	GGACGTCGGAGCAAGCTTGATTTAGGTG, CAGGAAACAGCTATGACCATGATTACGC
mCherry-mCitrine	GGACGTCGGAGCAAGCTTGATTTAGGTG, GTGCTGCTTCATGTGGTCGGGGTAG, CAGGAAACAGCTATGACCATGATTACGC
Nanog	GGACGTCGGAGCAAGCTTGATTTAGGTG, TCCTCTCCTGCTGTGGAGGTTAAGT, CAGGAAACAGCTATGACCATGATTACGC
Sox19b	GGACGTCGGAGCAAGCTTGATTTAGGTG, CGTAGCCGTCCATCCTCGGGCTGC, CAGGAAACAGCTATGACCATGATTACGC
Pou5f3	GGACGTCGGAGCAAGCTTGATTTAGGTG, GGCCAGAAATTAGGGTTCCATGGCG CAGGAAACAGCTATGACCATGATTACGC

2.1.1.3 Site-directed mutagenesis of Citrine --> mCitrine

The Nanog-Citrine pCS2+ and Citrine pCS2+ constructs were altered by quick-change (QC) site-directed mutagenesis to change Citrine to mCitrine (GCC → AAG, Alanine (A) → Lysine (K)). A 50 µL reaction was set up for forward and reverse primers separately (primers **Table 2.10**, QC reaction mix **Table 2.11**, PCR program **Table 2.12**A). A combined reaction was then set up, using 25 µL from each reaction, and 0.5 µL PfuUltra (PCR program **Table 2.12**B). The original plasmid was destroyed by incubation with 1 µL DpnI (NEB, R0176S) at 37 °C for 2 h, and 10 µL desalted reaction mix transformed into TOP10 *E.Coli* as above. Correct insertion was verified by colony PCR as previously described (primer combinations **Table 2.8**, PCR program T**able 2.4**). Plasmid DNA was prepared using the PureLink Quick Plasmid Miniprep Kit (Invitrogen, K210010) and sequenced by Sanger sequencing (IGC technical services, primers **Table 2.5**).

Table 2.10 mCitrine QC primers

Forward primer	Reverse primer
CAACCACTACCTGAGCTACCAGTCCAAGCTGAGCAAAG ACCCCAACGAGAAGC	GCTTCTCGTTGGGGTCTTTGCTCAGCTTGGACTGGTAG CTCAGGTAGTGGTTG

Table 2.11 QC PCR reagents

Reagent	Volume (µL)
PfuUltra II High-fidelity DNA Polymerase (Agilent, 600670)	0.5
10X PfuUltra buffer (Agilent, 600385)	5
Forward + Reverse primers, 10µM	1+1
Plasmid	50 ng
DMSO	5
dNTP mix, 2.5 mM each	1
ddH$_2$0	To 50 µL

Table 2.12 QC PCR program

	Step	Temperature (°C)	Time	Cycles
A	Initial denature	95	30 s	1
	Denature	95	30 s	3
	Anneal	55	1 min	
	Extend	68	1 min/ kb (+ 1 min)	
B	Initial denature	95	30 s	1
	Denature	95	30 s	18
	Anneal	55	1 min	
	Extend	68	1 min/ kb (+ 1 min)	
	Cool down	4	5 min	1
	Hold	10	hold	
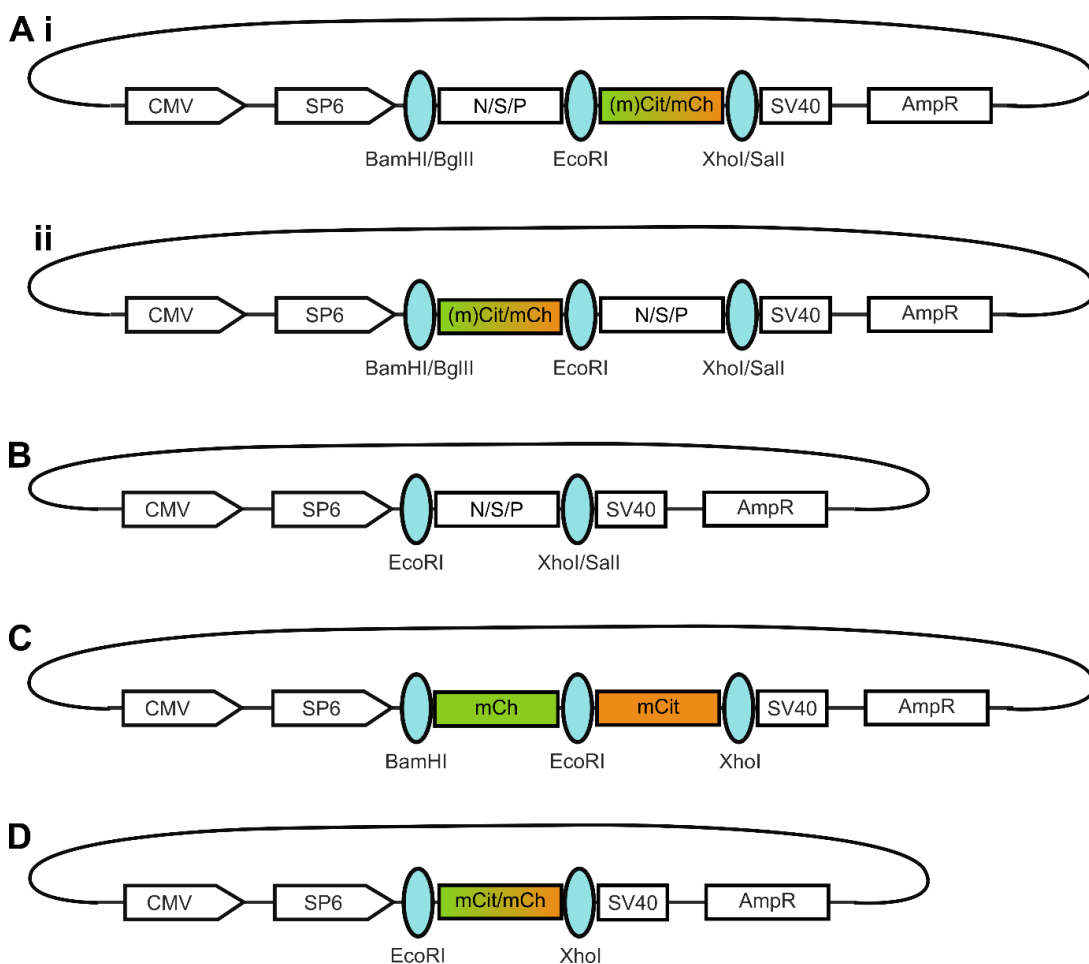
Figure 2.1 PSN and fluorophore pCS2+ constructs. *(cont. over page)*

The pCS2+ vector contains a CMV promoter for mammalian expression, SP6 promoter and SV40 poly(A) signal sequence for in vitro capped RNA synthesis, and Ampicillin resistance gene (AmpR). ***A)*** *Pou5f3 (P), Sox19b (S), or Nanog (N), tagged with (m)Citrine (mCit) or mCherry (mCh) at the* ***i.*** *C-terminus or* ***ii.*** *N-terminus. Inserts are linked by an EcoRI restriction site.* ***B)*** *Untagged P/S/N.* ***C)*** *Tandem mCh-mCit fusion, linked by EcoRI restriction site.* ***D)*** *mCh or mCit alone.*

2.1.1.4 PTF DBD and N-terminal mutants in pCS2+

Pfam annotations were used to define P/S/N DBD regions to remove; for the Nanog N-terminal mutant the sequence upstream of the DBD was removed. P/S/N sequences lacking the DBD or Nanog N-terminus were ordered from GeneArt in a pMA-RQ Amp resistant vector (Invitrogen). Nanog and Sox19b sequences were flanked by N-terminal BamHI and C-terminal EcoRI restriction sites, Pou5f3 by EcoRI and XhoI. This enabled restriction-digestion cloning (performed and analysed as above) to replace the P/S/N sequences in existing Nanog-mCitrine, Sox19b-mCherry, mCherry-Pou5f3 pCS2+ constructs (**Figure 2.1**A).

Glycerol stocks of all correct plasmids were made by adding 700 μL fresh culture to 300 μL 80% glycerol, and stored at -80 °C.

2.1.2 In vitro transcription

First, 5-10 μg pCS2+ plasmids were linearised using NotI-HF (NEB, R3189S), or KpnI-HF for Nanog constructs (NEB, R3142S), which cut downstream of the SV40 poly(A) signal sequence (**Figure 2.1**). Linearised plasmids were column purified using the QIAquick PCR Purification Kit (Qiagen, 28104), and eluted in ~ 30 μL ddH$_2$O. Capped RNA ('mRNA') was produced by *in vitro* transcription using the mMESSAGE mMACHINE SP6 Kit (Invitrogen, AM1340). 20 μL reactions were set up and incubated at 37 °C for 2h (**Table 2.13**). DNA was destroyed by incubating with 1 μL DNAse for 15 min at 37°c. mRNA was then purified by LiCl precipitation: 20 μL LiCl and 1 μL glycogen were added, and the reaction kept at -20 °C for 30 min, after which the tube was centrifuged at 21,000 g for 15 min at 4 °C. The supernatant was removed and washed with 1 mL 70% EtOH by re-centrifuging. After removing the

EtOH, the pellet was left to dry at RT (or 10 min at 50 °C), re-suspended in 30 µL ddH$_2$0, and stored at -80 °C.

Table 2.13 *In vitro* transcription reagents

Reagent	Volume (µL)
SP6 enzyme mix	2
2X NTP/CAP	10
10X SP6 reaction buffer	2
Linearised plasmid	1-1.2 µg
ddH$_2$0	To 20 µL

2.2 Zebrafish husbandry and techniques

2.2.1 Zebrafish husbandry

Fish were maintained in standard conditions, at 28.5 °C with 14h:10h light:dark cycles in accordance with UK Home Office regulations, UK Animals (Scientific Procedures) Act 1986 (amended 2013), and European Directive 2010/63/EU under project license PP7317786. Zebrafish work was performed under UK Home Office licence PPL PA3527EC3, PIL I04173724.

2.2.2 MZ mutant line maintenance and genotyping

MZ*nanog*, and MZ*spg793* zebrafish lines were a kind gift from Dr. D Onichtchouk, at the University of Freiburg. +/- lines were kept for maintenance, and in-crossed to generate -/- lines (embryos from MZ*spg793* +/- in-crosses were rescued with 50 pg Pou5f3 mRNA). Genotypes were verified by tail fin biopsies, in a protocol adapted from communications with Dr.D Onichtchouk and Dr.M Gao.

For genotyping, genomic DNA (gDNA) was extracted from tail fins. Individual tail fin biopsies were incubated in PCR tubes with 50 µL lysis buffer (**Table 2.14**) for 10 min at 98 °C, then kept at 4 °C. 6 µL 20 mg/mL Proteinase K solution were added to each tube, and reactions incubated at 55 °C o/n, followed by a further 10 min at 98 °C. gDNA was stored at -20 °C. For PCR reactions, gDNA was diluted 1:20 in ddH$_2$0 and

reactions set up with either MyTaq or DreamTaq PCR reagents (primers **Table 2.15**, PCR mixes and programs **Table 2.16** - **Table 2.19**). MZ*nanog* PCR products were assessed by restriction digestion with NdeI (NEB R3131S), as the mutation destroys an NdeI restriction site (WT products = 284 + 238 base pairs (bp), mutant = 523 bp). Digestion reactions (**Table 2.20**) were analysed on 2% LMP Agarose gels (Invitrogen, 16520050). MZsp*g* PCR products were assessed by Sanger sequencing (IGC technical services) using the forward PCR primer, to screen for the T → C mutation.

Table 2.14 Tail fin Lysis buffer

Reagent	Concentration
Tris-HCl (pH 8.0)	10 mM
KCl	50 mM
Tween20	0.3%
NP40	0.3%
EDTA	1 mM

Table 2.15 Primers for MZ mutant genotyping PCR

Genotype	Forward primer	Reverse primer	Annealing temp (°C)
MZ*nanog*	TCTAAACCCGCCCACAACC	GGTCGGGCTCAGTCTTGTTG	60
MZ*pou5f3*	GTCGTCTGACTGAACATTTTGC	GCAGTGATTCTGAGGAAGAGGT	58

Table 2.16 MyTaq PCR reagents for MZ mutant genotyping

Reagent	Volume (µL)
Diluted gDNA	2
Forward + Reverse primers, 10µM	1+1
MyTaq DNA Polymerase (Meridian Bioscience, BIO21105)	0.5
5X MyTaq Reaction Buffer	10
ddH$_2$0	35.5
	Total = 50µL/reaction

Table 2.17 MyTaq PCR program

Step	Temperature (°c)	Time	Cycles
Initial denature	95	1 min	1
Denature	95	15 s	32
Anneal	*Table 2.15	15 s	
Extend	72	10 s	
Cool down	4	5 min	1
Hold	10	hold	

Table 2.18 DreamTaq Green PCR reagents for MZ mutant genotyping

Reagent	Volume (µL)
2X DreamTaq Green PCR Master Mix (Thermo Scientific, K1081)	15
Diluted gDNA	2
Forward + Reverse primers, 10µM	1.5+1.5
ddH$_2$0	10
	Total = 30µL/reaction

Table 2.19 DreamTaq Green PCR program

Step	Temperature (°C)	Time	Cycles
Initial denature	98	1 min	1
Denature	98	30 s	32
Anneal	*Table 2.15	30 s	
Extend	72	30 s	
Cool down	4	5 min	1
Hold	10	hold	

Table 2.20 MZ*nanog* NdeI restriction digestion reaction

Reagent	Volume (µL)
PCR product	5
10X Cutsmart buffer (NEB)	3
NdeI-HF (NEB, R3131S)	0.5
ddH$_2$0	21.5
	Total = 30µL/reaction

2.2.3 Microinjection

Adult fish were set up in pair or group mating tanks the evening before, to separate males and females. Injection plates were prepared by pouring 1% agarose in E3 medium (0.33 mM CaCl$_2$, 0.17 mM KCl, 0.33 mM MgSO$_4$, 5 mM NaCl, Methylene Blue 0.00001%) into a 90mm dish (Fisher Scientific, 12664785), and placing a mold

(WPI, Z-MOLDS) on the agarose to create lanes while it sets. The v-shaped lanes help to orient embryos for microinjection. Needles were pulled from borosiliate glass capillaries (WPI, TW 100-4) using a micropipette puller (Intracel Flaming/brown micropipette puller model P-97, Sutter Instruments). Injection mixes were made up in ddH$_2$O, to a total volume of 2-4 µL on the day of injection and kept on ice. The injection plate was pre-warmed in the incubator (28.6 °C) on the day of injection. Separators were removed and mating tanks monitored to collect eggs immediately once laid. Eggs were rinsed with E3 medium in a strainer and transferred to a 90mm dish with E3 medium. A microinjection needle was loaded with the injection mix, using a micro-loader tip (Eppendorf, 5242956003), and mounted on a Picospritzer III microinjector (Intracel). The injection volume was calibrated to 500 picolitre (pL) using a 1 mm graticule with 0.01 mm divisions (Graticules Optic, S8), by injecting into a drop of mineral oil and adjusting the injection duration to achieve a diameter of 0.05 mm. Injections were viewed under a Nikon SMZ 645 stereomicroscope (Nikon Instruments, Japan). Embryos were transferred to the injection plate with minimal E3 to prevent drying out, and oriented in lanes to allow microinjection into the cell/yolk. After injection, embryos were transferred to a dish with fresh E3 medium and incubated at 28.6 °C for the desired length of time.

2.2.4 mRNA rescue experiments

Eggs from in-crosses of MZ*nanog* -/- or MZ*spg793* -/- fish were collected immediately after laying, and mRNA microinjections carried out into the cell, as outlined in section 2.2.3. mRNA quantities equimolar to rescuing wild-type (WT) mRNA amounts were injected: 150 pg Nanog WT/ 245 pg (m)Cit- or mCh-tagged Nanog, 50 pg Pou5f3 WT/ 76 pg (m)Cit- or mCh-tagged Pou5f3 (Lunde et al., 2004, Veil et al., 2018). Uninjected embryos served as a negative control. After microinjection, embryos were transferred to dishes containing fresh E3 medium, and incubated at 28.6 °C. At approximately 6 hpf, E3 was exchanged and unfertilised embryos removed (identified by lack of cell division). At 24 hpf embryos

were dechorionated (section 2.2.5.2) in the dish, and chorion debris removed. Embryo dishes were viewed on Nikon SMZ 1500 stereomicroscope, and imaged with a Nikon E 5400 camera attached via a Nikon MXA 5400 adapter (Nikon Instruments, Japan). From these images, embryos were sorted into four classes of rescue phenotypes, outlined in **Table 2.21**, adapted from (Veil et al., 2018) for MZ*nanog -/-*rescues, and (Reim and Brand, 2006) for MZ*spg793 -/-.*

Table 2.21 MZ mutant -/- rescue classes

Class	MZ*nanog -/-*	MZ*spg793 -/-*
I (No rescue)	Nectrotic cells/exploded	Nectrotic cells/exploded
II	Axis rescue (usually a head but no tail)	Axis rescue, dorsalised
III	Axis rescue, short tail and yolk extension	Axis + tail rescue, but dorsalised
IV	Like WT	Like WT

2.2.5 Preparation for live microscopy

2.2.5.1 Mounting of embryos in chorion

A drop of heptane glue (made by leaving sticky tape in a bottle of heptane o/n) was added to the well of a #1.5H glass coverslip 8-well chambered coverslip (8-well chamber) (ibidi, 80807) and left to dry. Individual embryos were transferred onto the glue, and oriented using tweezers. 0.7% LMP agarose in E3 medium (cooled to touch) was added, and embryos re-oriented using tweezers. Embryos were incubated at 28.6 °C until the desired stage, with extra E3 medium to prevent the agarose from drying out.

2.2.5.2 Manual Dechorionation

~32-64 cell-stage embryos were dechorionated in a 90 mm dish (Fisher Scientific, 12664785) coated thinly with 1% agarose in E3 medium, and filled with sufficient E3 to cover embryos. Two Dumostar #5 tweezers (Dumont, 500085) were used to tear open, then peel away the chorion from embryos. Embryos were transferred to the 8-well chamber using a glass aspirating pipette with the tip broken off to create a

sufficiently wide opening. Excess E3 medium was removed using a narrow-tipped pastette, and replaced with 0.7% LMP agarose in E3 medium (cooled to touch) – or in OptiPrep-Danieau's if indicated. Embryos were incubated at 28.6 °C until the desired stage, with extra E3 medium to prevent the agarose from drying out.

2.2.5.3 Deyolking

Embryo deyolking was done following advice given by Ksenia Kuznetsova and the instructions for OptiPrep in (Boothe et al., 2017). Embryos to be deyolked were dechorionated in 25% OptiPrep (Sigma-Aldrich, D1556) in 0.3% Danieau's medium (1740 mM NaCl, 21 mM KCl, 12 mM $MgSO_4 \cdot 7H_2O$, 18 mM $Ca(NO_3)_2$, 150 mM HEPES buffer). They were then deyolked at the 64-256 cell stage, using an eyelash mounted on a 0,6 x25mm micro-lance (Becton Dickinson, 23G 1" – Nr. 16) to separate yolk from cells (explants). Cell explants were transferred to 8-well chamber using a glass aspirating pipette. Excess medium was removed using a micro-lance mounted on a syringe, and replaced with minimal 0.7% LMP agarose in OptiPrep-Danieau's (cooled to touch) – or in E3 medium if indicated. The micro-lance was used to shift explants to the centre of the well where the lower level of agarose causes flattening. Explants were incubated at 28.6 °C until the desired stage, with extra E3 medium to prevent the agarose from drying out.

2.2.5.4 Dissociation

Embryo dissociation was adapted from methods in (Boothe et al., 2017, Hilbert et al., 2021). Embryos at the 32-64 cell stage were placed in a 1.5 mL DNA LoBind Eppendorf tube (Eppendorf, 0030108035) with 1 mL deyolking buffer (**Table 2.22**). Tubes were gently vortexed to make a cell/yolk suspension, and centrifuged for 1 min at 300 g. The supernatant was replaced with wash buffer (**Table 2.23**), and again vortexed and centrifuged. The supernatant was then replaced with 1 mL 0.8 mM $CaCl_2$/Dulbecco PBS. Tubes were vortexed and placed on a rotator for 30 min to prevent re-pelleting. For imaging, the cells were pelleted by centrifuging for 1 min at 300 g, resuspended in 0.7% LMP agarose with 0.8 mM $CaCl_2$, and transferred to an 8-well chamber.

Table 2.22 Deyolking buffer

Reagent	Concentration
Glycerol	10% (v/v H_2O)
NaCl	55 mM
KCl	1.75 mM
$NaHCO_3$	1.25 mM

Table 2.23 Deyolking wash buffer

Reagent	Volume (μL)
Glycerol	10% (v/v H_2O)
NaCl	110 mM
KCl	3.5 mM
$CaCl_2$	2.7 mM
Tris/HCl pH 8.5	10 mM

2.2.5.5 Staging and measuring nuclear diameter

Embryos were staged by time and morphology according to (Kimmel et al., 1995). Further staging was carried out by measuring nuclear diameter, calculated from nuclear volumes measured in (Reisser et al., 2018) (Fig. 3.7.E). Images acquired before FCS or AAT-FRET measurements were analysed in the LAS-X software (Leica Microsystems, Germany), measuring the diameter of nuclei as identified by expression of tagged PTFs or the brightfield channel.

2.2.6 Immunofluorescence

Protocol adapted from (Aljiboury et al., 2021): Embryos at the desired stage were placed in a 1.5mL Eppendorf tube and pFA, diluted in ddH_2O from a 16% stock (Thermo Scientific, 28908), was added at a final concentration of 4%. Embryos were first incubated for 2 h at 20-23 °C and mixed on the lowest setting (Eppendorf Thermomixer), then incubated o/n at 4 °C. The next day, pFA was removed and embryos washed twice quickly with 0.1% Triton X-100/PBS, and washed 3 times for 5 min with 0.5% Triton X-100/PBS. Embryos were dechorionated in 0.1% Triton X-100/PBS in a 35 mm plastic dish (Corning, 430165), with Dumostar #5 tweezers (Dumont, 500085), then returned to the Eppendorf tube. PBS-TritonX was replaced with 800 μL block buffer (**Table 2.24**) with 10% heat inactivated goat serum (Gibco,

16210064), and incubated for 1 h (20-23 °C). Block solution was removed and embryos incubated with chicken anti-GFP antibody (Abcam, ab13970), diluted 1:200 in block solution, o/n at 4 °C. The primary antibody in block solution was removed, embryos rinsed twice quickly, then washed 6 times for 20 min with 0.5% Triton X-100/PBS. This was replaced with goat anti-chicken IgY H&L, Alexa-594 secondary antibody (Abcam, ab150172), diluted 1:200 in fresh block solution, and incubated o/n at 4 °C. After the secondary antibody in block solution was removed, embryos were again rinsed twice quickly, then washed 4 times for 20 min with 0.5% Triton X-100/PBS. The wash was replaced with DAPI (1:1000 in 0.5% Triton X-100/PBS) for 30 min at 20-23 °C. After removing the DAPI solution, embryos were rinsed twice quickly, and washed 3 times for 20 min, with 0.5% Triton X-100/PBS, followed by a quick rinse with first 0.1% Triton X-100/PBS, then PBS. Embryos were deyolked on a glass slide, using a 0,6 x25mm microlance (Becton Dickinson, 23G 1" – Nr. 16). As much PBS as possible was removed using the microlance attached to a syringe. Embryos were mounted in 40 µL Prolong Gold (Invitrogen, P36930), adding a glass coverslip, and sealed with nail polish, and left to set in the dark for 24 h at 20-23 °C.

Table 2.24 Block buffer

Reagent	Concentration
DMSO	1x
BSA	40mg/mL
Triton-X	50%
PBS	1x

2.3 HeLa cell culture and transfection

HeLa cells were grown in standard growth medium (DMEM) (Gibco, 21969-035) supplemented with 10% Fetal Calf Serum, 0.1% Pen/Strep, 0.1% L-Glutamine (IGC technical services), at 37 °C and 5% CO_2. Cells were split 1:8 to 1:12 into a new T25 flask every 3-4 days: 1 mL trypsin was added to detach cells, quenched after 5-6 min with 4 mL DMEM, the suspension centrifuged for 5 min at 300 g, the cell pellet re-suspended in 1 mL DMEM. For transfection, cells were counted using a haemocytometer (Neubauer): 20 µL cell suspension were diluted 1:5 with 60 µL Trypan blue and 20 µL DMEM, and 10 µL pipetted onto the haemocytometer

(Neubauer). 6000 cells were seeded per well in 8-well chambers (ibidi, 80807) containing 200 μL DMEM and transfected the next day at ~60% confluence with 7.8 x 10^{-9} nmol DNA plasmid (~ 24-30 ng), using Lipofectamine 3000 (Invitrogen, L3000001). 25 μL DNA-lipid complex were added to each well. Microscopy was done the day after transfection.

2.4 Fluorescence Microscopy

Microscope incubators (Okolab) were set to 26.5 °C for live zebrafish embryos, or 37 °C and 5% CO_2 for HeLa cells.

2.4.1 Live wholemount microscopy

WT embryos were microinjected into the cell or yolk, at the 1-cell stage with 500 pL mRNA/dye mix containing 10 μM dye and 50-100 pg mRNA (50 pg mCherry-Pou5f3, 100 pg Sox19b-Citrine/ Citrine, 150 pg Nanog-Citrine). At 3 hpf, embryos were transferred to 8-well imaging chambers in E3 medium and imaged using an Andor Dragonfly spinning disk confocal microscope (Oxford Instruments). Z-stack images were acquired using a 20x 0.75 numerical aperture (NA) objective, 40 μm pinhole diameter, and an iXon EMCCD camera, with 5 μm step size and 1024x1024 pixels (px), to create a voxel size of 0.6x0.6x5 μm. mCherry/ A568, Citrine, and 488 were excited with 561 nm, 514 nm, 488 nm lasers, with filters set to collect peak emission wavelengths of 620nm, 540nm, 525nm respectively. Z-stacks were acquired consecutively for each channel.

2.4.2 Nuclear P/S/N distribution in live zebrafish embryos

Embryos were microinjected with ~60 ng/μL mRNA encoding Nanog-Citrine, Sox19b-Citrine, Citrine-Pou5f3, or mCherry-Pou5f3 and transferred to an 8-well chamber at approx. 1.5 hpf. Imaging was carried out on an SP5 point scanning confocal microscope (Leica Microsystems), equipped with an Argon laser, a diode-pumped solid-state (DPSS) laser, and PMTs. Images were acquired in the LAS-F software, using a 40x 1.1 NA water objective with ~15X digital magnification, 1024x1024 px, 200 Hz scan speed, 2x frame averaging. The Citrine and mCherry

channels were visualised by a 30% Argon laser, tuned by an Acousto-Optic Tunable Filter (AOTF) to 488 nm at 10-20% laser power, and the 561 nm DPSS laser at ~ 30 % laser power. PMTs were set to emission bandwidth 497nm - 580nm and 496nm - 549nm for the Citrine and mCherry channels respectively.

2.4.3 Nanog co-localisation with DNA in zebrafish embryo nuclei

Embryos were microinjected with 150 pg Nanog-Critrine mRNA and a final concentration of 174 µM SiR-DNA (Spirochrome, SC007), and either dissociated or mounted in the chorion. Imaging was carried out on the Stellaris 8 confocal point scanning microscope (Leica Microsystems) equipped with a white light laser (WLL) and HyD-S/ HyD-X detectors. Images of nuclei were acquired using the LAS-X software, with a 40x 1.1 NA water objective for chorionated embryos, or a 63x 1.4 NA oil objective for dissociated embryo cells. The Citrine and SiR-DNA channels were visualised sequentially by 30% 515nm laser line (HyD-S detector, 520nm - 642nm) and 652 nm laser line (HyD-X detector, 662nm - 834nm)., using 1024x1024 px, 200 Hz, 2x line average, with HyD-S detectors in counting mode.

2.4.4 Nanog co-localisation miR-430 transcription bodies in zebrafish embryo nuclei

Embryos were co-injected with 245 pg Nanog-mCitrine mRNA and the 3' Lissamine tagged miR-430 morpholino (7 µM final concentration), and mounted in the chorion. Embryos were imaged on the Stellaris 8 microscope. The Citrine and Lissamine channels were visualised with 30% 515 nm and 20% 580 nm laser lines, using a HyD-S (591nm - 631nm) and a HyD-X (522nm - 560nm) detector respectively. For the wholemount time-lapse, z-stack images were taken every 90s using a 40x 1.1 NA water objective, 512x512 px, 400 Hz, 2x line average, 2 Airy Units (AU), and a 2 µm z-step. For nuclei, images were taken using 1024x1024 px, 200 Hz, 2x line average, 1 AU.

2.4.5 Imaging of fixed zebrafish embryos and nuclei

Fixed embryos mounted in Prolong Gold were imaged on the Stellaris 8 microscope, visualising the DAPI and Alexa 594 channels with 4% 405 nm and 2% 590 nm (10% for nuclei), and HyD-S detectors in counting mode (425nm - 489nm for DAPI, 595nm - 655nm for Alexa 594). Wholemount images were acquired with a 20X 0.75 NA dry objective, using 1024x1024px, 200 Hz, and 2x line average. Images of nuclei were acquired with a 63x 1.4 NA oil objective, in lightning deconvolution mode, using 4464x4464 px, 512 Hz, and 3x line average.

2.4.6 Imaging HeLa cells

Cells were imaged on the Stellaris 8 microscope. The mCitrine and mCherry channels were visualised using 1% 515 nm and 587 nm laser lines. Images were acquired with a 40x 1.1 NA water objective, using 1024x1024px, 200 Hz, and HyD-S detectors (523nm - 569nm for mCitrine, 595nm - 657nm for mCherry).

2.5 Image Analysis

2.5.1 Processing live wholemount images to quantify expression across zebrafish embryos

2.5.1.1 Nuclear segmentation to extract nuclear intensities

Wholemount z-stack images of live embryos co-expressing tagged PTFs or Citrine with Alexa dyes were analysed in Fiji (ImageJ) (Schindelin et al., 2012). Nuclear segmentation was carried using the fluorophore intensity channel to create a mask of regions of interest (ROIs) within which to interrogate the original fluorophore and dye intensity channels (e.g. **Figure 3.4**B). For embryos expressing tagged PTFs, the mask was created by first subtracting the background (20 px rolling ball radius), applying the Gaussian Blur filter (2 px), and adjusting the intensity threshold (approx. 50-400). This mask was then subjected to segmentation analysis using the Trackmate with the built-in StarDist detector (Ershov et al., 2022), filtering spots by area (>41 µm). For embryos expressing Citrine, nuclear segmentation was carried out as above if possible, with first the Gaussian Blur filter (2 px), then background subtraction (10 px rolling ball radius) followed by the Gaussian Blur filter a second

time. Trackmate with Stardist was used as above, but spots were additionally filtered by circularity (>0.76), contrast (>0.14), and quality (>0.68). For images where automatic segmentation was not possible, ROIs were drawn by hand and converted to a mask. ROIs were linked between planes using Trackmate with Stardist. Intensity values of pixels in each ROI were then extracted as a .csv file using the 3D manager ImageJ suite (Ollion et al., 2013, Schindelin et al., 2012).

2.5.1.2 Processing nuclear intensity values

Data were imported into Python 3 (van Rossum, 1995) and processed using Pandas (McKinney, 2010) and NumPy (Harris et al., 2020). Pixel values were averaged across each ROI to give average nuclear intensity. The coefficient of variation (cv^2) of average nuclear intensity across each embryo, was calculated using **Equation 2.1**. Plots were created using the Seaborn package (Waskom, 2021).

Equation 2.1 Coefficient of variation of average nuclear intensities per embryo
Where σ is the standard deviation, and μ the mean of average nuclear intensities across each embryo.

$$CV^2 = \frac{\sigma^2}{\mu^2}$$

2.5.1.3 Representative images

Z-stacks were processed in Fiji, adjusting minimum/maximum brightness levels, and creating standard deviation (StDev) projections for each channel.

2.5.2 Processing nuclear distribution images in zebrafish embryos

Nucleus and wholemount images from fixed and live embryos (section 2.4.2-2.4.5,2.7) were processed in Fiji, by adjusting minimum/maximum brightness levels. For wholemount images, StDev projections were created for each channel. Images of nuclei acquired in lightning deconvolution mode were processed in LAS-X using standard settings in Lightning v6.2.1.3-46860387 (adaptive strategy, automatic contrast enhancement and cut-off, very high smooth-filter, no post-filter, alpha sum

abort criterion, Good's roughness regularisation) with 1 iteration for the DAPI channel, 7 iterations for the Alexa 549 channel.

2.5.2.1 Analysing Nanog-Citrine and miR-430 co-localisation over time

Wholemount z-stack time-lapses were processed in Fiji to analyse the co-distribution of Nanog-mCitrine and miR-430 intensities within nuclei. Nuclei were identified in the Nanog-mCitrine channel in individual z-plane images at single time-points. A line was drawn across the miR-430 foci in the nucleus, and the intensity of pixels was plotted along the line, for both channels. To create a representative image per time-point, z-stacks were processed to adjust minimum/maximum brightness levels, and creating StDev projections for each channel.

2.6 Fluorescence (Cross-) Correlation Spectroscopy

For initial FCS measurements, WT embryos were microinjected with ~60 ng/μL mRNA encoding Citrine- or mCherry-tagged Nanog, Sox19b, or Pou5f3. Embryos were placed in 8-well chambers containing E3 medium. For optimised FCS measurements, MZ*nanog -/-* or MZ*spg -/-* embryos were microinjected with 245 pg Nanog-Citrine or 76 pg mCherry-Pou5f3 mRNA, and mounted in the chorion. For FCCS measurements, WT embryos were co-injected with pairs of ~60 ng/μL mRNA encoding Citrine- or mCherry-tagged Nanog, Sox19b, or Pou5f3, or tagged-PTFs with Citrine/ mCherry fluorophores. Embryos were placed in 8-well chambers containing E3 medium. For co-injection FCS measurements, WT embryos were injected with mRNA encoding Citrine- or mCherry-tagged Nanog (150 pg), Sox19b (100 pg), or Pou5f3 (50 pg) alone, or co-injected with an untagged PTF. Embryos were placed in 8-well chambers containing E3 medium.

2.6.1 Measurements

FCS experiments were carried out on the Leica SP5 confocal adapted with two APD)PicoHarp 300 modules (Picoquant) for TCSPC in the red and green channels. Measurements were acquired in the LAS-AF software, using a 40x 1.1 NA water objective. The 30% Argon laser was tuned to 488 and 561 nm for green (Citrine) and

red (mCherry) channel measurements, using detectors set to 496-548 nm and 565-653 nm, respectively.

The OVE structural parameters (κ) were measured on every experimental day in calibration control measurements, using 10 nM Alexa 488 and/or 20 nM Alexa 568 dye-water solutions in a well adjacent to the embryos in the 8-well chamber. Dye FCS measurements were carried out with 2% 488 nm or 561 nm laser power. The dye solution was also used to adjust the objective's correction ring to minimise reflections from the coverslip, and to align the stage to focus ~ 20 μm from the bottom of the well.

For FCS/FCCS measurements in embryos, nuclear ROIs were selected by live screening in the measurement channel at ~20% laser power. Nuclei of intermediate/high fluorescence intensity were chosen, and digitally magnified to select a central ROI. Fluorescence intensity fluctuations were recorded for 50 s. For measurements of PTF diffusion, laser power was adjusted (~5-30%) to collect sufficient photons per measurement. For measurements of PTF concentration, laser power was kept constant per embryo and condition. Approximately 20 measurements were carried out for per embryo for approximately 3 embryos per condition.

Photon counts were monitored during acquisition, and measurements with count rates below 1000 counts per minute (cpm) discarded. If nuclei were too bright, they were pre-bleached using 100% laser power for a few s. As far as possible, care was taken to avoid photobleaching during measurements. Fluorescence fluctuation profiles with gross changes in average fluorescence intensity were discarded; sharp loss of signal is caused by movement of the nucleus to out-of-focus planes, sustained signal decrease by photobleaching (**Figure 2.2**).

FCS experiments on the Stellaris 8 were carried out in the same way, using HyD-X detectors to count photons in the red (593 nm - 722 nm) or green channels (520 nm - 623 nm). Measurements were acquired in the LAS-AX software, using a 40x 1.1 NA water objective. 20 % 488 nm and 587 nm laser lines were used for green (Alexa

488) and red (Alexa 568/mCherry) channel measurements respectively. Data were imported to SymPhoTime for further processing.

a) Stable
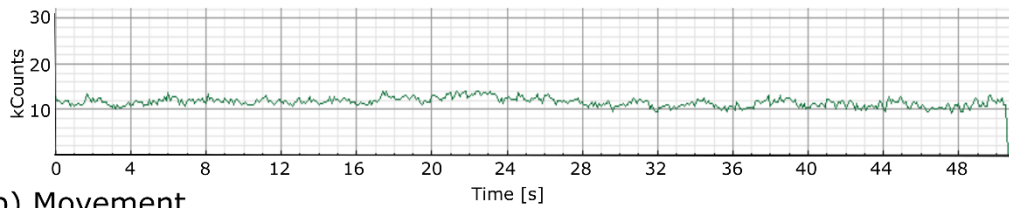
b) Movement
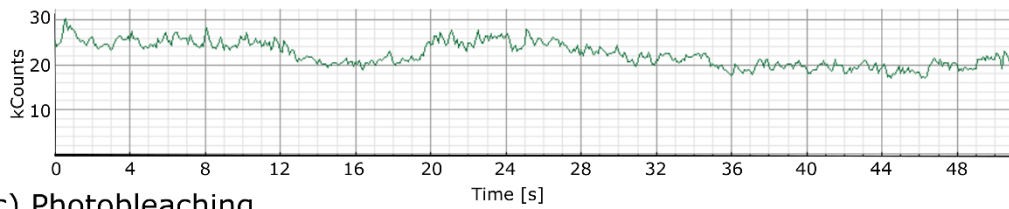
c) Photobleaching
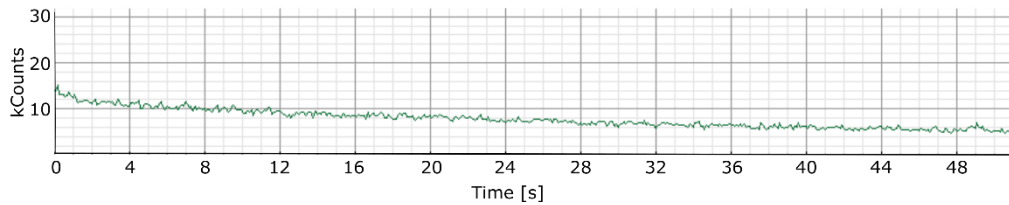
Figure 2.2 Examples of fluorescence intensity fluctuation profiles.

A) *Example of a stable number of counts over the 50s measurement period.* *B)* *Example of slow 'wavy' profile, which suggests movement of a large structure e.g. chromatin/ nucleus.* *C)* *Example of photobleaching, with steady decline of counts over the measurement period. b+c) would be discarded.*

2.6.2 Autocorrelation analysis

Time-Tagged Time Resolution (TTTR) data were analysed in the SymPhoTime 64 software (Picoquant). First, for each measurement, 20-30 s time windows featuring stable fluorescence intensity, preferentially towards the beginning of the measurement, were chosen for autocorrelation analysis. This compares the self-similarity of the signal over increasing lag-times (**Equation 1.1**). Autocorrelation functions (ACFs) were calculated using 3000 ms maximum lag time, 500 sampling points.

2.6.3 Cross-Correlation analysis

The similarity of signals in two channels (green, red) are compared to calculate the cross-correlation function (CCF) relative to the green and red channels (**Equation 1.3**). The Relative Cross-Correlation Amplitude (RCCA) is used to calculate the proportion of molecules interacting, relative to each channel (**Equation 1.4**).

2.6.4 Fitting ACFs

The dye measurement ACFs were fit to derive the κ-value, which is the length:diameter ratio of the observation volume element (OVE) for each channel: $\kappa = \frac{z_0}{w_0}$, where z_0 is the focal radius along the optical axis, and w_0 is the lateral focal radius, calculated at $\frac{1}{e^2}$ intensity using the V_{eff} (effective excitation volume/OVE). Dye ACFs were fit from 10^{-3} ms lag time until the ACF trends to zero, using least-squares fitting with the 3D triplet extended model, with one triplet (τ_{Trip}) and one fast-diffusing (τ_D) component (**Equation 1.2**).

The derived κ-value was noted for each dye (from the Alexa 488 curve for measurements in the green channel; from the Alexa 568 curve for the red). Experimental ACFs were then fit, as above, with one triplet (τ_{Trip}) and two fast-diffusing (τ_{D1}, τ_{D2}) components, and the respective κ-value as a fixed variable. In optimised FCS measurements, the τ_{Trip} component was only included to fit mCherry ACFs. Experimental ACFs were fit from 10^{-2} ms lag time until the ACF trends to zero. Fits were evaluated by eye and least squares analysis, and lag time bounds adjusted to optimise fits. In optimised FCS measurements, maximum lag time bounds were kept constant between measurements.

2.6.5 Analysis of ACFs, CCFs, and fitted values

ACFs and fitted values were exported and processed in Excel (Microsoft). Individual raw ACFs were shifted in the y-axis to flatten out at zero (not in optimised FCS measurements), normalised to a maximum $G(\tau)$ of 1 at 10^{-3} ms, averaged, and re-normalised. Aberrant FCS curves, displaying large deviations from zero at long lag times (**Figure 3.6**) were excluded from the average. Averaged and normalised ACFs,

as well as fitted τ_D, τ_{Trip}, ρ values from these measurements, were exported to python and plotted using the Seaborn package.

2.6.5.1 Estimating nuclear PTF concentration

The number of particles is proportional to the fluorescence intensity, and inversely proportional to the ACF amplitude at the y-intercept (**Equation 2.2**).

Equation 2.2 Relationship of ACF amplitude with number of particles (N) in the OVE (V_{eff})

$$G(0) = \frac{1}{N} = \frac{1}{V_{eff} \cdot G(0)}$$

The nuclear concentration (C), was estimated using the κ-value and nuclear volume at ZGA (~1.5 pL, taken from (Reisser et al., 2018)) (**Equation 2.3**).

Equation 2.3 Estimation of nuclear PTF concentration

$$C = \frac{\dfrac{1}{\pi^{1.5} \cdot \dfrac{1}{\kappa}^2 \cdot 10^{-15}}}{(6.022 \cdot 10^{23})} \cdot 10^9$$

2.6.6 Pinhole control experiments

2.6.6.1 Fluorophores expressed in WT embryos

WT embryos were injected with 150 pg mRNA encoding Citrine or 50 pg mCherry mRNA. mCherry embryos were kept in E3 medium, while half the Citrine embryos were mounted in 0.7% LMP agarose in E3, half kept in E3 medium, in an 8-well chamber. FCS measurements were carried out as described in section 2.6.1, four times per nucleus with different pinhole sizes (20, 50, 77, and 120 μm). ACFs were calculated as in section 2.6.2, and fit as in section 2.6.4, using a single τ_D component: fits including or excluding a τ_{Trip} component were compared by eye and least squares analysis. ACFs and fitted values were analysed as in 2.6.5.

2.6.6.2 Alexa 488 dye in vitro, SP5 vs. Stellaris 8

As for calibration control measurements, 10 nM Alexa 488 dye-water solution was placed in an 8-well chamber. For SP5 and Stellaris 8 FCS, measurements were carried out as described in section 2.6.1, across pinhole sizes indicated in section 2.6.6.1, and processed as in section 2.6.2 and section 2.6.4 with one τ_D and one τ_{Trip} component. ACFs and fitted values were analysed as in section 2.6.5.

2.6.6.3 Multi-point FCS

Experiments were carried out by J. J. Stoddart (JJS) D. K. Papadopoulous (DKP), S. Oasa (SO), and V. Vukojevic (V.V.) at the Karolinska Institute Stockholm. WT embryos were injected with mRNAs encoding Citrine-Pou5f3 (50 pg), Sox19b-Citrine (100 pg) or Nanog-Citrine (150 pg). mpFCS measurements were acquired on custom fFMI system as described in (Krmpot et al., 2019). This was made up of an Axio Observer D1 inverted epi-fluorescence microscope (Zeiss), a 63x 1.2 NA water objective, 488 nm laser, and a filter set for eGFP (470/40 nm excitation bandpass filter; 495 nm cutoff long pass dichroic mirror; 525/50 nm emission bandpass filter). The laser beam was expanded and split into 32x32 beams. Single photons were counted in parallel on a 32x32 array on a Single Photon Counting Camera SPC[2] (SPAD camera) (Micro Photon Devices MPD). Data was acquired and analysed using a software written in Embarcadero C++ Builder CE7 (Embarcadero Technologies).

2.7 FRET measurements

2.7.1 Intensity-based and AAT-FRET for controls

Methods adapted from paper in Chapter 2 (Auer et al., 2022):

MZ*nanog* -/- embryos were microinjected with equimolar amounts of mRNA (95 pg mCherry, 97 pg mCitrine, 192 pg mCherry-mCitrine), and a final concentration of 174 µM SiR-DNA. Embryos were dechorionated for imaging at approx. 3 hpf (section 2.2.5.2). Image data were acquired on the Stellaris 8 microscope, using the 40x 1.1 NA water objective.

2.7.1.1 Intensity-based and AAT-FRET

The donor (mCitrine) and SiR-DNA were imaged in frame sequential mode to create a z-stack with an 8 µm z-step size. mCitrine was imaged using the 515 nm laser line at 40% power with a HyD-X detector (523-570 nm) in photon counting mode for intensity-based FRET, TauContrast mode for AAT-FRET (Roberti, 2020). SiR-DNA was imaged using the 652 nm laser line at 20% power with a HyD-X detector (digital mode, 662-710 nm).

Varied image acquisition settings were used initially for AAT-FRET, as indicated. Optimised AAT-FRET acquisition settings (setting A in further experiments) imaged the donor with a 515 nm laser line at 40% power, with a HyD-X detector (523-570 nm) in TauContrast mode, the 40x 1.1 NA water objective with 1.44X digital magnification, 256x256 px, 200 Hz, 8 line accumulation, 2 AU, to acquire z-stack images with 8 µm z-step size.

To verify mCitrine, mCherry, and SiR-DNA expression levels, pre-acquisition images were taken for a single z-plane per embryo (setting pre-A in further experiments), using the 515 nm laser line at 30% power for mCitrine (HyD-detector, 523-570 nm), the 587 nm laser line at 30% power for mCherry (HyD-detector, 595-640 nm), and the 652 nm laser line at 20% power for SiR-DNA (HyD-X detector, digital mode, 662-710 nm). Images were acquired with 512x512 px, 400 Hz, 1 AU.

Acceptor Photobleaching was carried out for two z-planes on opposite ends of the z-stack. The acceptor (mCherry) was bleached using 100% 587 nm laser line for 30 s. Single z-plane intensity or AAT images were acquired pre- and post-photobleaching, with an additional channel to monitor mCherry intensity: 30% 587nm laser line with HyD detector (595-640nm). For AAT-FRET AccPb, the HyD-X detector was used in TauInteraction mode (Intensity, AAT, and mfD value given per pixel).

2.7.1.2 Sensitised Emission FRET

Z-stack images of the acceptor and SiR-DNA were acquired as above, imaging mCherry with the 515 nm laser line at 40% power with a HyD-X detector (TauContrast mode, 595-640 nm), and SiR-DNA with the 652 nm laser line at 20% power with a HyD-X detector (digital mode, 662-710 nm). Pre-acquisition images were acquired as for intensity-based or AAT-FRET.

Donor photobleaching was carried out for two z-planes on opposite ends of the z-stack. The donor was bleached using the 515 nm laser line at 100% power for 30 s. Single z-plane SE-images were acquired pre- and post- photobleaching, with an additional channel to monitor mCitrine intensity: 515 nm laser line at 30% power with a with HyD detector (523-570nm).

2.7.1.3 Nucleus segmentation

Images were processed in Fiji or LAS-X. 3D nuclear segmentation was carried out in Fiji after background removal and Gaussian blur filter in the SiR-DNA channel, and the resultant regions of interest (ROIs) were used to interrogate the mCitrine/mCherry intensity/AAT channels. For some images, mCitrine/mCherry intensity channels were used to verify/carry out segmentation. Background subtraction using a rolling ball radius of ~10 px and Gaussian blur of ~0.9 μm were performed on the SiR-DNA channel (settings varied for embryos with different SiR-DNA signal patterns). The resultant stack was used to perform 3D nuclear segmentation was carried out using Trackmate with StarDist. 2D ROIs representing segmented nuclei detected on each z-planes were filtered by manual thresholding of radius, signal-to-noise, and quality features, as well as manual inspection to remove false detections. The remaining detections were linked together using the Trackmate overlap tracker to create a 3D label stack which was used to extract the pixel intensity and AAT values for each nucleus from original image stack using the 3D ImageJ Suite. For single z-planes pre-/post-bleach images, nuclei were segmented manually (Fiji or LAS-X), and pixel intensity and AAT values were extracted for each nucleus.

2.7.1.4 Data processing

Nucleus ROI data were processed in Python 3, and plots were made using Seaborn. Pixels were binned into 0.1 ns AAT bins (matching the detector resolution), and pixel intensities for each AAT bin summed, creating an AAT vs. intensity plot for individual ROIs. These match the AAT plots imported from nuclei segmented in LAS-X. AAT plots were normalised to an intensity of 1, averaged across each condition, and re-normalised, to create line-graphs for visual comparison. The mean weighted AAT (MW AAT) per nucleus was calculated from individual ROI AAT plots (**Equation 2.4**).

Equation 2.4 Mean weighted AAT per nucleus

Where I is the Intensity at a given AAT (sum of photons counted in pixels with given AAT), and I_{max} is the maximum Intensity value for a given ROI

$$MW\ AAT = \frac{\sum(AAT \times \frac{I}{I_{max}})}{\sum(\frac{I}{I_{max}})}$$

mfD was calculated per pixel from AAT values (**Equation 2.5**, adapted from **Equation 1.6**). Mean weighted mfD was calculated as for Mean Weighted AAT. mfD and mean weighted mfD values <0 were set to 0, as the minimum fraction cannot be lower than 0%.

Equation 2.5 Minimum Fraction of Donor Interaction, mfD, per pixel.

Where MW AAT$_D$ is the donor MW AAT in absence of the acceptor, and AAT$_{D+A}$ is the donor AAT in presence of the acceptor.

$$mfD = \frac{1 - (\frac{AAT_{D+A}}{\sum MW\ AAT_D})}{((\frac{AAT_{D+A}}{2 * \sum MW\ AAT_D}) - 1)^2}$$

Intensity-based and Lifetime-based FRET Efficiency, E, were calculated using **Equation 2.6** and **Equation 2.7**.

Equation 2.6 Intensity-based FRET Efficiency.

Where I_{DA} is the is the average nuclear intensity of the donor in presence of the acceptor from across all 3 embryos and I_D is the average nuclear intensity of the donor alone.

$$E = 1 - \frac{I_{DA}}{I_D}$$

Equation 2.7 Lifetime-based FRET Efficiency.

Where τ_{DA} is the average AAT of the donor in presence of the acceptor from nuclei across all 3 embryos and τ_D is the average AAT of the donor alone.

$$E = 1 - \frac{\tau_{DA}}{\tau_D}$$

Intensity-based apparent FRET efficiency, E_a, was calculated for acceptor photobleaching using **Equation 2.8**.

Equation 2.8 Intensity-based apparent FRET Efficiency.

Where I_{DA} is the is the average nuclear intensity of the donor.

$$E_a = 1 - \frac{I_{DA(pre-bleach)}}{I_{DA(post-bleach)}}$$

Code deposited on Github: https://github.com/JuliaAuer/Auer2022---Non-fitting-FLIM-FRET-Zebrafish-embryos.

2.7.2 AAT- FRET for Nanog-mCitrine and Sox19b-mCherry

2.7.2.1 AAT-FRET measurements in chorionated embryos

Initial AAT-FRET measurements were carried out in MZ*nanog* -/- embryos microinjected with 245 pg mRNA encoding Nanog-mCitrine +/- 209 pg Sox19b-mCherry or 245pg mCherry-Pou5f3 mRNA. For experiments testing the effect of the GeneTools Blue miR-430 MO (blue MO) on Nanog-mCitrine AAT, WT embryos were microinjected with 245 pg mRNA encoding Nanog-mCitrine +/- blue MO (7 µM final concentration). Embryos were mounted in the chorion (section 2.2.5.1), and z-stack AAT images taken using setting A. Nuclei were manually segmented in LAS-X to

create one ROI per nucleus, in the z-plane where the nucleus was largest. AAT histograms per ROI were created in LAS-X, and exported for further processing in Python 3, as in section 2.7.1.4.

2.7.2.2 AAT-FRET measurements in dechorionated embryos

To compare AAT-FRET measurements in embryos mounted in the chorion versus dechorionated, MZ*nanog* -/- embryos were microinjected with 245 pg mRNA encoding Nanog-mCitrine +/- 209 pg Sox19b-mCherry mRNA. Half the embryos were mounted in the chorion, and half were dechorionated prior to mounting (section 2.2.5.1 or 2.2.5.2). To test Nanog-mCitrine and Sox19b-mCherry interactions in dechorionated embryos, MZ*nanog* -/- embryos were microinjected with 245 pg Nanog-mCitrine +/- 209 pg Sox19b-mCherry or 95 pg mCherry mRNA, co-injected with the blue MO (7 µM final concentration). Z-stack AAT images were acquired using setting A. Nuclei were segmented and data processed as in sections 2.7.1.3 and 2.7.1.4.

2.7.2.3 AAT-FRET measurements at the miR-430 transcription body

To test acquisition settings, the GeneTools Blue AAT was measured in WT embryos microinjected with the blue MO (7 µM final concentration). Embryos were dechorionated (section 2.2.5.2), and z-stack images acquired using the 440 nm laser line at 20% power with a HyD-S detector (451 nm – 510 nm), 1024x1024 px, 400Hz, 4x line average, 2 AU, and 1 µm z-step size. To create representative images, z-stacks were processed in Fiji to adjust minimum/maximum brightness levels, and creating StDev projections for each channel.

AAT z-stacks were acquired using the 440 nm laser at 20% power with a HyD-X detector (451 nm – 510 nm) in TauContrast mode, 5X digital magnification, 512x512px, 200Hz, 8x line accumulation, 2 AU, and 1 µm z-step size (setting B). miR-430 foci were manually segmented in LAS-X to create one ROI per miR-430 focus, in the z-plane where this was largest. AAT histograms were plotted per ROI in LAS-X, and values for no. pixels, mean ROI intensity, MW AAT and MW AAT StDev, generated in LAS-X, were extracted.

2.7.2.4 Optimisation of embryo preparation methods and image acquisition for AAT measurements at higher magnification.

WT embryos were co-injected with 245 pg mRNA encoding Nanog-mCitrine with 209 pg Sox19b-mCherry or 95 pg mCherry mRNA, and the blue MO (7 µM final concentration). Embryos were dechorionated (section 2.2.5.2) or deyolked (section 2.2.5.3), and mounted in 0.7 % LMP agarose with OptiPrep or E3 medium, as indicated. Single z-plane AAT images were taken for Nanog-mCitrine. The 509 nm or 515 nm laser lines were used as indicated with the HyD-X detector (520-570 nm) in TauContrast mode. A range of acquisition settings were used:

Setting C)

40x 1.1 NA water objective, 2.5X digital magnification, 512x512 px, 400 Hz, 8 line accumulation, 2 AU.

Setting D)

256x256 px, 200 Hz, 8 line accumulation, 2 AU. 40x 1.1 NA water objective (1.44X, 2X or 3X digital magnification) or 63x 1.4 NA oil objective (0.75X or 1.23X digital magnification) as indicated.

Setting E)

1. 40x 1.1 NA water objective with 2X digital magnification, 512x100 px, 100 Hz, 8 line accumulation, 2 AU.

2. 40x 1.1 NA water objective with 1.44X digital magnification, 256x256 px, 200 Hz, 8 line accumulation, 2 AU.

3. 63x 1.4 NA oil objective with 1.44X digital magnification, 512x512 px, 100 Hz, 8 line accumulation, 2 AU.

Setting F)

40x 1.1 NA water objective with 1.44X digital magnification, 256x256 px, 200 Hz, 8 or 12 line accumulation (for 515 nm or 509 nm laser lines respectively), 2 AU.

Nuclei were manually segmented in LAS-X to create one ROI per nucleus. AAT histograms per ROI were created in LAS-X, and exported for further processing in Python 3, as in section 2.7.1.4.

To analyse the high central AAT pattern, a line was drawn across the middle of the image, and the intensity/AAT of pixels was plotted along the line.

2.7.3 AAT-FRET measurements in HeLa cells

Cells were transfected as in section 2.3, to transiently express Nanog-mCitrine (or NΔH/NΔN) alone or with mCherry-Pou5f3 (or PΔH) /Sox19b-mCherry (or SΔH)/mCherry, or in control conditions to express mCitrine + mCherry/ tandem-fused mCherry-mCitrine. 20 µL live Hoechst 33342 dye - NucBlue™ Live ReadyProbes™ reagent (Invitrogen, R37605) – was added to control condition wells 30 min prior to imaging.

The donor (mCitrine), acceptor (mCherry), and Hoechst 33342 were imaged in frame sequential mode, to measure mCitrine AAT and verify expression levels in a single image. mCitrine was imaged using the 515 nm laser line at 1% power with a HyD-X detector (523-570 nm) in TauContrast mode or TauInteraction mode (additional mfD channel). Hoechst 33342 was imaged using the 405 nm diode laser at 2% power with a HyD-S detector (counting mode, 420-470 nm). mCherry was imaged using the 587 nm laser line at 2% power with a HyD-S detector (counting mode, 595-660 nm). Single z-plane images were acquired with acquisition setting G: 40x 1.1 NA water objective with 1.5X digital magnification, 512x512 px, 200 Hz, 2 line accumulation, 1 AU.

2.7.3.1 Nucleus segmentation and data processing

Images were processed in Fiji. Nuclear segmentation was carried out in the mCitrine channel (the Hoechst channel for control conditions), and the resultant ROIs were used to interrogate the AAT channels. 2D ROIs representing segmented nuclei were detected with StarDist 2D (Schmidt et al., 2018), using the versatile (fluorescent nuclei) model, with automatic settings chosen, except the probability/score threshold (0.67) and overlap threshold (0.4). False detections were removed by

manual inspection. A label image was created from the remaining detections, which was used to extract the pixel intensity and AAT values for each nucleus from original image stack using the 3D ImageJ Suite. These were exported for further processing in Python 3, as in section 2.7.1.4.

2.8   Statistical analysis

Statistics were analysed in R (version 4.2.1) (R Core Team, 2022), using linear mixed effect models (lme4, version 1.1-30). For MZ mutant rescue experiments, the proportion of class IV rescues was compared between conditions, including 'biological replicate' as a random effect. For FCS measurements, $\tau_D$slow and ρslow were compared between conditions, including 'embryo' as a random effect, or 'biological replicate' as a random effect for co-injection FCS measurements. For intensity- and AAT-FRET in zebrafish embryos, Intensity (log transformed for donor-intensity FRET and SE-FRET), and MW AAT were compared between conditions in including 'embryo' (and where appropriate 'biological replicate') as a random effect. For AAT-FRET in HeLa cells, MW AAT was compared between conditions in including 'field of view' and 'biological replicate' as a random effect.

The significance of pairwise comparisons between estimated marginal means was assessed with Emmeans (version 1.8.0), accounting for multiple testing using the Tukey method. P-values were displayed as: n.s. $p > 0.05$, * $p \le 0.05$, ** $p \le 0.01$, *** $p \le 0.001$, **** $p \le 0.0001$.

3 Harnessing FCS/FCCS to measure Nanog, Sox19b, and Pou5f3 chromatin binding dynamics and interactions during zebrafish ZGA

3.1   Introduction

PTFs regulate cell fate transitions by making chromatin accessible for the expression of new transcriptional programmes. As discussed in section 1.1.1, the kinetics with which PTFs engage with chromatin, i.e. the degree, length, and cooperativity of binding, might correlate with chromatin accessibility and transcription. Studying PTF chromatin binding dynamics and interactions can therefore inform understanding of their function. However, these aspects of PTF behaviour are most commonly studied *in vitro*. My aim was therefore to quantify PTF interactions and chromatin binding dynamics in a tractable *in vivo* model. I chose to study PSN during zebrafish ZGA, as these PTFs act individually and together to increase chromatin accessibility for the first transcriptional onset in development (Miao et al., 2022, Palfy et al., 2020, Veil et al., 2019) (section 1.4.4). The external fertilisation, high fecundity, fast development, and transparency of zebrafish embryos makes them well suited for live microscopy, as multiple embryos can be prepared and imaged in the course of one experimental day. Furthermore, many measurements can be done per embryo, which have a high cell count (1000+) during main ZGA, compared to mammals (2 cells) (section 1.4).

FCS was chosen to investigate whether PSN have unique chromatin binding dynamics, and whether their binding changes during ZGA. As detailed in section 1.3.3, the 'fast' and 'slow' components quantified by FCS can reflect populations that are either freely diffusing or that are undergoing transient non-specific interactions with DNA during target-site search (Table 3.1). Thus, separate or changing dynamics could indicate different activities of the PTFs on chromatin, or reflect the changing chromatin environment (Kaaij et al., 2018) (section 1.4.2). SMT would in theory provide more information about a range of PTF-chromatin binding dynamics, however it is very challenging to achieve the very high SNR required to track single molecules *in vivo* (section 1.3.2). FCS is therefore more accessible as many standard fluorescent proteins, and a relatively lower SNR, are suitable to follow a population of molecules.

FCS has been used to measure protein dynamics in zebrafish embryos, including plasma tethered diffusion of Wnt3-eGFP and Lyn-eGFP (Teh et al., 2015), and eGFP-IQGAP1 diffusion in muscle fibre cells (Shi et al., 2009). FCS even detected a larger proportion of GFP-Oct4 chromatin-bound diffusion in the mesendoderm vs. ectoderm of zebrafish blastula cells during late stage ZGA (3.5 hpf) (Perez-Camps et al., 2016).

Dual-colour FCCS was chosen as a useful extension to FCS, as it measures the co-diffusion and thereby interaction of spectrally distinct molecules (Bacia and Schwille, 2007) (section 1.3.5). In zebrafish embryos, one study used FCCS and FRET to show interactions between GFP-Nanog and mCherry-Oct4 in the mesendoderm during late ZGA by (Perez-Camps et al., 2016).

However, there are also many challenges when using F(C)CS to measure PTF dynamics and interactions. Indeed, studies of TF diffusion and chromatin binding by FCS, and studies of TF interactions by FCCS, are mostly carried out in cell lines (**Table 3.1** and **Table 3.2**). Even in these simpler models, it can be problematic to choose an appropriate model to fit ACFs, as more than one will often fit equally well (Mazza et al., 2012) (section 1.3.3.1). Most commonly, models include two components for fast (free) and slow (chromatin-bound) diffusion (Lam et al., 2012b, Mazza et al., 2012, Oasa et al., 2021, Siegel et al., 2013, Szaloki et al., 2015, Teh et al., 2015)– sometimes this is modelled as anomalous, or hindered, diffusion (Kaur et al., 2013, Perez-Camps et al., 2016). Some model short-lived and long-lived chromatin binding, in addition to a diffusing component in an attempt to quantify the kinetics of TF chromatin interactions (Cosentino et al., 2019, Romero et al., 2022, Verneri et al., 2020). It is debatable to what extent using more complex models are useful for interpreting F(C)CS data, which is a bulk technique i.e. while it relies on single photon detection resolution, autocorrelation reports on an average population of molecules observed over the measurement timeframe (Mueller et al., 2013). The use of two lasers and channels in FCCS can cause additional issues; misalignment of

the OVE for channels due to different chromatic aberrations and OVE sizes can lead to underestimation of cross-correlation (Bacia and Schwille, 2007).

Further challenges arise *in vivo*: cell movement and molecule aggregates can affect fluorescence intensity fluctuations (Mueller et al., 2013, Stasevich et al., 2010, Stortz et al., 2018). These effects could be mistaken for slow diffusion, and are often corrected for. The depth of focus for F(C)CS measurements is limited by increasing light scattering in thick tissues, caused in part by a refractive index mismatch. This could result in a distorted OVE and miscalculation of diffusion and concentration deeper inside the zebrafish embryo (Schwille and Haustein, 2002). Lastly, F(C)CS requires low concentration of fluorescent molecules and good SNR, which is a challenging combination to achieve in live 3D samples; endogenous tagging or transient expression must be tuned to avoid fluorescence levels which are too high to detect fluctuations by diffusion; thickness of the specimen generally reduces photons reaching the detector, worsening the SNR.

I therefore set out first to test the feasibility of using FCS to measure PSN chromatin binding dynamics in live embryos undergoing ZGA, with the goal to compare this behaviour between PTFs and through ZGA. The second aim of this chapter was to test whether FCCS could be used to probe PSN interactions.

Table 3.1 Examples of applications of FCS to study TF diffusion

Model	TF	Slow diffusion (ms τ_D or $\mu m^2/s$)	% slow	Fitting model - components	Acquisition time	Comments	Reference
H1299	p53-Halo	3 secs (residence time, rt)	20	2: diffusion (diff) + binding (bind)	100 s	Temporal Image Correlation Spectroscopy, photobleaching correction	(Mazza et al., 2012)
HeLa	eGFP-RAR	*0.05-0.1*	30-40	2 diff	10 x 8 s		(Brazda et al., 2011)
ESCs	YPet-OCT4	~7-8 short-lived (sL)	20-30	1 diff, 2 bind	3 min		(Romero et al., 2022)
		120-175 long-lived (lL)					
Human Embryonic Kidney (HEK)	OLIG2-eGFP	850	65	2 diff	20 s	mpFCS	(Oasa et al., 2021)
HeLa	FOS-eGFP	*0.26*	35	2 diff	6 x 8 s		(Szaloki et al., 2015)
NIH-3T3	VBP-L_ZIP	~50 rt (k_{off}),		Reaction dominant: diff (k_{on})+bind (k_{off})	10-20 s	2-photon FCS	(Michelman-Ribeiro et al., 2009)
		~500 association time (K_{on})					
Posterior silk gland cells	eGFP-FMBP-1	98 sL	14	3 diff	6x10 s		(Tsutsumi et al., 2016)
		3 lL	40				
Mouse pituitary GHFT1	mCer3-HP1a	*0.48*		2 diff	8-10 s		(Siegel et al., 2013)

mESCs	OCT4-YPet	~10 sL	~20-30	1 diff, 2 bind	3 min		(Verneri et al., 2020)
		~150 IL					
	YPet-SOX2	~7 sL	30				
		~100 IL	20				
Mouse embryo	OCT4-paGFP	2-cell: 13		2 diff (free + anomalous)	10-20s 7-10 x	Photoactivated (pa) FCS	(Kaur et al., 2013)
		8-cell: 36					
		Inner blastocyst (IB): 48					
		Outer blastocyst (OB): 11					
	paGFP-SOX2	IB: 39					
		OB: 29					
	CDX2-paGFP	IB: 25					
		OB: 54					
Mouse embryo	paGFP-SOX2	4-cell: 50-250 (150)	5-20 (11)				(White et al., 2016)
		Inner 16-32 cell: 200	18				
		Outer 16-32-cell: 150	13				
	OCT4-paGFP	4-cell: 50	0-5				
		Inner 16-32-cell: 220	13				

		Outer 16-32-cell: 150	10				
Zebrafish embryo	GFP- Oct 4	100-200	~25	2 diff (free + anomalous)	30 s		(Perez-Camps et al., 2016)
Induced Pluripotent Stem Cells (iPSC)	GFP- OCT 4	*0.24*	49	2 diff	?		(Lam et al., 2012b)
ESC		*0.26*	48				
Chinese Hamster Ovary (CHO)		*0.17*	15				
Mouse Embryonic Fibroblast (MEF)		*0.17*	21				
iPSC	mRFP- SOX2	*0.14*	46				
ESC		*0.22*	47				
CHO		*0.3*	37				
MEF		*0.26*	37				
Zebrafish embryo – muscle fibre cells	eGFP- IQGAP1	7 ms		1 diff (?)	?	Single-wave (SW) FCCS	(Shi et al., 2009)
ESC	Halo- SOX2	*0.16*	23.5	2 diff	?	2-photon FCS	(Chen et al., 2014a)
	Halo- OCT4	*0.18*	30				

Zebrafish embryos (plasma membrane)	Wnt3-eGFP	*1*	60	2 diff	15 s	150 µm pinhole	(Teh et al., 2015)
	Lyn-eGFP	*3*	65				
ESCs	NANOG-GFP	~30 short-lived	18	1 diff, 2 bind	353.8 s	20-40 µs sampling time	(Cosentino et al., 2019)
		~500 long-lived	17				
	OCT4-GFP	~15 short-lived	19		176.9 s		
		~150 long-lived					
	HP1a-GFP	16 short-lived	30		353.8 s		
		150 long-lived	22				

Table 3.2 Examples of applications of FCCS to study TF diffusion

Model	TF	Slow diffusion (ms TD or $\mu m^2/s$)	RCCA	Fitting model - components	Acquisition time	Comments	Reference
HeLa	c-FOS-eGFP + c-JUN-mRFP1	*0.3*	0.35	2 diff	6x10 s	Confocal FCCS (RCCA) SPIM-FCCS (relative conc) Cross-talk + photobleaching correction	(Pernus and Langowski, 2015)
	eGFP-mRFP1	*0.4*	0.45				
Mouse pituitary GHFT1	mCer3-HP1a + mRuby-BZip	*10* (HP1a), *22* (bIP)	7% green, 17% red	2 diff	10-20 s		(Siegel et al., 2013)
	mCer3-mRuby dimer	*13* (mCer3), *15* (mRuby)	17% green, 50% red				
Zebrafish embryo Mesendoderm	GFP-Nanog + mCherry-Oct4	*0.5* (Nanog), *0.84* (Oct4)	0.46 (ME)	2 diff (free + anomalous)	30 s	Crosstalk correction	(Perez-Camps et al., 2016)
	GFP-mCherry	23 $\mu m^2/s$ GFP, 18 $\mu m^2/s$ mCherry	0.78				
HeLa	c-FOS-eGFP + c-JUN-mRFP1	*0.19* (38%)	0.2	2 diff	6 x 8 s	SPIM-FCCS + FRET	(Szaloki et al., 2015)

HEK	eGFP-OLIG2 + Tomato-OLIG2	*0.25* (43%)	0.28	2 diff	10x20 s			(Oasa et al., 2020)
HeLa	eGFP-RAR + mCherry-RXR	*0.2* (20-40%)	0.6	2 diff	1-2 kHz frame rate	SPIM-FCCS w/ alternating laser excitation + FRET: background/baseline/bleaching correction		(Reho et al., 2020)
H1299 (epithelial-like lung cancer)	eGFP-p53 + mCherry-MDM2		25%	2 diff (free + anomalous)	5x10 s			(Du et al., 2018)
	eGFP -p53 + mCherry		10%					
	NLS-eGFP + mCherry		40%					
U-2 OS	P50-mCherry2 + p65-eGFP	*1* (10%) p65	0.55	2 diff	10x5 s	Background correction		(Tiwari and Kinjo, 2015)
	mCherry2-NLS + eGFP2-NLS		0.27					
HeLa	CREB1: eGFP-Activator + mRFP-Repressor		0.45	1-3 diff	?			(Sadamoto et al., 2011)
	eGFP-mRFP		0.8					
HeLa	c-FOS-eGFP + c-JUN-mCherry		34%	2 diff	6x10 s	FRET + FCCS		(Vamosi et al., 2008)
	eGFP-mRFP		13%					

Xenopus embryo Dorsal Marginal Zone explants (membrane)	Xwnt5a- eGFP + ROR2-mCherry	0.14	40%	1 diff	400 s (4 line scans)	Dual-focus + dual-colour line-scanning FCS	(Wallkamm et al., 2014)
CHO nuclear lysate	GFP-OCT4 + mCherry-SOX2		3.9%	1 diff			(Mistri et al., 2022)
	GFP-OCT4 + mCherry-NANOG/ mCherry-OCT4+GFP-NANOGW10A		12.5%/ 3.6%				
	GFP-Sox2 + mCherry-NANOG/ mCherry-SOX2 + GFP-NANOGW10A		26.1%/ 2.8%				
	GFP-NANOG + mCherry-NANOG/ mCherry-NANOG + GFP-NANOGW10A		19.8%/ 1.7%				
	GFP-mCherry/		46.2%/ 2.5%				

	GFP + mCherry						
CHO/ESCs lysate	GFP-OCT4+mRFP-SOX2	*39* (OCT4) *24* (OCT4 + SOX2 + 40 nM DNA)	26%	2 diff	?	FCS, SW-FCCS, ap-FRET, FRET-FLIM	(Lam et al., 2012b)
	mRFP-GFP		39%				

3.2 Expression of fluorescently tagged Pou5f3, Sox19b and Nanog in zebrafish embryos by mRNA microinjection

In order to use F(C)CS to study PSN chromatin binding and interactions during zebrafish ZGA, the PTFs should be fluorescently tagged without affecting their function. PSN were expressed by microinjecting embryos with mRNA encoding the fluorescently tagged PTFs mCherry and (m)Citrine. This choice was based on successful FC(C)S measurements of mCherry-/Citrine- tagged Sox2 and Pax6 diffusion and interactions by another student– albeit in HEK cells. Further, a previous student had cloned some PSN constructs and done encouraging first FCS measurements of mCherry-Pou5f3 in wild-type (WT) embryos. The least disruptive tagging strategies were identified by testing how well each construct rescues the phenotype of MZ mutant embryos, and their expression was assessed by microscopy.

Others have shown that PSN mRNA microinjection rescues the gastrulation arrest of the corresponding MZ mutants, in a concentration-dependent manner: 50 picogram (pg) Pou5f3 mRNA rescued MZ*spg793* -/- embryos (Lunde et al., 2004, Reim and Brand, 2006), while 150 pg Nanog mRNA rescued MZ*nanog* -/- embryos, to produce fertile adults (Gagnon et al., 2018, Veil et al., 2018). MZ*sox19b* -/- embryos develop normally, due to redundancy of SoxB1 factors after ZGA, with only a brief delay in gastrulation (Gao et al., 2022, Palfy et al., 2020). However, knockdown of the additional SoxB1 factors results in axis elongation defects, rescued by 5-20 pg Sox19b mRNA (Gao et al., 2022). Rescue was generally scored in four classes, from no rescue (class I) to like WT (class IV) (Reim and Brand, 2006, Veil et al., 2018). The mRNA quantities and scoring of rescue classes established in these experiments were used to test different Nanog and Pou5f3 constructs - the MZ*sox19b* -/- line was not available at the time.

MZ*nanog* -/- and MZ*spg793* -/- embryos were microinjected with mRNA encoding Nanog or Pou5f3, tagged N- or C- terminally with mCherry or (m)Citrine, or untagged as positive control. Uninjected MZ mutant embryos were included on

every experimental day as a negative control. Rescue of the gastrulation-arrest phenotype was scored around 24 hpf (**Figure 3.1**Ai,Bi).
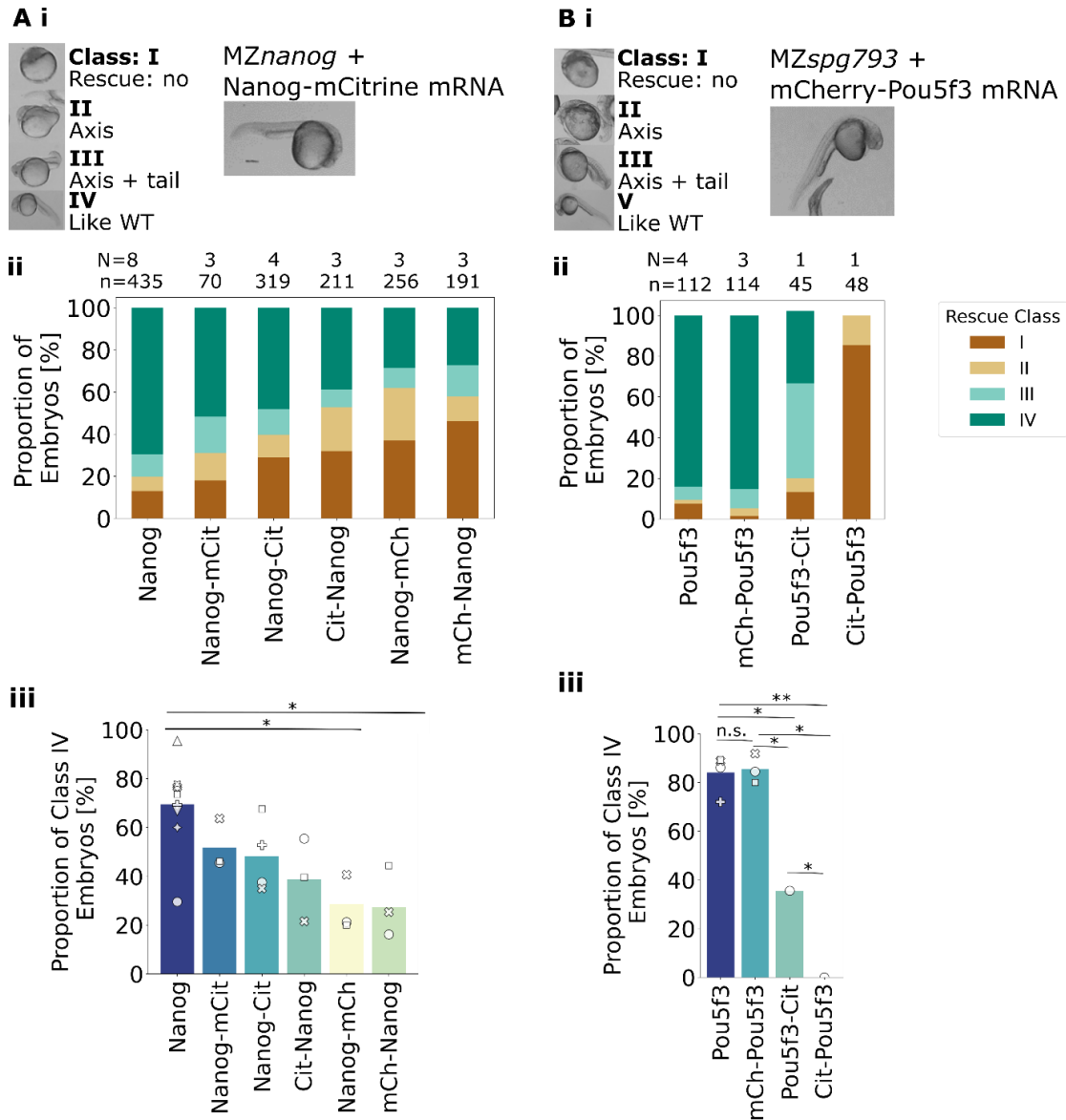
Figure 3.1 Rescue of MZ mutant embryos by fluorescently tagged PTF mRNA.
*PTF mRNAs were microinjected into MZnanog -/- or MZspg793 -/- mutant embryos at rescue amounts, and embryos scored 24 hpf (methods 2.2.3-2.2.4). **A+B) i.** Representative images of rescue classes for **A)** MZnanog -/- and **B)** MZspg793 -/- embryos, adapted from (Reim and Brand, 2006, Veil et al., 2018). (cont. over page)*

*Also representative images 24 hpf of class IV rescue phenotype for **A)** MZnanog -/- embryo rescued with Nanog-mCitrine mRNA**, B)** MZspg793 -/- embryo rescued with mCherry-Pou5f3 mRNA. **A+B) ii.** Stacked bar plots of proportion (%) of embryos in each rescue class, average across replicates, for **A)** MZnanog -/- and **B)** MZspg793 -/-. **A+B) iii.** Bar plots of % of class IV rescues, shapes denote different experimental days. N = 1-8 biological replicates (b.r.)/experimental days, n=45-435 embryos. Statistics were analysed using linear mixed effect models, and pairwise comparison of means (methods 2.8). n.s. p>0.05, * p≤ 0.05, ** p ≤ 0.01.*

For both PTFs, the fluorophore and its placement affected MZ mutant embryo rescue. Nanog tagged with (m)Citrine best rescued MZ*nanog* -/- embryos, particularly when tagged at the C-terminus (**Figure 3.1**Aii). Nanog-Citrine rescued on average 48.2% of embryos to a class IV phenotype, versus 69.5% for untagged Nanog (p=0.28, **Figure 3.1**Aiii,**Appendix Table 7.1**). The monomeric Citrine (mCitrine) construct was only created for later experiments, and Nanog-mCitrine rescued embryos only slightly better than Nanog-Citrine, with on average 51.7% scored as class IV rescue (p=0.59 vs. Nanog). The opposite tagging strategy was best for MZ*spg793* -/- embryos (**Figure 3.1**Bii): mCherry-Pou5f3 rescued on average 85.4% of embryos to a class IV phenotype, compared to 84.1% for untagged Pou5f3 (p=0.99 vs Pou5f3). Pou5f3-Citrine and Citrine-Pou5f3 were significantly worse, with 35.6% (p=0.03 vs Pou5f3) and 0% (p=0.01 vs Pou5f3) of embryos scored as class IV rescue respectively (**Figure 3.1**Biii, **Appendix Table 7.1**). Since mCherry-Pou5f3 consistently rescued embryos as well as untagged Pou5f3, other constructs were not tested further.
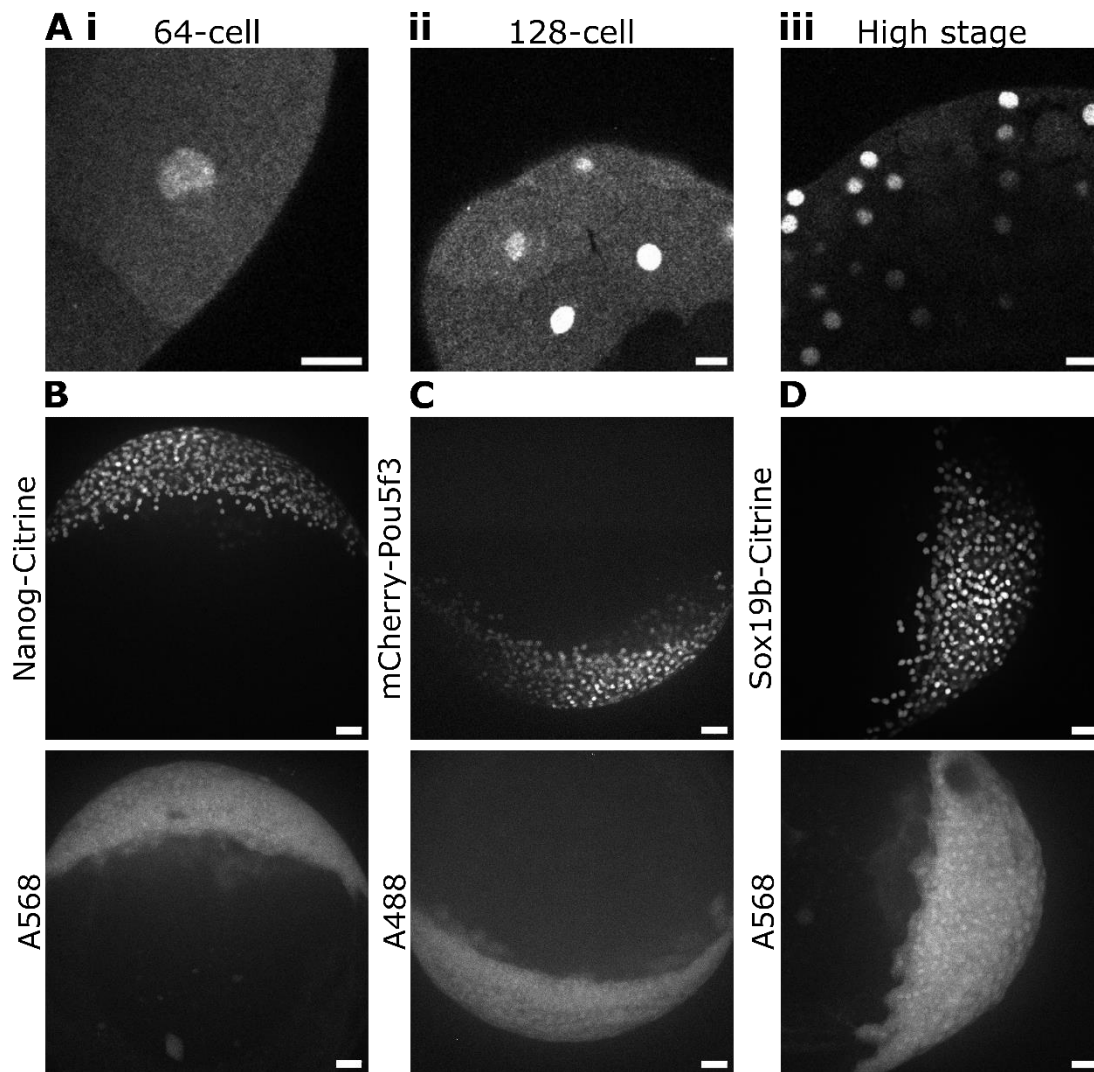
Figure 3.2 Comparison of distribution of fluorescently tagged PSN vs. co-injected dye in live embryos.

*A) Representative single z-plane images of Nanog-Citrine overexpressed in WT embryos, at **i.** 64-cell stage, **ii.** 128-cell stage, and **iii.** High stage (methods 2.7.1.1 setting pre-A), scale bar = 20 micrometres (μm). **B-D)** Representative z-stack images of WT embryos overexpressing **B)** Nanog-Citrine, **C)** mCherry-Pou5f3, or **D)** Sox19b-Citrine, co-injected with Alexa 568 (A568) or Alexa 488 (A488) dye. Images are standard deviation (StDev) projections of the z-stack for each channel (methods 2.4.1), scale bar = 50 μm.*

Next, I tested whether mRNA microinjection can feasibly be used to express tagged PSN in embryos for microscopy. PSN expression levels during ZGA, nuclear localisation, and distribution across embryos, were verified in live imaging, initially by overexpression of Nanog-Citrine, mCherry-Pou5f3, or Sox19b-Citrine in WT embryos. Expression was visible from early ZGA, becoming brighter as ZGA progressed (**Figure 3.2**A). PSN localised to nuclei, however nuclear PSN levels were visibly variable within an embryo, and in some embryos, expression was regionalised (**Figure 3.2**C).

To test whether this was an artefact of microinjection, fluorescently tagged PSN were co-injected with 50 µM Alexa 568 or Alexa 488. Live imaging showed that the dye was distributed more evenly across embryos (**Figure 3.2**B-D). The dye had an overall similar coefficient of variation (cv^2), of nuclear intensities per embryo, to tagged PSN (**Figure 3.3**Bii,Cii). However the Alexa 568 dye had a larger intensity range than the Citrine-tagged PSN in some embryos (**Figure 3.3**Ai,Ci), and these embryos also had a higher dye cv^2 (**Figure 3.3**Aii,Cii).
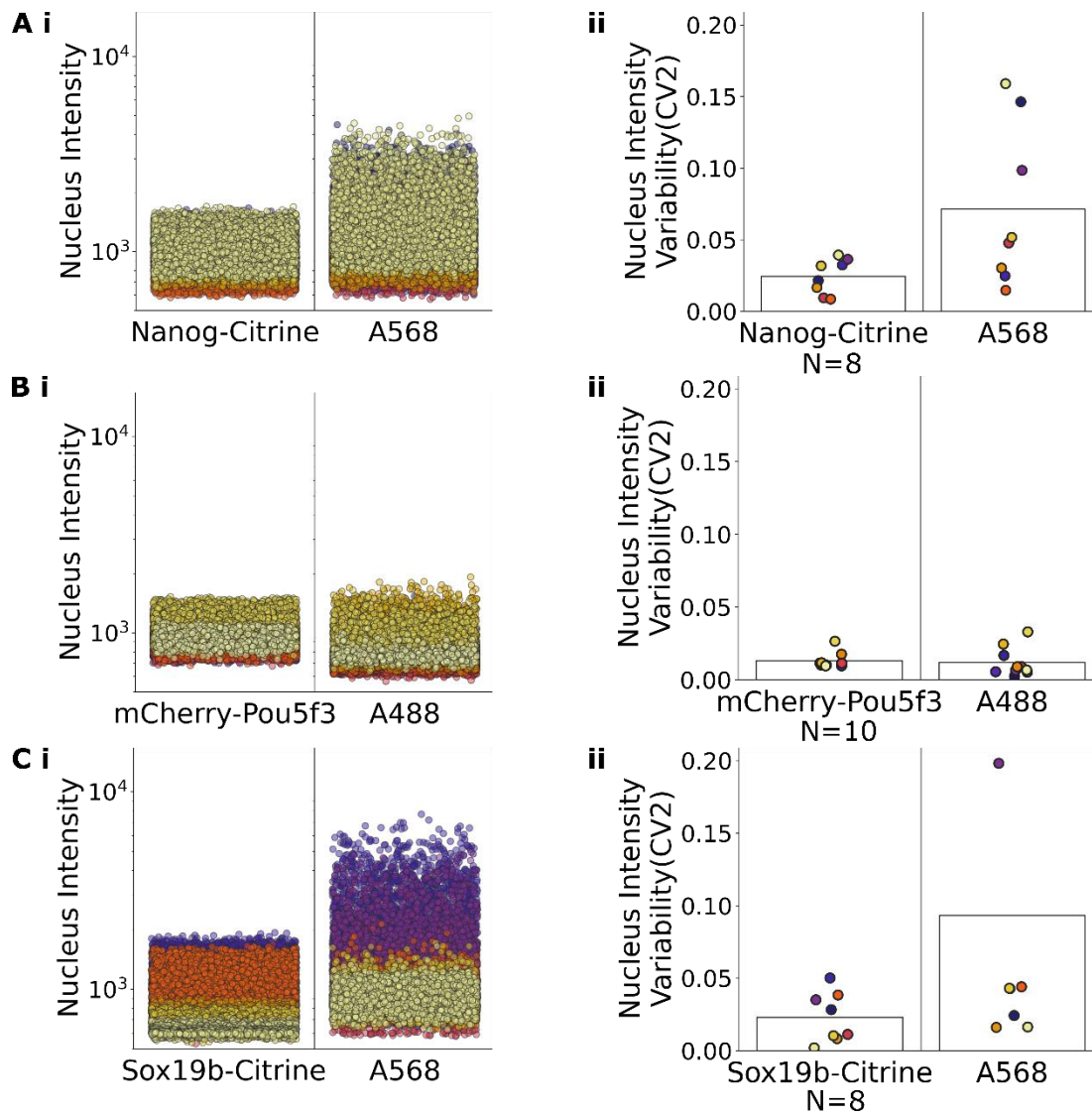
Figure 3.3 Nuclear fluorescence variability of fluorescently tagged PSN vs. co-injected dye in embryos.

 *Nuclear intensities for fluorophore and dye channels were quantified from z-stack images (methods 2.5.1 example mask in **Figure 3.4**B) of WT embryos expressing **A)** Nanog-Citrine/Alexa 568 (A568), **B)** Sox19b-Citrine/Alexa 568, or **C)** mCherry-Pou5f3/Alexa 488 (A488). **A-C) i.** Scatterplots of nucleus intensity, **ii.** Barplots of the coefficient of variation (cv²) of nuclear intensities per embryo (coloured by embryo). B.r.=3, N=8-10 embryos.*

When Citrine mRNA was co-injected with Alexa 568 dye, the same trend of more frequent regionalised distribution, but lower overall variability of nuclear levels was observed for Citrine (**Figure 3.4**A,Cii). Tagged PSN and Citrine may in some embryos be distributed regionally due to microinjection into the edge of a cell: faster diffusion of the dye than mRNA could lead to asymmetrical mRNA segregation in the following cell divisions. Higher range of nuclear Alexa 568 dye intensities (**Figure 3.3**A-C,**Figure 3.4**C) could, in contrast, be due to variable nuclear uptake.
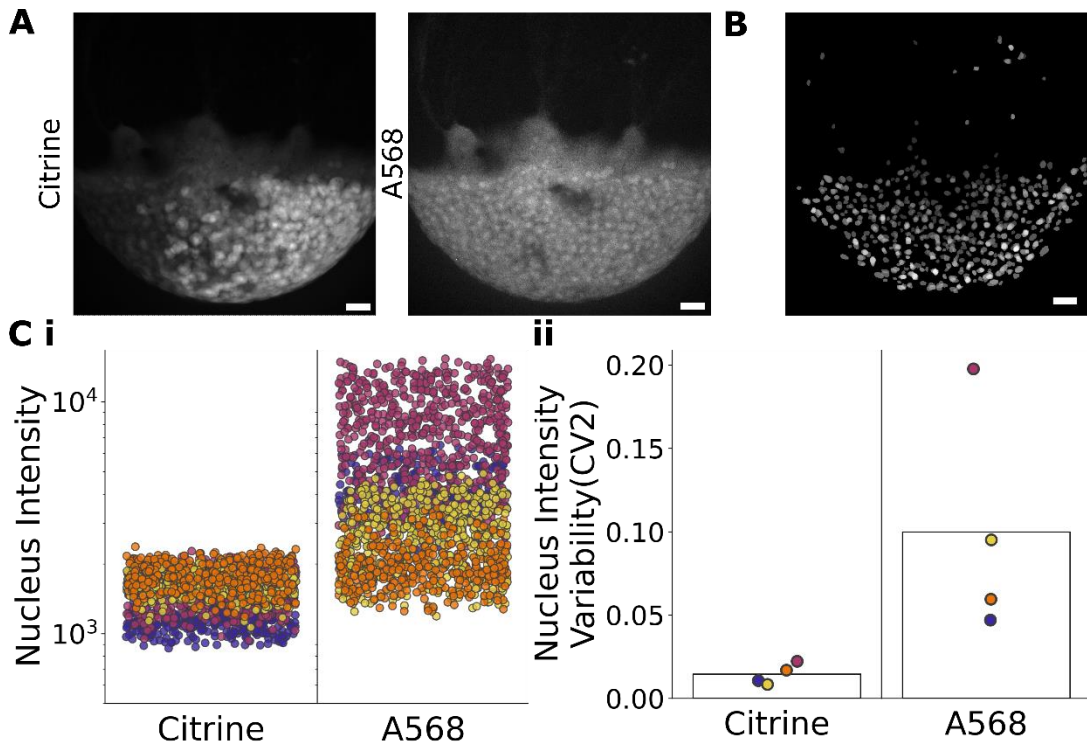
Figure 3.4 Nuclear fluorescence variability of fluorescent protein vs. dye in live embryos.

A) *Representative WT embryo co-injected with Citrine mRNA and Alexa 568 (A568), images are StDev projections of the z-stack of each channel (methods 2.4.1).* **B)** *Example StDev projection of segmentation mask used to measure pixel intensities in nuclei (methods 2.5.1).* **C) i.** *Scatterplots of nuclear Alexa 568/Citrine intensity, and* **C) ii.** *Barplots of the cv² of nuclear intensities per embryo (coloured by embryo) (methods 2.5.1). b.r. = 2, N=4 embryos. Scale bar = 50 μm.*

Overall, tagging Nanog and Pou5f3 with fluorophores such as mCherry and (m)Citrine did not disrupt their ability to rescue MZ mutant embryos (**Figure 3.1**), and allowed characterisation of PSN nuclear expression (**Figure 3.2**). Microinjection did introduce variability in levels and regional distribution between some embryos (**Figure 3.2**,**Figure 3.3**,**Figure 3.4**). Biologically relevant measurements of PSN expression levels and their variability require endogenous expression of fluorescently tagged PSN to avoid these effects. Attempts to generate zebrafish lines expressing these were unsuccessful. Thus, for further experiments, fluorescently tagged PSN were expressed by microinjection and embryos with regionalised or low expression were excluded.

3.3 Measuring Pou5f3, Sox19b and Nanog diffusion by FCS

To test whether FCS could measure PSN dynamics during zebrafish ZGA, N-terminal Citrine- or mCherry-tagged PSN (not all constructs were available) were initially overexpressed in WT embryos. FCS measurements were done during main ZGA at approx. 3 hpf, in the nuclei of embryos (**Figure 3.5**). ACFs were fit with a diffusion model including two diffusion components (τ_D) and a triplet blinking component (τ_{Trip}) (section 1.3.3, **Equation 1.2**). Nanog and Sox19b ACFs were shifted, and the proportion of slow-diffusing molecules (ρslow) was generally slightly higher, compared to Pou5f3 (**Figure 3.5**A,B). This could indicate that Nanog and Sox19b exhibit more transient chromatin interactions. Yet neither the ρslow nor the speed of slow-diffusing molecules ($\tau_D$slow) differed significantly between PTFs (**Figure 3.5**B,C). This is likely due to the high variability of fitted values between embryos and replicates for the same condition.

There was however a more noticeable (yet insignificant) fluorophore-specific trend. ACFs for Citrine-tagged PSN show greater autocorrelation at shorter lag-times (0.01 – 10 ms) than mCherry-tagged PTFs, possibly meaning that a greater proportion of Citrine molecules are freely-diffusing (**Figure 3.5**A). It is important to note that the $\tau_D$slow for mCherry-tagged PSN was in the seconds-range, whereas the expected slow component diffusion speed measured by FCS is more commonly in the ms-

range (**Table 3.1**). Rather, this suggests that issues in measurement and analysis, such as fluorescence signal artefacts, or inappropriate fitting, disproportionally affected one fluorophore.
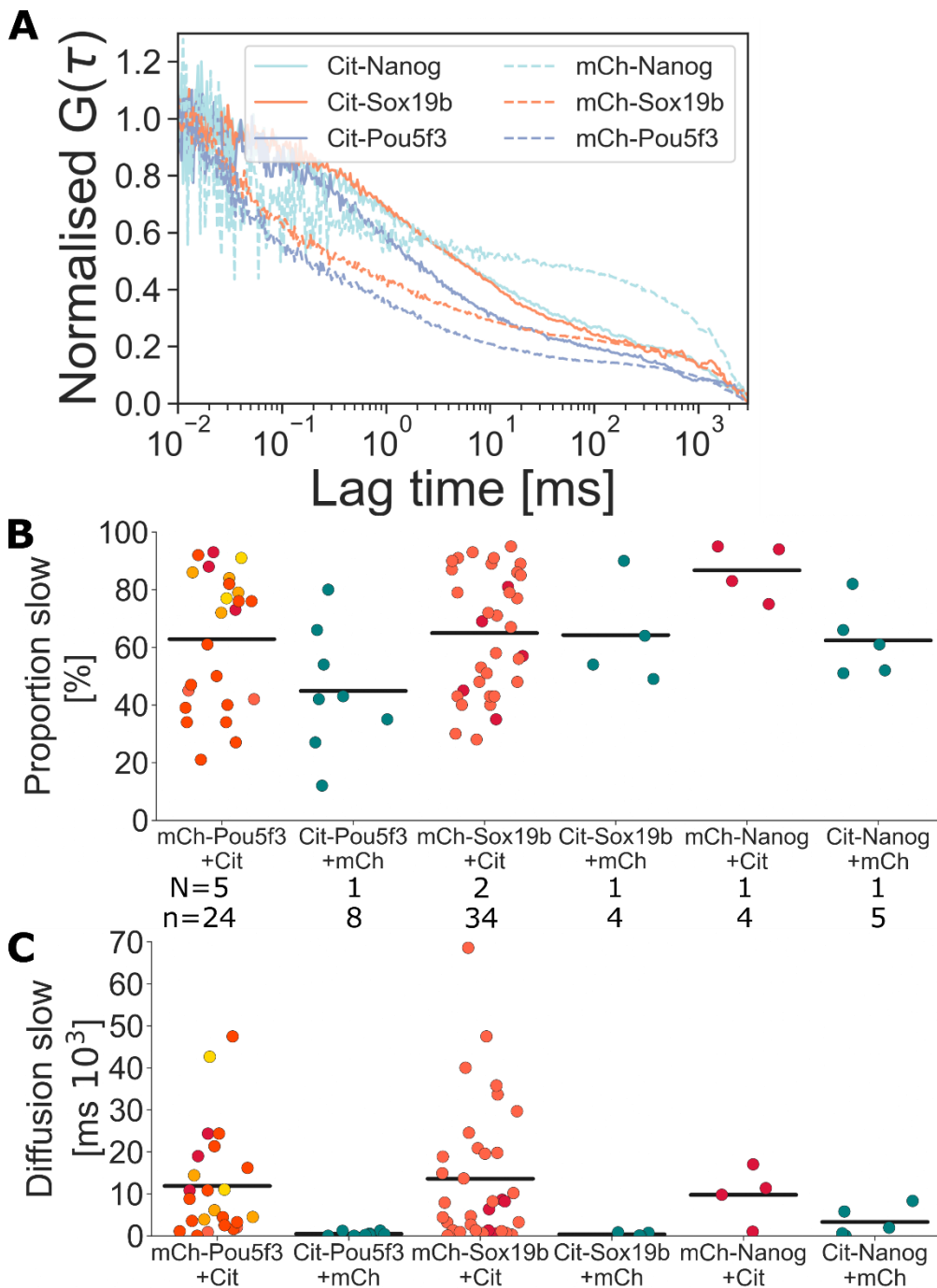
Figure 3.5 Measurement by FCS of diffusion of differently tagged PSN at ZGA.

(cont. over page)

FCS measurements were carried out at ~3 hpf in nuclei of WT embryos overexpressing PSN N-terminally tagged with Citrine (Cit) or mCherry (mCh).
A) *Normalised average autocorrelation functions (ACFs) (methods 2.6).* ***B-C)*** *Scatterplots of fitted values for* ***B)*** *proportion (ρslow) of slow-diffusing molecules and* ***C)*** *diffusion time of slow-diffusing molecules (τ$_D$slow), hue represents separate embryos, black line is mean value throughout. B.r. = 1-2, N=1-5 embryos, n=4-63 nuclei. Statistics were analysed using linear mixed effect models, and pairwise comparison of means (methods 2.8), all n.s. (p>0.05).*

Comparison of fluorescence fluctuation profiles, ACFs, and fitted curves showed that photobleaching was prevalent. The steady decrease in fluorescence signal results in higher autocorrelation at long lag-times (>100 ms), which could be misinterpreted as increased slow diffusion (**Figure 3.6**A). Photobleaching also selectively depletes molecules with true slow diffusion, leading to underestimation of their contribution. Higher laser powers were used in mCherry FCS measurements to achieve comparable photon counts to Citrine, as mCherry is less bright (Quantum yield mCherry = 0.22 (FPbase, 2023b, Shaner et al., 2004) vs. Citrine = 0.76 (FPbase, 2023a, Griesbeck et al., 2001)). mCherry-tagged PSN could therefore be particularly affected by photobleaching. Additionally, mCherry aggregates may cause overestimation of slow diffusion (Costantini et al., 2015, Landgraf et al., 2012).

Finally, the movement of large structures such as nuclei or the whole embryo can cause transient peaks or seconds-range fluctuations in the average fluorescence intensity (**Figure 3.6**B,C). This leads to aberrant autocorrelation, seen as deviations from the ACF's trend towards zero, at long lag-times (**Figure 3.6**A-C, magenta arrows). The maximum lag-time (where G(τ) flattens out, reaches y=0, or terminates, indicated by blue/orange/magenta arrows respectively) will affect the calculated τ$_D$ and ρ for molecules in the fast and slow components. Therefore, to draw reliable conclusions from FCS experiments, extensive improvements to measurements and analysis were required, such as reducing photobleaching, and excluding fluorescence fluctuation profiles with artefacts.
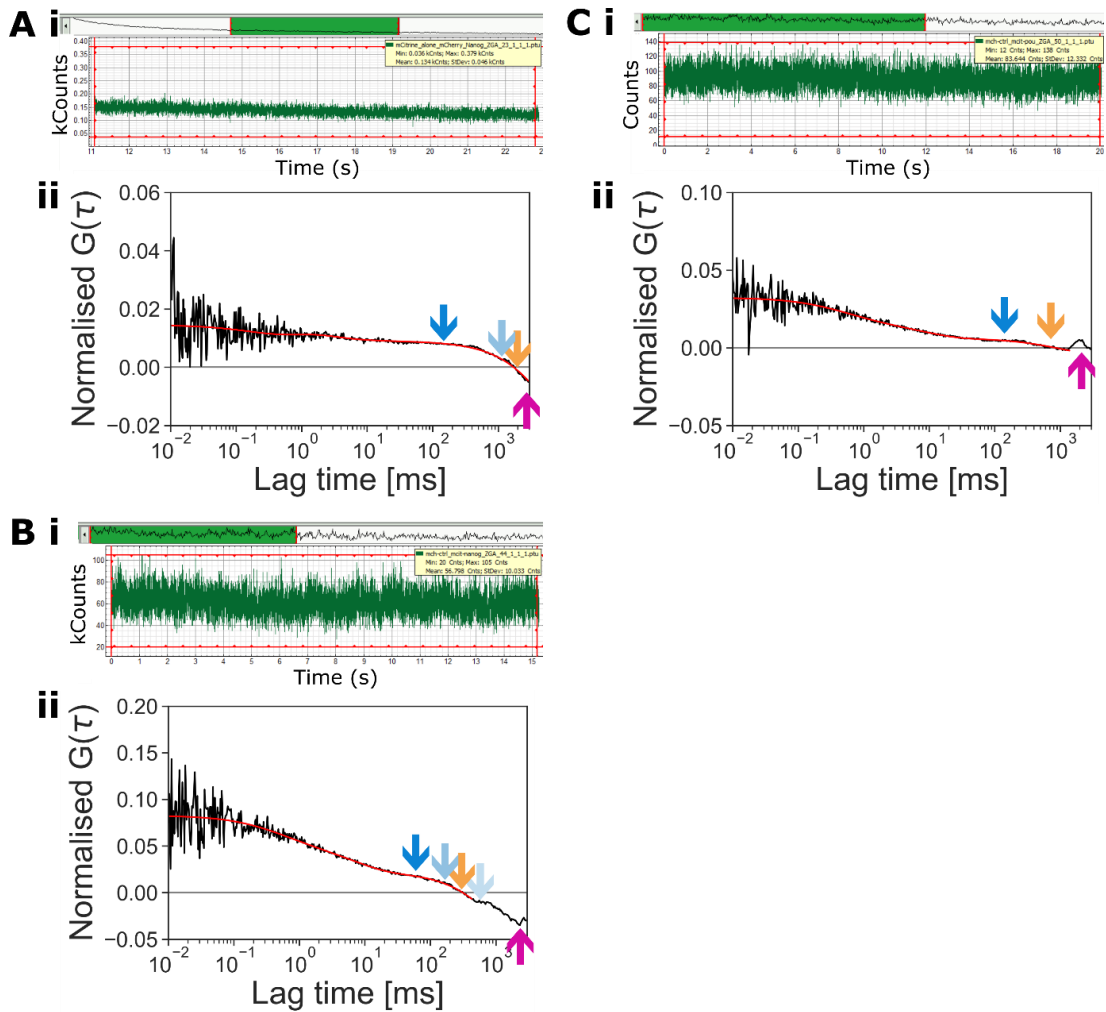
Figure 3.6 Troubleshooting ACF calculation and fitting.

A-C) i. Examples of fluorescence fluctuation profiles, snapshot from SymPhoTime software, time window selected for autocorrelation analysis highlighted in green and magnified in plot below. ii. Resultant raw ACFs (black, fitted curves red). Blue arrows indicate flattening of ACF, orange arrows indicate y=0, magenta arrows indicate deviation of ACF from 0 after y=0.

3.4 Optimisation of FCS measurements

Another interpretation of mCherry-tagged PSN seeming to diffuse more slowly than Citrine-tagged PSN (**Figure 3.5**) was that the fluorophores have different photophysical properties. A common example is triplet blinking, which happens when a fluorophore enters and leaves the dark triplet state, causing fluorescence intensity fluctuations in the microsecond (μs) timescale (Turro, 1991). Triplet blinking therefore results in ACFs with high autocorrelation between 1-10 μs. Accordingly, an extra component (τ_{Trip}) is included in fitting models for fluorophores displaying triplet blinking. However τ_{Trip} can often be confused with fast τ_D in fitting. To test whether mCherry or Citrine display triplet blinking, and what μs range this would occur in, their diffusion in zebrafish nuclei was measured using different pinhole sizes. As the fluorophores will take longer to diffuse across a larger pinhole, τ_D and τ_{Trip} should be more distinct; a new ACF component will emerge for measurements at larger pinholes, which will not scale with pinhole size because triplet blinking is not a diffusive process.

As expected, a right-shift was observed for mCherry and Citrine ACFs with increasing pinhole sizes, reflecting longer diffusion time (**Figure 3.7**A,B). However, accurate fitting of mCherry ACFs required inclusion of a τ_{Trip} from 50-120 μm pinhole sizes (**Figure 3.7**A,C). As expected, τ_{Trip} remained constant at 142 μs (+/- 33.7) on average, whereas the τ_D increased with pinhole size from 0.149 ms (+/- 0.0177) to 1.47 ms (+/- 0.208). No second component was observed in Citrine ACFs, and fitting gave a τ_D which increased with pinhole size 0.133 ms (+/- 0.0275) to 0.331 ms (+/- 0.0597) (**Figure 3.7**B,D). It is interesting to note that the mCherry τ_D increases about 10-fold with larger pinholes, compared to an about 3-fold increase for the Citrine τ_D. This reflects the slower τ_D measured for mCherry- vs. Citrine-tagged PSN, and could be an artefact of mCherry tending to form aggregates (Costantini et al., 2015, Landgraf et al., 2012).

A τ_{Trip} (constrained to 0-100 μs) was therefore included in fitting of ACFs for PSN tagged with mCherry, but not for (m)Citrine. Similarly, reasonable fitting of fast

diffusion ($\tau_D$fast) was checked by comparison to the fluorophore τ_D calculated at the standard 77 µm (1 Airy Unit) pinhole size: 1.05 ms (+/- 0.524) for mCherry, or 0.30 ms (+/- 0.0857) for Citrine.
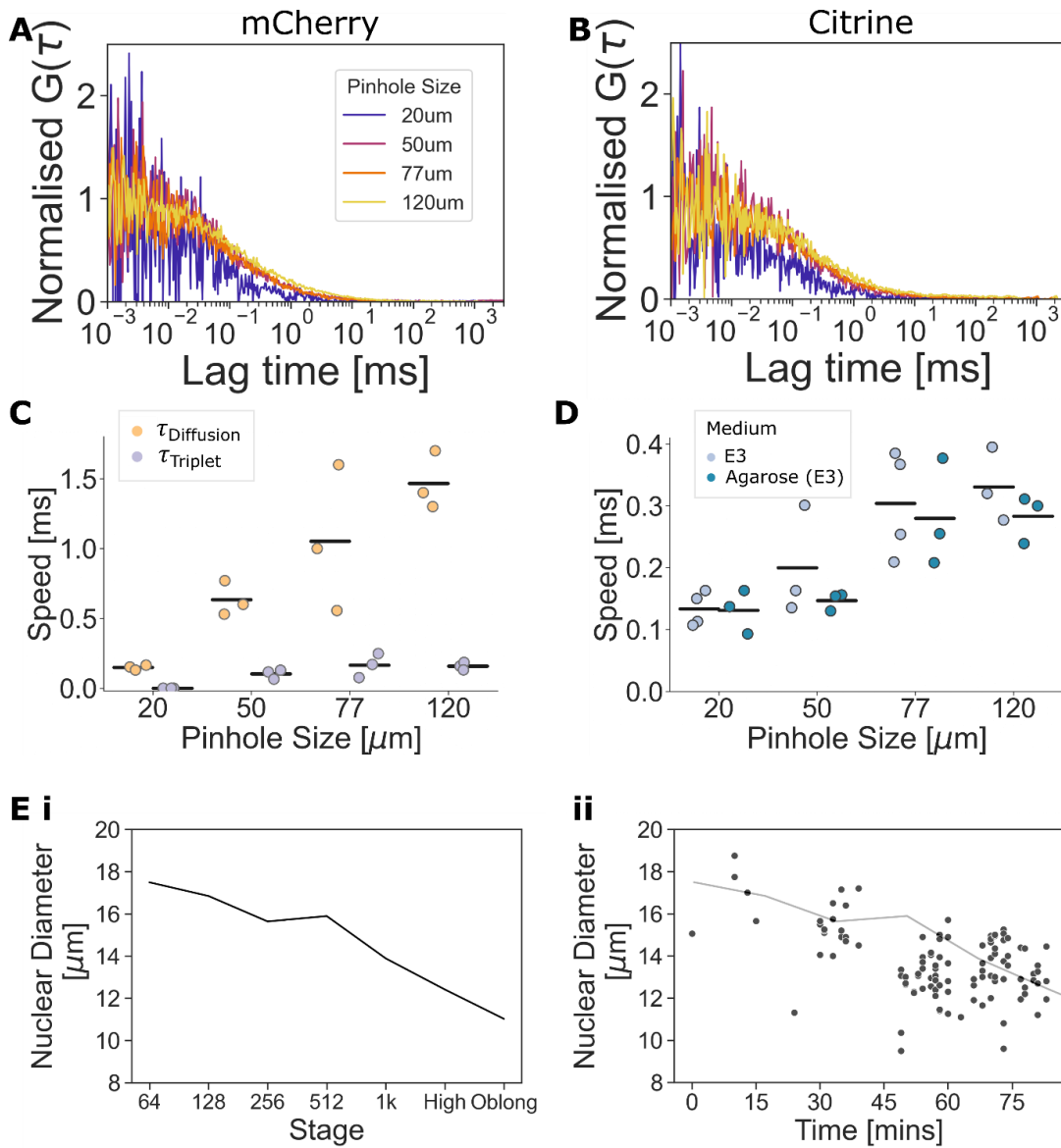
Figure 3.7 Optimisation of ACF fitting parameters by pinhole controls, embryo staging by nuclear diameter.

*FCS measurements across pinhole sizes in WT embryos expressing mCherry/Citrine (methods 2.6.6.1). **A+B)** Normalised average ACFs for embryos in E3, expressing **A)** mCherry or **B)** Citrine. **C+D)** Scatterplots of **C)** mCherry τ_D and triplet state (τ_{Trip})(ms),*

(cont. over page)

D) *Citrine τ_D for embryos in E3 versus mounted in 0.7% LMP agarose (methods 2.2.5.1). B.r.=1, N=3-4 embryos, n=3-4 nuclei.* **E) i.** *Nuclear diameter (μm) at different cell cycle stages, calculated from nuclear volume measurements of embryos expressing mEos2-Sox19b (Reisser et al., 2018) (methods 2.2.5.5).* **ii.** *Nuclear diameter (μm) in MZspg793 -/- embryos rescued with mCherry-Pou5f3, from approx. 2-3.3 hpf. b.r.=1, N=2, n=109 nuclei.*

The effect of slow fluorescence fluctuation artefacts did not seem to improve when mounting embryos in agarose to reduce their movement. The τ_D of Citrine was unchanged in pinhole controls, compared to embryos kept in E3; the τ_D increased from 0.131 ms (+/- 0.0354) to 0.283 ms (+/- 0.0388) (**Figure 3.7**D). However, mounted embryos could be better oriented to face cells towards the objective, making more nuclei accessible for FCS measurements.

Finally, embryo staging was refined by measuring nuclear diameter in addition to morphology. Others have measured the changing nuclear volume in embryos expressing mEos2-Sox19b (Reisser et al., 2018). These values were used to calculate an expected nuclear diameter per stage (**Figure 3.7**Ei). A similar trend in nuclear diameter, measured from images taken approximately 2-3.3 hpf, was observed in MZ*spg793* -/- embryos expressing mCherry-Pou5f3 (**Figure 3.7**Eii). The large variability in measured nuclear diameter was likely due to inconsistency in choosing a z-plane at the centre of the nucleus, as well as fluctuations of nuclear volume during each cell cycle. Consequently, morphology and nuclear diameter provided a combined guide to stage embryos, but measurements were grouped into 'early' (128-512 cell; ~2.25-3 hpf) and 'main' (1K cell-oblong; ~3-4 hpf) stage ZGA.

3.5 Nanog-Citrine and mCherry-Pou5f3 dynamics measured by FCS are constant across ZGA

FCS measurements were then carried out on Nanog-Citrine and mCherry-Pou5f3 in rescued MZ*nanog -/-* and MZ*spg793 -/-* embryos, respectively. Due to time constraints and de-commissioning of the microscope used for the original FCS measurements, only two biological replicates could be completed for Nanog-Citrine on the old SP5 confocal microscope, and one biological replicate for mCherry-Pou5f3 on the new Stellaris 8. Diffusion was consistently slower for fluorophores and dyes measured on the Stellaris 8 versus the SP5, perhaps due to the different detectors (**Appendix Figure 7.1**). This compromised comparison of diffusion times between the PTFs. The optimisations in section 3.4 did to an extent improve measurements and fitting. This could be seen by ACFs relaxing to 0 (**Figure 3.8**A), and was quantified in the τ_D values which were now within the expected ms range (**Figure 3.8**C).

It is interesting that Nanog-Citrine again exhibited more slow diffusion than mCherry-Pou5f3 when comparing their ACFs at 1-100 ms (**Figure 3.8**A), and the ρslow (**Figure 3.8**B), albeit not significantly. Perhaps a greater proportion of Nanog transiently binds chromatin in target-site search, or diffuses slowly in oligomers or foci (section 5.4).The slight right-shifts seen in both Nanog-Citrine and mCherry-Pou5f3 ACFs from early to main stage ZGA suggest their diffusion slows during ZGA, but also did not translate to significantly different fitted values (**Figure 3.8**A,B-D). Nanog and Pou5f3 may diffuse more slowly as ZGA progresses because their DNA binding sites become increasingly accessible (Kaaij et al., 2018).
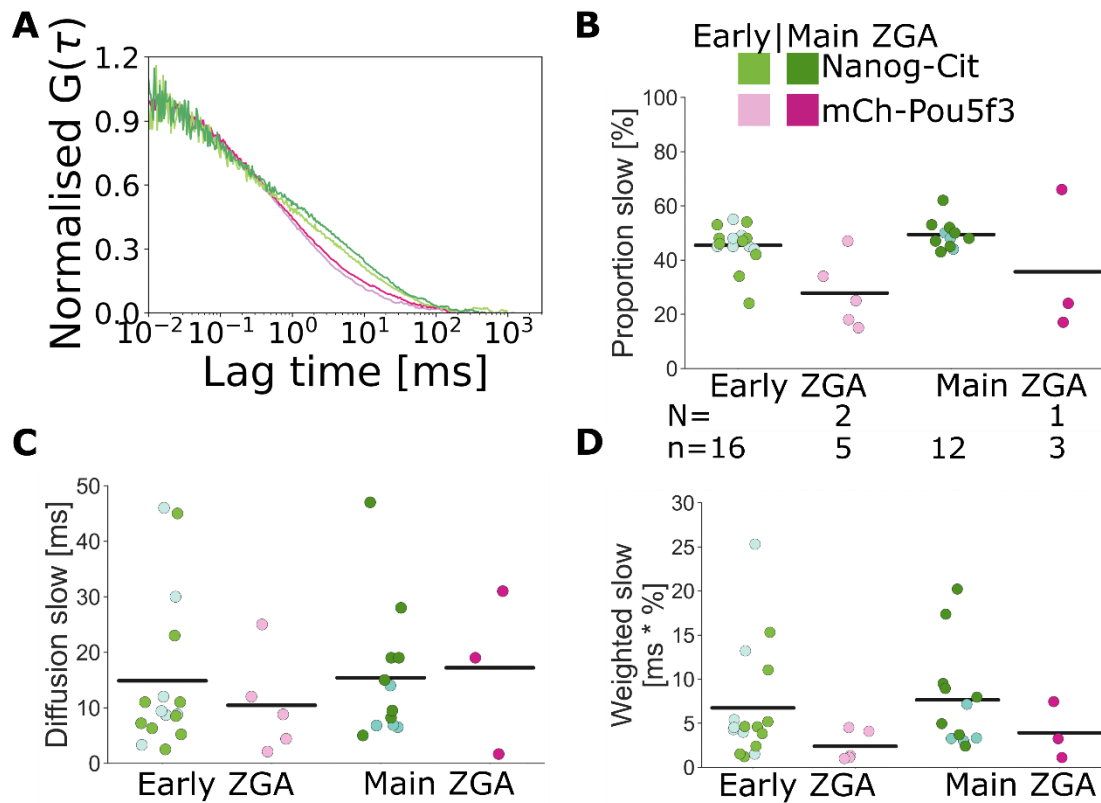
Figure 3.8 Nanog-Citrine and mCherry-Pou5f3 diffusion measured by FCS in rescued MZ mutant embryos.

*FCS measurements in MZnanog -/- or MZspg -/- embryos rescued with Nanog-Citrine or mCherry-Pou5f3 mRNA, respectively (methods 2.6). **A)** Normalised average ACFs for Nanog-Citrine and mCherry-Pou5f3 at early (128-512 cell; ~2.25-3hpf) and main (1K cell-oblong; ~3-4 hpf) stage ZGA. **B-D)** Scatterplots of **B)** $\tau_D$slow. **C)** ρslow, and **D)** $\tau_D$slow weighted by ρslow. B.r. = 2 for Nanog-Citrine (green vs. blue)/1 for mCherry-Pou5f3. N=1-2 embryos for mCherry-Pou5f3 (Nanog-Citrine not recorded), n= 3-16 nuclei. Statistics were analysed using linear mixed effect models, and pairwise comparison of means (methods 2.8), all n.s. (p>0.05).*

However, it remained unclear whether the measurement variability (see raw ACFs in **Appendix Figure 7.5**) was due to heterogeneity in PTF dynamics between nuclei, and whether differences in ρslow/ $\tau_D$slow between PTFs and time-points were due to characteristic PTF activity on chromatin - or simply noise and artefacts in measurements. This was compounded by the inability of FCS to detect 'immobile'

molecules, such as the seconds-range DNA residence times reported for (P)TFs (Hemmerich et al., 2011, Mueller et al., 2013). Taken together, I concluded that further optimisation of FCS measurements and analysis was not worthwhile, as this technique is not well-suited to dissect chromatin binding dynamics of PSN during ZGA in zebrafish embryos.

3.6 Measuring Pou5f3, Sox19b and Nanog interactions by FCCS

3.6.1 FCCS is not suitable to probe interactions of Citrine and mCherry tagged PSN

A final question was whether the PTFs interact. This could be probed using FCCS to measure the co-diffusion, or interaction, of differently tagged PSN. As a proof of principle, FCCS was carried out first in WT embryos overexpressing pairwise combinations of mCherry- and Citrine-tagged PSN. As controls, tagged PSN were co-expressed with mCherry or Citrine fluorophores (**Figure 3.9**, **Appendix Figure 7.6**). The degree of interaction was quantified by the RCCA, which gives the proportion of interacting molecules normalised to each channel (section 1.3.5, **Equation 1.4**).

Usually, the RCCA is only calculated from the channel with the lower G(0) amplitude; this gives the maximum proportion of interaction as concentration is inversely proportional to ACF amplitude, but is proportional to CCF amplitude. However, it was noted that there was a consistent difference in RCCA between channels in the control FCCS measurements: more interaction was always detected relative to the tagged PTF, than the co-injected fluorophore; for Citrine-tagged PSN + mCherry the RCCA was always higher relative to the Citrine, versus mCherry, and vice-versa (**Figure 3.9**C, **Appendix Figure 7.6**). This may in part be due to tagged PSN consistently having a lower concentration than the fluorophores (**Appendix Figure 7.6**A-B,C-Div-v). Yet similarly for co- injected pairs of Citrine-tagged and mCherry-tagged PSN, the proportion of interacting molecules was always higher relative to the mCherry- versus Citrine-tagged PTF. The RCCA of PSN pairs was never

consistently higher than the relevant controls, even when only comparing the highest RCCA per channel. Differences in photostability between fluorescent molecules could also account for the different RCCA between channels. However, as Citrine and mCherry have very close emission and excitation spectra (**Figure 3.10**), cross-talk, bleed-through, and FRET are very likely and render FCCS measurements with this fluorophore pair inconclusive.
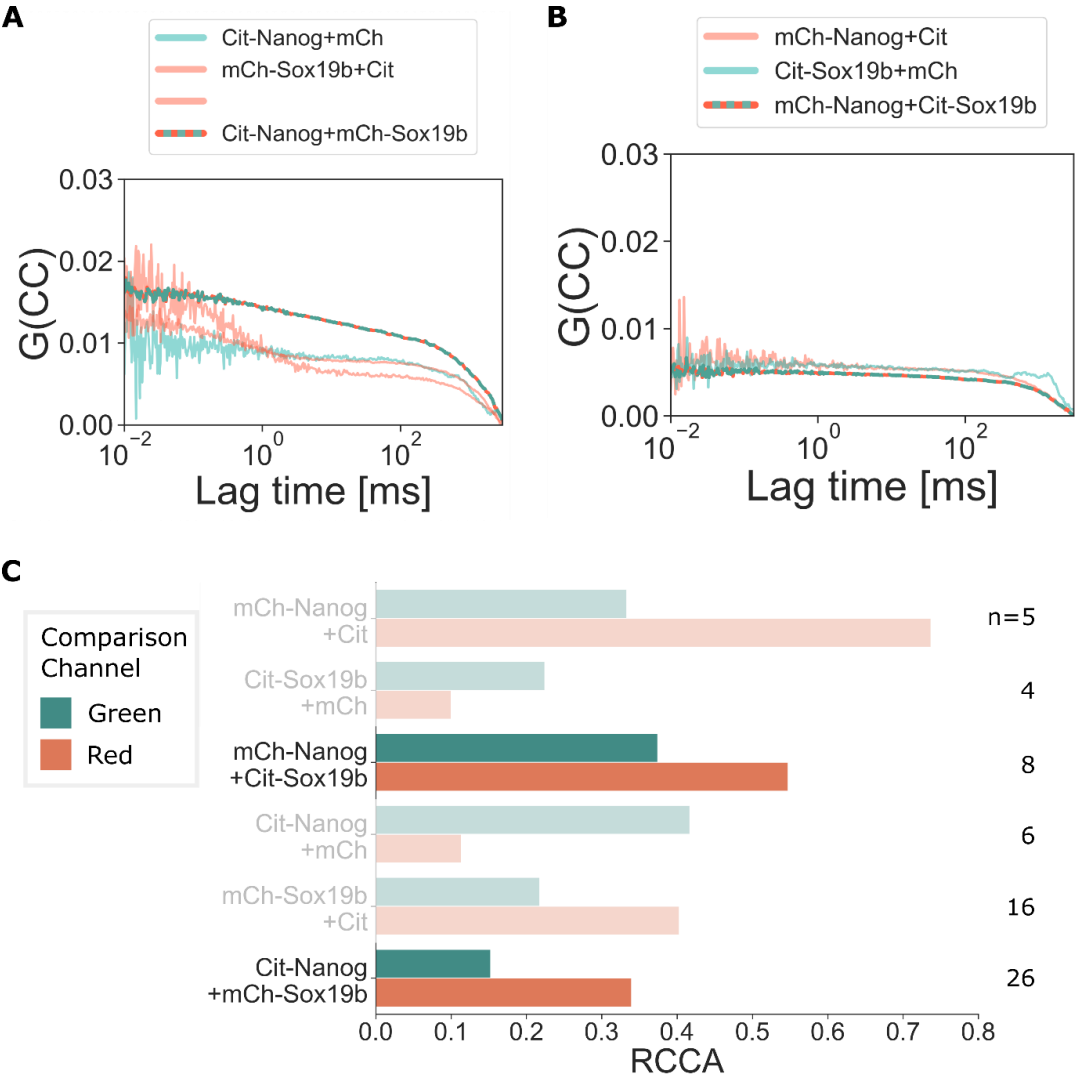
Figure 3.9 PTF interactions measured by FCCS.

FCCS measurements were carried out at main ZGA (methods 2.6), in WT embryos expressing tagged Nanog+Sox19b in pairs or individually with the opposite fluorophore as controls. (cont. over page)

*A+B) Average cross-correlation functions (CCFs) for A) Citrine (Cit)-Nanog + mCherry (mCh), mCherry-Sox19b+Citrine, Citrine-Nanog + mCherry-Sox19b B) mCherry-Nanog + Citrine, Citrine-Sox19b+mCherry, mCherry-Nanog + Citrine-Sox19b. C) Barplot of Relative Cross Correlation Amplitudes (RCCA) calculated using CCFs in A+B, and ACFs in **Appendix Figure 7.6** (methods 2.6.3). n=4-26 nuclei.*
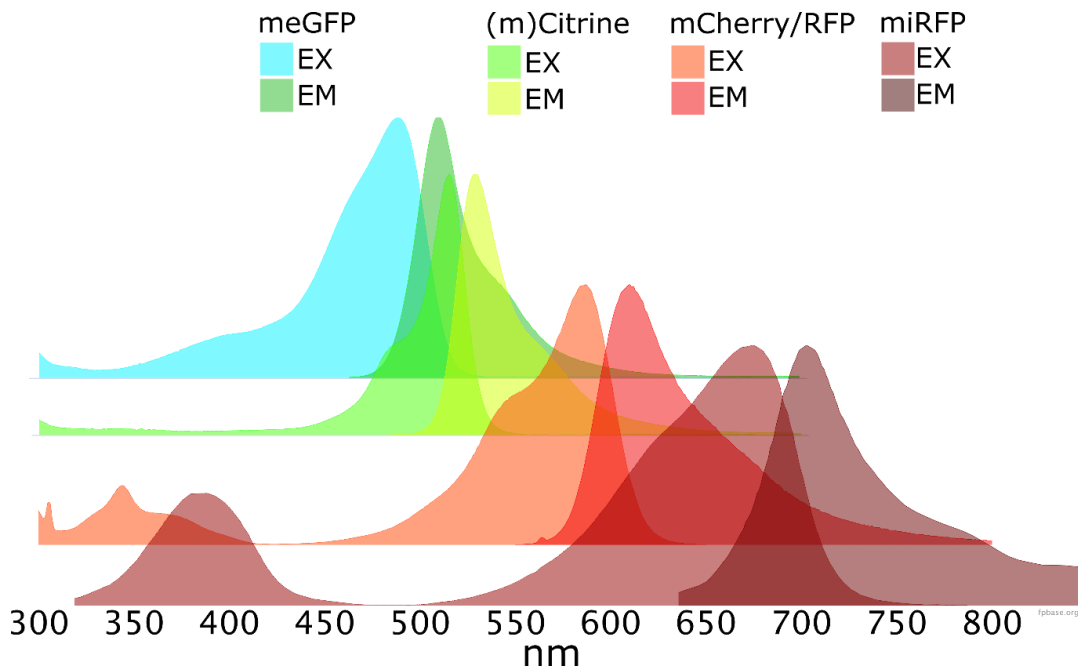
Figure 3.10 Excitation (EX) and emission (EM) spectra of meGFP, (m)Citrine, mCherry/RFP, and miRFP.

Normalised intensity vs. wavelength. Adapted from FPbase.org.

3.6.2   Changes to PSN diffusion upon co-expression of an untagged PSN are not detected by FCS

Finally, previous FCS data (from experiments prior to optimisation) were analysed for an indication of interaction, which could be further investigated by an alternative method to FCCS. Here, the change in $\tau_D$slow of tagged PSN was measured when a second untagged PSN was added. PTFs which co-bind DNA could for example have higher affinity for their binding sites (section 1.1.1.3), causing the $\tau_D$slow to decrease or the ρslow to increase. The Sox19b-Citrine ACF was right-shifted at main ZGA when co-injected with Nanog (**Figure 3.11**A). The Nanog-Citrine ACF was similarly right-shifted when co-injected with Pou5f3, at early ZGA (**Appendix Figure 7.7**Bi). In contrast, Nanog-Citrine and Sox19b-Citrine ACFs were left-shifted at main stage ZGA upon co-injection with Pou5f3 (**Appendix Figure 7.7**A-Bi).

However, neither the fitted values for $\tau_D$slow nor ρslow changed significantly between conditions (**Figure 3.11**B,C, **Appendix Figure 7.7**A-Cii-iii). Perhaps any potential effect was masked by tagged PTFs interacting with endogenous partners in WT embryos. More importantly, changes to chromatin binding could be in the stably-bound PTF population which, as discussed in section 3.5, FCS is not able to detect. Therefore, I could not clearly conclude whether PSN interact - either directly to affect each-others' transient chromatin binding dynamics, or more indirectly as in collaborative competition and assisted loading models (section 1.1.1.3).

To conclude, the inappropriate fluorophore combination, and the limited slow diffusion measured, made FCCS and FCS inappropriate to probe PSN-PSN interactions in this system. Nevertheless, the slight indication of Nanog - Sox19b interaction in co-injection FCS (**Figure 3.11**A,B) was congruent with findings of Nanog-dependent Nanog/Sox19b co-localisation to miR-430 transcription bodies (Kuznetsova et al., 2023). This encouraged me to make use of the spectral overlap between (m)Citrine and mCherry to instead probe Nanog-Sox19b interactions by FRET.
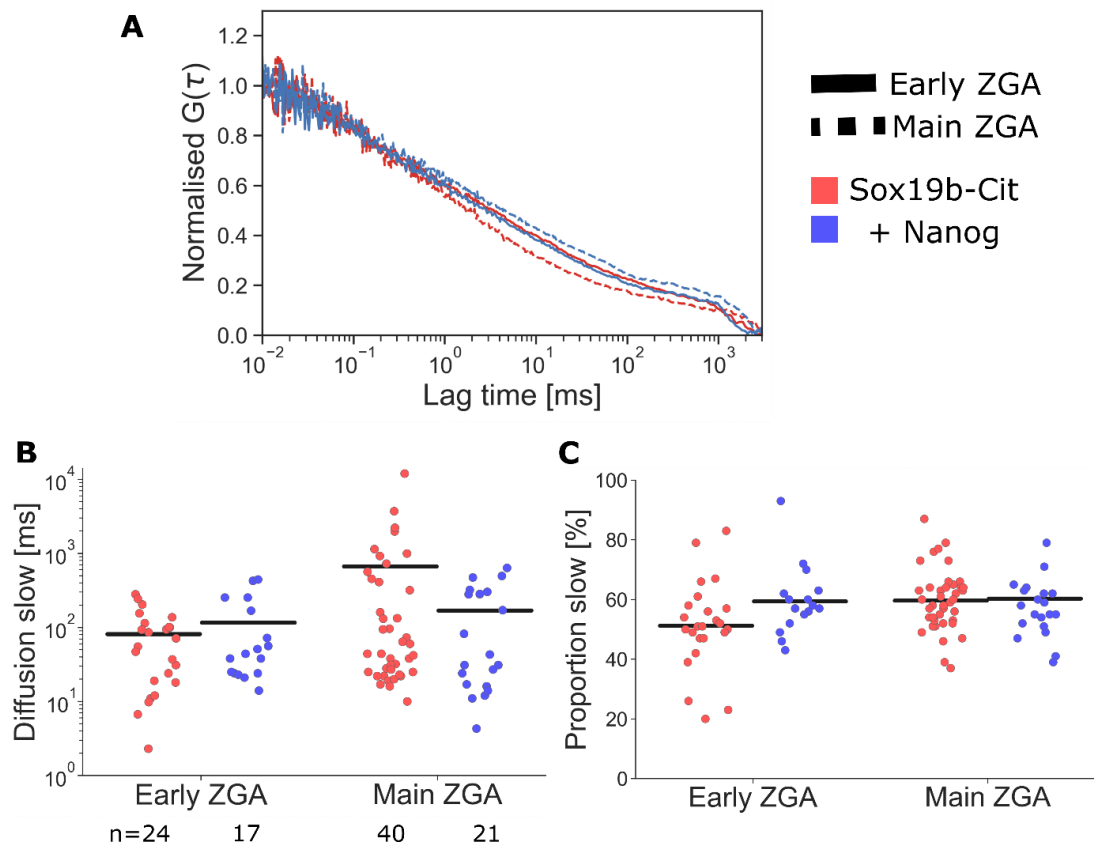
Figure 3.11 Indirect measurement of PSN interactions by FCS.

*Measurements were carried out in WT embryos expressing Sox19b-Citrine +/- untagged Nanog, at early and main stage ZGA (methods 2.6). **A)** Normalised average ACFs. **B+C)** Scatterplots of fitted values for **B)** $\tau_D$slow and **C)** ρslow. B.r. = 3, n=17-40 nuclei. Statistics were analysed using linear mixed effect models, and pairwise comparison of means (methods 2.8), all n.s. (p>0.05).*

.

3.7   Discussion

3.7.1 Fluorescent tags can maintain PSN function to rescue MZ mutants

mCherry-Pou5f3 and Nanog-(m)Citrine sufficiently rescued the respective MZ*spg793* -/- and MZ*nanog* -/- embryos (**Figure 3.1**). However, MZ*spg793* -/- was rescued much more efficiently than MZ*nanog* -/-, even by WT mRNA. This could be due to mRNA quality, injection accuracy, or the lower number of biological replicates. Using a co-injected dye to screen only successfully injected embryos might mitigate some of the technical error and raise the rescue efficiency closer to published values (88%, 15/17 embryos; (Gagnon et al., 2018). Perhaps there are also more subtle distinctions between incomplete rescue phenotypes for MZ*spg793* -/-. While both maternal Nanog and Pou5f3 are required for epiboly and ventral specification, Nanog has an additional role in the yolk syncytial layer (Veil et al., 2018), and Pou5f3/Sox19b regulate dorsoventral patterning (Gao et al., 2022). As such dorsoventral patterning defects may only become apparent after 24 hpf, monitoring larvae until 4 days post fertilisation may improve rescue detection accuracy.

Opposite tagging strategies seemed to be better for Nanog and Pou5f3, both with regard to the fluorophore and the terminus. PSN do have a common preference for the tag at the terminus furthest from the DBD (**Appendix Figure 7.2**). This suggests that tagging could affect chromatin binding, and this could be tested by EMSA. The contribution of differential mRNA stability, translation efficiency, or protein stability to MZ mutant embryo rescues should be analysed by qPCR and Western blot.

3.7.2   mRNA microinjection is suitable for visualisation of fluorescently tagged PSN, although hampered by regionalised expression

mRNA microinjection into the cell proved to be a suitable means of expressing fluorescently tagged PSN in zebrafish embryos, although sometimes causing

regionalised expression (**Figure 3.2**). Later tests showed that yolk injection did not reduce variability of nuclear PSN levels (**Appendix Figure 7.3**). Further limitations of microinjection are the inaccuracies caused by inconsistent microinjector pressure, or by the injection mix escaping out of the embryo during injection or needle retraction. Generation of zebrafish lines expressing fluorescently tagged PSN from the endogenous locus would avoid the need for microinjection. Attempts to do this by CRISPR-Cas9 were unsuccessful.

 Endogenous expression would also allow measurement of the spatial variability in nuclear PSN levels and dynamics, to study whether these are linked to a first specification step, such as the embryonic deep layer/enveloping layer differentiation (Stapel et al., 2017). Multi-point FCS (mpFCS), for example, uses a 1024x1024 illumination matrix to provide spatial information on concentration and diffusion (Krmpot et al., 2019). Preliminary mpFCS data showed that the Citrine-Pou5f3 nuclear concentration was less variable than Nanog-Citrine or Sox19b-Citrine (**Appendix Figure 7.4**), and is in agreement with my imaging data (**Figure 3.2**).

3.7.3 FCS is not an optimal technique to study PSN diffusion and chromatin binding dynamics in zebrafish ZGA

The technical challenges of FCS experiments in this *in vivo* system, such as movement, and fluorophore features including triplet blinking, photobleaching, and aggregation, made it difficult to distinguish biological effects from noise and artefacts. Some optimisation to measurements and analysis was possible (**Figure 3.7**): FCS measurements for PSN rescuing agarose mounted MZ mutants, and more stringent selection of time windows for autocorrelation analysis, gave rise to higher quality ACFs (**Figure 3.8**A). These could be fit to derive $\tau_D$slow values within the expected ms range (**Figure 3.8**C). A trend towards more slow diffusion for Nanog-Citrine than mCherry-Pou5f3 was observed, similar to initial experiments in WT embryos (**Figure 3.5**). However, no significant differences were detected between PTFs or early vs. main stage ZGA.

The complexity of zebrafish embryos may contribute to the variability of τ_D values, which would need to be mitigated in extensive further optimisation. For example, heterogeneous PSN distribution within nuclei (**Figure 5.6**) will be interpreted as very slow diffusion which cannot be distinguished from possible chromatin binding. Comparative experiments with DBD-mutant or oligomerisation-mutant PSN (section 5.3) could disentangle the relative contributions to slow diffusion. Further, successive measurements in the fast-dividing embryos will most likely capture different cell cycle stages, or even different cell cycles, which could have differential PTF-chromatin binding. Improving staging accuracy to measure only S-phase dynamics in selected cell stages (e.g. 128-cell and 1000-cell) would significantly reduce the already low-throughput experiments.

The slow fluorescence fluctuations observed (**Figure 3.6**) may arise from the embryo rotating within the chorion, cell movement during division. Removing the chorion and yolk of embryos before mounting in agarose could reduce rotation, as well as improving signal, but this posed further challenges (**Figure 5.12**). Chromatin movement, in the time-range of 100s ms, which also be confused with slow PTF diffusion but would be difficult to control for (section 1.3.3.1). Finally, measurements from incompletely rescued MZ mutant embryos, for example due to lowered injection volume, should be removed retrospectively by scoring rescues at 24 hpf.

It could also be useful to switch to more photostable, bright, and non-aggregating, fluorescent tags such as the recently published mScarlet3 (Gadella et al., 2023). This may improve accuracy of measuring slow diffusion, by reducing aggregation artefacts, and the selective photobleaching of slow molecules (sections 3.3,3.4). Photo-activatable tags such as paGFP would allow fine-tuning of count rates for high SNR, and have been used for FCS measurements in live mouse embryos (Kaur et al., 2013, White et al., 2016). Optical sectioning by SPIM, or multi-photon microscopy, could substantially improve the SNR and penetration depth (section 1.3.1). Applications of FCS/FCCS with SPIM (Capoulade et al., 2011, Pernus and

Langowski, 2015, Reho et al., 2020, Szaloki et al., 2015, Wohland et al., 2010) and 2-photon microscopy (Michelman-Ribeiro et al., 2009) have been published.

However further work using FCS to study PSN chromatin binding dynamics in zebrafish ZGA was not considered worthwhile: it is crucially limited by being a bulk method which cannot 'see' the seconds-range stable (P)TF-chromatin residence times (Hemmerich et al., 2011, Mueller et al., 2013, Stortz et al., 2018). Variants such as scanning FCS (Petersen et al., 1986) or Image Correlation Spectroscopy (ICS) (Priest et al., 2021, Srivastava and Petersen, 1996), would allow slower diffusion to be followed. SMT would be most appropriate method to tease apart a range of dynamics exhibited by PTF subpopulations (section 1.3.2) (Izeddin et al., 2014, Lord et al., 2010, Mueller et al., 2013). Comparisons to the dynamics of non-pioneer TFs, in addition to DBD mutants, could help to determine whether PSN directly engage with chromatin to increase its accessibility at ZGA, or only engage transiently to recruit effectors such as Brd4 (Miao et al., 2022).

3.7.4 PSN interactions during zebrafish ZGA cannot be reliably probed by FCCS using mCherry and Citrine tags

My FCCS data was not clearly interpretable, most likely due to the choice of fluorophores (**Figure 3.9**, **Figure 3.10**, **Appendix Figure 7.6**). mCherry and Citrine seem to be a remarkably unbecoming combination for FCCS, exhibiting cross-talk, bleed-through, FRET, and differential photobleaching, all of which can affect the observed degree of cross-correlation. Unequal photobleaching or FRET between fluorophores can cause cross-correlation to be underestimated; cross-talk and bleed-through can wrongly show cross-correlation (Ng et al., 2018). While it would theoretically be possible to correct for these effects (Foo et al., 2012), changing fluorophores would be more effective. For example, mCherry is commonly combined with eGFP (**Table 3.2**), as this pair has less spectral overlap (**Figure 3.10**). A far-red fluorophore such as miRFP would be an even more spectrally separated partner for eGFP/mCitrine (**Figure 3.10**).

However FCCS faces the same limitations as FCS, so weak or infrequent interactions, and slowly diffusing or immobile molecules, cannot be detected. Overall, I conclude that FCCS is not useful to study the interactions of PSN in zebrafish ZGA, and is especially problematic when using mCherry and (m)Citrine. By contrast, these fluorophores seemed to be a good FRET pair, and this was leveraged to continue interrogating PSN interactions by AAT-FRET.

4   Adapting Lifetime-based AAT to measure interactions in zebrafish embryos by AAT-FRET

4.1 Introduction

The advantage of FRET as an imaging method is that measurements of interaction kinetics and distance are combined with spatial and temporal information (Halavatyi and Terjung, 2017). Similar to mpFCS (Krmpot et al., 2019), this can create a pixel-by-pixel map to pinpoint, for example, TF subnuclear distribution. Yet unlike FCS and FCCS, interactions between slowly diffusing or immobile molecules can be detected using FRET (Bacia and Schwille, 2007, Halavatyi and Terjung, 2017). FRET therefore seemed to be a good alternative technique to investigate whether PSN interact in zebrafish embryos during ZGA, and if so, whether this is linked to the observed heterogeneity of PSN nuclear distribution (section 5.4).

First, I needed to characterise the suitability of mCitrine (donor) and mCherry (acceptor) as a FRET pair in this system. Green and red fluorophore combinations are common, due to their lower cross-talk compared to the traditional yellow and cerulean pairs (Bajar et al., 2016, Kremers et al., 2006). Yet generally, brighter and more photostable pairs than mCitrine and mCherry are used, such as Clover and mRuby2, or GFP/eGFP and mCherry/mRFP1 (Lam et al., 2012a, Lam et al., 2012b, Reho et al., 2020, Szaloki et al., 2015, Vamosi et al., 2008). I found only one example using mCitrine and mCherry in FLIM-FRET, to study interactions between SNARE complex proteins in the plasma membrane of dendritic cells (Verboogen et al., 2017). FLIM-FRET has also been used to study PTF interactions in zebrafish embryos, but here interactions between GFP-Nanog and mCherry-Oct4 were shown, in the late ZGA mesendoderm (Perez-Camps et al., 2016). The excitation and emission spectra of the aforementioned FRET pairs are depicted in **Figure 4.1**. An mCherry-mCitrine tandem fusion was therefore used to verify that FRET could be detected for this pair in zebrafish embryos.
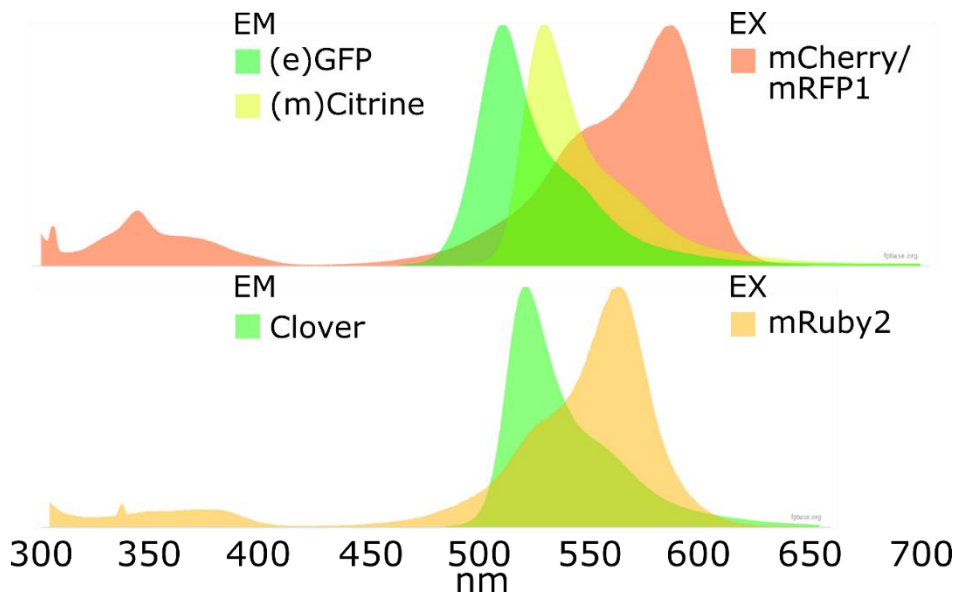
Figure 4.1 Emission (EM) and excitation (EX) spectra of selected FRET pairs.

Normalised intensity vs. wavelength. (e)GFP and (m)Citrine (donor) emission spectra overlapping mCherry/mRFP1 (acceptor) excitation spectrum, and Clover (donor) emission spectrum overlapping mRuby2 (acceptor) excitation spectrum. Adapted from FPbase.org.

I used traditional intensity-based FRET assays to begin with. These compare the donor or acceptor intensity, when present individually or in combination, and monitor changes upon photobleaching to destroy the interaction partner (**Table 4.1**) (Halavatyi and Terjung, 2017).

Table 4.1 Summary of intensity-based FRET techniques used in these experiments

Assay	Measure	Conditions
Intensity FRET	Donor intensity	1. Donor/acceptor- tagged proteins 2.-ve controls: a) donor alone b) donor + acceptor fluorophores 3. +ve controls (donor-acceptor fusion)
Acceptor Photobleaching (AccPb)		1,2b,3 pre + post AccPb
Sensitised emission (SE-FRET)	Acceptor intensity, using donor-exciting laser	1,2b,3 4. –ve control: acceptor alone
Donor Photobleaching		1,2b,3 pre + post photobleaching

However, intensity-based FRET is sensitive to the relative concentration of donor and acceptor molecules, and affected by photobleaching. Intensive correction for these factors, as well as for cross-talk and bleed-through are required (Jares-Erijman and Jovin, 2003). These assays were therefore particularly affected by the inaccuracy of mRNA microinjection into zebrafish embryos (section 3.2). Lifetime (τ) - based FRET was a better choice as τ is not affected by concentration or photobleaching (Datta et al., 2020), and mCitrine and mCherry have distinct τ's (FPbase, 2023b, FPbase, 2023c, Mukherjee et al., 2022b, Verboogen et al., 2017).

The Leica Stellaris 8 TauSense tools offered a new way to record fitting-free τ based information (Roberti, 2020), using hybrid GaAsP detectors (section 1.3.1) (Schweikhard, 2020). The AAT of photons across the measurement window is recorded per pixel, providing on-the-fly τ -based information (Padilla-Parra et al., 2011). This can be converted to an estimation of the degree of interaction, the mfD (Alvarez, 2022, Padilla-Parra et al., 2008, Padilla-Parra et al., 2009) (section 1.3.6.1). AAT and mfD benefit from faster acquisition and analysis times than traditional FLIM-FRET, where the decay curve of single photon arrival times is fit to derive τ, requiring high photon counts for accuracy (Li et al., 2010, Padilla-Parra et al., 2011). This seemed particularly useful for the fast development and low SNR of zebrafish embryos, relative to imaging cells *in vitro*. However, as AAT is an average value per pixel, with a resolution of 0.1 ns, detection sensitivity is lost versus single-photon detecting FLIM-FRET (Roberti, 2020, Schweikhard, 2020). Therefore, the second characterisation step was to test whether measurements of mCitrine and mCherry AAT in zebrafish embryos were comparable to expected values, and whether a reduction in mCitrine AAT could be detected upon FRET.

4.2 Non-fitting FLIM-FRET facilitates analysis of protein interactions in live zebrafish embryos

These experiments were published in the paper appended below (Auer et al., 2022). Laura Murphy advised on and helped to develop the image analysis workflow. David Li and Dong Xiao advised on setup and optimisation for AAT measurements. Experiments were conceptualised by me and Ann Wheeler, all experimental and analysis work was carried out by me. (**https://doi.org/10.1111/jmi.13162**):

Journal of Microscopy | RMS

Non-fitting FLIM-FRET facilitates analysis of protein interactions in live zebrafish embryos

Julia M. T Auer[1] | Laura C Murphy[1] | Dong Xiao[2] | David U. Li[2] |
Ann P Wheeler[1]

[1]MRC Human Genetics Unit, Institute of
Genetics and Cancer, The University of
Edinburgh, Edinburgh, UK

[2]Department of Biomedical Engineering,
University of Strathclyde, Glasgow, UK

Correspondence
Ann Wheeler, MRC Human Genetics
Unit, Institute of Genetics and Cancer,
The University of Edinburgh, Edinburgh,
UK.
Email: ann.wheeler@ed.ac.uk

Abstract

Molecular interactions are key to all cellular processes, and particularly interesting to investigate in the context of gene regulation. Protein–protein interactions are challenging to examine in vivo as they are dynamic, and require spatially and temporally resolved studies to interrogate them. Foerster Resonance Energy Transfer (FRET) is a highly sensitive imaging method, which can interrogate molecular interactions. FRET can be detected by Fluorescence Lifetime Imaging Microscopy (FLIM-FRET), which is more robust to concentration variations and photobleaching than intensity-based FRET but typically needs long acquisition times to achieve high photon counts. New variants of non-fitting lifetime-based FRET perform well in samples with lower signal and require less intensive instrument calibration and analysis, making these methods ideal for probing protein–protein interactions in more complex live 3D samples. Here we show that a non-fitting FLIM-FRET variant, based on the Average Arrival Time of photons per pixel (AAT− FRET), is a sensitive and simple way to detect and measure protein–protein interactions in live early stage zebrafish embryos.

KEYWORDS
confocal microscopy, FRET, live imaging, model organisms

1 | INTRODUCTION

Interactions between proteins, DNA and RNA molecules drive cellular processes, including signal transduction, transcriptional regulation and chromatin organisation. To understand the function of dynamic molecular interactions, they must be characterised with spatial and temporal resolution. This is a particular challenge for complex specimens such as developing embryos or organoids. 3D scanning of thick samples increases image acquisition time, decreasing the temporal resolution to study interactions. Light scattering increases and photon penetrance decreases proportionally to depth imaged within the sample, reducing signal to noise in the output image. Thick samples can also have artefacts caused by spherical aberration.[1] These can be partially mitigated by use of specialised equipment, such as objectives matched to the refractive index of the sample, resonant scanning or spinning disk confocal microscopy to speed 3D image acquisition, or lightsheet microscopy to improve optical sectioning (Mitchell et al. 2017). We set out to find a technique capable of probing and measuring protein
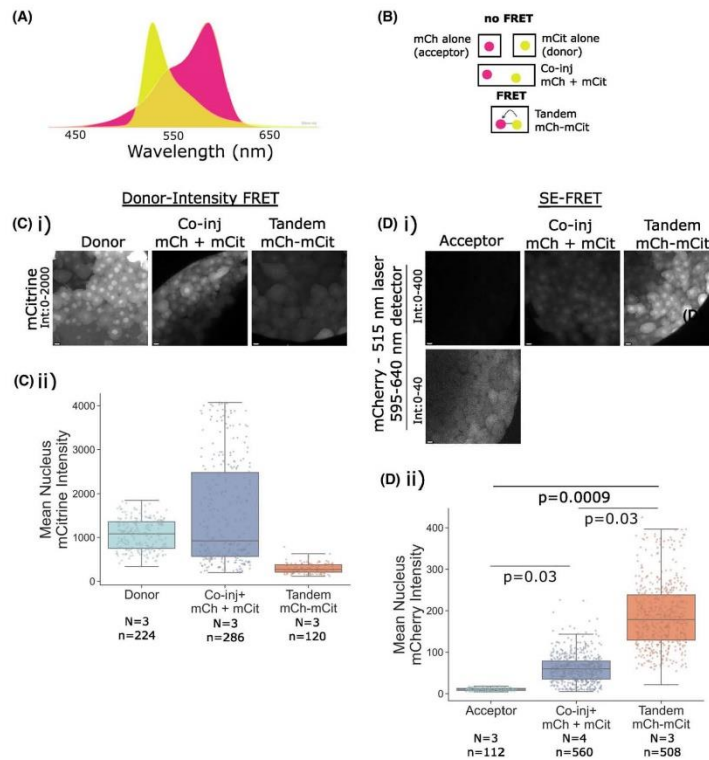
FIGURE 1 Donor intensity FRET and sensitised emission FRET show mCitrine and mCherry is a suitable FRET pair in live early zebrafish embryos. (A) Donor emission (mCitrine, yellow) and acceptor excitation (mCherry, pink) spectra. (B) Conditions compared in FRET and AAT− FRET assays: mCitrine (donor) or mCherry (acceptor) alone. Co-injection of mCherry + mCitrine (Co-inj mCh + mCit), mCherry–mCitrine tandem fusion, with a Glu-Phe linker (Tandem mCh-mCit). Equimolar amounts of mRNA encoding fluorophores were microinjected at the 1-cell stage. (C) Donor intensity FRET assay, embryos expressing of donor alone, Co-inj mCh + mCit, Tandem mCh-mCit. (i) Representative confocal images. (ii) Box and whisker plots of mean nuclear intensities of mCitrine (embryos/condition (N) = 3, nuclei (n) = 120–286, biological replicate (b.r.) = 1). (D) Sensitised emission FRET (SE-FRET) assay (using 515 nm laser and 595–640 nm detector), embryos expressing acceptor alone, Co-inj mCh + mCit, Tandem mCh-mCit. (i) Representative confocal images. (ii) Box and whisker plots of mean nuclear intensities of mCherry (N = 3–4, n = 112–508, b.r. = 1). All images represent maximum intensity projections through the z-stack, scale bar = 10 μm, Int = displayed intensity range. Data were fit with linear mixed effect models and estimated marginal means compared pairwise.

interactions in a live 3D organism, such as an early zebrafish embryo, which does not require complicated microscope setups and involved analysis.

Two common methods for investigating molecular interactions using confocal imaging are Bimolecular Fluorescence Complementation (BiFC),[2,3] and Foerster Resonance Energy Transfer (FRET). FRET is the nonradiative energy transfer from an excited donor fluorophore ('donor') to an acceptor fluorophore ('acceptor') when donor and acceptor are within 10 nm, and the respec-

tive emission and excitation spectra overlap[4] (Figure 1). Quenching of the donor fluorophore by the acceptor by FRET causes reduction of the donor and increase of the acceptor fluorescence intensity. FRET can therefore be measured by monitoring donor and/or acceptor intensity. The degree of spectral overlap and the donor–acceptor proximity affect the energy transfer efficiency (FRET efficiency).[5] This means that FRET efficiency can be a measure of the distance as well as the level of interaction between two proteins of interest, when these are

tagged with a donor and an acceptor. However, the relative orientation of donor and acceptor molecules, as well as the refractive index of the medium between them, can also affect the FRET efficiency.[6,7] FRET can therefore provide real-time measures about two fluorescently tagged interaction partners: stoichiometry, subcellular location, proximity and the degree of interaction and its temporal dynamics (e.g. through the cell cycle).[6,8–10]

Intensity-based FRET methods include donor intensity FRET, acceptor photobleaching (AccPb) and sensitised emission (SE-FRET). Donor intensity FRET compares the donor intensity in the presence and absence of the acceptor. In AccPb the recovery of donor intensity is measured upon acceptor fluorophore photobleaching.[6] SE-FRET measures the acceptor intensity (illuminated by a donor-exciting laser) in the presence versus absence of the donor (reviewed in Ref. [8]). However, by quantifying intensities these methods are sensitive to relative concentration and photobleaching. They are also highly dependent on the performance of filters in the microscope system, as spectral bleed-through and autofluorescence can cause misinterpretation of signal readout. Furthermore, aberrations caused by non-uniform sample illumination can affect intensity-based measurements in 3D samples.[11] Appropriate controls and robust analysis are therefore required to accurately report FRET efficiency.[6] These factors make intensity-based FRET assays less suitable for detecting interactions in live 3D samples.

Lifetime-based FRET assays (Fluorescence Lifetime Imaging Microscopy-FRET; FLIM-FRET) are the gold standard for quantitative FRET experiments. Fluorescence lifetime (τ) is the time a fluorophore spends in the excited state, that is, the time between excitation and fluorescent photon emission. τ is not affected by concentration and photobleaching.[11] Upon FRET, the donor τ is reduced as the excited donor emits fewer fluorescent photons and spends less time in the excited state. FRET is measured by the reduction in donor τ in the presence and absence of the acceptor. The readout of donor τ allows the fraction of donor molecules interacting with acceptor to be measured. The recovery of donor τ can also be monitored upon AccPb.[6] Importantly, light scattering in thick samples does not affect fluorescence τ recorded if the delay caused is shorter than the detector time resolution.[11] FLIM-FRET is therefore a highly quantitative measure of interactions, and more suitable for live 3D samples.

Measuring τ traditionally uses specialised equipment. Single photon counting detectors are needed to measure when individual photons emitted from a fluorophore arrive at the detector, relative to the excitation of a pulsed laser.[11] τ can also be measured in the frequency-domain, but requires a modulated laser and detector.[12] In the time-domain, τ is calculated by fitting the exponential decay of single photons detected throughout a measurement window by time tagged photon counting, or time correlated single photon counting (TCSPC).[13] Photons can also be detected in user-defined time intervals with time-gated detectors.[14] In the simplest case, FLIM-FRET fluorescence decay curves are fitted with a bi-exponential model to calculate the τ and fraction of two components: FRETing and non-FRETing donor molecules. However, accurate fitting requires several considerations and intensive computational analysis. For example, the donor's characteristic fluorescence decay may itself be multiexponential and can be affected in donor–acceptor fusions. The instrument's contribution to photon arrival times (Instrument Response Function, IRF) must also be measured and corrected for.[15] TSCPC FLIM-FRET requires high photon counts, dependent on the τ precision and dynamic range and signal-to-noise ratio.[16] For example, photon counts in the order of 10^6–10^7 have been reported in cells.[17,18] Therefore, fitting FLIM-FRET is not ideal to assay dynamic interactions in live 3D organisms with low signal-to-noise ratio.

Non-fitting FLIM-FRET assays have been developed which perform well in lower-signal samples. For example, phasor plots distinguish different populations of molecules, including autofluorescence, FRETing and non-FRETing molecules. For each pixel, the fluorescence decay histogram is transformed to a vector and assigned a point on the phasor plot.[19] This reduces computation, albeit at the cost of some spatial information.[20] An even simpler method interrogates the Average Arrival Time (AAT) of photons, which are counted per pixel over the acquisition period. This generates an on-the-fly map of τ-based information which can be used for semiquantitative τ comparisons.[21] Further to comparing donor τ in the presence or absence of the acceptor to derive FRET efficiency, the minimum extent of interaction can be estimated by converting AAT values to mfD (minimum fraction of interacting donor).[20,22] This can be visualised directly, or calculated post-acquisition (Leica article[23]). AAT− FRET assays are simple to perform since the only calibration required is a negative internal control, the donor alone. As no curve fitting is performed, the precision of AAT measurements is less affected by low photon counts. Time for data collection and processing can therefore be shorter than in TSCPC.

We performed AAT− FRET in live early zebrafish embryos to measure protein–protein interactions. Zebrafish embryos develop quickly, and external fertilisation and development allow easy manipulation and imaging. mRNAs encoding fluorescently tagged proteins of interest are injected at the 1-cell stage, and expression can be observed from approximately 2 h post-fertilisation (2hpf), around Zygotic Genome Activation

(ZGA), reviewed in Ref. (24). Despite the potential of FLIM-FRET to probe dynamic molecular interactions, few have implemented the method to-date in developing zebrafish.[25] In this study, we used the Leica Stellaris 8 equipped with GaAsP-Avalanche Photodiode hybrid detectors. In addition to high photon detection efficiency and low (<1.5 ns) detector dead-time, the improved photon counting precision of the new Power Counting technology enhances the single photon counting and dynamic range of Power HyD-X detectors (Leica application note[26]). This particularly improves imaging sensitivity in samples with low signal-to-noise ratio. Furthermore, combining these detectors with a pulsed white light excitation laser enables analysis of τ of a wide range of fluorophores with a 'standard' confocal configuration and image analysis tools.

We used recent developments in detector sensitivity and on-the-fly image analysis of AAT and mfD to demonstrate that AAT− FRET is an accessible new method to analyse dynamic protein interactions in complex live organisms, such as early zebrafish embryos.

2 | RESULTS

2.1 | mCitrine and mCherry show detectable FRET in live embryos

AAT− FRET requires a high FRET efficiency donor–acceptor pair such as mCitrine and mCherry (Figure 1A). mCitrine, the donor has a high quantum yield at 0.74 and long τ (2.9 ns).[27] mCherry has a lower quantum yield at 0.22 and τ (1.6 ns),[28] which makes it a good acceptor with low cross-talk.[11] To quantify FRET in our system we carried out donor intensity FRET and SE-FRET. We compared the nuclear fluorescence intensities of embryos expressing the donor/acceptor alone, or co-injected mCherry and mCitrine, as negative controls, with a tandem-fused mCherry and mCitrine as a positive control, where donor and acceptor are linked by two amino acids (Glu-Phe) corresponding to an EcoRI site (Figure 1B). Equimolar amounts of mRNA encoding fluorophores were microinjected at the 1-cell stage, and confocal z-stack images of embryos were acquired ~3 hpf.

While the mean nuclear mCitrine intensity was lowest in the tandem mCherry–mCitrine, this was not significant ($p = 0.054$, Figure 1C). AccPb-FRET (reviewed in Refs. [6] and [29]) was carried out to confirm FRET, by comparing donor intensity in two z-planes per embryo, pre- vs. postphotobleaching of the acceptor for 30 s. A slight increase in mCitrine intensity was observed in the tandem mCherry–mCitrine (+3.8 a.u., Supplementary Figure 1A and Bi), but this was not significant compared to the co-injected mCherry + mCitrine. This suggests that the sensitivity of

donor intensity FRET to detect interactions in this system is limited.

SE− FRET was used to further characterise these positive and negative controls (Figure 1D). The mean nuclear mCherry intensity, measured by exciting the donor, was lowest for the acceptor alone, increasing for co-injected mCherry + mCitrine ($p = 0.03$), and increasing further for the tandem mCherry–mCitrine ($p = 0.0009$ vs. acceptor alone). While the expression of mCherry, measured by exciting the acceptor directly, was higher for tandem mCherry–mCitrine, the fold-change was much smaller (approx. 2-fold [$p = 0.03$] vs. approx. 17-fold [$p = 0.0009$]) (Supplementary Figure 1E). We also photobleached the donor for 30 s, comparing SE acceptor intensity pre- vs. post-photobleaching, in two z-planes per embryo. The decrease in mCherry intensity was significantly larger in the tandem mCherry–mCitrine than co-injected mCherry + mCitrine ($p = 0.002$, Supplementary Figure 1C and Di). This shows that the tandem mCherry–mCitrine construct undergoes FRET.

Intensity-based FRET assays were difficult to interpret as donor and acceptor intensities were affected by factors other than FRET, such as spectral bleed-through, and low signal penetrance depending on proximity of embryos and nuclei to objective. mRNA microinjection variability, differential mRNA expression, and protein stability could also affect fluorescent protein levels, as seen in the difference in mCitrine expression levels within conditions for donor-intensity FRET (Figure 1C), and mCherry expression between conditions for SE-FRET (Supplementary Figure 1E) . This makes precise determination of FRET efficiency difficult. We conclude that mCherry and mCitrine are a suitable FRET pair, but that intensity-based FRET assays are not sensitive or robust enough to measure protein–protein interactions in zebrafish.

2.2 | AAT-based measurements of mCitrine and mCherry reflect expected lifetime values

FLIM uses the change in the τ of the FRET donor as a measure of molecular interactions (Figure 2A). As mentioned previously, this is a more robust measure of FRET, which does not depend on fluorescence intensity, and is not affected by photobleaching. However, traditional fitting FLIM-FRET was not suitable for our system. The fast 15- to 20-min cell cycle[31] and large volume of zebrafish embryos are not compatible with the long acquisition time per image which would be required to collect sufficient photons for TCSPC FLIM-FRET due to the low signal-to-noise ratio.[16]

Therefore, we investigated a recent implementation of non-fitting FLIM, which allows faster image acquisition
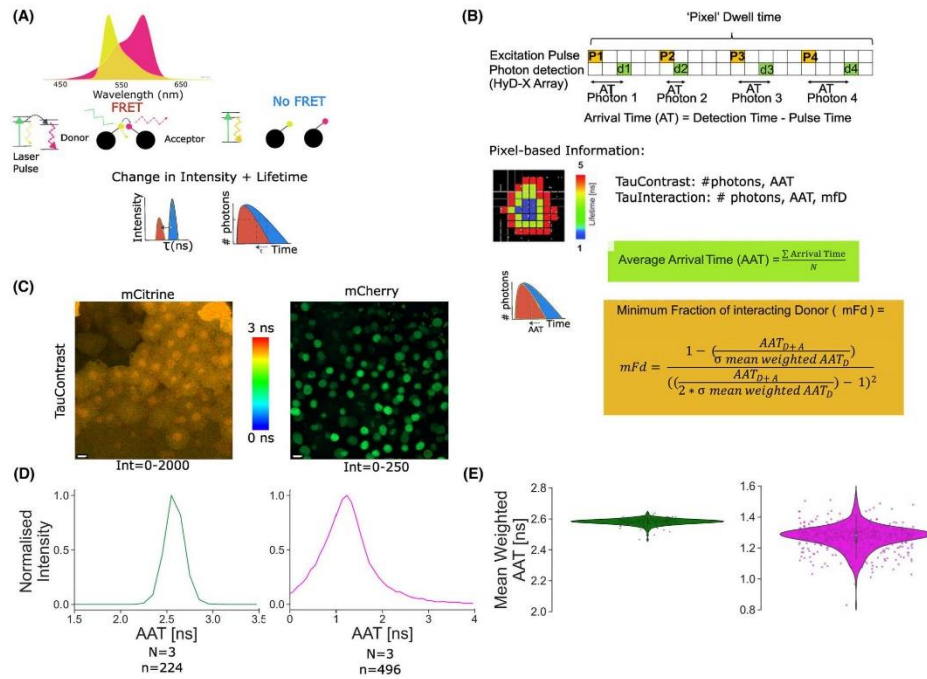
FIGURE 2 Average pixel arrival time (AAT) values for mCitrine and mCherry reflect expected fluorescence lifetime values. (A) Schematic of how AAT-FRET works. (B) Schematic of AAT, describing how AAT and minimum Fraction of Donor interaction (mFD) are calculated. (C) Representative confocal images of mCitrine and Sox19b-mCherry) acquired in TauContrast mode, giving AAT and intensity values per pixel. Images represent maximum intensity projections through the z-stack, scale bar = 10 μm. (D) Lineplots of AAT versus the summed intensities of pixels with each AAT value, averaged and normalised per condition, for nuclei expressing mCitrine or Sox19b-mCherry. (E) Violin plots comparing nuclear mean weighted AAT for mCitrine ($N = 3$, $n = 224$, b.r. = 1) and mCherry ($N = 3$, $n = 496$, b.r. = 1).

by requiring lower photon counts, $\sim$ 100 photons per pixel.[18,20] In AAT$-$ FRET, the average arrival time of photons (AAT) is recorded per pixel, with a resolution of 0.1 ns (Leica application note[21]) (Figure 2B, Section 4). mCitrine has a high τ of 2.9 ns which lowers by 0.15 - 0.75 ns in the presence of an mCherry-tagged interaction partner or a tandem fusion.[27] The difference in τ between FRETing and non-FRETing donor, and of the acceptor mCherry (1.6 ns) is larger than the 0.1 ns detector resolution, making mCitrine–mCherry an ideal FRET pair for AAT$-$ FRET.

Since τ is affected by conditions including the pH, temperature, viscosity and medium polarity (described in Ref. [31]), and AAT may further differ from τ values due to the calculation method,[20] AATs in our system may differ to published values. We therefore characterised the donor and acceptor AAT of our chosen FRET pair in live early zebrafish embryos. AATs were measured on a confocal system fitted with high sensitivity photon counting detectors and a pulsed white light laser (Section 4). mCitrine and a Sox19b-mCherry fusion mRNA were microinjected separately into 1-cell stage embryos. Z-stack images were acquired in TauContrast mode (Leica Microsystems), at 8 μm intervals, for 3 embryos per condition (Figure 2C). This provided intensity and an AAT values for each pixel (Figure 2B). These were converted to lineplots of AAT versus the summed intensities of pixels with each AAT value, averaged and normalised per condition (Figure 2D, Section 4). The mean weighted AAT for mCitrine and Sox19b-mCherry were on average 2.58 ns for mCitrine and 1.27 ns for mCherry, slightly lower than literature values (2.9 ns and 1.6 ns respectively) (Figure 2E and Table 1).[27] Taken together, this shows that mCitrine and mCherry are a suitable FRET pair and that AAT is fast and sensitive enough to facilitate lifetime-based data acquisition across the developing zebrafish embryo in 3D.

T A B L E 1   Comparison of AAT values measured (Figure 3) and fluorescence lifetime (τ) values reported in Ref. (27) for Stx3-mCitrine and Ref. (28) for mCherry

Fluorescent protein	Lifetime reported in literature (ns)	Measured lifetime (ns)
mCitrine	2.90	2.58
mCherry	1.6	1.27

T A B L E 2   Image acquisition time and pixel dwell time for acquisition parameters tested, times given to 3 sig. fig. (±standard deviation)

Condition for point scanning		Acquisition time /image (s)	Pixel dwell time (μs)
Pixel array (area sampled)	128×128 (1.56 μm^2)	4.19 ± 0.276	30.80
	256×256 (0.79 μm^2)	5.22 ± 0.182	15.40
	512×512 (0.40 μm^2)	7.71 ± 0.072	7.69
Scan speed	100 Hz	7.84 ± 0.044	30.80
	200 Hz		
	400 Hz	4.06 ± 0.379	6.34
Line accumulation	4	5.12 ± 0.032	15.40
	8		
	16	5.36 ± 0.037	15.40
Pinhole size	1 AU	5.17 ± 0.013	15.40
	2 AU		

2.3 | Optimisation of spatial resolution, acquisition speed and photon counts for AAT− FRET

Having chosen a suitable FRET pair, we optimised acquisition parameters to detect dynamic nuclear interactions by AAT− FRET in rapidly developing zebrafish embryos. At ZGA (∼3 hpf), these have large nuclei, approximately 13–14 μm diameter,[31] and short cell cycles (15–20 min[29]). To capture as many nuclei as possible per embryo within a single cell cycle, spatial and temporal resolution need to be balanced with sufficient photon counts for precise AAT measurements.

A high 1.2 numerical aperture objective was selected to provide a large enough working distance to focus on nuclei at different depths. Water immersion was used to minimise artefacts caused by refractive index mismatch to zebrafish nuclei. 1.44× digital magnification was chosen so that the embryo filled the field of view. For preliminary analysis, single z-plane images of embryos expressing co-injected mCherry + mCitrine were acquired in TauContrast mode, varying the pinhole size, pixel array, scan speed and line accumulation (Supplementary Figure 2). The precision of AAT values measured per nucleus versus image acquisition time was assessed by comparing pixels per nucleus, intensity per nucleus, AAT lineplots and standard deviation of mean weighted AAT, pixel dwell time and image acquisition time (Figure 3A and B, Table 2 and Supplementary Table 1). Fewer larger pixels increased photon counts

per pixel and thereby AAT precision (Figure 3A and B and Supplementary Table 1) and decreased the acquisition time almost twofold (Table 2). However the resolution achieved using the largest pixels (128×128, 1.6 μm^2) was too low to give useful spatial information in nuclei of 13–14 μm diameter. Slower scan speeds and increased line accumulation also improved AAT precision by increasing photons collected per pixel (Figure 3A and B and Supplementary Table 1), but slower scanning increased acquisition times almost twofold, to 8 s per image (Table 2). Line accumulation minimally affected acquisition time (Table 2).

Since we could not acquire 3D information at Nyquist resolution within the 15- to 20-min cell cycle, we decided that opening the pinhole and acquiring a larger optical section would enable more precise AAT measurements, as more photons per pixel could be collected, without compromising the axial resolution (Figure 3A and B and Supplementary Table 1). For these studies the intermediate 256 × 256 pixels, 200 Hz, 8-line accumulation, and the larger 2 Airy Unit (AU) pinhole were selected, as a compromise between precise AAT measurements, spatial resolution and acquisition time (Figure 3C). These settings also achieved the recommended pixel dwell time of ∼15 μs (Table 2).[14] DNA was labelled with SiR-DNA dye to enable semiautomatised segmentation of nuclei (Figure 3D). Variable or diffuse SiR staining could result from nuclear export,[33] cell cycle stage desynchronisation at ZGA,[24] and post-ZGA establishment of compact heterochromatin in zebrafish.[34]
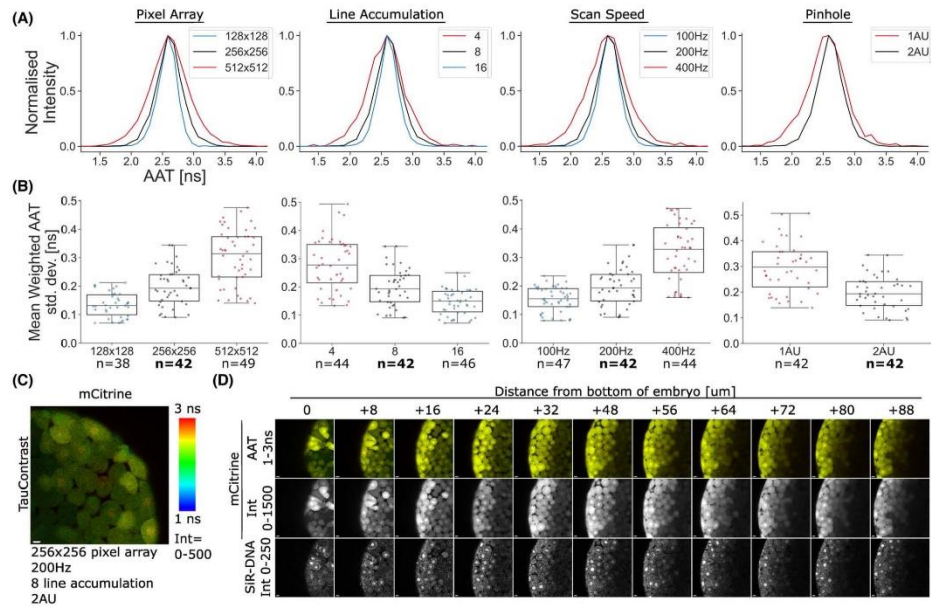
FIGURE 3 Optimisation of acquisition parameters for mCitrine TauContrast images. (A, B) Pixel array, line accumulation, scan speed, and pinhole size were varied, with baseline settings of 256 × 256 px, 200 Hz, 8 line accumulation, 2AU, in embryos expressing co-inj mCh + mCit. (A) Average nuclear AAT lineplots, from single z-plane images were acquired in TauContrast mode. (B) Box and whisker plots of standard deviation of mean weighted AAT per nucleus ($N = 3$, $n = 38$–49, bold = baseline, b.r. = 1). (C) Representative single z-plane TauContrast image of optimised acquisition parameters. (D) Z stack through a representative AAT data set taken from zebrafish embryo expressing mCit, Z step = 8 μm. Top to bottom: mCit Taucontrast image, mCit intensity, SiR-DNA intensity. Scale bar = 10 μm, Int = displayed intensity range, AAT = displayed AAT range.

Finally, given the slow image acquisition times (5–5.5 s per z-plane, Table 2) and large z-volume ~40–70 μm – depending on embryo orientation – a compromise between spatial and temporal resolution also had to be made in the z-axis. 8 μm z sections were chosen (Figure 3D). In summary, confocal acquisition parameters were varied to find settings giving the highest photon counts and lateral resolution for the nucleus ROIs, while minimising acquisition time and photodamage to enable as many optical sections through the developing embryo to be collected within the short cell cycle.

2.4 | AAT-based measurements detect FRET in live embryos

We then tested the sensitivity of AATs measured in Tau-Contrast mode to detect protein–protein interactions in our system, using the same fluorophore controls as pre-

viously (Figure 1B). The calculated mean weighted AAT of mCitrine decreased by 0.16 to 2.44 ns on average in zebrafish nuclei expressing tandem mCherry–mCitrine versus the donor alone ($p < 0.0001$, Figure 4B). The mean weighted AAT of mCitrine in the presence of co-injected mCherry did not change significantly compared to mCitrine alone. This indicates that our system is sensitive enough to detect FRET between mCitrine and mCherry (Figure 4A and B).

AccPb provided additional evidence that AAT measurements detect changes in lifetime due to FRET (Figure 4C–E). We observed that the mean weighted AAT of the donor increased slightly within nuclei by 0.022 ns on average upon AccPb, for the tandem mCherry–mCitrine (Figure 4D, $p = 0.01$). This was a significantly larger change in mean weighted AAT than for co-injected mCherry + mCitrine ($p = 0.01$, Figure 4C–E). This verified that FRET can be detected by measuring the change in mCitrine AAT.
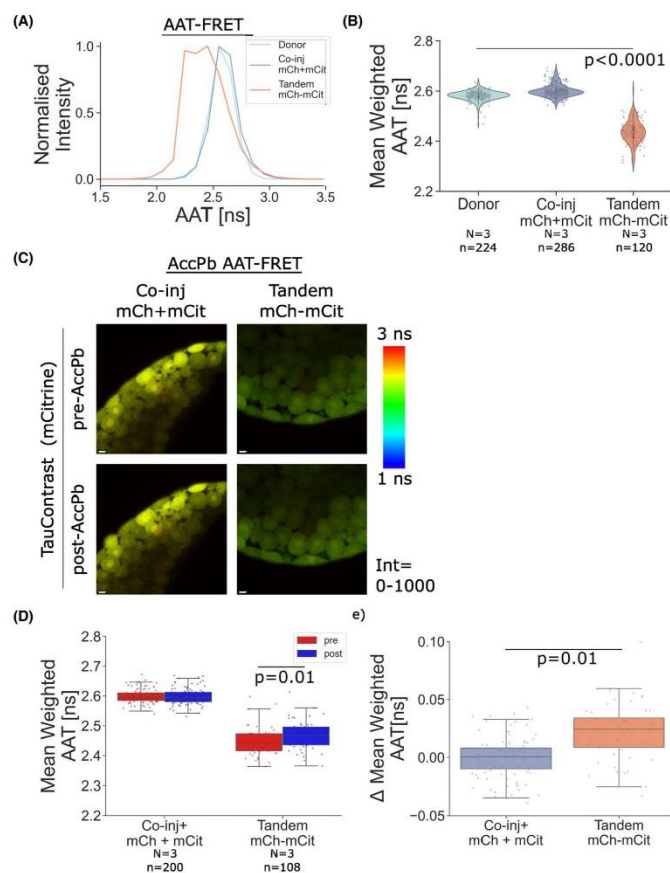
FIGURE 4 AAT− FRET can detect protein interactions in live zebrafish embryos. (A) Average nuclear mCit AAT lineplots from z-stacks acquired in TauContrast mode. (B) Violin plots showing mCit mean weighted AAT per nucleus ($N = 3$, $n = 120–224$, b.r. = 1). (C) AccPb AAT− FRET assay: Pre- and post-AccPb images were acquired in TauContrast mode after z-stacks, for two z-planes in the same embryos used for AAT− FRET. Representative single z-plane TauContrast confocal images of donor channel pre- and post-AccPb, scale bar = 10 μm, Int = displayed intensity range. (D) Box and whisker plot of mean weighted AAT pre- vs. post-AccPb, for individual nuclei ($N = 3$, $n = 108–200$, b.r. = 1). (E) Box and whisker plot of difference (Δ) in mean weighted AAT pre- vs. post-AccPb, for individual nuclei. Data were fit with linear mixed effect models and estimated marginal means compared pairwise.

2.5 | AAT-based minimum fraction of donor interaction (mfD) can estimate degree of donor–acceptor interaction in live zebrafish embryos

An estimate of donor–acceptor interaction, mfD, was calculated by comparing the AAT of the donor alone, versus in the presence of an acceptor[20] (Section 4). Data

were collected using TauContrast mode for z-stacks and TauInteraction mode for individual z-plane images (Figure 5C). TauInteraction is an implementation of the mfD metric[20,23] and provides an mfD value per pixel in addition to intensity and AAT value. TauInteraction mode was used for on-the-fly image analysis and representative images (Figure 5C). AATs acquired in TauContrast mode were used to calculate mfD values values per pixel,
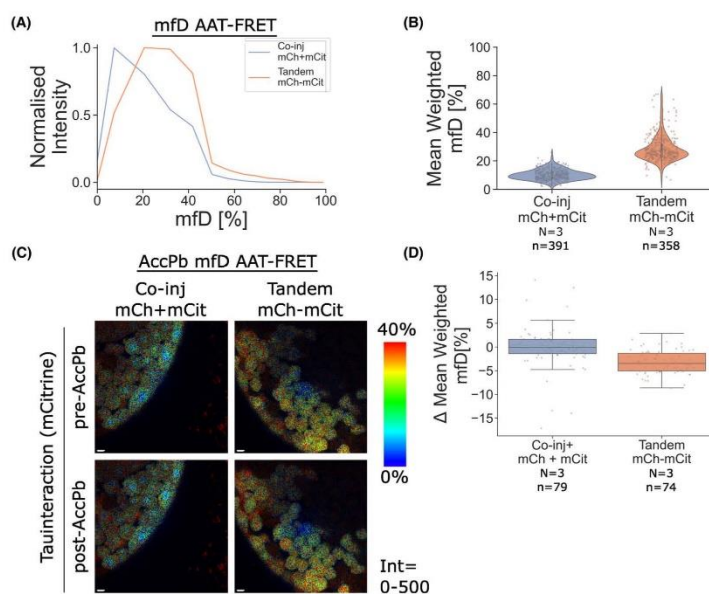
FIGURE 5 AAT-based minimum fraction of interacting donor molecules (mfD) can estimate degree of donor–acceptor interaction in live zebrafish embryos. (A) Average nuclear mfD lineplots converted from AAT values from z-stacks acquired in TauContrast mode. The mfD was calculated from AAT values per pixel, compared to the average mean weighted AAT of the donor alone (Section 4). (B) Violin plots showing mean weighted mfD per nucleus ($N = 3$, $n = 358$–391; donor alone calibration $N = 1$, $n = 133$, b.r. = 1). (C) AccPb AAT− FRET assay: pre- and post-AccPb images were acquired for mCit in TauInteraction mode after z-stacks, for two z-planes in the same embryos used for AAT FRET. Representative single z-plane TauInteraction confocal images of mfD pre- and post-AccPb, scale bar = 10 μm, Int = displayed intensity range. (D) Box and whisker plot of difference (Δ) in mean weighted mfD pre- vs. post-AccPb, for individual nuclei ($N = 3$, $n = 74$–79, b.r. = 1)

post-acquisition. The average mean weighted AAT for the donor alone (2.6 ns) was used to convert AAT to mfD (Figure 5A). By calculating the mean weighted mfD, we estimated that on average 27.9% of donor molecules are interacting with acceptor molecules in embryos expressing the tandem mCherry–mCitrine, versus 8.4% in co-injected mCherry + mCitrine (Figure 1B). This is in the same range as the 27–29% mfD reported for an eGFP-mCherry fusion.[23,34] As mfD underestimates the degree of molecular interaction,[22] this indicates that our mCherry–mCitrine construct shows a high degree of FRET efficiency, which can be detected by AAT− FRET in live zebrafish embryos.

AccPb was carried out as previously described, by comparing the mean weighted mfD of individual nuclei pre- versus post-AccPb (Figure 5C and D). The mean weighted mfD of the tandem mCherry–mCitrine decreased by −5.11% on average, versus an increase of 0.96% for co-injected mCherry + mCitrine (Figure 5D). This is in line with tandem mCherry–mCitrine undergoing FRET.

In summary, we show that using AAT− FRET and estimated mfD measures the degree of protein–protein interactions in live early stage zebrafish embryos.

3 | DISCUSSION

Here, we show the application a τ -based FRET assay, AAT− FRET and mfD[20] and analyse protein–protein interactions in live 3D organisms with low signal-to-noise ratios. AAT− FRET does not require instrument calibration, definition of donor τ decay characteristics or time-intensive photon decay fitting or computation to analyse protein interactions. A further advantage is faster acquisition times compared to TCSPC FLIM. Using the built-in software, it is also possible to qualitatively assess AAT and mfD on-the-fly using the TauContrast and TauInteraction modes.

We outline considerations, optimisation of acquisition parameters and controls for AAT− FRET assays to detect

and measure interactions in early zebrafish embryos. We verified that mCitrine and mCherry are a suitable FRET pair in this system by intensity-based FRET assays (Figure 1, Section 4) and validated this using AccPb (Supplementary Figure 1). We then showed that τ-based AAT values are comparable to literature τ values for mCitrine and mCherry (Figure 2) to ensure that mCitrine and mCherry can be used to interrogate interactions by τ-based AAT− FRET in live zebrafish embryos. Finally, we showed, using the Stellaris 8 TauSense tools, that AAT− FRET and derived estimate of interaction extent (mfD) can detect interactions in a control tandem mCherry– mCitrine protein expressed in early zebrafish embryos (Figures 4 and 5). Others have reported marginally larger τ changes for mCitrine–mCherry in FLIM-FRET experiments to measure Stx3-VAMP3 interactions in dendritic cells.[27] We note that τ and changes due to FRET depend on the cellular environment and the calculation method.[20] Different linkers affecting mobility of fluorophore tags may also define the probability of FRET to occur between tags of interacting proteins.

The difference in fluorescence characteristics between the tandem mCherry–mCitrine, the co-injected mCherry + mCitrine and donor/acceptor alone controls was more pronounced in AAT− FRET (Figures 1C and D and 4A–C and Supplementary Figure 1). We found that the mCitrine AAT decreased by 0.16 ns ($p < 0.0001$, Figure 4B) and estimated a minimum of 27.9% donor molecules interacting with acceptor molecules (Figure 5B), in the tandem mCherry–mCitrine compared to the donor alone. We used AccPb to verify these differences were due to FRET in the tandem fusion. We showed that the mCitrine AAT recovered by 0.022 ns ($p = 0.01$, Figure 4D and E) within nuclei in the tandem mCherry–mCitrine compared to the donor alone, and fewer donor molecules interacted (−5.11%, Figure 5C and D). We conclude that AAT− FRET assays are sensitive enough, and more robust than intensity-based FRET assays, which are affected by variability in relative donor and acceptor expression levels, for the investigation of protein–protein interactions in zebrafish embryos.

This non-fitting approach does have trade-offs compared to TCSPC FLIM-FRET: AAT− FRET collects τ data of a population of photons per pixel rather than per photon, so the ability to resolve τ populations is limited by the 0.1 ns AAT resolution. The mfD measure is an underestimate of donor–acceptor interaction,[22] additionally limited by the AAT resolution. In the current configuration of our instrument, detecting AAT− FRET is therefore limited to FRET pairs for which the donor τ reduction is greater than 0.1 ns. Lower photon counts still affect the precision of measured AAT values (Figure 3 and Table 1). The number of photons collected can be affected by protein expression levels, embryo orientation and proximity to the objective.

τ values may also vary between samples due to differences in the environment such as pH and temperature,[11] causing variability in AAT measurements between embryos or experimental days. Use of an internal control for each biological replicate, such as the AAT of the donor alone, is therefore necessary.

Furthermore, photobleaching for AccPb assays in zebrafish embryos was challenging as the light intensity decreases drastically throughout the sample. More effective photobleaching (see Supplementary Figure 1) would require assaying individual nuclei with increased magnification, which would however slow overall acquisition time for assaying multiple nuclei within each embryo. In addition to this, AccPb is an end-point assay, and therefore cannot be used to investigate dynamic interactions. The timescale of each measurement cycle (approximately 40 s for our individual z-planes) is not comparable to dynamic protein interactions.

AAT− FRET is an excellent method, which facilitates investigation of the spatial and temporal dynamics of molecular interactions in live complex organisms. Zebrafish embryos in particular offer a quick and simple system to measure interactions due to their ease of manipulation and fast expression of mRNA microinjected proteins from 2 hpf. We would expect that further enhancement in detector sensitivity and development of methods such as light-sheet FLIM-FRET[35] would lead to methods such as AAT− FRET being used more widely and could mitigate the need for compromising acquisition parameters, such as optical sectioning, as was necessary for this work (Figure 3). Overall, AAT− FRET is a suitable method to semiquantitatively measure protein interactions in live 3D samples.

4 | MATERIALS AND METHODS

4.1 | mRNA microinjections and embryo mounting for imaging

Zebrafish were maintained in accordance with UK Home Office regulations, UK Animals (Scientific Procedures) Act 1986, amended in 2013 and European Directive 2010/63/EU under project license 70/8000 and P8F7F7E52. All experiments were approved by the Home office and AWERB (University of Edinburgh Ethics Committee). Fish stocks used were: Maternal-zygotic Nanog-null (MZ*nanog*⁻/⁻). Adult fish were maintained at ∼28.5°C under 14:10 light:dark cycles. Embryos were kept at 28.5°C in embryo medium (E3) and staged according to the reference table provided by Kimmel and colleagues (Kimmel et al., 1995). mRNA was made by in vitro transcription of pCS2+ constructs (sp6 mmessage mmachine kit, Invitrogen).

Embryos were microinjected at 1-cell stage with equimolar amounts of mRNA (95 pg mCherry, 97 pg mCitrine, 192 pg mCherry–mCitrine), and SiR-DNA (Spirochrome) at a final concentration of 174 μM, in 500 pL. Embryos were manually dechorionated 1 h post-fertilisation (hpf), prior to mounting in low-melting-point agarose (0.7% in E3). Imaging was carried out ~3 hpf (1000-cell stage) at 26.5°C.

4.2 | Confocal imaging including FRET

AAT and confocal imaging was carried out on a Leica Stellaris 8 Confocal Microscope with White Light Laser (WLL), HyD-X and HyD-S detectors and a 40 × 1.2 NA water-immersion objective lens. AAT FRET images were acquired using the Stellaris 8 TauSense tools, (https://media.nature.com/original/magazine-assets/d42473-020-00364-w/d42473-020-00364-w.pdf).
Image data were acquired in Frame Sequential mode. For intensity-based and AAT− FRET, donor (mCitrine) and SiR-DNA were imaged to create a z-stack with an 8-μm z-step size, using the 515 nm laser at 40% power with a HyD-X detector (523–570 nm), and the 652 nm laser at 20% power with a HyD-X detector (digital mode, 662–710 nm), respectively. To verify protein expression levels, pre-acquisition images were taken for a single z-plane per embryo, using the 515 nm laser at 30% power for mCitrine (HyD-detector, 523–570 nm), using the 587 nm laser at 30% power for mCherry (HyD-detector, 595–640 nm) and using the 652 nm laser at 20% power laser for SiR-DNA (HyD-X detector, digital mode, 662–710 nm).

Acceptor photobleaching was carried out for two z-planes on opposite ends of the z-stack. The acceptor (mCherry) was bleached using 100% 587 nm laser for 30 s. Pre- and post-bleach images were acquired with same settings as above for mCitrine and SiR-DNA, and an additional channel to monitor mCherry intensity: 30% 587 nm laser with HyD detector (595–640 nm).

For intensity-based FRET, the the HyD-X detector was used in photon counting mode. For AAT− FRET, the HyD-X detector was used in TauContrast mode (Intensity and AAT value given per pixel). For AAT− FRET Acc-Pb, the HyD-X detector was used in TauInteraction mode (Intensity, AAT and mfD value given per pixel).

For SE-FRET, acceptor (mCherry) and SiR-DNA were imaged to create a z-stack with an 8-μm z-step size, using the 515 nm laser at 40% power with a HyD-X detector (Tau-Contrast mode, 595–640 nm), and 652 nm laser at 20% power with a HyD-X detector (digital mode, 662–710 nm), respectively. Pre-acquisition images were acquired as for intensity-based or AAT− FRET. Donor photobleaching

was carried out for two z-planes on opposite ends of the z-stack. The donor (mCitrine) was bleached using the 515 nm laser at 100% power with a laser for 30 s. Pre- and post-bleach images were acquired with same settings as above for mCherry and SiR-DNA, and an additional channel to monitor mCitrine intensity: 515 nm laser at 30% power with a with HyD detector (523–570 nm).

4.2.1 | Image analysis

Images were processed in Fiji (ImageJ)[36] or LAS-X (Leica Microsystems). 3D nuclear segmentation was carried out in Fiji after background removal and Gaussian blur filter in the SiR-DNA channel, and the resultant regions of interest (ROIs) were used to interrogate the mCitrine–mCherry intensity/AAT channels. For some images, mCitrine/mCherry intensity channels were used to verify/carry out segmentation. Background subtraction using a rolling ball radius of ~10 pixels and Gaussian blur of ~0.9 μm were performed on the SiR-DNA channel (settings varied for embryos with different SiR-DNA signal patterns). The resultant stack was used to perform 3D nuclear segmentation was carried out using Track-mate with the built-in StarDist detector (Ershov et al. 2022). 2D ROIs representing segmented nuclei detected on each z-planes were filtered by manual thresholding of radius, signal-to-noise, and quality features, as well as manual inspection to remove false detections. The remaining detections were linked together using the Trackmate overlap tracker to create a 3D label stack, which was used to extract the pixel intensity and AAT values for each nucleus from original image stack using the 3D ImageJ Suite.[36,37] For single z-planes pre-/post-bleach images, nuclei were segmented manually (Fiji or LAS-X), and pixel intensity and AAT values were extracted for each nucleus.

4.2.2 | Data processing

Nucleus ROI data from Fiji processing, giving an intensity and AAT value per pixel were imported into Python 3[38] and processed using Pandas[39] and NumPy.[40] Plots were made using Seaborn.[41] Pixels were binned into 0.1 ns AAT bins (matching the detector resolution), and pixel intensities for each AAT bin summed, creating an AAT versus intensity plot for individual ROIs. These match the AAT plots imported from nuclei segmented in LAS-X. AAT plots were normalised to an intensity of 1, averaged across each condition and re-normalised to create line graphs for visual comparison. The mean-weighted AAT per nucleus was calculated from individual ROI AAT plots using the

calculation:

$$\text{Mean weighted } AAT = \frac{\sum \left(AAT \times \frac{I}{I_{max}} \right)}{\sum \left(\frac{I}{I_{max}} \right)},$$

where I is the Intensity at a given AAT (sum of photons counted in pixels with given AAT) and I_{max} is the maximum Intensity value for a given ROI.

mfD was calculated per pixel from AAT values. Mean weighted mfD was calculated as for Mean Weighted AAT.

$$mFd = \frac{1 - \left(\frac{AAT_{D+A}}{\sum \text{mean weighted} AAT_D} \right)}{\left(\left(\frac{AAT_{D+A}}{2\times \sum \text{mean weighted} AAT_D} \right) - 1 \right)^2}.$$

mfD and mean weighted mfD values <0 were set to 0, as the minimum fraction cannot be lower than 0%.

Intensity-based and lifetime-based FRET Efficiency were calculated.

$$E = 1 - \frac{I_{DA}}{I_D},$$

where I_{DA} is the is the average nuclear intensity of the donor in presence of the acceptor from across all 3 embryos and I_D is the average nuclear intensity of the donor alone.

$$E = 1 - \frac{\tau_{DA}}{\tau_D},$$

where τ_{DA} is the average AAT of the donor in presence of the acceptor from nuclei across all 3 embryos and τ_D is the average AAT of the donor alone.

Intensity-based apparent FRET efficiency was calculated for acceptor photobleaching:

$$E_a = 1 - \frac{I_{Donor+Acceptor(pre-bleach)}}{I_{Donor+Acceptor(post-bleach)}}.$$

4.2.3 | Statistics

Mean intensity (log transformed for donor-intensity FRET and SE-FRET), and AAT were compared between conditions in R (version 4.2.1),[43] using linear mixed effect models (lme4, version 1.1–30) including 'embryo' as a random effect. The significance of pairwise comparisons between estimated marginal means was assessed with emmeans (version 1.8.0), accounting for multiple testing using the Tukey's method.

4.2.4 | Scripts

Jupyter notebooks and R scripts used for data processing and statistics were uploaded to: https://github.com/JuliaAuer/Auer2022—Non-fitting-FLIM-FRET-Zebrafish-embryos

ORCID

Dong Xiao https://orcid.org/0000-0002-2901-9253
Ann P Wheeler https://orcid.org/0000-0001-8617-827X

REFERENCES

1. Schneckenburger, H., & Richter, V. (2021). Challenges in 3D live cell imaging. *Photonics*, 8(7), 275.
2. Hu, C. D., Chinenov, Y., & Kerppola, T. K. (2002). Visualization of interactions among bZIP and Rel family proteins in living cells using bimolecular fluorescence complementation. *Molecular Cell*, 9(4), 789–798.
3. Wang, S., Wang, S., Ding, M., Chen, X., Chang, L., & Sun, Y. (2017). Development of bimolecular fluorescence complementation using rsEGFP2 for detection and super-resolution imaging of protein-protein interactions in live cells. *Biomedical Optics Express*, 8(6), 3119–3131.
4. Forster, T. (1946). Energiewanderung und fluoreszenz. *Die Naturwissenschaften*, 33(6), 166–175.
5. Stryer, L., & Haugland, R. P. (1967). Energy transfer: A spectroscopic ruler. *PNAS*, 58(2), 719–726.
6. Jares-Erijman, E. A., & Jovin, T. M. (2003). FRET imaging. *Nature Biotechnology*, 21(11), 1387–1395.
7. Knox, R. S., & van Amerongen, H. (2002). Refractive index dependence of the förster resonance excitation transfer rate. *The Journal of Physical Chemistry B*, 106(20), 5289–5293.

8. Halavatyi, A., & Terjung, S. (2017). Measuring molecular dynamics and interactions by Förster resonance energy transfer (FRET). In A. Wheeler, & R. Henriques (Eds.). *Standard and super-resolution bioimaging data analysis* (pp. 83–97). John Wiley & Sons Ltd.

9. Zhuo, X., & Knox, B. E. (2022). Interaction of human CRX and NRL in live HEK293T cells measured using fluorescence resonance energy transfer (FRET). *Scientific Reports, 12*(1), 6937.

10. Zaccolo, M., De Giorgi, F., Cho, C. Y., Feng, L., Knapp, T., Negulescu, P. A., Taylor, S. S., Tsien, R. Y., & Pozzan, T. (2000). A genetically encoded, fluorescent indicator for cyclic AMP in living cells. *Nature Cell Biology, 2*(1), 25–29.

11. Datta, R., Heaster, T. M., Sharick, J. T., Gillette, A. A., & Skala, M. C. (2020). Fluorescence lifetime imaging microscopy: Fundamentals and advances in instrumentation, analysis, and applications. *Journal of Biomedical Optics, 25*(7), 1–43.

12. Gratton, E., Breusegem, S., Sutin, J., Ruan, Q., & Barry, N. (2003). Fluorescence lifetime imaging for the two-photon microscope: Time-domain and frequency-domain methods. *Journal of Biomedical Optics, 8*(3), 381–390.

13. Becker, W. (2021). The bh TCSPC handbook (9th edn.). Available on www.becker-hickl.com

14. Li, D. D., Ameer-Beg, S., Arlt, J., Tyndall, D., Walker, R., Matthews, D. R., Visitkul, V., Richardson, J., & Henderson, R. K. (2012). Time-domain fluorescence lifetime imaging techniques suitable for solid-state imaging sensor arrays. *Sensors (Basel), 12*(5), 5650–5669.

15. Xiao, D., Sapermsap, N., Safar, M., Cunningham, M. R., Chen, Y., & Li, D. D. (2021). On synthetic instrument response functions of time-correlated single-photon counting based fluorescence lifetime imaging analysis. *Frontiers in Physics, 9*, 635645.

16. Li, D. U., Rae, B., Andrews, R., Arlt, J., & Henderson, R. (2010). Hardware implementation algorithm and error analysis of high-speed fluorescence lifetime sensing systems using center-of-mass method. *Journal of Biomedial Optics, 15*(1), 017006.

17. Peter, M., Ameer-Beg, S. M., Hughes, M. K., Keppler, M. D., Prag, S., Marsh, M., Vojnovic, B., & Ng, T. (2005). Multiphoton-FLIM quantification of the EGFP-mRFP1 FRET pair for localization of membrane receptor-kinase interactions. *Biophysical Journal, 88*(2), 1224–1237.

18. Padilla-Parra, S., Auduge, N., Coppey-Moisan, M., & Tramier, M. (2011). Non fitting based FRET-FLIM analysis approaches applied to quantify protein-protein interactions in live cells. *Biophysical Reviews, 3*(2), 63–70.

19. Digman, M. A., Caiolfa, V. R., Zamai, M., & Gratton, E. (2008). The phasor approach to fluorescence lifetime imaging analysis. *Biophysical Journal, 94*(2), L14–6.

20. Padilla-Parra, S., Audugé, N., Coppey-Moisan, M., & Tramier, M. (2008). Quantitative FRET analysis by fast acquisition time domain FLIM at high spatial resolution in living cells. *Biophysical Journal, 95*(6), 2976–88.

21. Roberti, M. J., Lopez, L. O., Ossato, G., Steinmetz, I., Haas, P., Hecht, F., & Alvarez, L. A. J. (2020). Application Note: TauSense: A fluorescence lifetime-based tool set for everyday imaging. *Nature Methods, 17*(9). https://www.nature.com/articles/d42473-020-00364-w

22. Padilla-Parra, S., Audugé, N., Lalucque, H., Mevel, J. C., Coppey-Moisan, M., & Tramier, M. (2009). Quantitative comparison of different fluorescent protein couples for fast FRET-FLIM acquisition. *Biophysical Journal, 97*(8), 2368–2376.

23. Alvarez, L., Roberti, J., Ossato, G., & Leica Microsystems. (2022). TauInteraction – Studying molecular interactions with TauSense. [cited 2022 14.11.2022]; Available from: https://www.leica-microsystems.com/science-lab/life-science/tauinteraction-studying-molecular-interactions-with-tausense/

24. Schulz, K. N., & Harrison, M. M. (2019). Mechanisms regulating zygotic genome activation. *Nature Reviews Genetics, 20*(4), 221–234.

25. Perez-Camps, M., Tian, J., Chng, S. C., Sem, K. P., Sudhaharan, T., Teh, C., Wachsmuth, M., Korzh, V., Ahmed, S., & Reversade, B. (2016). Quantitative imaging reveals real-time pou5f3-nanog complexes driving dorsoventral mesendoderm patterning in zebrafish. *eLife, 5*, e11475.

26. Schweikhard, V., Alvarez, L. A. J., Roberti, M. J., Birk, H., & Giske, A. (2020). Application Note: The Power HyD family of detectors for confocal microscopy. *Nature Methods, 17*(10). https://www.nature.com/articles/d42473-020-00398-0

27. Verboogen, D. R. J., González Mancha, N., Ter Beest, M., & van den Bogaart, G. (2017). Fluorescence lifetime imaging microscopy reveals rerouting of SNARE trafficking driving dendritic cell activation. *eLife, 6*, e23525.

28. Mukherjee, S., Manna, P., Hung, S. T., Vietmeyer, F., Friis, P., Palmer, A. E., & Jimenez, R. (2022). Directed evolution of a bright variant of mCherry: Suppression of nonradiative decay by luorescence lifetime selections. *The Journal of Physical Chemistry B, 126*(25), 4659–4668.

29. Goldman, R. D., Swedlow, J. R., & Spector, D. L. (2010). *Live cell imaging: A laboratory manual* (2nd edn.). Cold Spring Harbor Press.

30. Kimmel, C. B., Ballard, W. W., Kimmel, S. R., Ullmann, B., & Schilling, T. F. (1995). Stages of embryonic development of the zebrafish. *Developmental Dynamics, 203*(3), 253–310.

31. Berezin, M. Y., & Achilefu, S. (2010). Fluorescence lifetime measurements and biological imaging. *Chemical Reviews, 110*(5), 2641–2684.

32. Reisser, M., Palmer, A., Popp, A. P., Jahn, C., Weidinger, G., & Gebhardt, J. C. M. (2018). Single-molecule imaging correlates decreasing nuclear volume with increasing TF-chromatin associations during zebrafish development. *Nature Communications, 9*(1), 5218.

33. Lukinavičius, G., Blaukopf, C., Pershagen, E., Schena, A., Reymond, L., Derivery, E., Gonzalez-Gaitan, M., D'Este, E., Hell, S. W., Wolfram, G. D., & Johnsson, K. (2015). SiR–Hoechst is a far-red DNA stain for live-cell nanoscopy. *Nature Communications, 6*(1), 8497.

34. Laue, K., Rajshekar, S., Courtney, A. J., Lewis, Z. A., & Goll, M. G. (2019). The maternal to zygotic transition regulates genome-wide heterochromatin establishment in the zebrafish embryo. *Nature Communications, 10*(1), 1551.

35. Tramier, M., Zahid, M., Mevel, J. C., & Masse, M. J., & Coppey-Moisan, M. (2006). Sensitivity of CFP/YFP and GFP/mCherry pairs to donor photobleaching on FRET determination by fluorescence lifetime imaging microscopy in living cells. *Microscopy Research and Technique, 69*(11), 933–939.

36. Mitchell, C. A., Poland, S. P., Seyforth, J., Nedbal, J., Gelot, T., Huq, T., Holst, G., Knight, R. D., & Ameer-Beg, S. M.

(2017). Functional in vivo imaging using fluorescence lifetime light-sheet microscopy. *Optics Letters*, *42*(7), 1269–1272.

37. Schindelin, J., Arganda-Carreras, I., Frise, E., Kaynig, V., Longair, M., Pietzsch, T., Preibisch, S., Rueden, C., Saalfeld, S., Schmid, B., Tinevez, J. Y., White, D. J., Hartenstein, V., Eliceiri, K., Tomancak, P., & Cardona, A. (2012). Fiji: An open-source platform for biological-image analysis. *Nature Methods*, *9*(7), 676–682.

38. Ollion, J., Cochennec, J., Loll, F., Escudé, C., & Boudier, T. (2013). TANGO: A generic tool for high-throughput 3D image analysis for studying nuclear organization. *Bioinformatics*, *29*(14), 1840–1841.

39. van Rossum, G. (1995). Python reference manual. CWI.

40. McKinney, W. (2010). Data structures for statistical computing in python. In *9th Python in Science Conference*. Austin, Texas.

41. Harris, C. R., Millman, K. J., van der Walt, S. J., Gommers, R., Virtanen, P., Cournapeau, D., Wieser, E., Taylor, J., Berg, S., Smith, N. J., Kern, R., Picus, M., Hoyer, S., van Kerkwijk, M. H., Brett, M., Haldane, A., Del Río, J. F., Wiebe, M., Peterson, P., … Oliphant, T. E. (2020). Array programming with NumPy. *Nature*, *585*(7825), 357–362.

42. Waskom, M. L. (2021). seaborn: Statistical data visualization. *The Journal of Open Source Software*, *6*(60), 3021. https://doi.org/10.21105/joss.03021

43. R Core Team, R. (2022). *R: A language and environment for statistical computing*. Vienna, Austria: R Foundation forbStatistical Computing.

SUPPORTING INFORMATION

Additional supporting information can be found online in the Supporting Information section at the end of this article.

How to cite this article: Auer, J. M. T., Murphy, L. C., Xiao, D., Li, D. U., & Wheeler, A. P. (2022). Non-fitting FLIM-FRET facilitates analysis of protein interactions in live zebrafish embryos. *Journal of Microscopy*, 1–14. https://doi.org/10.1111/jmi.13162

4.2.1 Paper Supplementary figures

a)

b) i)

b) ii)

c)

d) i)

(figure cont. over page)

e)

d) ii)
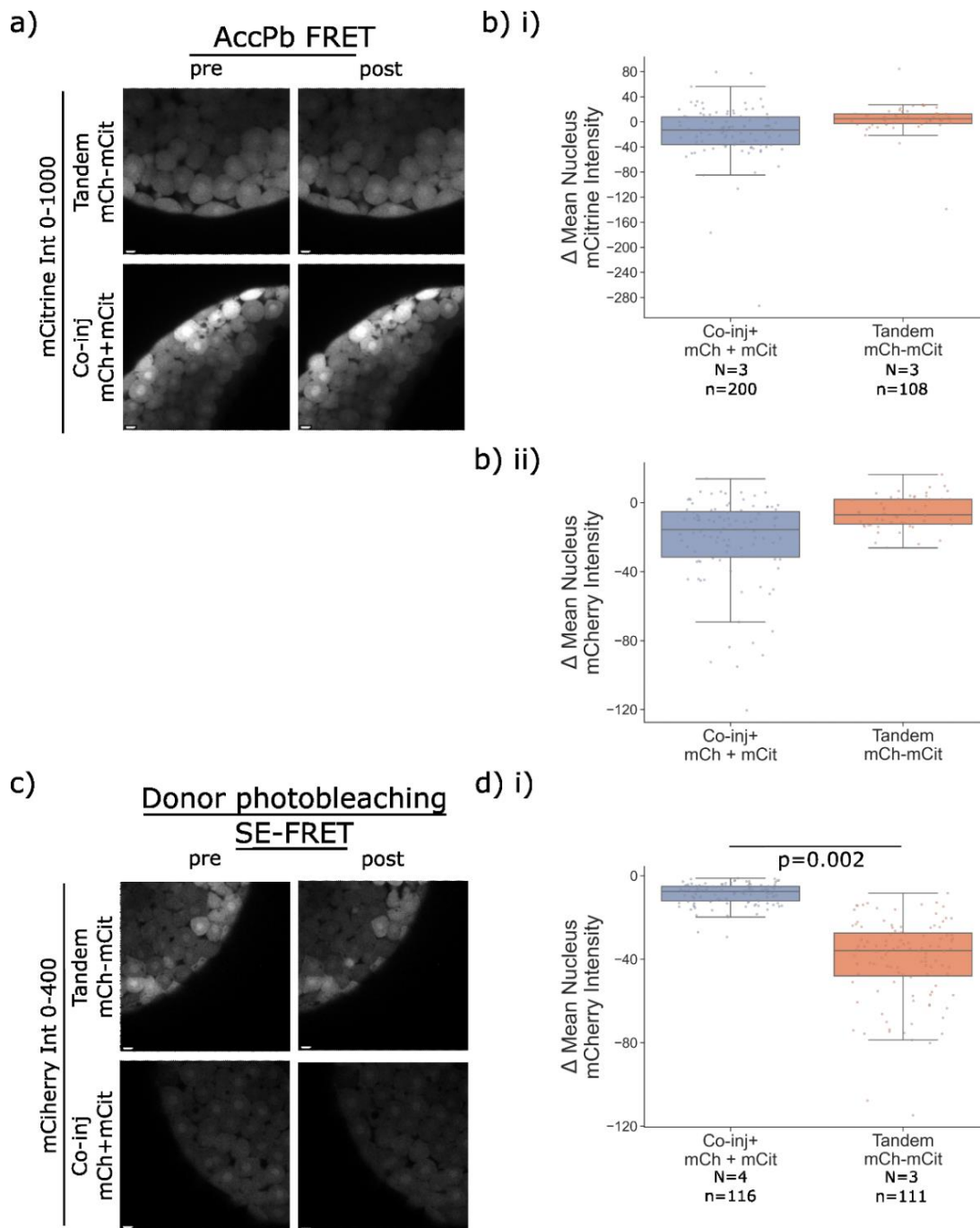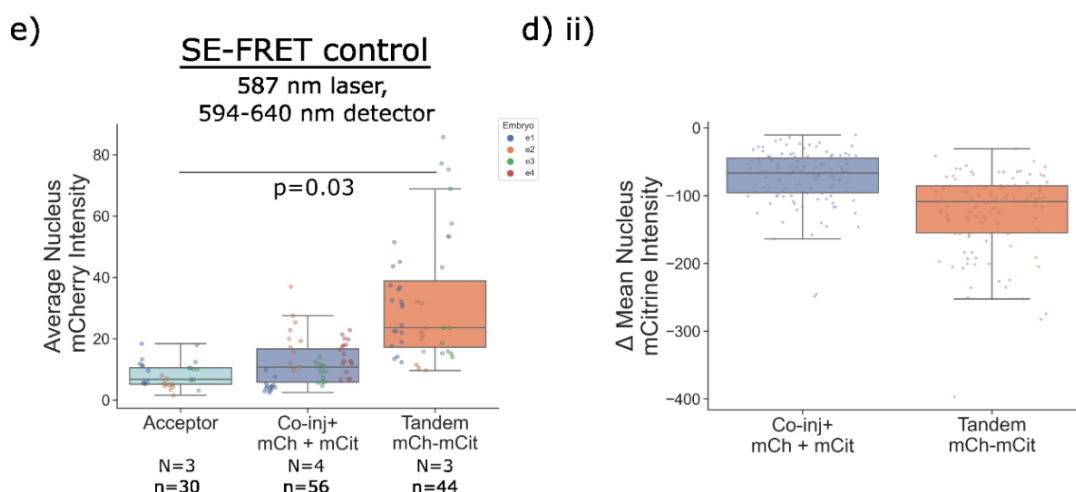
Paper *Supplementary Figure 1* Acceptor Photobleaching FRET, Sensitised emission FRET and Donor photobleaching (accompanies main Figure 1).

a-b) Acceptor photobleaching (AccPb) assay, embryos expressing co-inj mCh + mCit, Tandem mCh-mCit. Pre- and post- donor bleaching donor intensity FRET images were acquired after z-stacks, for two z-planes in the same embryos used for donor intensity FRET (Figure 1c). a) Representative single z-plane confocal images of mCitrine intensity pre- and post- AccPb. b) i) Box and whisker plot showing difference (Δ) in mCitrine intensity per nucleus, before and after 30s AccPb. b) ii) Box and whisker plot of Δ in mCherry intensity per nucleus, pre- and post- AccPb (N=3, n=108-200, b.r.=1). c-d) Donor photobleaching SE-FRET assay, embryos expressing co-inj mCh + mCit, Tandem mCh-mCit. Pre- and post- donor bleaching SE-FRET images were acquired after z-stacks, for two z-planes in the same embryos used for SE-FRET (Figure 1d). c) Representative single z-plane confocal images of mCherry intensity pre- and post- AccPb. Images were acquired using the 515nm laser at 40% power, and the 595-640nm detector. d) i) Box and whisker plot of Δ in mCherry intensity per nucleus, before and after 30s donor photobleaching (N=3-4, n=111-116, b.r.=1).

(cont. over page)

d) ii) *Box and whisker plot of Δ in mCitrine intensity per nucleus, pre- and post-donor photobleaching.* ***e)*** *Control of mCherry expression for SE-FRET (using the 594nm laser at 30% power and the 595-640nm detector), embryos expressing acceptor alone, Co-inj mCh + mCit, Tandem mCh-mCit. Box and whisker plot of average nuclear mCherry intensity (N=3-4, n=30-44, b.r.=1). Scale bar = 10μm, Int= displayed intensity range. Data were fit with linear mixed effect models and estimated marginal means compared pairwise.*
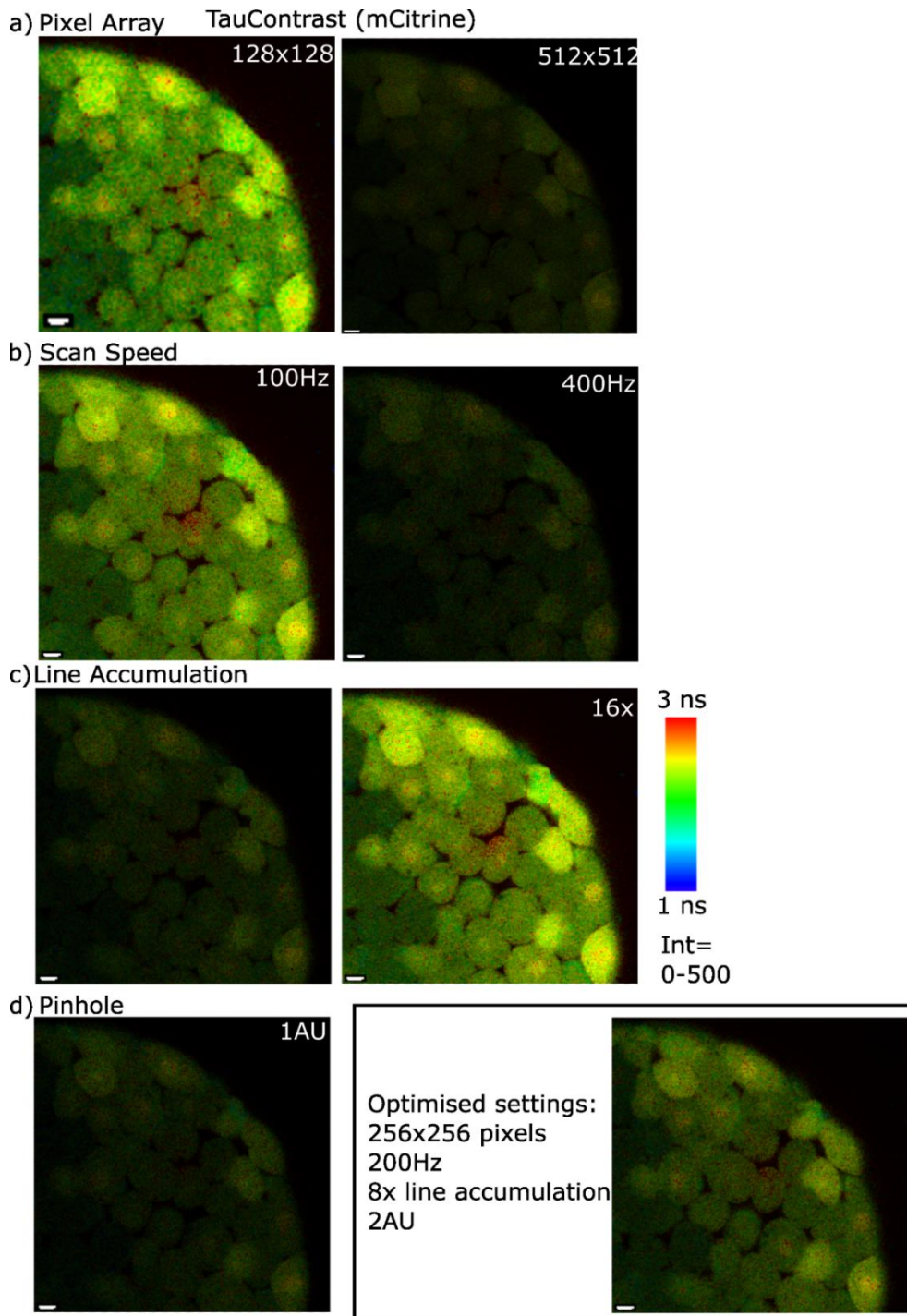
Paper *Supplementary Figure 2* Acquisition parameter optimisation (accompanies main Figure 3).

Single z-plane confocal mCitrine TauContrast images of one representative embryo expressing co-inj mCh + mCit. Parameters varied: a) pixel array b) scan speed c) line accumulation d) pinhole size. Scale bar = 10μm, Int= displayed intensity range.

Paper *Supplementary Table 1:* Acquisition parameter optimisation (accompanies main Figure 3, main Table 2)

AAT range, Mean Weighted AAT, Mean Intensity, and Pixels per nucleus for acquisition parameters tested , given to 3 sig. fig. (+/- standard deviation).

Condition for Point Scanning		AAT range /Nucleus [ns]	Mean Weighted AAT /Nucleus [ns]	Mean Nucleus Intensity [12 bit]	Pixels /Nucleus
Pixel Array (area sampled)	128 x 128 (1.56 µm²)	0.567 +/- 0.218	2.58 +/-0.0660	685 +/- 470	41.9 +/- 13.7
	256 x 256 (0.791 µm²)	1.03 +/- 0.372	2.61 +/-0.0483	321 +/- 231	151 +/- 63.8
	512 x 512 (0.395 µm²)	1.90 +/- 0.671	2.61 +/-0.0528	145 +/- 110	570 +/- 230
Scan Speed	100 Hz	0.811 +/- 0.248	2.61 +/-0.0561	532 +/- 395	158 +/- 49.8
	200 Hz				
	400 Hz	1.67 +/- 0.591	2.58 +/-0.0551	136 +/- 99.6	136 +/- 57.3
Line Accumulation	4	1.45 +/- 0.465	2.58 +/-0.0750	159 +/- 114	137 +/- 64.9
	8				
	16	0.760 +/- 0.255	2.61 +/-0.0513	606 +/- 435	138 +/- 57.5
Pinhole size	1 AU	1.60 +/- 0.620	2.56 +/-0.0609	145 +/- 105	135 +/- 64.5
	2 AU				

143

4.3 Discussion

4.3.1 mCitrine and mCherry are a suitable FRET pair, but intensity-based FRET assays are too variable in zebrafish embryos

My first aim was to characterise whether mCitrine and mCherry are an appropriate FRET pair to examine interactions in zebrafish embryos during ZGA. As expected from their high degree of spectral overlap (**Figure 4.1**), intensity-based FRET assays indicated mCitrine and mCherry could be used as a FRET pair. Overexpression of an mCitrine-mCherry tandem fusion showed a non-significantly reduced donor intensity versus mCitrine alone, and co-injected mCitrine + mCherry, which increased slightly upon AccPb. In SE-FRET the acceptor intensity was significantly higher in the mCherry-mCitrine tandem fusion, versus controls, and fell significantly upon donor photobleaching (**Paper Figure 1, Suppl. Figure 1**).

The acceptor intensity-based assays may have given clearer results because the lower intensity of indirectly excited mCherry would be expected to lead to reduced variability. By contrast, in the donor intensity assays the mCitrine intensity, when directly excited, was more variable – particularly in embryos expressing separate mCherry + mCitrine (**Paper Figure. 2C**). Further, donor photobleaching may be more sensitive than AccPb as mCitrine is less photostable than mCherry: mCitrine $t_{1/2} \approx 30$ s (Lee et al., 2020), mCherry $t_{1/2} = 68$ s (Shu et al., 2006). Clearly these assays are susceptible to differences in donor/acceptor concentration caused by mRNA microinjection. While results could have been improved by correcting for different concentrations and cross-talk, a more robust assay was needed to detect interactions in this system.

4.3.2 AAT-FRET and mfD can more robustly detect interactions between mCitrine and mCherry, given sufficient photon counts

My second aim was therefore to test whether interactions can be more reliably detected by AAT-FRET. AAT clearly reflected τ data, as mCitrine and mCherry AATs were only slightly lower than published τ values (**Paper Figure 2C-E, Paper Table 1**).

This could be due to differences between the lasers and detectors used, or simply the different methods of calculation. A significantly decreased donor mean weighted (MW) AAT was measured in embryos overexpressing the mCherry-mCitrine tandem fusion, versus controls (**Paper Figure 4**). This also recovered significantly following AccPb. Correspondingly, a higher MW mfD was estimated for the mCitrine-mCherry tandem fusion compared to controls, which decreased upon AccPb (**Paper Figure 5**).

However, while these trends were recapitulated in a second biological replicate, these differences were not significant (**Appendix Figure 7.8**). The baseline MW AAT of mCitrine alone was higher than in the first biological replicate. Average nuclear intensities were also lower across all conditions, and a smaller decrease MW AAT between mCitrine alone and mCherry-mCitrine was measured. As shown in Paper Figure 3 (also **Paper Table 2**, and **Paper Suppl. Table 1**), lower photon counts reduce the precision of measured AAT values. This may explain the similar but non-significant decrease in MW AAT in the second biological replicate.

Variability in fluorescence intensity may arise between embryos and replicates for technical reasons besides mRNA microinjection accuracy, such as fluctuations in injection volume, or embryo orientation and proximity to the objective. τ values may also vary between samples due to differences in the environment such as pH and temperature (Berezin and Achilefu, 2010, Datta et al., 2020), causing variability in AAT measurements between embryos or biological replicates. Use of an internal control for each biological replicate, such as the AAT of the donor alone, is therefore a necessary indicator and mitigation of τ or detection variability between replicates.

A further cause of variability could be the heterogeneity of the SiR-DNA dye: differential nuclear levels and cytoplasmic aggregates (**Paper Figure 3D**) affected the quality of nuclear segmentation. Indeed, in some cases the low SiR-DNA dye SNR meant that fluorophore or bright-field channels had to be used for segmentation. Subsequently, nuclei were detected in unequal methods,

distribution, and number between embryos, which could affect the AATs compared. Addition of verapamil was shown to improve DNA labelling efficiency and homogeneity, by inhibiting the efflux pump-driven nuclear export of SiR-DNA dye (Lukinavičius et al., 2015). The effect of verapamil on AAT and FRET between proteins of interest would need to be tested.

Comparing the variability between biological replicates of intensity- versus AAT-based FRET assays does demonstrate that AAT is more robust: while there was a 3-fold difference in AAT-FRET efficiency of the tandem versus separate donor and acceptor between different replicates, there was a 13-fold difference in the intensity FRET efficiency.

4.3.3 Underestimation of interactions by AAT-FRET and mfD could limit detection of weak interactions and require particularly large shifts in donor τ

AAT-FRET and mfD underestimate the degree of interaction because they are based on pixel averages. Thus to be detected in a sample that is challenging to image, such as a zebrafish embryo, it is important to have a fluorophore pair with high FRET efficiency, large (> 0.1 ns) donor τ reduction, and a strong or frequent interaction. In the mCherry-mCitrine tandem fusion a small but significant (0.16 ns) decrease in AAT was detected versus controls (**Paper Figure 4**), and about 27.9% donor molecules were estimated to interact. This calls into question whether a similar shift in AAT can be detected when donor and acceptor are not fused. Given more time, a further positive control, in which known interactors are tagged with mCitrine and mCherry, could have been useful.

Comparative measurements using traditional FLIM-FRET could help to determine whether the small AAT decrease is due to the method's detection sensitivity, or the fluorophore pair. While there is a high degree of spectral overlap between mCitrine and mCherry compared to other common FRET pairs (**Figure 4.1**), this may not cause a large enough shift in donor τ. Alternatively, a more flexible linker in the

tandem fusion could improve the probability of donor and acceptor molecules being in the correct relative orientation for efficient FRET (Jares-Erijman and Jovin, 2003, Wriggers et al., 2005). Finally, the differential maturation time of mCherry (15 minutes (FPbase, 2023b, Shu et al., 2006)) and mCitrine (≈30 minutes (Liu et al., 2018a)) could reduce the proportion of molecules undergoing FRET and lead to further underestimation of interaction (Bajar et al., 2016, Scott and Hoppe, 2015).

4.3.4 Further optimisation is required for sub-nuclear or temporal resolution

There is a significant trade-off between spatial and temporal resolution, and photon counts (**Figure 1.4**). Acquisition settings were therefore optimised initially to measure the AAT of whole nuclei. To sample nuclei across each embryo, z-stacks with 8 µm step-size, 0.79 µm^2 pixel size were acquired at 200Hz with a 2 Airy Unit pinhole, and 8 x line accumulation (**Paper Figure 3, Suppl. Figure 2, Paper Table 2, Suppl. Table 1**). These settings provided sufficient photon counts per nucleus, and were fast enough to acquire z-stack images of multiple embryos per cell cycle (approx. 1-2 minutes per z-stack).

Higher photon counts and SNR could be required to detect an AAT shift between separate interaction partners, as the FRET efficiency will be lower. Optimisation would be especially important for measurements at higher spatial or temporal resolution, to detect interaction heterogeneity within nuclei, or to track changes across a cell cycle. If the z-stack range were reduced, settings could be changed for slower image acquisition to collect more photons. Yolk removal or improved optical sectioning by SPIM (Tramier et al., 2006) would again be options.

Overall, these results show that AAT and mfD can detect FRET between mCitrine and mCherry in a tandem fusion in zebrafish embryo nuclei. This encouraged further experiments to investigate interactions between mCitrine- and mCherry-tagged PSN during ZGA.

5 Testing AAT-FRET to probe Nanog and Sox19b interactions during zebrafish ZGA

5.1 Introduction

I showed in Chapter 4 that AAT is capable of detecting FRET between mCitrine and mCherry in zebrafish embryos. I next assessed whether this was a suitable method to investigate interactions between tagged PSN in zebrafish ZGA. It could be expected that the donor AAT shift would be reduced in the presence of any potential interactions, which may be infrequent and result in lower FRET efficiency, versus tandem-fused fluorophores. Further optimisation therefore focused on improving AAT precision, by comparing the feasibility of embryo preparation methods to increase the SNR. Chorion and yolk removal would increase the signal by bringing the embryo cells closer to the objective and reduce noise by removing background fluorescence. However, these require more skilled embryo manipulation techniques, and may lower the throughput of experiments even further, while potentially affecting the embryo development.

An alternative strategy was to focus on areas within zebrafish nuclei where PSN interactions may concentrate –on DNA, or at a specific actively transcribing gene locus. While labelling DNA consistently in live embryos proved challenging (**Paper Figure 3**), the two large miR-430 transcription bodies formed during ZGA have been successfully labelled using fluorescently tagged morpholinos (MOs) against the nascent RNA ((Hadzhiev et al., 2019, Sato et al., 2019). Sox19b and Nanog (SN) co-localise at these transcription bodies during ZGA, in a Nanog-dependent manner (Kuznetsova et al., 2023), and are required for the expression of miR-430 (Lee et al., 2013, Miao et al., 2022). AAT-FRET measurements at these sub-nuclear ROIs could be a promising strategy to investigate functional interactions between SN. This required extensive testing, first to determine whether (m)Citrine- and mCherry-tagged PSN form foci similar to the reported mNeonGreen-tagged PSN foci (Kuznetsova et al., 2023) and whether SN also co-localise to MO-labelled miR-430 transcription bodies. Next, measurements were carried out using a GeneTools blue-tagged miR-430 MO to examine possible effects on Nanog-mCitrine AAT. Finally,

optimisation was attempted for high magnification images, to allow measurement of FRET by AAT at miR-430 transcription bodies.

As discussed, TFs interact directly or indirectly, and at different stages of their DNA cognate site search; forming complexes mediated by their AD or IDR domains; facilitating each-others' binding to adjacent cognate sites; or bridged by a common partner once bound (sections 1.1.1.1-1.1.1.3). Comparing interaction, by AAT-FRET, between WT and DBD mutant PSN could shed some light on their mode of interaction. A C-terminal tryptophan repeat (WR) has been shown to mediate homodimerisation of mouse NANOG, as well as its interaction with SOX2 through aromatic ring stacking between NANOG W and SOX2 tyrosine (Gagliardi et al., 2013, Mullin et al., 2017). While zebrafish Nanog does not have a WR, it has IDRs in its N- and C-terminus and is relatively enriched for W residues (**Appendix Figure 7.2**Bi). Either end, together with the DBD, seem to be required for Nanog to form foci at miR-430 transcription bodies (Kuznetsova et al., 2023). Yet zebrafish Nanog and mouse NANOG are functionally conserved in cross-species rescue experiments, and the N-terminus of zebrafish Nanog is required for its dimerisation (Schuff et al., 2012, Theunissen et al., 2011). Accordingly, it was hypothesised that the IDRs or relative W enrichment in zebrafish Nanog could drive foci formation and interaction with Sox19b, by non-specific clustering or dimerisation. Interactions between SN were compared for WT Nanog or for a Nanog lacking its N-terminal domain. HeLa cells were chosen as a more accessible system to assay (P)SN interactions, and their dependence on (P)SN-DNA binding. The ease of transfection, compared to microinjection, allowed high-throughput experiments with multiple conditions, and the substantially higher SNR of a single layer of cells increased the sensitivity of AAT-FRET assays.

5.2 AAT-FRET indicates interaction between Nanog and Sox19b during main ZGA

The optimised AAT-FRET acquisition settings from Chapter 4 were used to test interactions between Nanog-mCitrine and Sox19b-mCherry. mCherry was chosen for Sox19b to complement Nanog-mCitrine. While most F(C)CS studies listed in Tables 3.1 and 3.2 tag the mammalian homolog SOX2 at the N-terminus, SNAP (19.4 kda) and NanoLUC (19.1kda) tags at the C-terminus also maintain SOX2 function in mESCs (Strebinger et al., 2019). I therefore chose to tag Sox19b at the C-terminus as this was further from Sox19b's DBD (section 3.7.1, **Appendix Figure 7.2**).

MZ*nanog* -/- embryos were microinjected with rescuing amounts of Nanog-mCitrine alone, or Nanog-mCitrine plus Sox19b-mCherry. Embryos were initially mounted in their chorions, to acquire AAT-FRET images at early and main ZGA (section 3.4). No difference in Nanog-mCitrine AAT was detected at early ZGA: the MW AAT was on average 2.77 ns for Nanog-mCitrine alone, and 2.78 ns in the presence of Sox19b-mCherry (**Figure 5.1**A). At main ZGA the MW AAT decreased slightly in the presence of Sox19b-mCherry, from on average 2.77 ns to 2.73 ns (p=0.072, **Figure 5.1**B,C). This suggests that SN interact directly during main ZGA. Initial experiments did not reveal any interaction between Nanog-mCitrine and Pou5f3-mCherry (**Appendix Figure 7.9**).

AAT values for Nanog-mCitrine alone were less variable at main versus early ZGA (**Figure 5.1**Aii,Bii), likely due to the greater number of high intensity nuclei (**Figure 5.1**D). Nevertheless, variability rendered the AAT shift at main ZGA insignificant (when not accounting for embryos and replicates, e.g. in MannWhitneyU analysis, p=0.001). Clearly higher SNR was needed to improve the precision of AAT values, to detect the perhaps infrequent SN interactions, and the small donor AAT shift (0.16 ns, **Chapter 4**). The 'safe zone' of nucleus intensity for precise AAT measurements was determined by assessing the spread of MW AAT values against nucleus intensity (**Appendix Figure 7.10**Bvi).
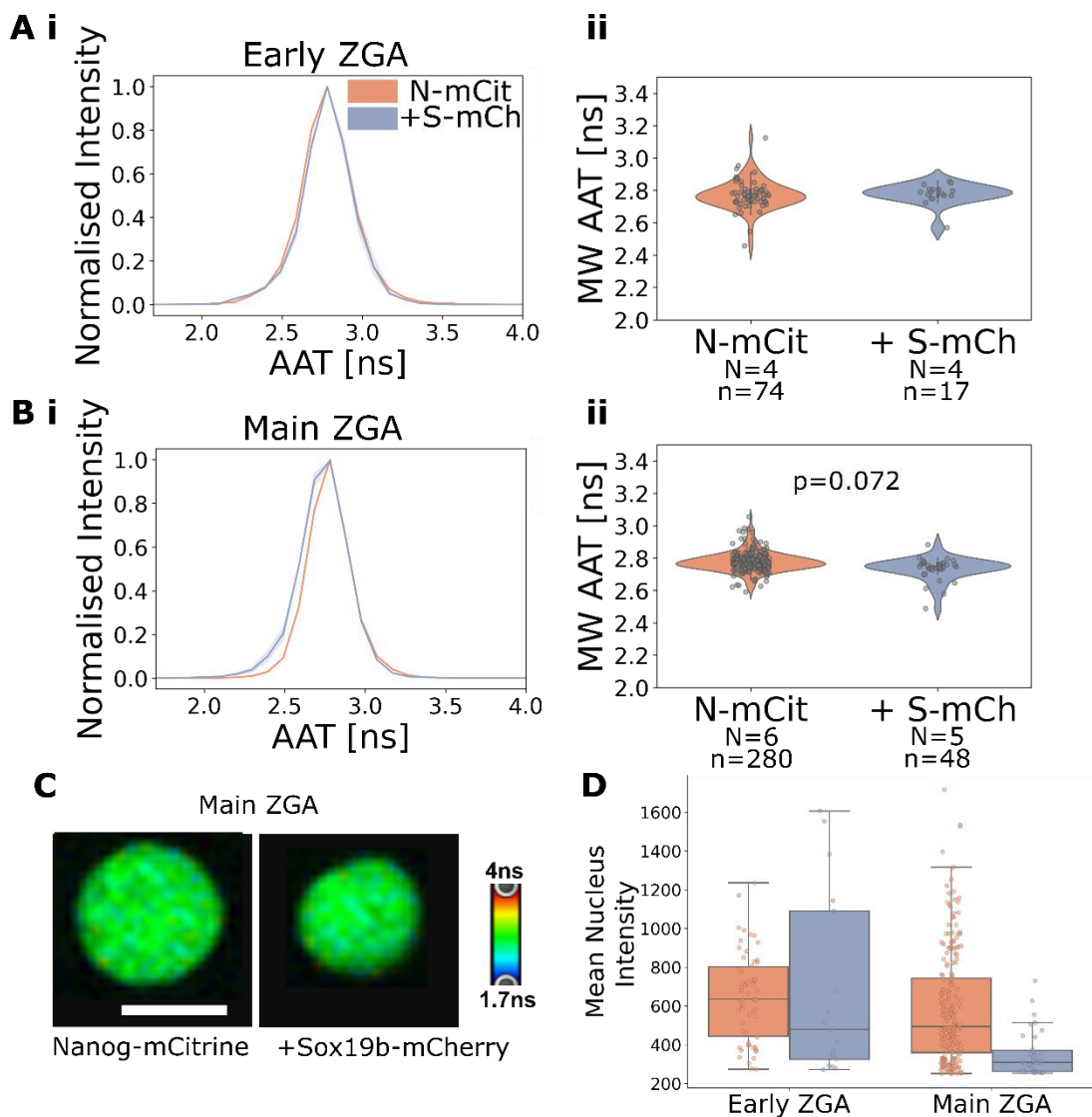
Figure 5.1 AAT-FRET measurements to test Nanog-mCitrine and Sox19b-mCherry interactions.

*MZnanog -/- embryos expressing Nanog-mCitrine (N-mCit) +/- Sox19b-mCherry (S-mCh) were mounted in the chorion (methods 2.2.5.1) and z-stack images were acquired in TauContrast mode (methods 2.7.2.1, setting A) at **A)** early and **B)** main ZGA. Measurements from nuclei with a mean intensity < 250 were excluded. **i** Average nuclear AAT lineplots and **ii** mean weighted AAT (MW AAT) violin plots for measurements at each stage. **C)** Representative AAT images of nuclei at main ZGA, for both conditions, scale bar = 10 µm. D) Boxplots of mean nucleus intensity for embryos in each condition B.r. = 2, N= 4-6 embryos, n= 17-280 nuclei. Statistics were analysed using linear mixed effect models, and pairwise comparison of means (methods 2.8).*

Removing the chorion by manual dechorionation increased Nanog-mCitrine intensity almost 2-fold, from a mean nucleus intensity average of 133 to 227 ((*figure cont. over page)*

Av). The donor AAT precision increased ((*figure cont. over page)*

Ai) while only marginally affecting the MW AAT ((*figure cont. over page)*

Aiv, 2.41 ns vs. 2.46 ns, respectively – see **Figure 5.11** addressing lower than expected AAT values). Embryos co-expressing Nanog-mCitrine and Sox19b-mCherry showed a similar trend ((*figure cont. over page)*

B). This confirmed that dechorionating embryos could improve the precision of AAT measurements.

SN interactions were therefore tested in dechorionated embryos (**Figure 5.2**). Indeed, there was a more apparent AAT-FRET shift: The MW AAT of Nanog-mCitrine decreased by 0.33 ns in the presence of Sox19b-mCherry compared with mCherry alone, from 2.49 ns to 2.16 ns (p=0.15) versus 2.45 ns (p=0.99), respectively (**Figure 5.2**Aii). The Nanog-mCitrine intensity followed the same trend (**Figure 5.2**B,C). Unfortunately, further biological replicates could not be acquired due to time constraints and increasingly noisy AAT-FRET images (**Figure 5.2**B - discussed further in **Figure 5.11**).

In the meantime experiments were carried out in HeLa cells which, being a flat layer of cells directly adjacent to the coverslip, provided a high SNR system requiring far lower laser power.
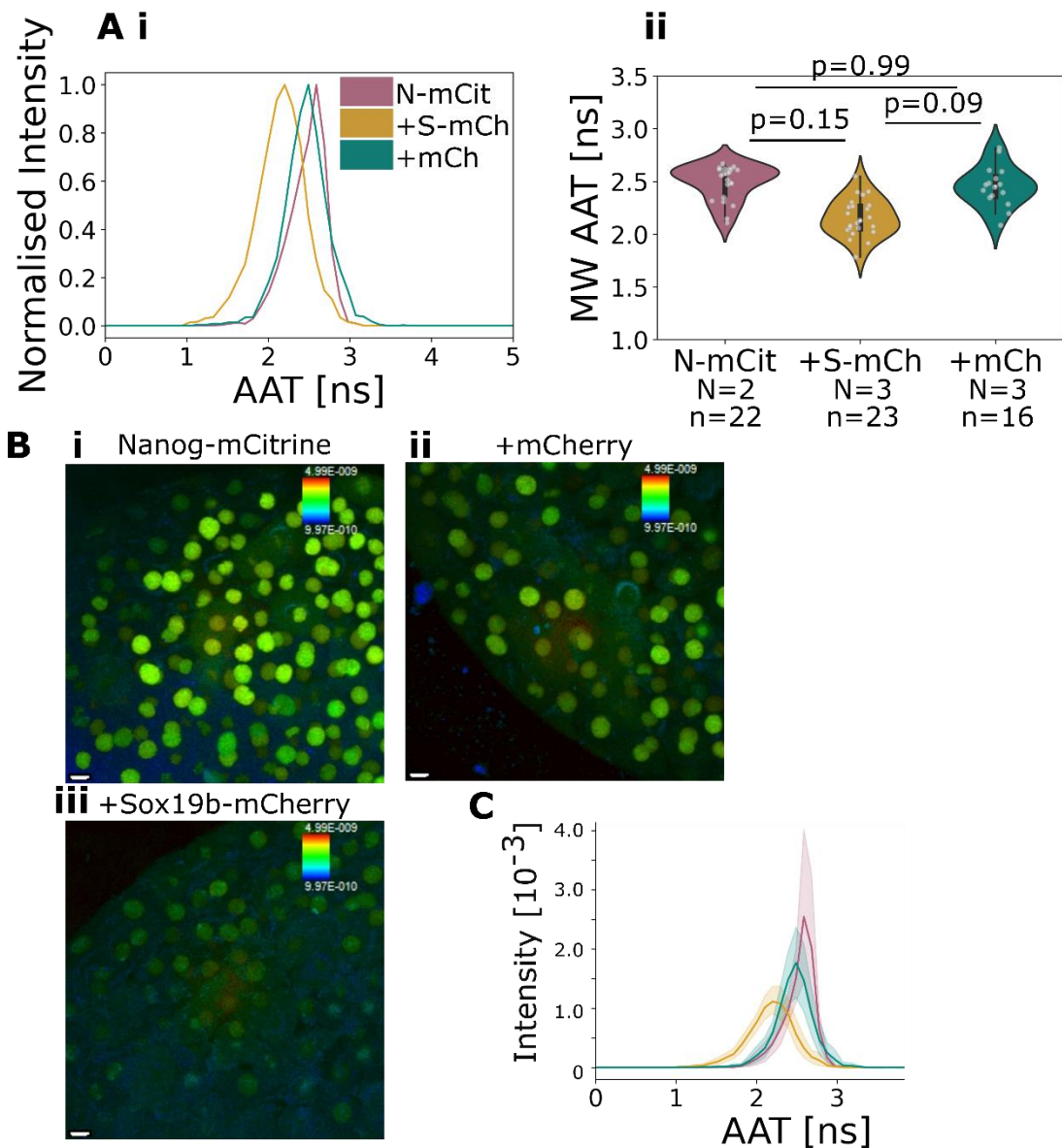
Figure 5.2 AAT-FRET measurements in dechorionated embryos to test Nanog-mCitrine and Sox19b-mCherry interactions.

*MZnanog -/- embryos expressing Nanog-mCitrine (N-mCit) +/- Sox19b-mCherry (S-mCh) or mCherry (mCh), co-injected with a miR-430 MO, were dechorionated (methods 2.2.5.2) and z-stack images were acquired in TauContrast mode at main ZGA (methods 2.7.2.2, setting A). Measurements from nuclei with a mean intensity < 200 were excluded. **A) i** Average nuclear AAT lineplots and **ii** MW AAT violin plots for each condition. **B)** Representative AAT images of nuclei at main ZGA, for each condition, scale bar = 10 µm, AAT range = 0-4 ns. (cont. over page)*

C) *Non-normalised AAT lineplots for each condition. B.r. = 1, N=2-3 embryos, n=16-23 nuclei. Statistics were analysed using linear mixed effect models, and pairwise comparison of means (methods 2.8).*

5.3 Nanog - Sox19b interactions in HeLa cells are affected by DNA binding

HeLa cells were chosen as a more high-throughput system with high SNR to test whether SN interact on DNA. The average MW mfD of tandem mCherry-mCitrine was substantially higher when measured in HeLa cells (51.1%, **Figure 5.3**Bii), versus embryos (27.9%, **Paper Figure 5**). AAT-FRET measurements also verified that Nanog-mCitrine and Sox19b-mCherry interact in HeLa cells (**Figure 5.3**A-C). The Nanog-mCitrine MW AAT decreased by 0.33 ns when co-expressed with Sox19b-mCherry, from on average 2.59 ns to 2.26 ns (p<0.0001) (**Figure 5.3**Bi, **Appendix Table 7.2**,**Appendix Table 7.3**). The MW mfD increased from 9.78% to 36.68% (**Figure 5.3**Bii, **Appendix Table 7.2**). Nanog-mCitrine and mCherry-Pou5f3 also did not show clear interaction in HeLa cells (**Appendix Figure 7.9**). Due to time constraints, no further experiments were carried out to test this pair.
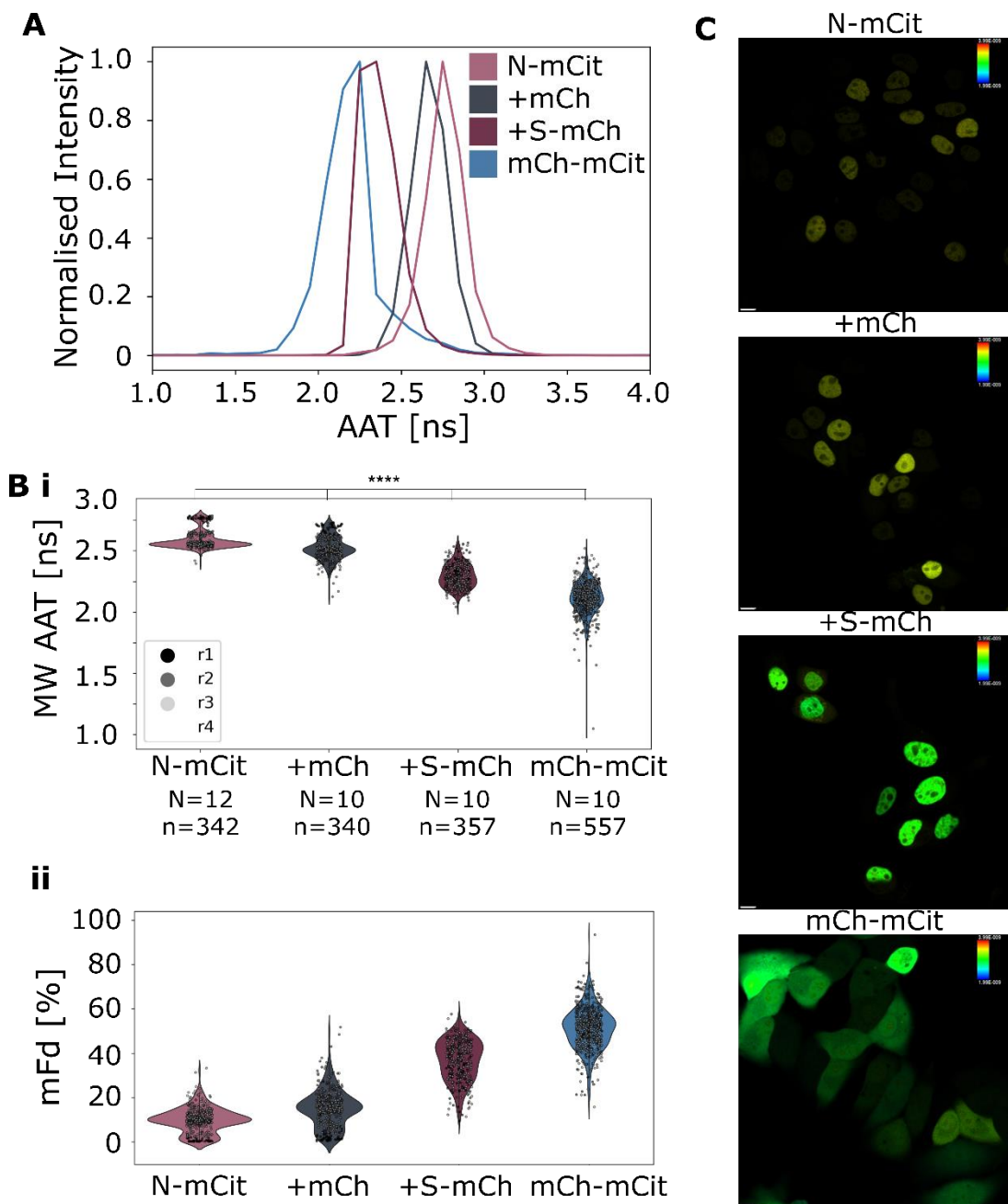
Figure 5.3 AAT-FRET measurements testing Nanog-Sox19b interaction in HeLa cells

Single z-plane images of HeLa cells transiently expressing Nanog-mCitrine (N-mCit),

Nanog-mCitrine + mCherry (mCh), Nanog-mCitrine + Sox19b-mCherry (S-mCh), or

mCherry-mCitrine (mCh-mCit) (methods 2.3) were acquired in TauContrast mode

(methods 2.7.3, setting G). **A)** *Average nuclear AAT lineplots, from 1 b.r..* **B)** *Violin*

*plots for **i** MW AAT and **ii** MW minimum fraction of donor interaction (mfD) across*

conditions, from all b.rs. **C)** *Representative AAT images for conditions, scale bar = 10*

µm, AAT range = 0-3 ns, Intensity range = 0-2056. (cont. over page)

To test whether the interaction between SN depends on their ability to bind DNA, tagged constructs lacking the Nanog homeodomain and Sox19b high mobility group DBDs (NΔH, SΔH) were generated. Deletion of either DBD significantly reduced the interaction (**Figure 5.4**, **Appendix Table 7.2**,**Appendix Table 7.3**). Compared to WT Nanog-mCitrine plus Sox19b-mCherry, the MW AAT of Nanog-mCitrine decreased significantly to 2.43 ns with NΔH, and 2.45 ns with SΔH (both p<0.0001, **Figure 5.4**A). The average MW mfD decreased to 23.47% for NΔH, 22.53% for SΔH (**Figure 5.4**B). This indicates that, in HeLa cells, some interactions between SN involve the DNA binding activity of both. Variability may arise from unequal transfection efficiency, or lowered cell survival due to SN overexpression.

Alternatively, there may be sub-populations of SN complexes that are differentially affected by DNA binding ability. SN distributions were therefore compared between conditions, both in single and co-expression (**Figure 5.5**). Images acquired in TauInteraction mode gave mfD values per pixel, to assess the sub-nuclear distribution of the degree of interaction (**Figure 5.5**Ciii-Fiii). Nanog-mCitrine had variable nuclear distribution in HeLa cells, from large patchy non-homogenous domains to distinct foci (**Figure 5.5**Ai,iv), perhaps due to different levels of overexpression between cells. Sox19b-mCherry was similarly non-homogenously distributed, but did not form foci by itself (**Figure 5.5**Bi). Co-expressed WT Nanog-mCitrine and Sox19b-mCherry seemed to have overlapping patchy distribution patterns, which were more heterogeneous than those in individual expression, but no Nanog-mCitrine foci were observed (**Figure 5.5**Ei-ii). TauInteraction images suggest more interaction in areas with high SN levels of (**Figure 5.5**). This suggests that WT SN interactions are not homogenously distributed, but that WT Nanog does not recruit WT Sox19b into discrete foci within HeLa nuclei. It would be interesting to monitor whether SN co-expression changes their co-localisation with chromatin.
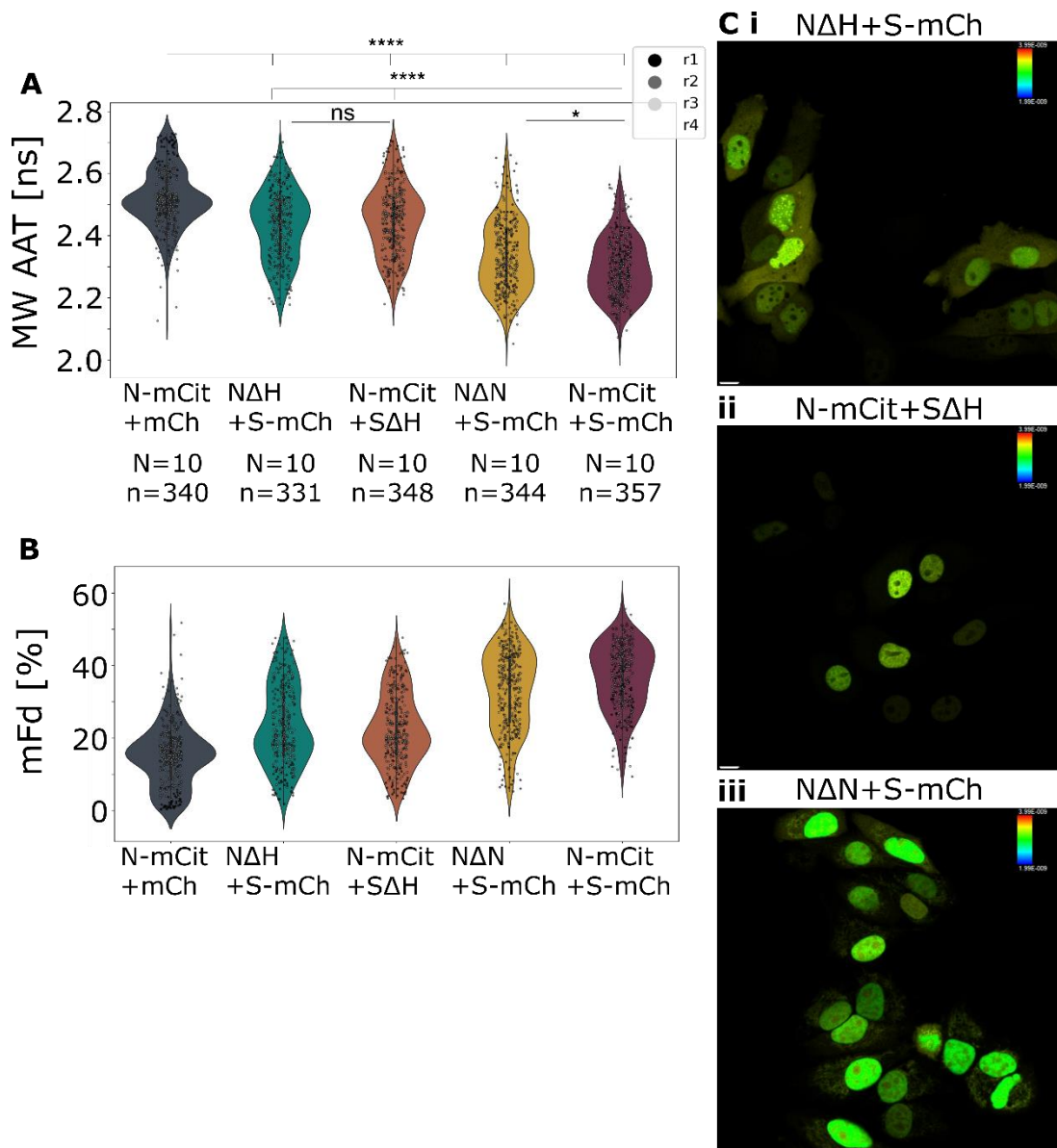
Figure 5.4 AAT-FRET measurements to test DBD mutant Nanog and Sox19b interactions in HeLa cells.

*Transiently expressed Nanog-mCitrine (N-mCit)+ mCherry (mCh), NanogΔHOM-mCitrine (NΔH) + Sox19b-mCherry (S-mCh), Nanog-mCitrine + Sox19bΔHMG-mCherry (SΔH), or NanogΔNterm-mCitrine (NΔN) + Sox19b-mCherry, or Nanog-mCitrine + Sox19b-mCherry in HeLa cells. Single z-plane images were acquired in TauContrast mode (methods 2.7.3, setting G). **A)** Violin plots for MW AAT across conditions. **B)** Violin plots for MW mfD across conditions. (cont. over page)*

C) *Representative AAT images for* ***i.*** *NanogΔHOM-mCitrine + Sox19b-mCherry,* ***ii.*** *Nanog-mCitrine + Sox19bΔHMG-mCherry,* ***iii.*** *NanogΔNterm-mCitrine + Sox19b-mCherry. Scale bar = 10 µm, AAT range = 0-3 ns, Intensity range = 0-2056. B.r. = 4, N=10 images, n=331-357 nuclei. Statistics were analysed using linear mixed effect models, and pairwise comparison of means (methods 2.8).*

Deleting SN DBDs altered their distribution in HeLa cells: both NΔH and SΔH were more cytoplasmic than their WT equivalents (**Figure 5.5**B). The foci seen in some HeLa cells expressing WT Nanog-mCitrine were more frequent and larger for NΔH (**Figure 5.5**Ai-ii,iv-v). WT Sox19b-mCherry sometimes co-localised with NΔH foci, and interacted with mutant Nanog there (**Figure 5.5**D). This suggests that overexpressed NΔH may be sequestered into larger foci, and recruit WT Sox19b-mCherry, interacting away from DNA.

Conversely, SΔH no longer formed large patchy non-homogenous domains, but was found in large cytoplasmic foci, and small low-concentration nuclear foci (**Figure 5.5**Bii). When WT Nanog-mCitrine was co-expressed with SΔH, they co-localised to small higher-concentration foci (**Figure 5.5**Ei-ii). The resolution of TauInteraction images was not high enough to see whether interactions were enriched here (**Figure 5.5**E.iii). This supports the interpretation that DBD deletion causes sequestration of overexpressed SN into foci. Further, WT Nanog may positively influence foci formation already driven by additional factors - such as sequestration in overexpression, or clustered DNA binding sites at endogenous regulatory elements.

Deletion of the N-terminal domain (NΔN) led to loss of Nanog foci (**Figure 5.5**Aiii). Co-expressed NΔN and WT Sox19b-mCherry again seemed to overlap, but were distributed more homogenously than the in large patchy domains seen for WT Nanog-mCitrine plus Sox19b-mCherry (**Figure 5.5**F). In whole nuclei there was a modest effect on SN interactions measured by AAT-FRET: the average MW AAT was 2.33 ns (p=0.017 vs. WT Nanog-mCitrine and Sox19b-mCherry), and average MW mfD 33.02% (**Figure 5.4**A,B, **Appendix Table 7.2**,**Appendix Table 7.3**).

Overall, over-expressed SN seem to interact in HeLa cells, relying to some extent on their DBDs and Nanog's N-terminus. Although in a different system, and in overexpression (see section 5.6.2), this is largely consistent with SN foci co-localising to miR-430 transcription bodies in zebrafish nuclei at ZGA, in a Nanog dependent manner, with Nanog requiring its DBD and either N- or C-terminal domain to form foci (Kuznetsova et al., 2023).

A **i** WT   **ii** NΔH   **iii** NΔN

iv   **v**   **vi**

B **i** WT   **ii** SΔH

iii   **iv**

Nanog-mCitrine

Sox19b-mCherry

(Figure cont. over page)

C i Nanog-mCitrine **ii** Sox19b-mCherry **iii** TauInteraction

WT

D ii Nanog-mCitrine **ii** Sox19b-mCherry **iii** TauInteraction

NΔH
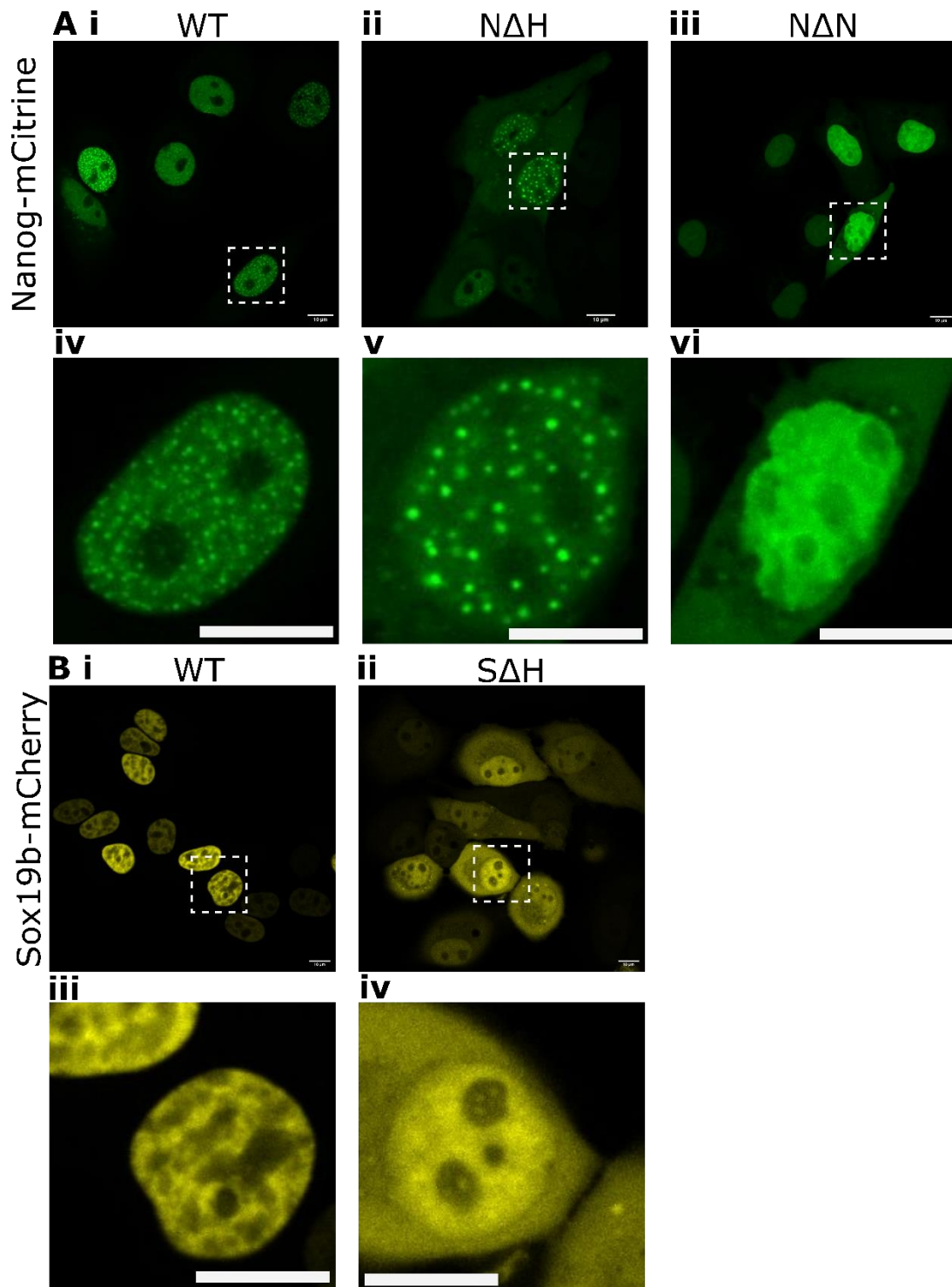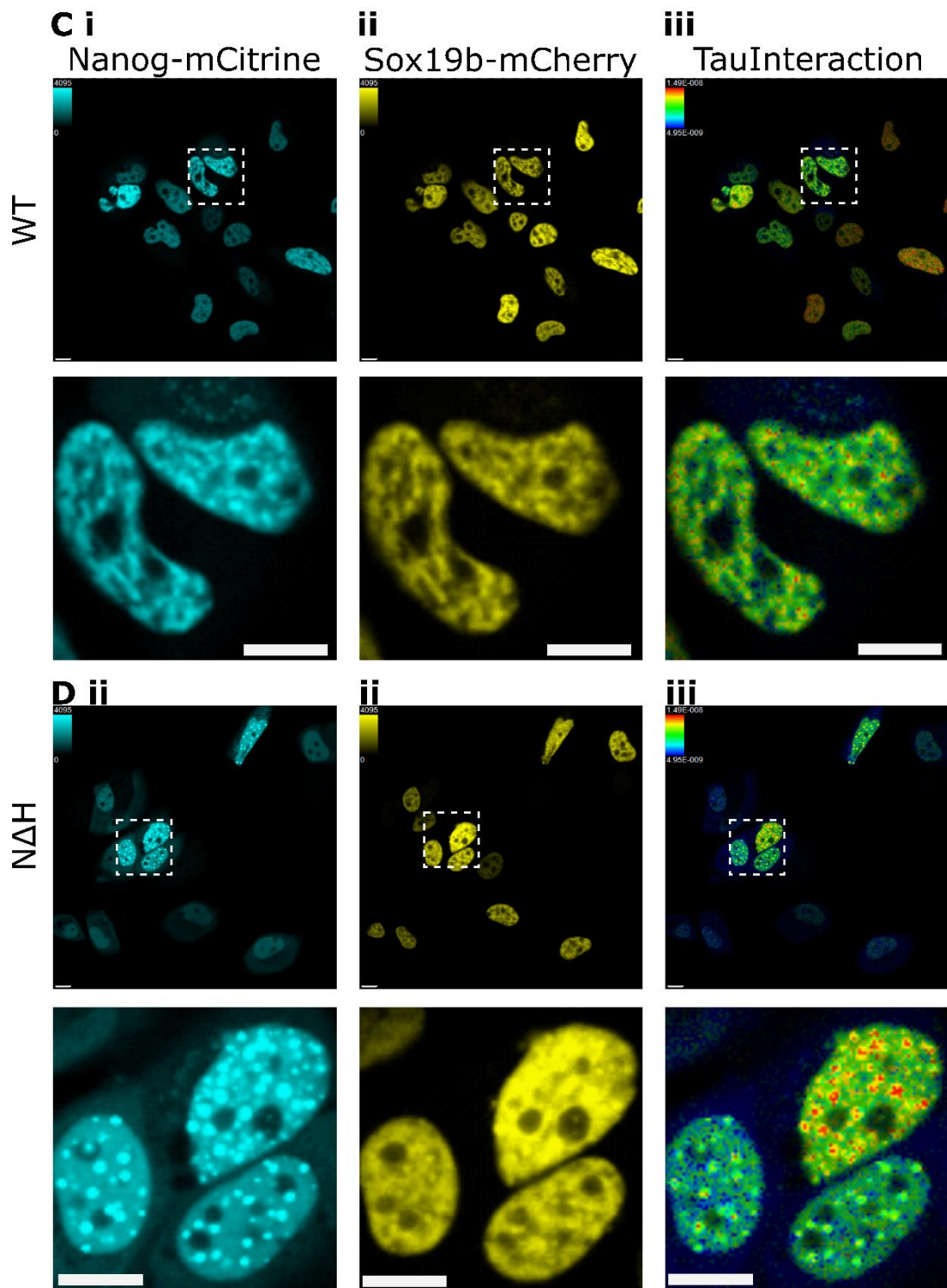
(Figure cont. over page)
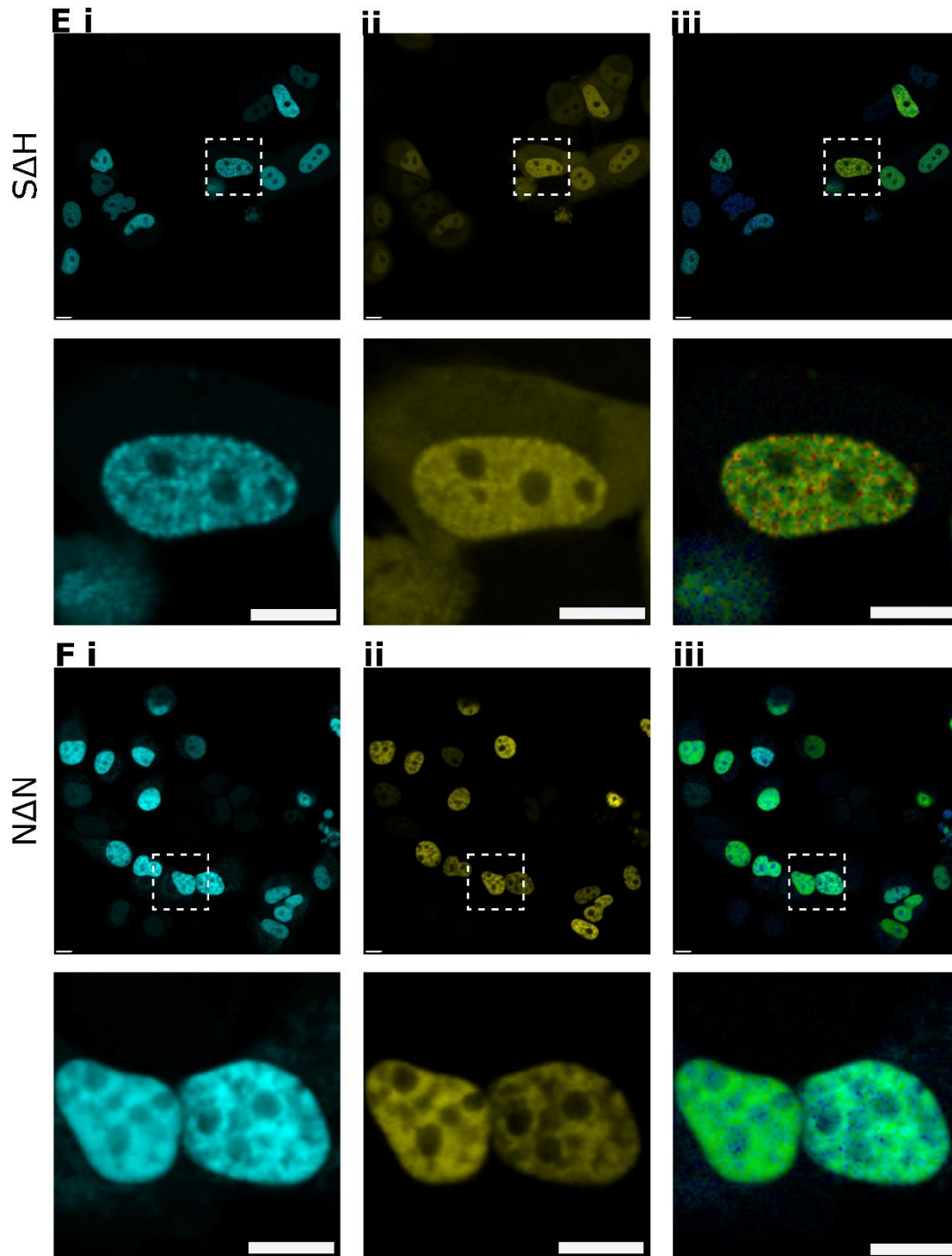
Figure 5.5 Distribution of Nanog and Sox19b vs. mutants in HeLa cells.

Single z-plane images (methods 2.4.6), of Nanog-mCitrine, NanogΔHOM-mCitrine (NΔH), NanogΔNterm-mCitrine (NΔN), Sox19b-mCherry, or Sox19bΔHMG-mCherry (SΔH) transiently expressed in HeLa cells. (cont. over page)

*A-B) Representative intensity images of single transfections for **A)** Nanog-mCitrine **i.** WT, **ii.** NanogΔHOM-mCitrine, and **iii.** NanogΔNterm-mCitrine, **iv-vi** are magnifications of nuclei in white dotted box, **B)** Sox19b-mCherry **i.** WT, **ii.** Sox19bΔHMG-mCherry, **iii-iv** are magnifications of nuclei in white dotted box. Scale bar = 10 μm. B.r. = 1, N=8 images. **C-F)** Representative images of **i-ii** intensity channels and **iii.** TauInteraction channel (methods 2.7.3, setting G) for co-transfected SN **D)** WT+WT, **E)** NanogΔHOM-mCitrine + WT Sox19b-mCherry, **F)** WT Nanog-mCitrine + Sox19bΔHMG-mCherry, and **G)** NanogΔNterm-mCitrine + WT Sox19b-mCherry. Scale bar = 10 μm, mfD range = 20-60%. B.r. = 1, N=5 images.*

5.4 PSN form dynamic nuclear foci during ZGA

Interactions between SN could be enriched at miR-430 transcription bodies, and therefore be more apparent in AAT-FRET measurements. As PSN foci seen by others were with mNeonGreen tags (Kuznetsova et al., 2023), it was first tested whether the PTFs behaved similarly when tagged with (m)Citrine and mCherry – the mCitrine tag was not available for earlier experiments.

Nanog-Citrine, Sox19b-Citrine, and Citrine-Pou5f3 were non-homogeneously distributed within nuclei, when they were initially overexpressed in WT embryos (**Figure 5.6**). Citrine-tagged PSN formed dynamic nuclear foci, and seemed to associate with mitotic chromosomes during early and main ZGA (**Figure 5.6**A-C). Similar distribution was observed for Nanog-mCitrine rescuing MZ*nanog -/-* embryos and co-expressed Sox19b-mCherry (**Figure 5.6**D,E, **Appendix Figure 7.12**). Nanog-mCitrine had a more noisy and cytoplasmic distribution than Nanog-Citrine, perhaps due to the change in microscope and acquisition settings, or a lower quality of mRNA prep. The nuclear distribution of Pou5f3 seemed to be more affected by the fluorophore tag than Nanog or Sox19b: mCherry-Pou5f3 was distributed homogeneously within WT nuclei (**Figure 5.6**F). As smaller foci were reported for mNeonGreen-tagged Pou5f3 than Nanog or Sox19b (Kuznetsova et al., 2023), the dimmer and less overexpressed mCherry-tagged Pou5f3 could be just below the threshold for foci formation or detection.
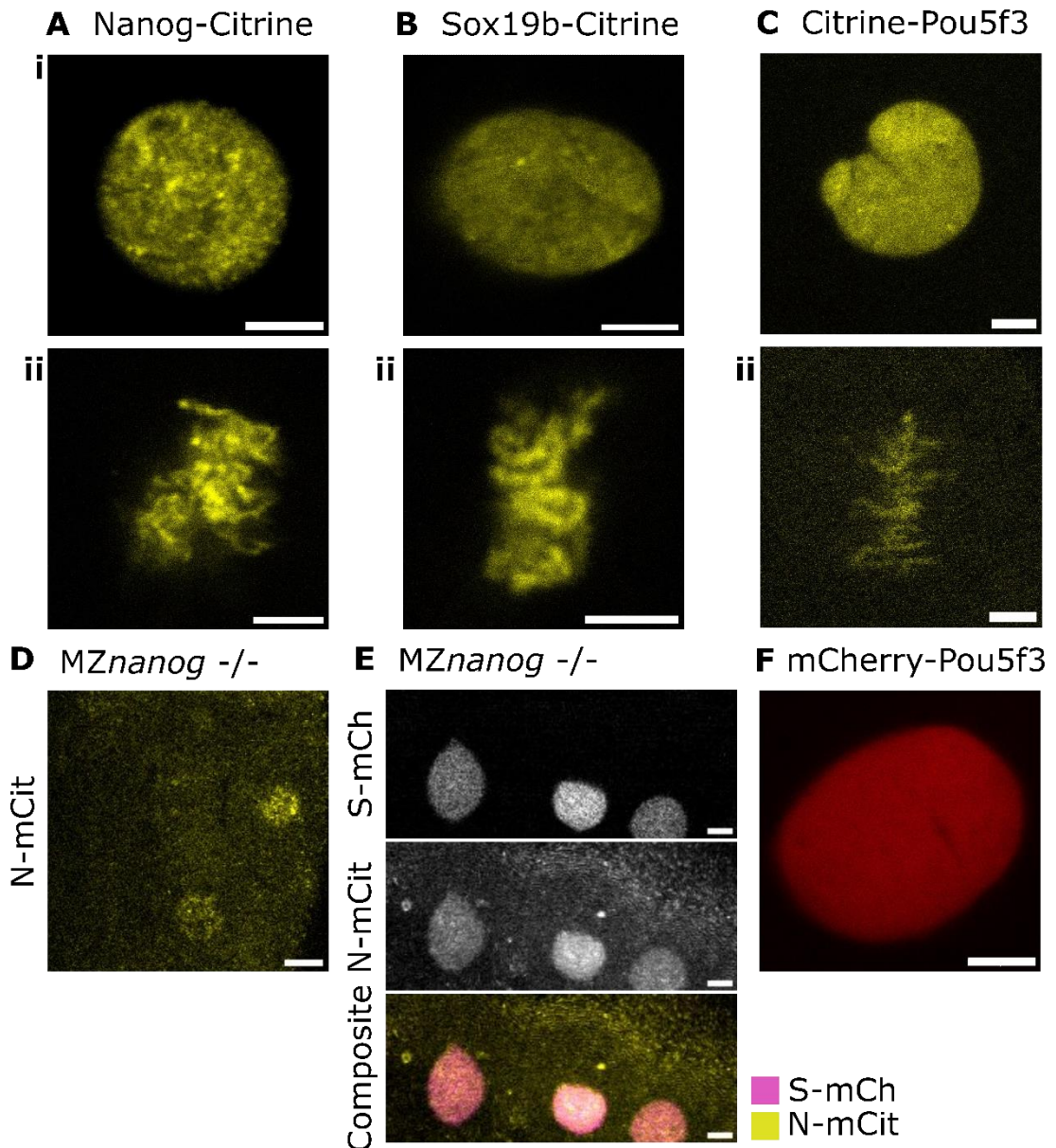
Figure 5.6 Nuclear distribution of fluorescently tagged PSN.

A-C, F) Single z-plane images of WT embryos overexpressing A) Nanog-Citrine, B) Sox19b-Citrine, C) Citrine-Pou5f3, F) mCherry-Pou5f3, were acquired in i Interphase and ii Mitosis durin early and main ZGA, (methods 2.4.2). n= 2-3 embryos, b.r. = 2. Scale bar = 5 μm. D+E) Single z-plane images of MZnanog -/- embryos expressing D) Nanog-mCitrine (N-mCit) or E) Nanog-mCitrine + Sox19b-mCherry, co-injected with the blue miR-430 MO (acquired during AAT-FRET measurements (methods 2.7.1, setting A for Nanog-mCitrine/ pre-A for Sox19b-mCherry). Scale bar = 5 μm. See App. Fig. 12 for miR-430 channel and magnification.

Nanog-Citrine co-localised with mitotic chromosomes labelled with co-injected SiR-DNA dye (**Figure 5.7**A). This suggests that it may exhibit mitotic bookmarking (Teves et al., 2016). To study the co-localisation of Nanog-Citrine foci with DNA, embryos were dissociated, allowing the use of a higher magnification objective with shorter working distance. Some, but not complete, overlap of DNA and Nanog-Citrine foci was observed (in nuclei, **Figure 5.7**B). This could be explained by different populations of Nanog activity, including chromatin-binding, concentration in DNA-excluded transcription bodies (Hadzhiev et al., 2019, Hilbert et al., 2021, Sato et al., 2019), or sequestering of excess Nanog (Klosin et al., 2020). More detailed study of these foci was prevented by the low-throughput and limited success of dissociating embryos, as well as variable DNA labelling by SiR-DNA dye (discussed in 4.2).
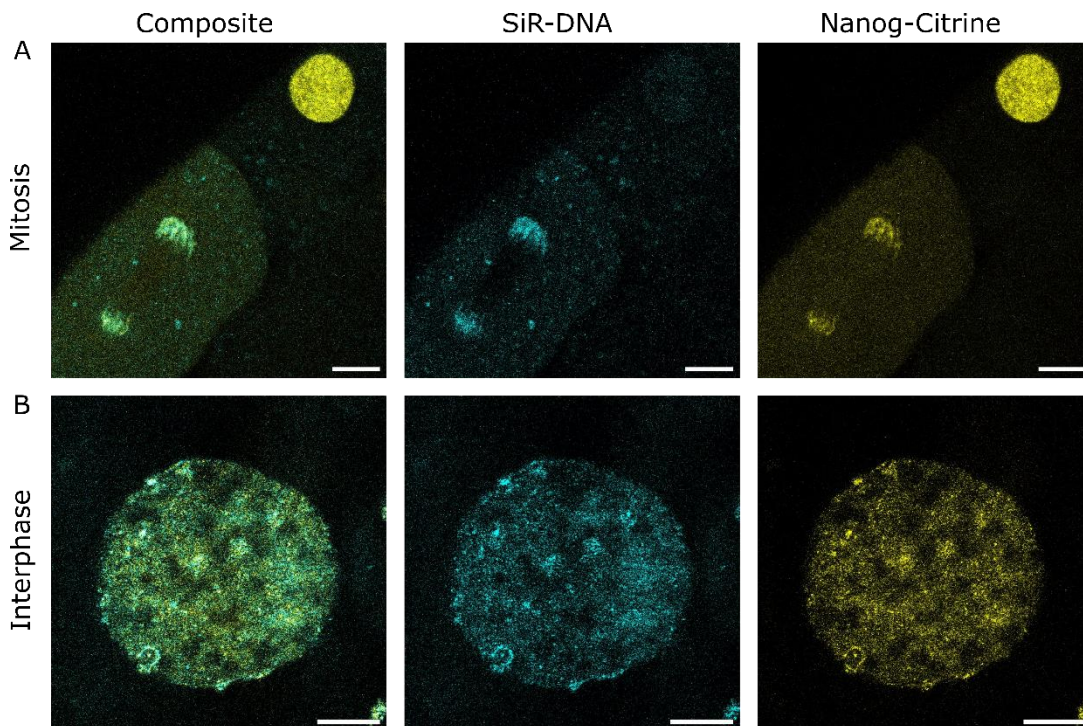
Figure 5.7 Co-localisation of Nanog-Citrine with DNA in live embryos at interphase and mitosis.

*WT embryos overexpressing Nanog-Citrine, DNA labelled with co-injected SiR-DNA dye (methods 2.4.3). **A)** Representative image of DNA (SiR-DNA) and Nanog-Citrine in a mitotic cell from an embryo mounted in the chorion. (cont. over page)*

B) *Representative image of SiR-DNA and Nanog-Citrine in a cell at interphase, from a dissociated embryo (methods 2.2.5.4). Scale bar = 10 μm, B.r. = 1.*

Finally, reduced clustering and loss of mitotic association were observed in fixed WT embryos overexpressing a rescuing amount of Nanog-mCitrine (**Figure 5.8**). The loss of mitotic association in fixed samples is consistent with observations that TF interactions with mitotic chromosomes are very transient and are lost upon fixation with formaldehyde (Teves et al., 2016). Nanog foci may similarly be formed by weak and transient interactions, which is supported by observations of their dynamic nature during live imaging.
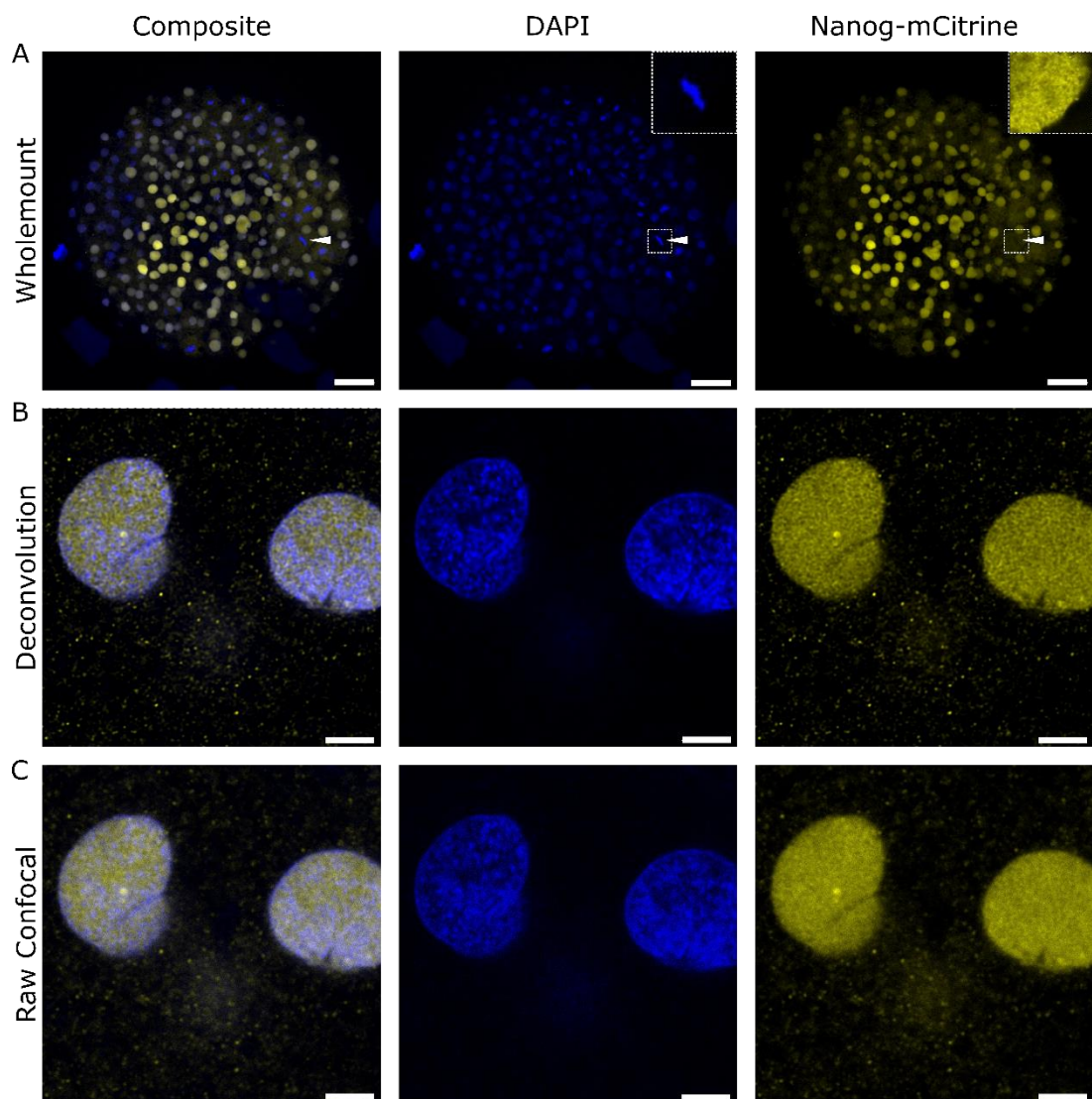
Figure 5.8 Co-localisation of Nanog-mCitrine and DNA in fixed WT embryos.

(cont. over page)

*WT embryos overexpressing Nanog-mCitrine were fixed at approx. 3 hpf (methods 2.2.6). **A)** Representative StDev projections of the z-stack wholemount image of DNA (DAPI) and Nanog-mCitrine (methods 2.4.5). Arrow indicates mitotic cell, single z-plane magnified in inset. Scale bar = 50 μm. **B)** Representative deconvolved single z-plane image of DNA (DAPI) and Nanog-mCitrine (methods 2.4.5, 2.5.2). **C)** Raw images (standard confocal mode, before deconvolution) of images in B). Scale bar = 5 μm, B.r. =1.*

5.5 Testing AAT-FRET to detect interactions at miR-430 transcription body

Next, I tested whether the Nanog-mCitrine foci also co-localise with the miR-430 transcription body. Nascent miR-430 transcripts were visualised by a fluorescently tagged MO (Hadzhiev et al., 2019, Sato et al., 2019). Nanog-mCitrine foci did not often co-localise with miR-430 foci (**Figure 5.9**). In some cases there was no miR-430 signal (**Figure 5.9**A), while in others Nanog-mCitrine foci seemed to be excluded from large miR-430 foci (**Figure 5.9**B,C), or simply independent (**Figure 5.9**D). It is likely that Nanog-mCitrine foci localise to miR-430 transcription bodies more in early interphase, or early ZGA (Hadzhiev et al., 2023, Kuznetsova et al., 2023). As the transcription body grows, the nascent miR-430 RNA may be displaced further from the gene locus, where PSN bind (Hilbert et al., 2021). Co-injected embryos were therefore followed in time-lapse imaging; Nanog-mCitrine did seem to co-localise with miR-430 more in the early cell cycle (**Figure 5.9**Ei vs. ii, iii vs. iv, **Appendix Figure 7.13**). Interactions between Nanog and Sox19b at miR-430 transcription bodies may therefore be more apparent during early interphase.
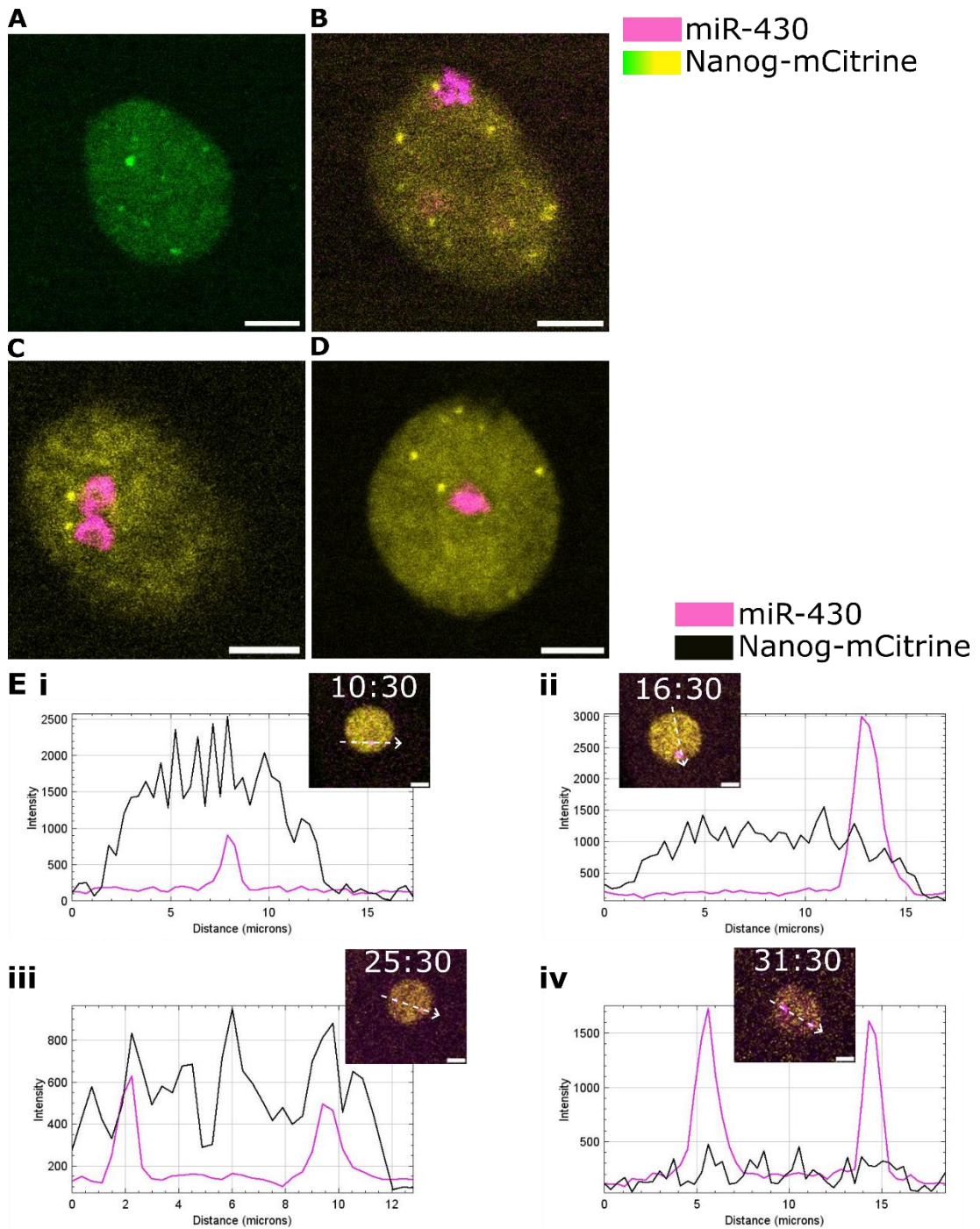
Figure 5.9 Visualising overlap of Nanog-mCitrine foci and miR-430 transcription bodies.

WT embryos co-injected with Nanog-mCitrine mRNA and Lissamine-tagged miR-430 MO. **A-D)** *Single z-plane images, taken at ZGA (methods 2.4.4), scale bar = 5 µm. B.r. =1.* **E)** *A z-stack image was acquired every 90 s during early ZGA (methods 2.4.4,* **Appendix Figure 7.13**). *(cont. over page)*

i-iv. Representative single z-plane images of nuclei at indicated time-points, from the z-stacks in Appendix Figure 7.13 (white insets), lineplots of Nanog-mCitrine and miR-430 intensities across nuclei (white arrow) (methods 2.5.2.1). Scale bar = 5 μm. B.r. =1.

Next, I tested whether co-injection of the miR-430 MO affects the Nanog-mCitrine AAT. A GeneTools blue-tagged miR-430 MO (blue miR-430 MO) was used to enable three-colour imaging with Sox19b-mCherry. miR-430 transcription bodies could be seen (**Figure 5.10**A). Images were acquired at higher magnification, and miR-430 transcription bodies were selected as ROIs (**Figure 5.10**Bi). This resulted in precise AAT values of ~ 2.1 ns for the blue miR-430 MO (**Figure 5.10**Bii-iii). However, the nuclear Nanog-mCitrine intensity was lowered in the presence of the blue miR-430 MO (**Figure 5.10**C), and the MW AAT decreased from on average 2.46 ns to 2.20 ns (**Figure 5.10**D). Brighter nuclei seemed to be less affected; removing dim nuclei resulted in less variable Nanog-mCitrine AATs, and the average MW AAT increased slightly from 2.40 ns to 2.49 ns in addition of the blue miR-430 MO (**Figure 5.10**E). The lowered Nanog-mCitrine intensity may increase AAT noise (discussed in **Paper Figure 3**). Alternatively, there may be bleed-through of the blue MO AAT into the Nanog-mCitrine AAT detection channel, contributing more prevalently in nuclei with low Nanog-mCitrine intensity to lower the overall detected AAT (**Figure 5.10**D). The blue MO may even itself FRET with mCitrine (and mCherry) (**Appendix Figure 7.14**). As the AAT of Nanog-mCitrine, even in the presence of miR-430, is reduced more when co-expressed with Sox19b-mCherry than mCherry alone (**Figure 5.2**), it may suffice to exclude low intensity nuclei as in **Figure 5.10**E to help mitigate this effect.
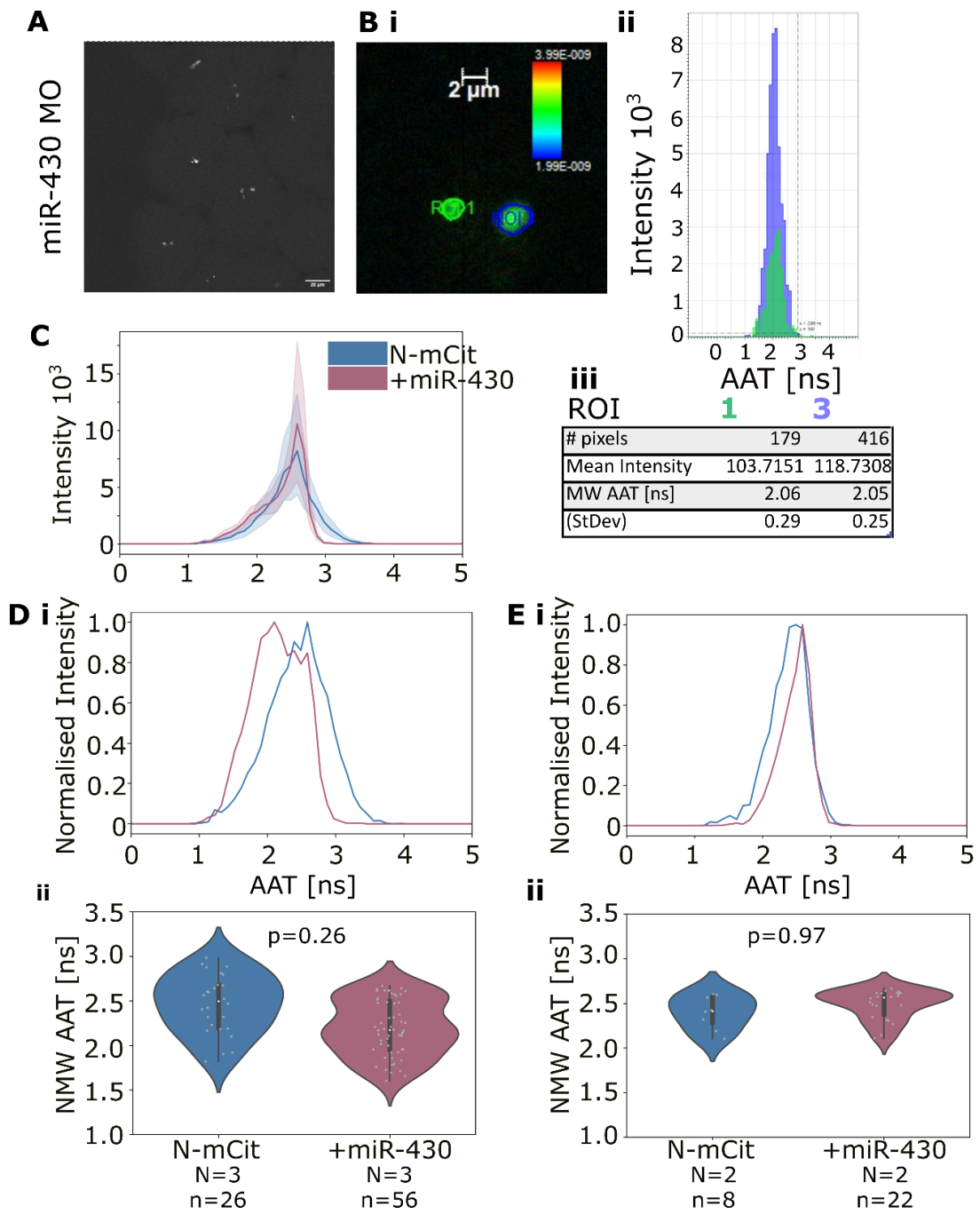
Figure 5.10 Testing AAT measurements at miR-430 transcription body.

A+B) WT embryos were microinjected with blue miR-430 MO to acquire z-stack images (methods 2.7.2.3). A) Representative z-stack projection (StDev) of miR-430 intensity, scale bar = 10 μm. B) i. Example single z-plane AAT image of miR-430 foci (ROI1: green, ROI3: blue) in a nucleus (setting B), scale bar = 2 μm, AAT range = 1-3 ns (cont. over page)

*ii. AAT histograms, and **iii.** ROI information (no. pixels, Mean ROI intensity, MW AAT in ROI, StDev of MW AAT). **C-E)** WT embryos were microinjected with mRNA encoding Nanog-mCitrine, +/- blue miR-430 MO to acquire single z-plane AAT images (methods 2.7.2.4, setting A) **C)** Non-normalised average nuclear AAT lineplots. **D)** Measurements from all nuclei. **i** Average nuclear AAT lineplots and **ii** violin plots of MW AAT. **E)** Measurements from nuclei with a mean intensity > 200. **i** Average nuclear AAT lineplots and **ii** violin plots of MW AAT. B.r. = 1, N=2-3 embryos, n=8-56 nuclei. Statistics were analysed using linear mixed effect models, and pairwise comparison of means (methods 2.8).*

Again, further SNR optimisation was attempted, at high enough magnification to get sufficient resolution for segmentation of miR-430 transcription bodies. First, yolk removal (deyolking) in addition to dechorionation increased the Nanog-mCitrine intensity compared to dechorionation alone (**Figure 5.11**A). This improved the precision of Nanog-mCitrine AAT measurements in nuclei by almost 2-fold, from an average standard deviation of nucleus MW AAT values of 0.39 to 0.19 (**Figure 5.11**Aiii). While 5X digital magnification could be used to measure the blue miR-430 MO AAT, the increased laser dose per unit area led to photobleaching of Nanog-mCitrine. Instead, 2X magnification, and a rectangular image with 512x100px enabled fast, photobleaching-free acquisition (methods 2.7.2.4 setting E1, **Appendix Figure 7.15**A).

Increasing the digital magnification highlighted a pattern of high central and low edge AAT (**Figure 5.11**B, **Appendix Figure 7.15**A). The size of the central high AAT area grew with distance from the objective (**Appendix Figure 7.15**B). While nuclei at the centre of the image could be excluded at the lower magnifications used previously (**Figure 5.1**,**Figure 5.2**), this was not possible at higher magnifications. This made Nanog-mCitrine AAT, and any differences due to FRET, impossible to distinguish from noise. This pattern seemed to increase over time, regardless of embryo preparation method, (e.g. *(figure cont. over page)*

Bii-iii, taken before Aii-iii) and interfered variably between samples, particularly in embryos with low Nanog-mCitrine intensity (**Figure 5.2**B.i vs. iii). The same problem was encountered using a higher magnification 63x oil-immersion objective (**Appendix Figure 7.16**).
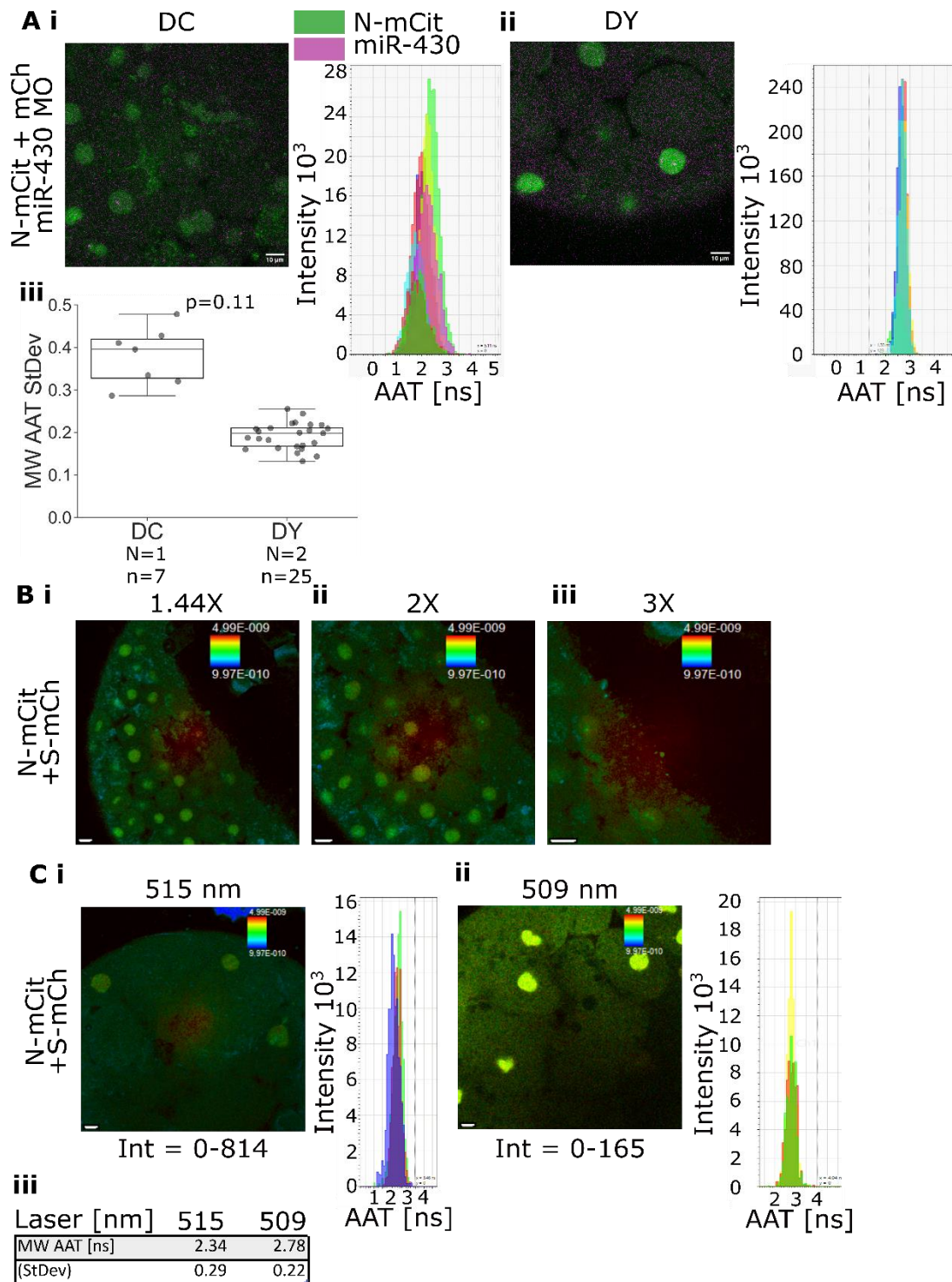
Figure 5.11 Optimisation of embryo prep and image acquisition for AAT-FRET.

(cont. over page)

A) *WT embryos co-injected with Nanog-mCitrine + mCherry mRNA, and the blue miR430 MO single z-plane images were acquired (methods 2.7.2.4, setting C).*

*Examples of **i.** a dechorionated and **ii.** a deyolked embryo, representative images of Nanog-mCitrine (green) and miR-430 MO (magenta) intensities, AAT histograms of Nanog-mCitrine (nuclear ROIs), **iii.** Boxplot of Nanog-mCitrine MW AAT StDev. N=1-2 embryos, n=8-25 nuclei. Statistics were analysed using linear mixed effect models, and pairwise comparison of means (methods 2.8). **B-C)** WT embryos co-injected with the blue miR-430 MO, and Nanog-mCitrine or Nanog-mCitrine + Sox19b-mCherry mRNA, z-stack images were acquired (methods 2.7.2.4). **B) i-iii** Representative single z-plane images of embryos co-expressing Nanog-mCitrine + Sox19b-mCherry, taken at **i.** 1.44X, **ii.** 2X, **iii.** 3X digital magnification (setting D). **C)** Representative single z-plane images of embryos co-expressing Nanog-mCitrine + Sox19b-mCherry, taken with **i.** 515 nm or **iii.** 509 nm excitation laser setting F), Nanog-mCitrine AAT histograms, **iii.** MW AAT and StDev. Scale bar = 10 μm, AAT range = 0-4 ns. B.r. = 1.*

Lower signal due to mRNA degradation was ruled out, as images were unaltered when injecting fresh mRNA. It was therefore considered whether the AAT pattern was caused by reflections from the high power (40%) laser onto the detector; no such pattern was discernible in HeLa AAT measurements, which were acquired at 1% laser power. Indeed, shifting the excitation laser and detector wavelengths further apart (and increasing line accumulation to make up for less efficient mCitrine excitation) resulted in AAT measurements closer to expected values (~2.78 ns, **Figure 5.11**C**Figure 5.12**, **Appendix Figure 7.17**A,B).

However, upon deyolking the FRET between Nanog-mCitrine and Sox19b-mCherry was lost: the MW AAT of Nanog-mCitrine remained the same across conditions, from on average 2.86 ns alone, to 2.85 ns when co-expressed with mCherry, or 2.83 ns with Sox19b-mCherry (**Figure 5.12**Ai,Bii). To determine whether this was due to sample preparation, different combinations of preparation methods and mounting media were tested for embryos across conditions (**Figure 5.12**Ai,B, **Appendix Figure 7.17**A,C). The embryo preparation method – deyolking vs. dechorionation – did in fact effect the most significant differences within conditions (**Figure 5.12**Ai). The mounting medium seemed not be relevant, as a similar trend was seen for embryos

mounted in E3 medium (**Appendix Figure 7.17**A,C, **Appendix Table 7.4**,**Appendix Table 7.5**). Deyolked embryos had comparatively larger nuclei, again regardless of mounting medium (**Figure 5.12**B, **Appendix Figure 7.17**C), indicating slowed cell division, and abnormal development (Schauer et al., 2020).

Disruptive deyolking may therefore interfere with possible biological interactions. This was confirmed by experiments with control fluorophores (Chapter 4): these behaved as expected, irrespective of embryo preparation and mounting medium (**Figure 5.12**Aii, **Appendix Figure 7.17**Bi, **Appendix Table 7.4**,**Appendix Table 7.5**). In deyolked embryos mounted in Optiprep, the average mCitrine MW AAT was 0.13-0.14 ns lower for embryos expressing tandem mCherry-mCitrine (2.65 ns) versus mCitrine alone (2.78 ns) or co-injected mCitrine + mCherry (2.79, both p<0.0001) (**Figure 5.12**Aii, **Appendix Table 7.4**,**Appendix Table 7.5**). Thus, improved embryo manipulation would be required to take advantage of the increased SNR in deyolked embryos, in order to continue optimising higher-magnification AAT-FRET measurements at the miR-430 transcription body.
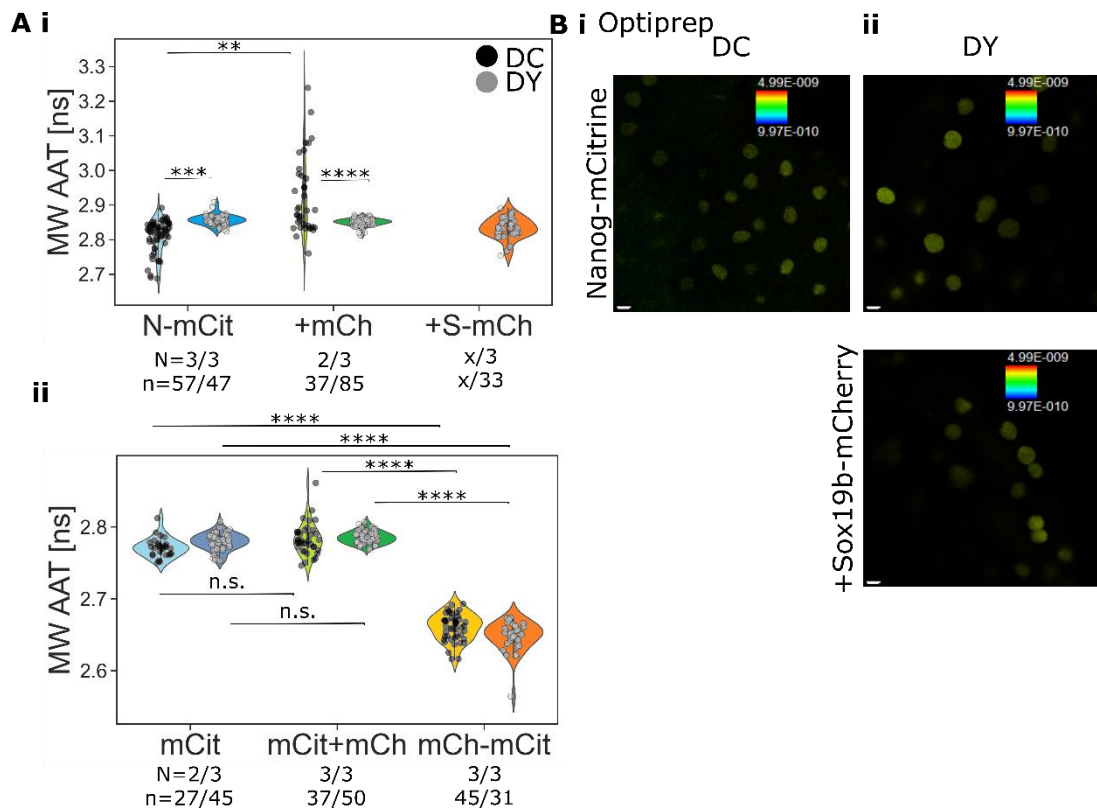
Figure 5.12 Effect of deyolking on control versus biological interactions.

WT embryos were injected with mRNA encoding control (mCitrine, tandem mCherry-mCitrine, or separate mCherry + mCitrine) or SN conditions (Nanog-mCitrine or Nanog-mCitrine + Sox19b-mCherry). Single z-plane image were acquired for deyolked (DY) or dechorionated (DC) embryos mounted in optiprep (methods 2.7.2.4, setting F, 509 nm laser). ***A)*** *Violin plots of MW AAT for* ***i.*** *control conditions,* ***ii.*** *SN conditions.* ***B)*** *Representative AAT images of SN condition embryos* ***i.*** *DC or* ***ii.*** *DY. Scale bar = 10 μm, AAT range = 0-4 ns. B.r.= 1, N=2-3 embryos, n=27-85 nuclei. Statistics were analysed using linear mixed effect models, and pairwise comparison of means (methods 2.8).*

5.6 Discussion

5.6.1 AAT-FRET measurements require higher SNR to confidently show Nanog-mCitrine and Sox19b-mCherry interact during ZGA

AAT-FRET did give some indication that SN interact during zebrafish ZGA. The MW AAT of Nanog-mCitrine decreased, at main ZGA, in the presence of Sox19b-mCherry in embryos that were in the chorion (**Figure 5.1**). However, detection was challenging in this system, as low SNR caused high variability in AAT values (**Figure 5.1**). This limited the conclusions that could be drawn for early ZGA, and reduced significance of the AAT shift at main ZGA. Perhaps a combination of brighter new-generation fluorophores would have provided higher SNR - mNeonGreen for example is brighter and more photostable than mCitrine (Shaner et al., 2013), and forms a better FRET pair with mScarlet I than mCherry (Bindels et al., 2017, McCullock et al., 2020). FRET may also be detected more clearly by AAT in dechorionated embryos (**Figure 5.2**), yet only one b.r. could be completed, in which embryos were co-injected with the blue miR-430 MO (**Figure 5.10** – further discussed in section 5.6.3).

Indeed, the AAT decreased 2-fold more in these dechorionated embryos co-expressing Nanog-mCitrine plus Sox19b-mCherry, than for dechorionated embryos expressing tandem mCherry-mCitrine (**Figure 5.2**, **Paper Figure 4**). As any potential interactions should cause less frequent and lower efficiency FRET than tandem-fused fluorophores, it could be that the fused fluorophores were not optimally oriented, and thus would require a more flexible linker to increase FRET efficiency. Given more time, the SN experiments should be repeated with the 509 nm excitation laser, to show that the lowered Nanog-mCitrine AAT, when co-expressed with Sox19b-mChery, is not simply due to noise caused by laser reflection (**Figure 5.11**). Similarly, AccPb and SE-FRET assays (**Paper Figures 1, 4, Suppl. Figure 1**) should be done to verify that the AAT shift seen for Nanog-mCitrine is indeed due to FRET with Sox19b-mCherry.

AAT-FRET did not detect Nanog-mCitrine and mCherry-Pou5f3 interaction in zebrafish embryos or HeLa cells (**Appendix Figure 7.9**,**Appendix Figure 7.11**). Yet others have shown by FLIM-FRET that Nanog and Pou5f3 interact in zebrafish embryos, albeit during late ZGA (Perez-Camps et al., 2016). Perhaps these PTFs do not interact during main ZGA. However, to confirm that AAT does not simply lack the resolution to see the small τ-shift of a low proportion of donor molecules, experiments could be done in double mutant MZ*nanog;spg793* embryos to raise the frequency of Nanog-Pou5f3 interactions. An orthogonal technique such as co-immunoprecipitation would be needed to validate PSN interactions.

5.6.2 Nanog and Sox19b interactions in HeLa cells may be affected by DNA binding ability

Experiments in HeLa cells verified that SN could in principle interact (**Figure 5.3**), and that this may depend to a degree on their DBD (**Figure 5.4**). The NΔN mutant had less effect on interactions with Sox19b-mCherry than the NΔH mutant, and neither entirely abolished FRET, raising the question of whether SN form freely diffusing dimers which subsequently bind to DNA, or whether there is hierarchical DNA binding – for example Nanog may recruit Sox19b to form DNA-bound complexes.

Although less frequent, interactions between WT/DBD mutant SN are indeed enriched in foci. These foci are most prevalent when either DBD is lost, are largest for NΔH, but SΔH foci seem to grow in the presence of WT Nanog-mCitrine. This suggests that SN interaction in HeLa cells is not necessarily scaffolded by DNA; interactions of probably freely diffusing SN are maintained without DBDs. Transfection of lower DNA concentrations might show to what extent the foci are an overexpression artefact. Interactions between SΔH and NΔH should also be tested.

This system could be used to carry out FCCS, with a suitable fluorophore pair, to measure the proportion of freely-diffusing versus DNA-bound interacting molecules with different WT/DBD mutant combinations. Importantly, experiments with point

mutations to disrupt each PTF's DNA binding would confirm that loss of interaction and change in nuclear distribution is not due to larger-scale disruption caused by the loss of the entire DBD. Constructs were made with point mutations predicted by homology modelling to abolish DNA binding, without destabilising the proteins. There was not enough time to confirm mutants by EMSA, before carrying out AAT-FRET experiments.

The loss of Nanog's N-terminus less significantly reduces the proportion of SN interaction (**Figure 5.4**), but the remaining interactions are not visibly regionalised into foci (**Figure 5.5**). Perhaps the IDR or W enrichment increase the propensity of foci which are seeded by either a specific DNA interaction (e.g. zebrafish miR-430 transcription bodies) or non-specific sequestration. Interactions with Sox19b could be enriched here due to the high availability of interaction partners. To further dissect the role of Nanog IDR/ W enrichment and DBD in foci formation and Sox19b interactions, the N- and C- termini should be mutated by substituting W residues (Mullin et al., 2017), or removing just the IDR. These should be tested in combination with DNA binding point mutations. AAT-FRET and FCS could confirm whether zebrafish Nanog forms dimers and/or oligomers.

However, HeLa cells are an immortalised cancer cell line with extensive chromosomes disruptions including rearrangements and chromothripsis (Landry et al., 2013), as well as different TF-chromatin binding profiles (Jing et al., 2018). This altered biology could result in under- or misrepresentation of Nanog and Sox19b chromatin binding and interactions. Thus a more biologically relevant *in vitro* system could have been ESCs, were mammalian homologs of zebrafish Nanog and Sox19b bind and regulate gene expression (Avilion et al., 2003, Chambers et al., 2003). Most importantly, once relevant mutations are confirmed in HeLa assays, they should be tested in zebrafish embryos to confirm that these changes in SN interactions and distribution are relevant to zebrafish ZGA (Kuznetsova et al., 2023).

5.6.3 Testing Nanog and Sox19b interactions at miR-430 transcription bodies by AAT-FRET is limited by SNR and choice of MO labels

Nanog-(m)Citrine and Sox19-mCherry form foci (**Figure 5.6**, **Appendix Figure 7.12**), however Nanog-mCitrine foci rarely overlap the MO-labelled miR-430 transcription bodies (**Figure 5.9**). As suggested, this could be as the nascent RNA is displaced from the miR-430 locus with time. To test this, more images should be acquired at high resolution to measure whether the miR-430 MO foci tend to be adjacent to Nanog foci, rather than randomly distributed – this could be assessed using Ripley's K function. Perhaps PSN interact more during early interphase – especially at the miR-430 transcription body. This would best be investigated by a time-lapse of AAT-FRET measurements across cell cycles, as it would be difficult to accurately stage and select only early interphase during microscopy. Without a consistent DNA dye, staging would need to be done by nuclear morphology, and there would be a very short time-window due to the fast cell cycles.

Acquisition settings were optimised to image miR-430 transcription bodies at higher magnification: 512x100px images, taken at 2X magnification allowed segmentation of miR-430 foci (methods 2.7.2.4 setting E1, **Appendix Figure 7.15**). However, increasing magnification focused on a background AAT pattern, so that noise impeded further imaging. This was later resolved by increasing the separation between laser line and detector wavelengths (**Figure 5.11**). Additionally, although deyolking embryos improved the SNR, in my hands this also disrupted cell division and possible SN interactions (**Figure 5.12**). These challenges delayed experiments, and could not be entirely resolved.

If pursued further, many improvements would be required including; ensuring that miR-430 transcription bodies with co-localised SN are captured at higher frequency (e.g. in early interphase); acquiring images with sufficient SNR either by more skilled deyolking, dissociating embryos, or SPIM microscopy; testing a higher magnification silicon-immersion objective to improve resolution for miR-430 ROIs while maintaining a large working distance.

Finally, the miR-430 MO could be labelled with a more spectrally distinct fluorophore, as the blue MO emission spectrum overlaps significantly with the excitation spectrum of both mCitrine and mCherry (**Appendix Figure 7.14**). FRET between the MO and mCitrine could explain the lowered Nanog-mCitrine intensity and AAT (**Figure 5.10**). As mentioned in section 5.6.1, the blue miR-430 MO may even FRET more with mCherry than mCitrine. However, this was compared in whole nuclei ROIs where Nanog-mCitrine foci rarely overlap with miR-430 transcription bodies. Any FRET would therefore be mostly with 'background' MOs that are not labelling nascent miR-430 transcripts. Further, as the AAT of Nanog-mCitrine decreased more in the presence of Sox19b-mCherry than mCherry alone (**Figure 5.2**), the blue MO may not interfere with specific FRET between Nanog-mCitrine and Sox19b-mCherry. Assays suggested in section 5.6.1 could verify this. Tagging the miR-430 MO with a more spectrally distinct fluorophore, for example in the far-red spectrum, would be challenging as GeneTools offer a limited selection of fluorophores to label their MOs.

To conclude, these experiments show that SN may interact during zebrafish ZGA, and their interaction in HeLa cells partially depends on either DBD, as well as Nanog's N-terminus. Further investigation into the mode of interaction and its dependence on PSN-DNA binding and Nanog's IDR/W enrichment during zebrafish ZGA, or their interaction in miR-430 transcription bodies, would require substantially more work which was outside the scope of this thesis.

6 Concluding remarks

The first aim of my thesis was to study the chromatin binding of PTFs Pou5f3, Sox19b, and Nanog, while they regulate the onset of transcription during ZGA in zebrafish (Lee et al., 2013, Leichsenring et al., 2013). TF-chromatin binding dynamics may be linked to their activity; DNA residence time is linked to transcriptional output (Callegari et al., 2019, Trojanowski et al., 2022). The dynamics of PTF-chromatin binding could also reflect their chromatin-opening activity: in mouse embryogenesis PTFs SOX2 and OCT4 (mammalian homologs of zebrafish Sox19b and Pou5f3) display more stable chromatin binding, while chromatin accessibility increases (Gao et al., 2018, Ladstatter and Tachibana, 2019, Li et al., 2018, Wu et al., 2016). Measuring the chromatin binding dynamics of PSN throughout ZGA could give insight into the mechanisms by which PTFs make chromatin permissible for transcription.

TF diffusion and interactions have not been studied extensively in zebrafish – let alone during early/main ZGA (**Table 3.1**,**Table 3.2**) (Perez-Camps et al., 2016). I therefore began by testing whether PSN chromatin binding dynamics could be measured in live zebrafish embryos during ZGA using FCS. This method was chosen as it does not require sparse labelling, or extremely high SNR, as compared to SMT (section 1.3.2).

However FCS measurements in zebrafish embryos were challenging, in part due to the choice of fluorophores, but mainly because the fast development and low SNR of the early embryos severely restricted measurement quality and throughput. To an extent, I was able to improve measurements and analysis by choosing fluorophore-specific fitting models (section 3.4) and using rescued MZ mutant -/- embryos rather than WT overexpression (section 3.2,3.5). The average ACFs showed that Nanog-Citrine displayed slightly slower diffusion than mCherry-Pou5f3 during ZGA, and that both Nanog and Pou5f3 diffusion became a little slower in main versus early ZGA (**Figure 3.8**). Yet this was not reflected significantly in the $\tau_D$slow and ρslow values derived from fitting, perhaps because the few optimised FCS measurements I managed to complete were very variable. As discussed in section

3.7.3, measurement acquisition would need to be further improved in order to distinguish biological variability from noise. By comparison, it is arguably simpler to identify the difference of SOX2 chromatin binding between nuclei in slower developing mouse embryos with only 2 to 32 cells. In zebrafish, mpFCS diffusion maps (Krmpot et al., 2019) would help to investigate spatial patterns in PSN behaviour across embryo regions.

However, my experiments suggested that FCS was not the most suitable method to investigate PSN chromatin binding in zebrafish ZGA. I could not conclude whether Nanog and Pou5f3 simply do not display any characteristic chromatin binding or binding-site search dynamics during ZGA, whether noisy measurements in the zebrafish embryos hindered accurate detection of PSN chromatin-bound diffusion, or whether FCS could not quantify the range of their chromatin binding dynamics. To disentangle this, the diffusion of a non-pioneer TF versus a PTF could be compared by FCS in zebrafish embryos, and in cells *in vitro*. Ideally, further experiments to investigate how PSN interact dynamically with chromatin during zebrafish ZGA should be carried out using SMT, with photoactivatable fluorescent tags, and more specialised microscopy techniques such as SPIM to improve optical sectioning and SNR.

My second aim was to determine whether PSN interact during ZGA. At some ZGA genes, these PTFs jointly affect chromatin accessibility (Miao et al., 2022). The earliest transcribed ZGA gene, miR-430, requires PSN (Hadzhiev et al., 2023, Lee et al., 2013), and it has recently been suggested that Nanog drives the formation of miR-430 transcription bodies, to which Sox19b co-localises (Kuznetsova et al., 2023). I therefore wanted to investigate whether PSN interact directly, and whether this involved chromatin binding. This could improve our understanding of how (P)TFs work together to make chromatin accessible for transcription. While (m)Citrine and mCherry transpired not to be a suitable fluorophore pair to investigate PSN co-diffusion by FCCS (section 3.6), I was able to probe interactions between mCitrine- and mCherry-tagged PSN by FRET.

I used a non-fitting version of FLIM, termed AAT, to detect FRET (Roberti 2020). I optimised image acquisition to obtain τ-based AAT values per pixel in zebrafish embryos (**Paper Figure 3**, section 1.3.6.1). A small 0.16 ns AAT shift was seen upon FRET between control fluorophores in embryos (**Paper Figuress. 4,5**). This encouraged me to use AAT-FRET to explore interactions between Nanog-mCitrine and Sox19b-mCherry during ZGA. While I did see SN interactions during main ZGA (**Figure 5.1Figure 5.2**), I could not detect interactions between Nanog-mCitrine and mCherry-Pou5f3.

Previous work suggests that Nanog and Pou5f3 may interact to an extent: studies have shown a balance of cooperation and competition between gene regulation by Pou5f3 and Nanog, which co-regulate ventral specification via BMP and Vox (Perez-Camps et al., 2016, Veil et al., 2018), but have opposing roles in Her3 expression: Nanog represses and Pou5f3 activates. However this antagonism was shown to take place via separate regulatory elements (Onichtchouk et al., 2010, Veil et al., 2018). This suggests that Nanog and Pou5f3 might only interact directly at a subset of their target sites. To ensure that interactions between fluorescently tagged PSN are not diluted by interactions with their endogenous counterparts, experiments should be carried out in double mutant MZ -/- embryos. This improved experimental setup may in particular show more clearly whether Nanog and Pou5f3 interact. It would further be interesting to test interactions between Sox19b and Pou5f3, although recent work suggests that they mostly act independently to increase chromatin accessibility (Gao et al., 2022). In addition to AccPb assays, monitoring whether increasing the acceptor concentration affects the donor AAT shift, would confirm interactions.

Further experiments, especially to detect interactions at the miR-430 locus, were stalled by technical issues (sections 5.2,5.5). In future experiments, FRET detection could be improved by choosing a brighter fluorophore pair with a larger shift in donor τ upon FRET, for example mNeonGreen and mScarlet I (McCullock et al., 2020). Using SPIM could improve the SNR without the need for deyolking embryos.

To investigate SN interactions specifically at the miR-430 locus, far-red MO labels should be explored, and a high-magnification objective with low NA, such as silicon immersion objectives, should be used.

I was able to show that SN can, in principle, interact in HeLa cells (**Figure 5.3**), and that their interaction may to some extent rely on their DBDs, and Nanog's N-terminus (**Figure 5.4**,**Figure 5.5**). Improvements to FRET detection sensitivity are required to carry out parallel experiments in zebrafish embryos

The processing of 4D data in Lattice Light Sheet Microscopy (LLSM) intensity-FRET (O'Shaughnessy et al., 2019) coupled to FLIM, such as SPIM-FLIM (Funane et al., 2018), would, as discussed improve the SNR, but also allow the creation of FLIM-FRET maps to examine PSN interactions across zebrafish embryos. Combining this with TCSPC would be optimal, to improve the τ resolution. Building an array of SPAD detectors significantly speeds up TCSPC-FLIM acquisition, as shown in multiphoton FLIM of a GTPase biosensor in zebrafish larvae (Poland et al., 2014). Alternative non-fitting τ calculations should also be explored, as these perform better than fitting in lower SNR (section 1.3.6.1). For example, τ can be calculated from photons collected in two overlapping time gates, using machine learning algorithms (Li et al., 2012, Zang, 2022). Preliminary experiments showed that this was possible on the Stellaris, but could not be continued due to time constraints.

Perhaps imaging methods orthogonal to FRET would be better suited to the low SNR of zebrafish embryos: emerging imaging methods to probe protein-protein interactions, such as proximity-assisted photoactivation (PAPA) combined with SMT (Graham et al., 2022) may be less hampered by noise, and could be tested to explore the interplay of PSN interaction and chromatin binding dynamics.

Finally, a wider range of fluorophore tags should be tested for PSN, not only to find more suitable fluorophores for FCS, FCCS, or FRET. I showed that Nanog and Pou5f3 are sensitive to the position and composition of the tag (**Figure 3.1**). This may be linked to intrinsic fluorophore properties; mCherry may aggregate, and slower diffusion was measured in initial FCS experiments (**Figure 3.5**); Citrine may increase

the propensity of PSN to form foci (**Figure 5.6**). Interestingly, mCherry-Pou5f3 rescued MZ*spg793* -/- embryos significantly better than Citrine-Pou5f3, while only Citrine-Pou5f3 displayed clusters. The interplay of fluorophores effects on PSN dynamics, aggregation, and foci formation should therefore be examined. RT-qPCR and Western blot could indicate changes to mRNA and/or protein stability, and DNA binding could be tested by EMSAs. Different forms of monomeric tags, with PSN expressed at different levels, as well as endogenously, could show to what extent the observed foci reflect the endogenous PSN behaviour.

Overall, I have shown that measurements of PSN chromatin-binding and interactions are very challenging in low-SNR systems such as live zebrafish embryos. Nevertheless, I have shown that AAT-FRET can be a useful semi-quantitative method to probe interactions, and used this in HeLa cells to show that Nanog and Sox19b can in principle interact. Equipment and sample preparation, and choice of fluorophores, are all important parameters for successful quantitative fluorescence microscopy. Improvements in these areas would capacitate future studies of PSN interactions and chromatin binding during zebrafish ZGA, including correlations between these activities and subsequent differentiation.

7 Appendix

Appendix Table 7.1 P-values for Figure 3.1

Comparison			p.val	sign
Cit-Pou5f3	vs	mCh-Pou5f3	0.0104	*
Cit-Pou5f3	vs	Pou5f3	0.0091	**
Cit-Pou5f3	vs	Pou5f3-Cit	0.0836	*
mCh-Pou5f3	vs	Pou5f3	0.9879	ns
mCh-Pou5f3	vs	Pou5f3-Cit	0.034	*
Pou5f3	vs	Pou5f3-Cit	0.0303	*
Cit-Nanog	vs	mCh-Nanog	0.9381	ns
Cit-Nanog	vs	Nanog	0.096	ns
Cit-Nanog	vs	Nanog-Cit	0.9685	ns
Cit-Nanog	vs	Nanog-mCh	0.9623	ns
Cit-Nanog	vs	Nanog-mCit	0.9047	ns
mCh-Nanog	vs	Nanog	0.0112	*
mCh-Nanog	vs	Nanog-Cit	0.5334	ns
mCh-Nanog	vs	Nanog-mCh	1	ns
mCh-Nanog	vs	Nanog-mCit	0.4264	ns
Nanog	vs	Nanog-Cit	0.2797	ns
Nanog	vs	Nanog-mCh	0.0145	*
Nanog	vs	Nanog-mCit	0.588	ns
Nanog-Cit	vs	Nanog-mCh	0.5989	ns
Nanog-Cit	vs	Nanog-mCit	0.9996	ns
Nanog-mCh	vs	Nanog-mCit	0.4838	ns
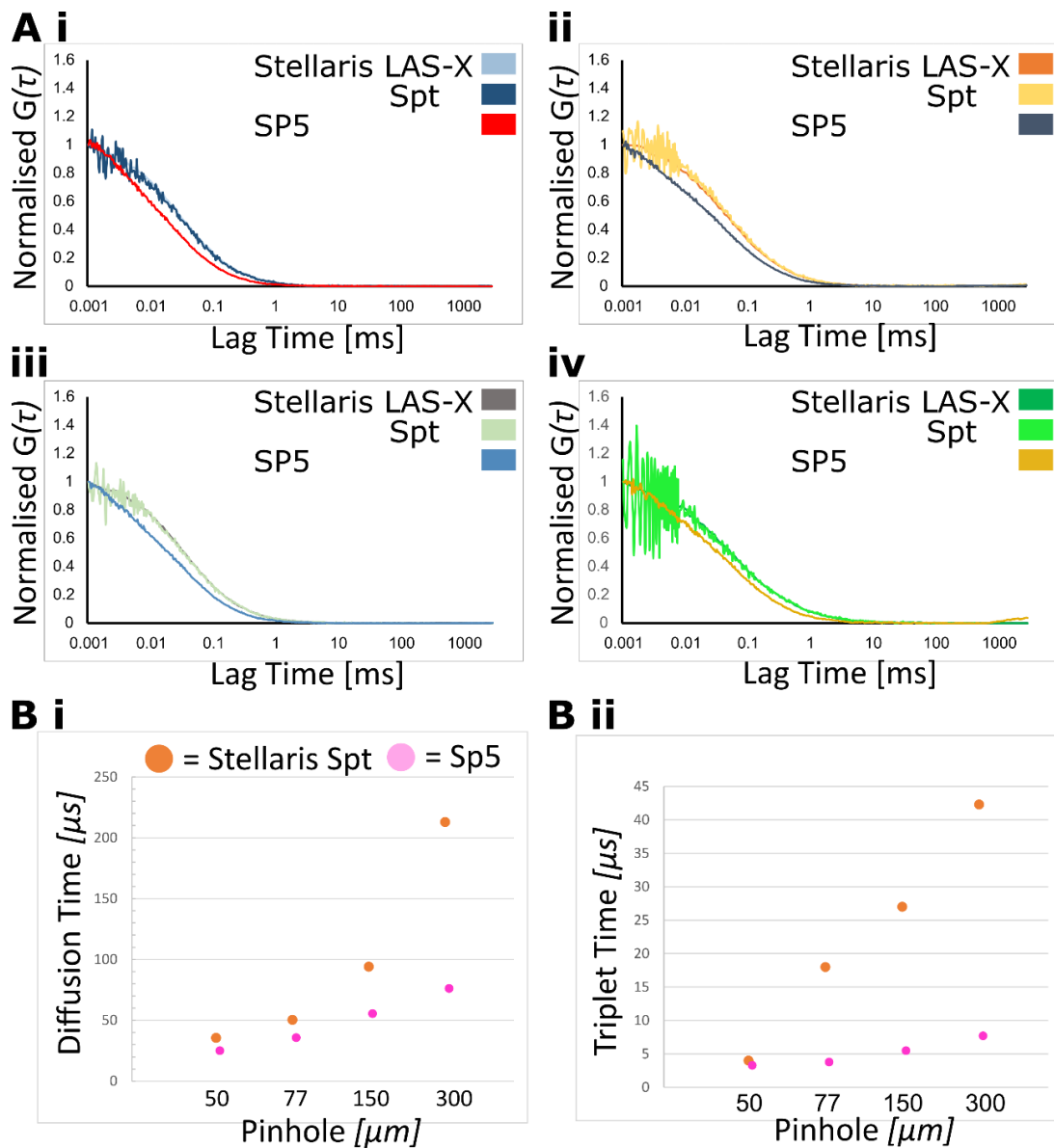
Appendix Figure 7.1 Comparison of FCS measurements on Stellaris 8 versus Sp5 confocal microscopes.

*In vitro FCS measurements were carried out at different pinhole sizes for Alexa 488, using the Stellaris 8 or Sp5 microscope (methods 2.6.6.2). ACFs were calculated in LAS-X or SymPhoTime (Spt) software, and fit in Spt. **A)** Normalised ACFs for Alexa 488 at **i.** 50 μm, **ii.** 77 μm (1 Airy Unit), **iii.** 150 μm, **iv.** 300 μm pinhole sizes. **B)** Plots of fitted values for Alexa 488 **i.** diffusion (τ_D) and **ii.** triplet (τ_{Trip}) time.*
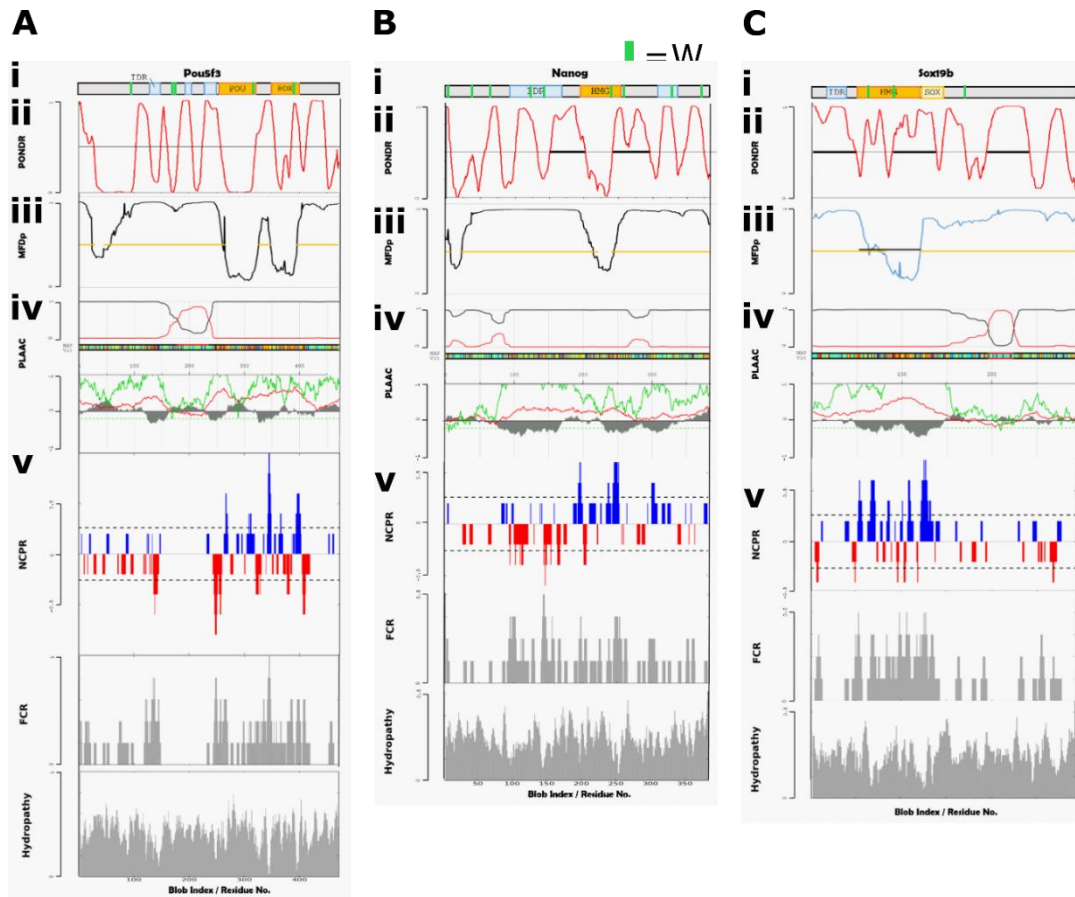
Appendix Figure 7.2 Sequence-based analysis of A) Pou5f3, B) Nanog and C) Sox19b.

i. Schematic representation of domain structure using Pfam for DNA binding domains/motifs (orange) and MobiDB Lite for predicted intrinsically disordered regions (IDRs, blue) (Necci et al., 2017). Positions of tryptophan residues (W) are indicated by green lines. ii. PONDR and iii. MFDp are additional predictors of IDRs (Mizianty et al., 2010, Romero et al., 2004). iv. PLAAC predicts prion-like regions (overlap of red/black lines), intrinsic disorder (PLAAC – red line, PAPA – green line, and the Fold Index (grey area, positive indicates folding) (Lancaster et al., 2014). v. CIDER analyses; NCPR shows Net Charge Per Residue (averaged across a sliding window of 10 residues); FCR shows Fraction of Charged Residues; Hydrophathy (Das and Pappu, 2013).
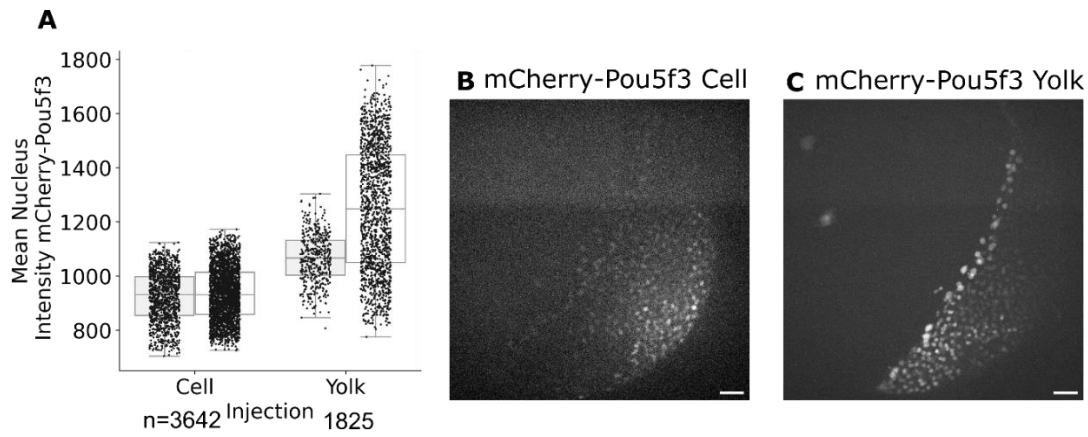
Appendix Figure 7.3 Comparison of injection region for PSN distribution.

*WT embryos microinjected with mRNA encoding mCherry-Pou5f3, into the cell or the yolk (methods 2.4.1). **A)** Box plots of mCherry-Pou5f3 mean nuclear intensity. **B+C)** Representative images, of StDev projections for z-stack images. Scale bar = 50 μm. B.r.=1, N=2 embryos, n=1825-3642 nuclei.*

A - multi point FCS (mpFCS)

Illumination matrix | Fluorescence | Concentration | Diffusion map

B — Nanog-Citrine

C — Sox19b-Citrine

D — Citrine-Pou5f3

G(τ) vs Lag time (ms)
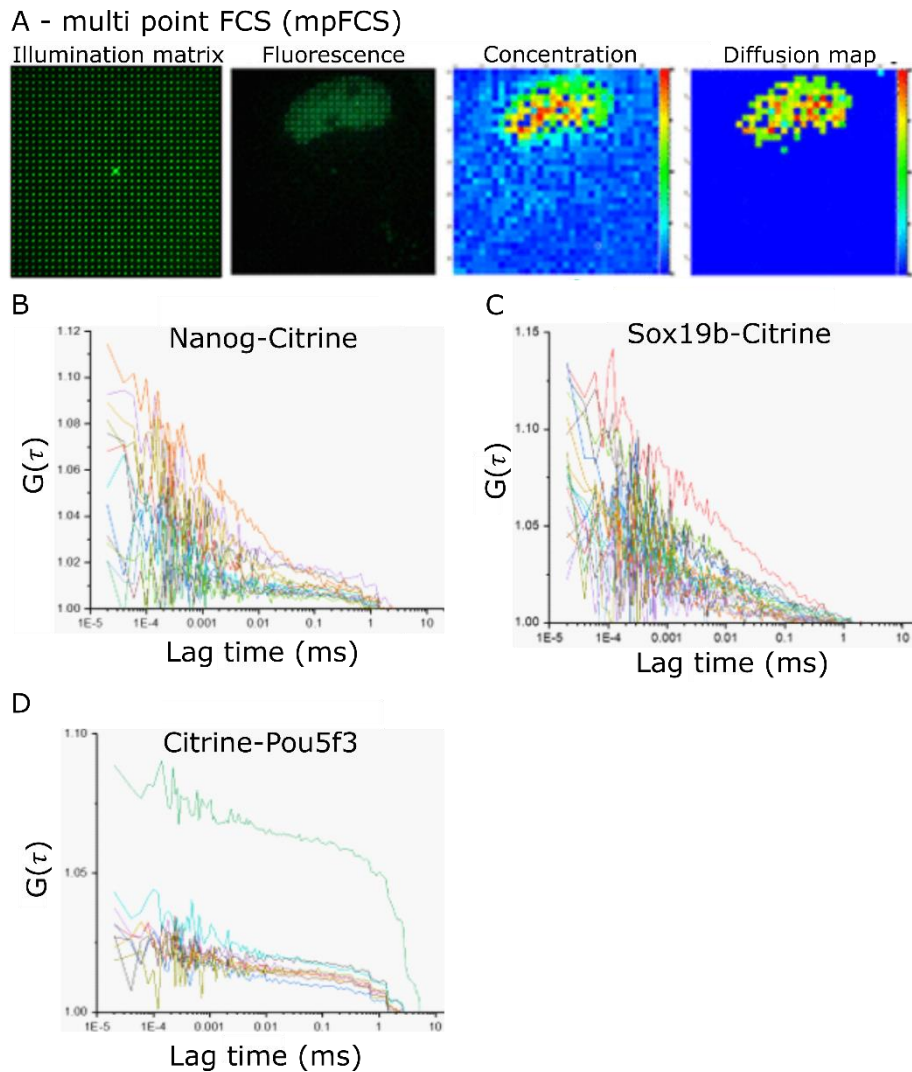
Appendix Figure 7.4 Preliminary multi-point FCS measurements for PSN.

A) Schematic of the illumination matrix used in multi-point (mpFCS), and the outputs: fluorescence intensity, calculated maps of concentration/ diffusion, taken from (Krmpot et al., 2019). B-D) ACFs from mpFCS carried out in WT embryos overexpressing B) Nanog-Citrine, C) Sox19b-Citrine, or D) Citrine-Pou5f3 (methods 2.6.6.3.) Preliminary mpFCS experiments were carried out by J.S., D.P., and S.O. in collaboration with V.V., at the KI Stockholm.

196
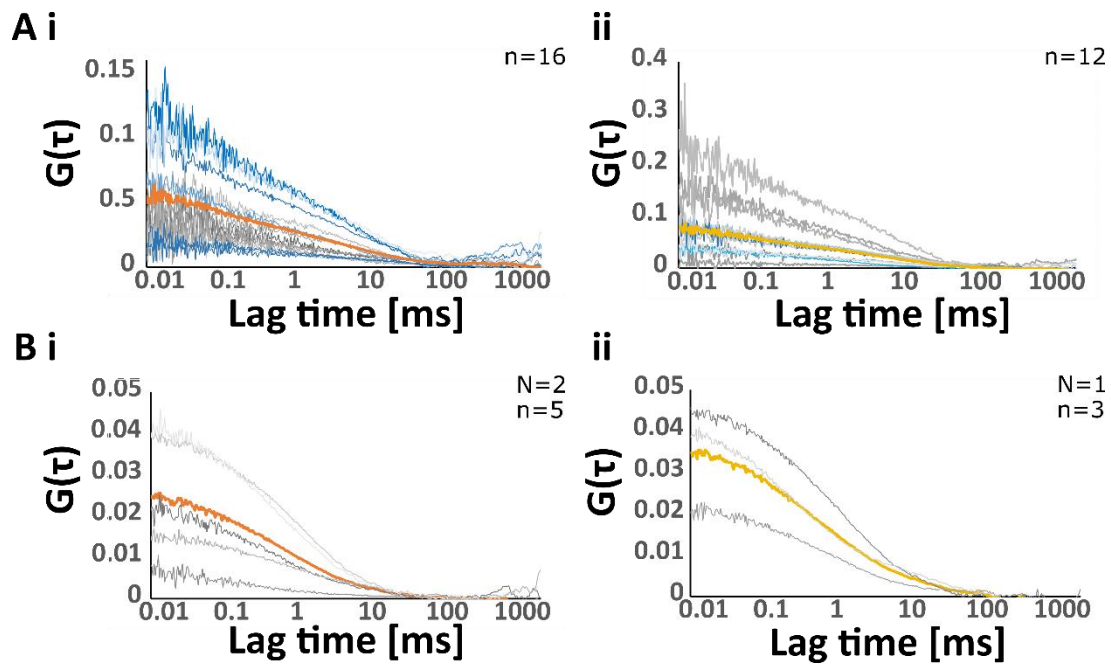
Appendix Figure 7.5 Nanog-Citrine and mCherry-Pou5f3 diffusion measured by FCS in rescued MZ mutant embryos (accompanies Figure 3.8).

*FCS measurements in MZnanog -/- or MZspg -/- embryos rescued with Nanog-Citrine or mCherry-Pou5f3 mRNA, respectively (methods 2.6). **A)** Raw (blue or grey by b.r.) and average (orange) ACFs for Nanog-Citrine at i. early and ii. main ZGA. **B)** Raw (grey) and average (orange) ACFs for mCherry-Pou5f3 at i. early and ii. main ZGA. B.r. = 2 for Nanog-Citrine 1 for mCherry-Pou5f3. N=1-2 embryos for mCherry-Pou5f3 (Nanog-Citrine not recorded), n= 3-16 nuclei.*
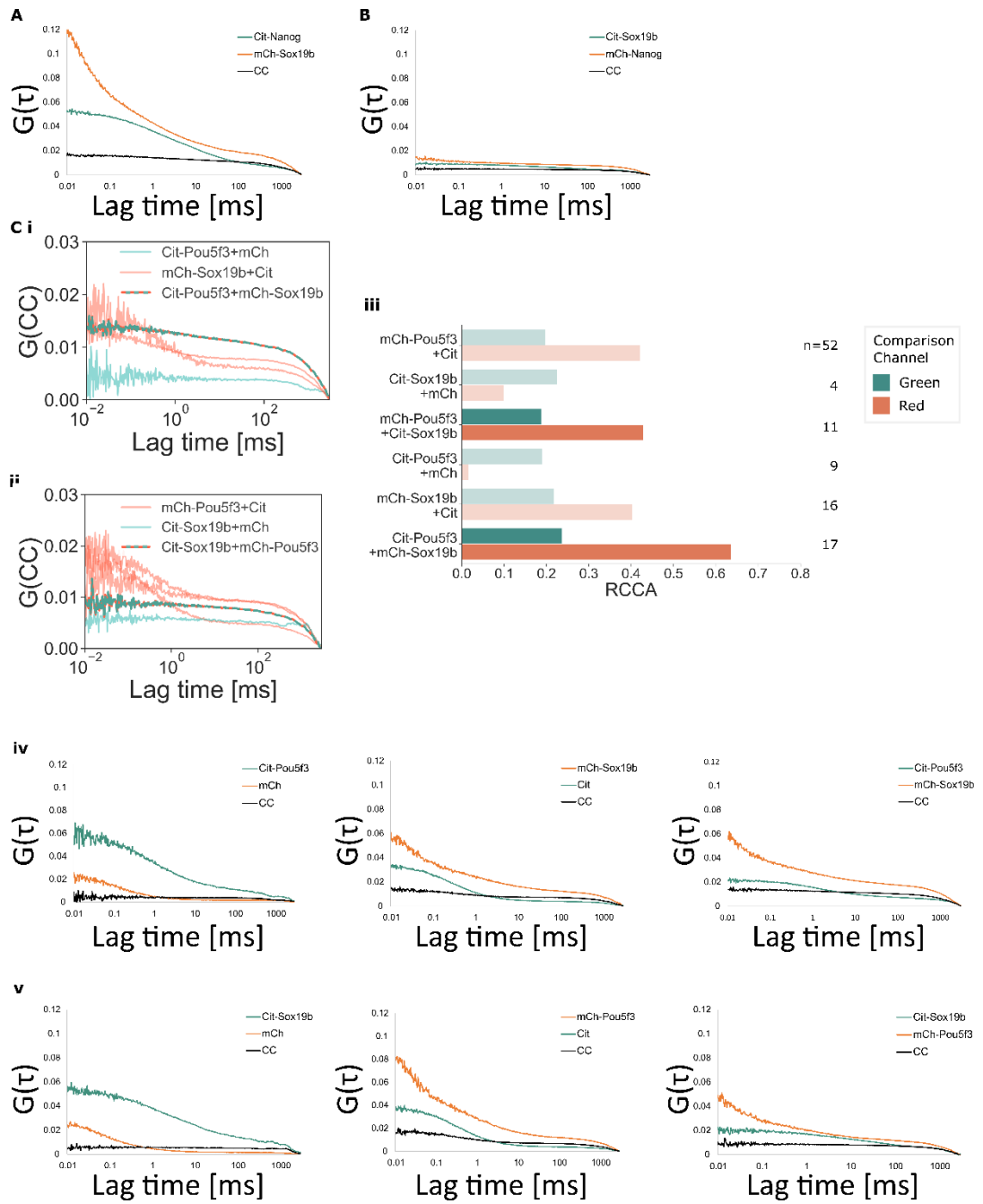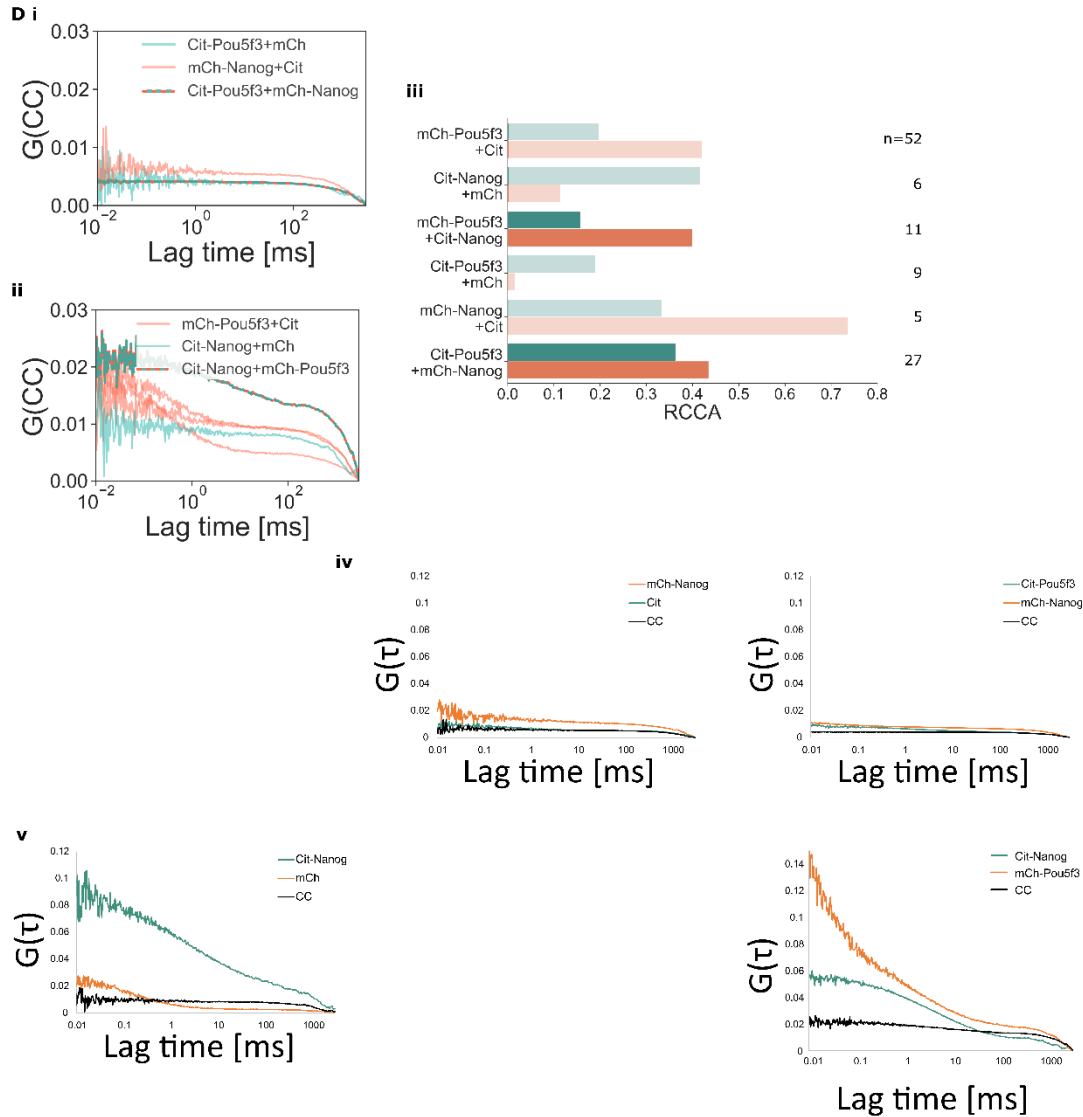
Appendix Figure 7.6 PSN interactions measured by FCCS (accompanies Figure 3.9)

*FCCS measurements were carried out at main ZGA (methods 2.6), in WT embryos expressing Citrine (Cit)/mCherry (mCh)-tagged PSN in pairs or individually with the opposite Citrine/mCherry fluorophore as controls. **A+B)** Average ACFs and CCFs for **A)** Citrine-Nanog + mCherry-Sox19b and **B)** mCherry-Nanog + Citrine-Sox19b. **C+D)** Opposite tag combinations for **C)** Pou5f3 + Sox19b and **D)** Pou5f3 + Nanog, **i.+ii.** Average CCFs for controls and PSN pairs, **iii.** Barplots of RCCAs calculated from **iv.+v** (methods 2.6.3). Average ACFs and CCFs per condition. n=4-52 nuclei.*
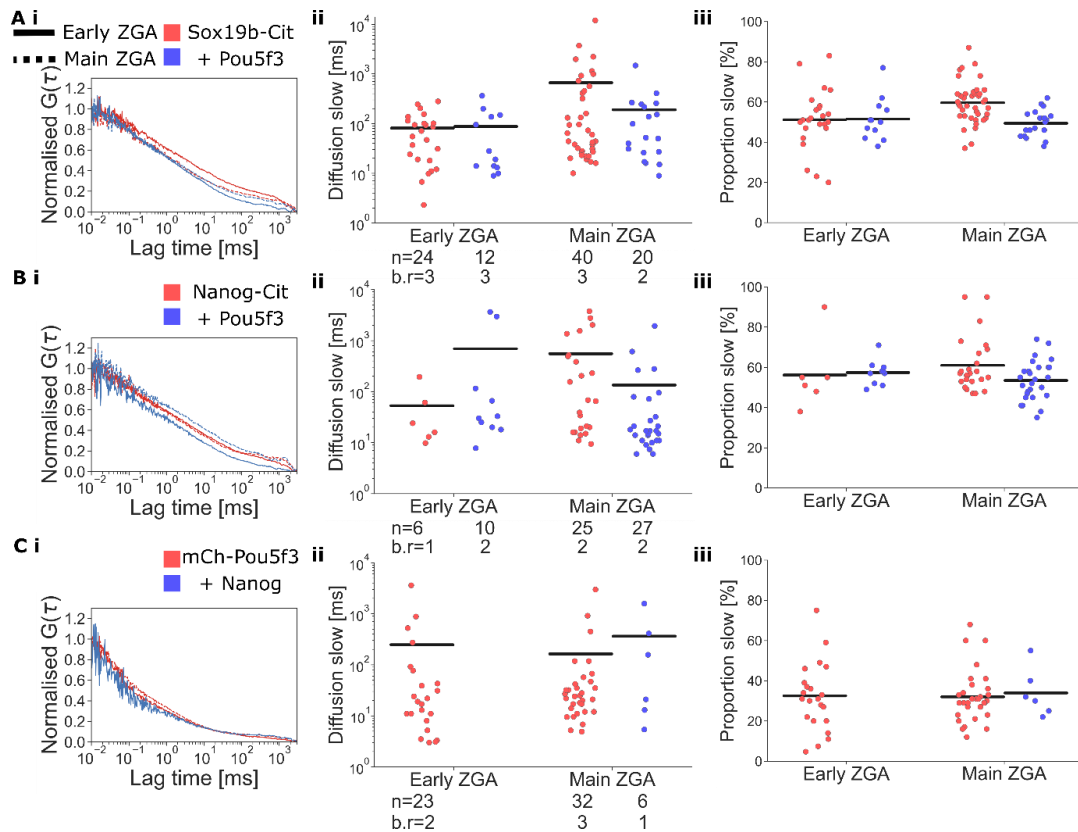
Appendix Figure 7.7 Indirect measurement of PSN interactions by FCS (accompanies Figure 3.11).

*Measurements were carried out in WT embryos expressing tagged PSN +/- untagged PSN, at early and main stage ZGA (methods 2.6). **A-C) i.** Normalised average ACFs **ii.** Scatterplots of fitted values for $\tau_D slow$ and **iii.** $\rho slow$, for **A)** Sox19b-Cit +/-/ Pou5f3, **B)** Nanog-Cit +/- Pou5f3, **C)** mCh-Pou5f3 +/- Nanog. B.r. =1-3 experimental days, n=6-32 nuclei. Statistics were analysed using linear mixed effect models, and pairwise comparison of means (methods 2.8), all n.s. (p>0.05).*
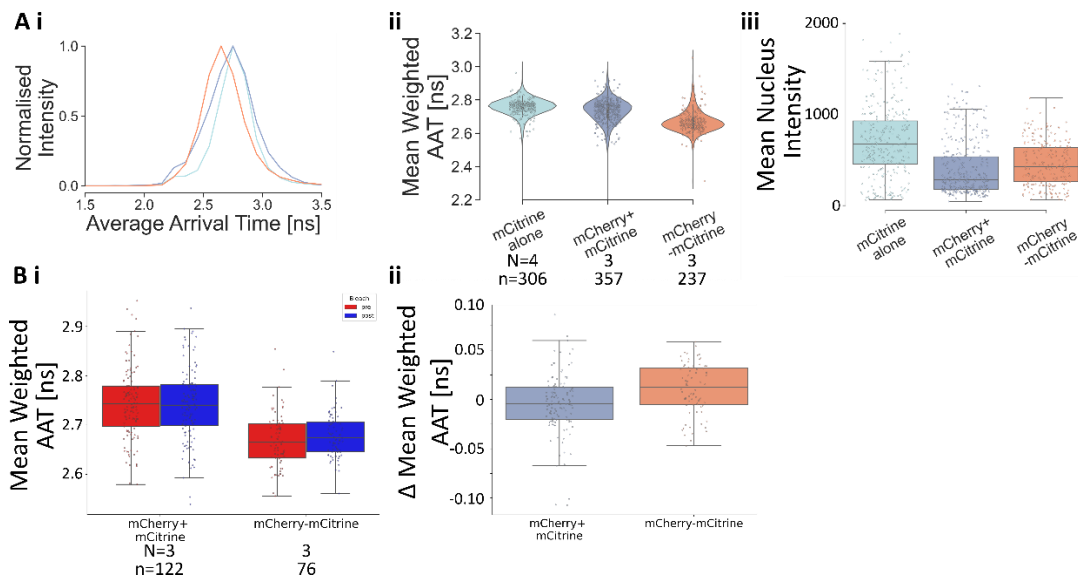
Appendix Figure 7.8 (Replicate 2 for Paper Figure 4) AAT-FRET can detect protein interactions in live zebrafish embryos.

 A) **i.** *Average nuclear mCitrine AAT lineplots from z-stacks acquired in TauContrast mode (methods 2.7.1),* ***ii.*** *Violin plot of MW AAT per nucleus,* ***iii.*** *Boxplot of mean nucleus intensity.* ***B)*** *Acceptor photobleaching (AccPb) AAT-FRET assay.* ***i.*** *Boxplot of MW AAT pre- vs. post-AccPb,* ***ii.*** *Boxplot of difference (Δ) in MW AAT pre- vs. post-AccPb for individual nuclei. N =3-4 embryos, n=76-306 nuclei. Statistics were analysed using linear mixed effect models, and pairwise comparison of means (methods 2.8), all n.s. (p>0.05).*
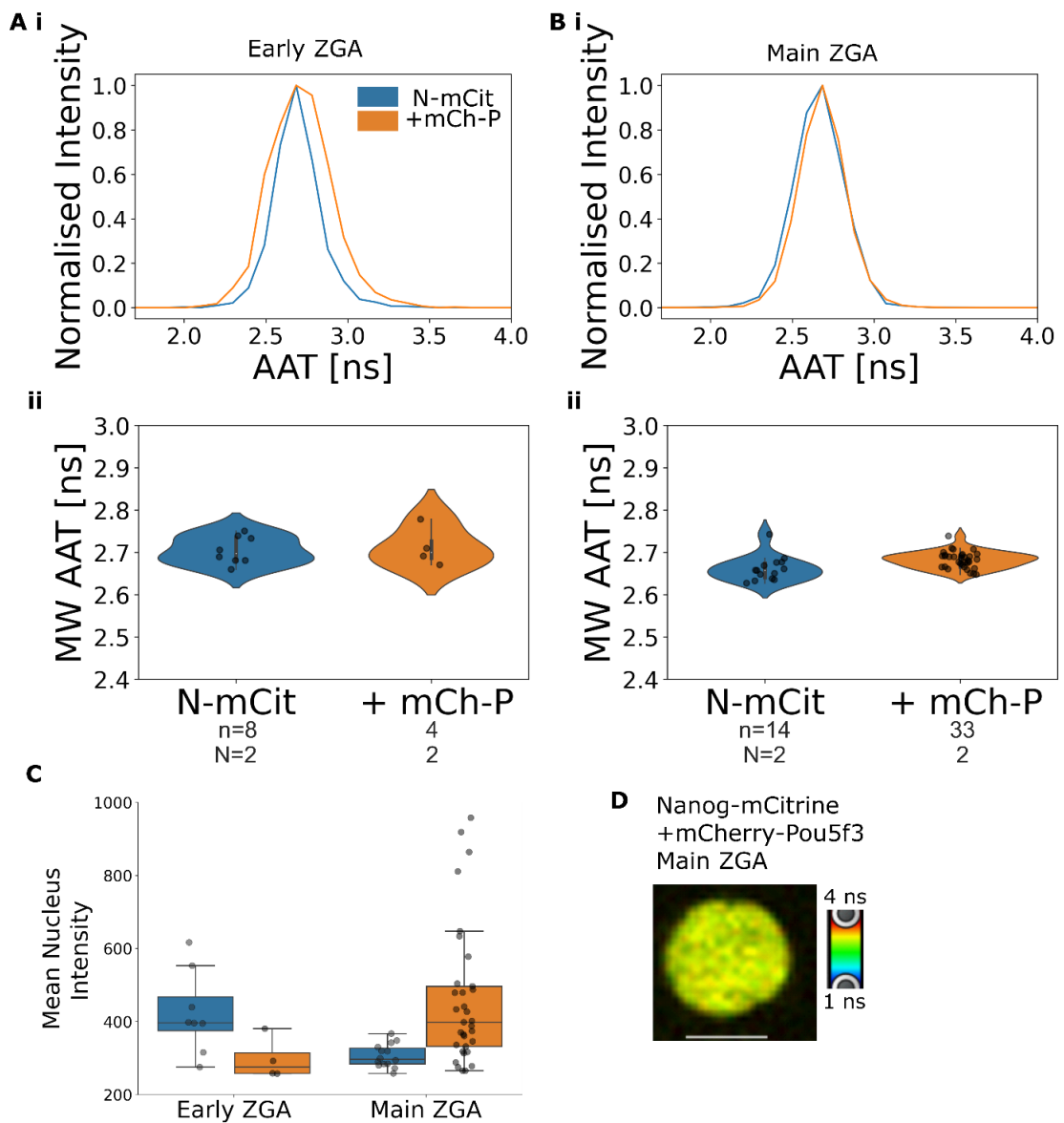
Appendix Figure 7.9 AAT-FRET measurements to test Nanog-mCitrine and mCherry-Pou5f3 interactions.

*MZnanog -/- embryos were microinjected with mRNA encoding Nanog-mCitrine (N-mCit) or equimolar Nanog-mCitrine + mCherry-Pou5f3 (mCh-P) mRNA, imaged using setting A (methods 2.7.1) at **A)** early and **B)** main ZGA. Measurements from nuclei with a mean intensity < 250 were excluded. **i** Average nuclear AAT lineplots and **ii** MW AAT violin plots for measurements at each stage. **C)** Boxplots of mean nucleus intensity. **D)** Representative AAT image of Nanog-mCitrine + mCherry-Pou5f3 at main ZGA, scale bar = 10 μm. B.r. = 1, N=2 embryos, n= 4-33 nuclei.*

A i — Nanog-mCitrine

ii — Chorion

iii — Dechorionated

iv

v
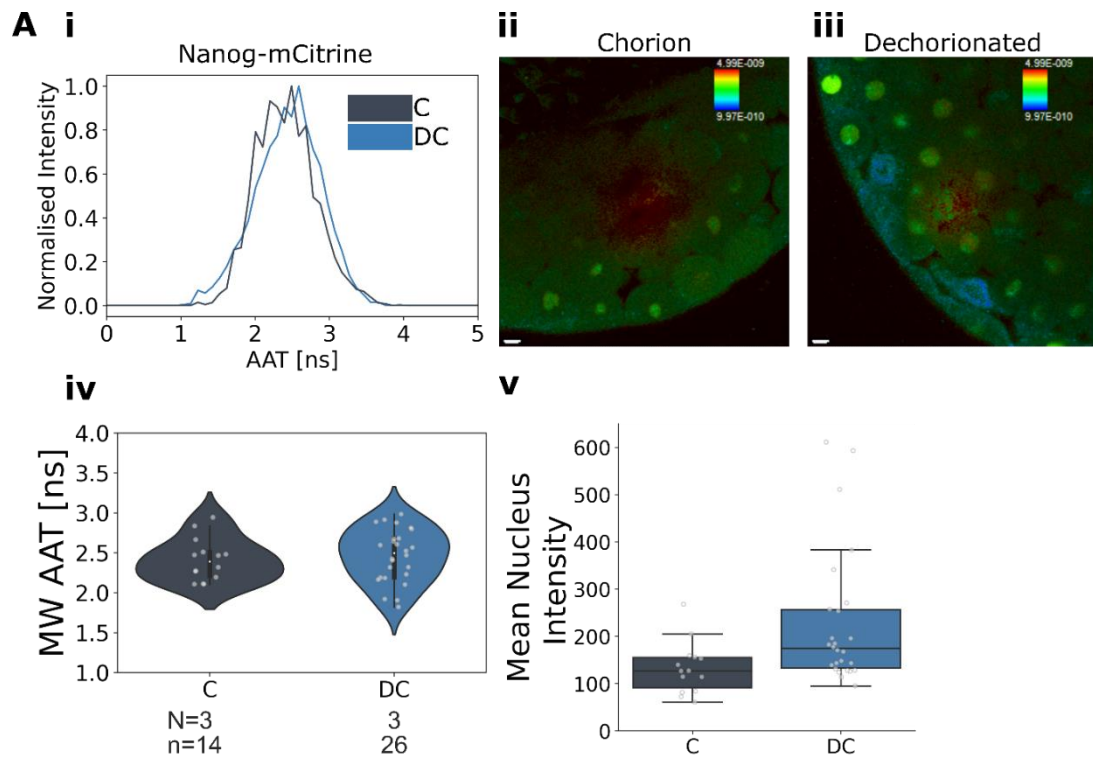
(figure cont. over page)
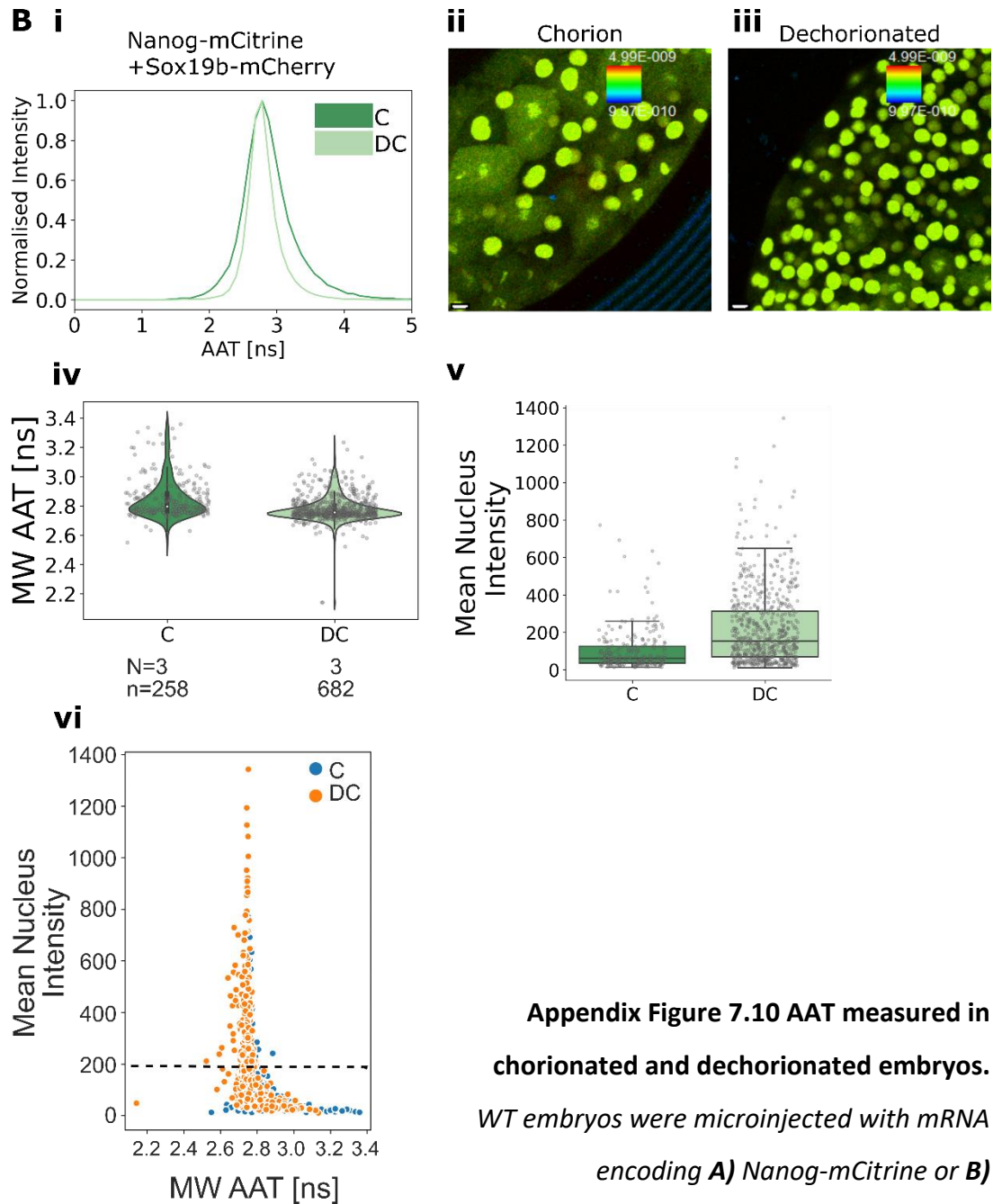
Appendix Figure 7.10 AAT measured in chorionated and dechorionated embryos.
*WT embryos were microinjected with mRNA encoding **A)** Nanog-mCitrine or **B)** equimolar Nanog-mCitrine + Sox19b-mCherry mRNA, mounted in chorion (C) or dechorionated (DC), and imaged using setting A (methods 2.7.1). For Nanog-mCitrine channel **i** Average nuclear AAT lineplots **ii-iii** Representative AAT images of Nanog-mCitrine, **iv** Violin plots of MW AAT, **v** Box and whisker plots of mean nucleus intensity, and **vi** scatterplot of mean nucleus intensity vs. MW AAT (dotted line indicates 'safe zone'). Scale bar = 10 μm, AAT range = 0-4 ns. B.r. = 1, N=3 embryos, n=258-682 nuclei.*

Appendix Table 7.2 Average MW AAT and MW mfD values for AAT-FRET measurements to test WT and DBD mutant Nanog and Sox19b interactions in HeLa cells (Figure 5.3,Figure 5.4)

Condition	Average MW AAT [ns]	Average mFd [%]
mCh-mCit	2.11713131	51.103132
N-mCit+mCh	2.52118618	14.987749
N-mCit+S-mCh	2.29573371	36.680941
N-mCit+sox19bHMG-mcherry	2.44921799	22.532419
N-mCit	2.59197403	9.7774311
nanogHOM-mCit+S-mCh	2.43038927	23.466027
nanogN-mCit+S-mCh	2.33210967	33.024659

Appendix Table 7.3 p-values for AAT-FRET measurements to test WT and DBD mutant Nanog and Sox19b interactions in HeLa cells (Figure 5.3,Figure 5.4)

Comparison			p.val	sign.
(mCh-mCit)	vs	(N-mCit)	<.0001	****
(mCh-mCit)	vs	(N-mCit+mCh)	<.0001	****
(mCh-mCit)	vs	(N-mCit+S-mCh)	<.0001	****
(mCh-mCit)	vs	(N-mCit+sox19bHMG-mcherry)	<.0001	****
(mCh-mCit)	vs	(nanogHOM-mCit+S-mCh)	<.0001	****
(mCh-mCit)	vs	(nanogN-mCit+S-mCh)	<.0001	****
(N-mCit)	vs	(N-mCit+mCh)	<.0001	****
(N-mCit)	vs	(N-mCit+S-mCh)	<.0001	****
(N-mCit)	vs	(N-mCit+sox19bHMG-mcherry)	<.0001	****
(N-mCit)	vs	(nanogHOM-mCit+S-mCh)	<.0001	****
(N-mCit)	vs	(nanogN-mCit+S-mCh)	<.0001	****
(N-mCit+mCh)	vs	(N-mCit+S-mCh)	<.0001	****
(N-mCit+mCh)	vs	(N-mCit+sox19bHMG-mcherry)	<.0001	****
(N-mCit+mCh)	vs	(nanogHOM-mCit+S-mCh)	<.0001	****
(N-mCit+mCh)	vs	(nanogN-mCit+S-mCh)	<.0001	****
(N-mCit+S-mCh)	vs	(N-mCit+sox19bHMG-mcherry)	<.0001	****
(N-mCit+S-mCh)	vs	(nanogHOM-mCit+S-mCh)	<.0001	****
(N-mCit+S-mCh)	vs	(nanogN-mCit+S-mCh)	0.017	*
(N-mCit+sox19bHMG-mcherry)	vs	(nanogHOM-mCit+S-mCh)	0.9251	ns
(N-mCit+sox19bHMG-mcherry)	vs	(nanogN-mCit+S-mCh)	<.0001	****
(nanogHOM-mCit+S-mCh)	vs	(nanogN-mCit+S-mCh)	<.0001	****
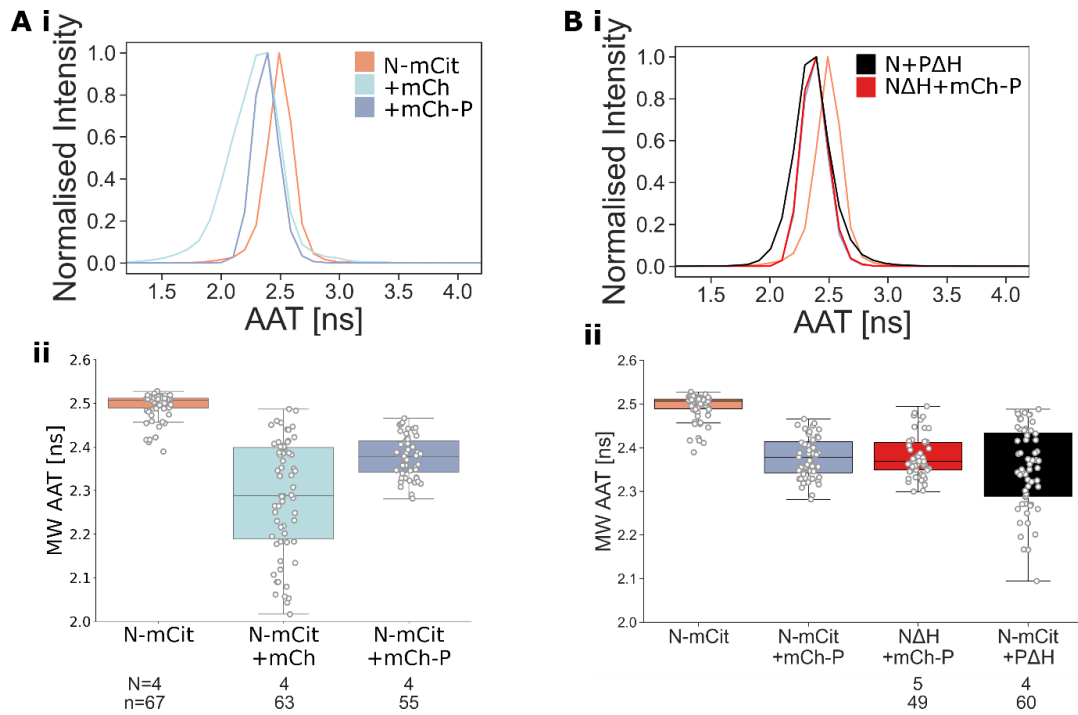
Appendix Figure 7.11 AAT-FRET measurements to test Nanog and Pou5f3 interactions in HeLa cells.

*HeLa cells were transfected to transiently express **A)** control conditions Nanog-mCitrine (N-mCit), Nanog-mCitrine + mCherry (mCh), Nanog-mCitrine + mCherry-Pou5f3 (mCh-P), and **B)** mutant conditions Nanog-mCitrine + mCherry-Pou5f3ΔHOM (PΔH), or Nanog ΔHOM-mCitrine (NΔH) + mCherry-Pou5f3. Images were acquired using setting G (methods 2.7.3). **A+B) i.** Average nuclear AAT lineplots, for **A)** control and **B)** mutant conditions. **A+B) ii.** Violin plots for MW AAT across conditions. B.r. = 1, N=4-5 images, n=49-63 nuclei.*
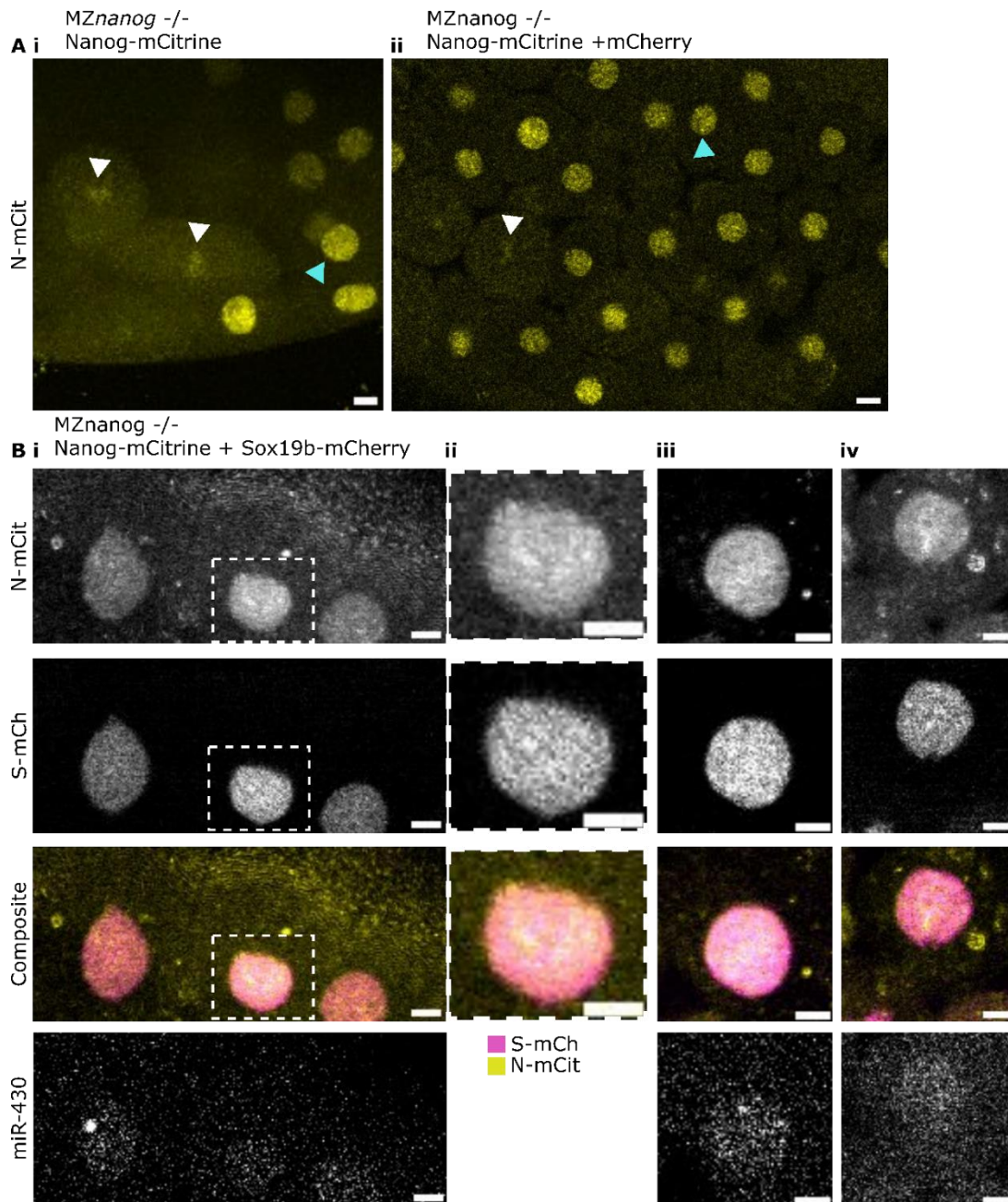
Appendix Figure 7.12 Nanog-mCitrine and Sox19b-mCherry foci.

*MZnanog -/- embryos expressing **A) i.** Nanog-mCitrine (N-mCit), **ii.** + mCherry, **B)** + Sox19b-mCherry (S-mCh) + GeneTools blue miR-430 MO (miR-430). **A)** Representative Nanog-mCitrine intensity images, were acquired using setting A (2.7.1). Cyan/white triangles indicate clusters/mitotic association, scale bar = 10 μm **B) i** Representative image for Nanog-mCitrine/Sox19b-mCherry/miR-430 intensity channels, were acquired using setting E1 (2.7.2.4), (**ii** magnified from inset in **i**), **iii, iv** separate images taken in same embryo, scale bar = 5 μm.*
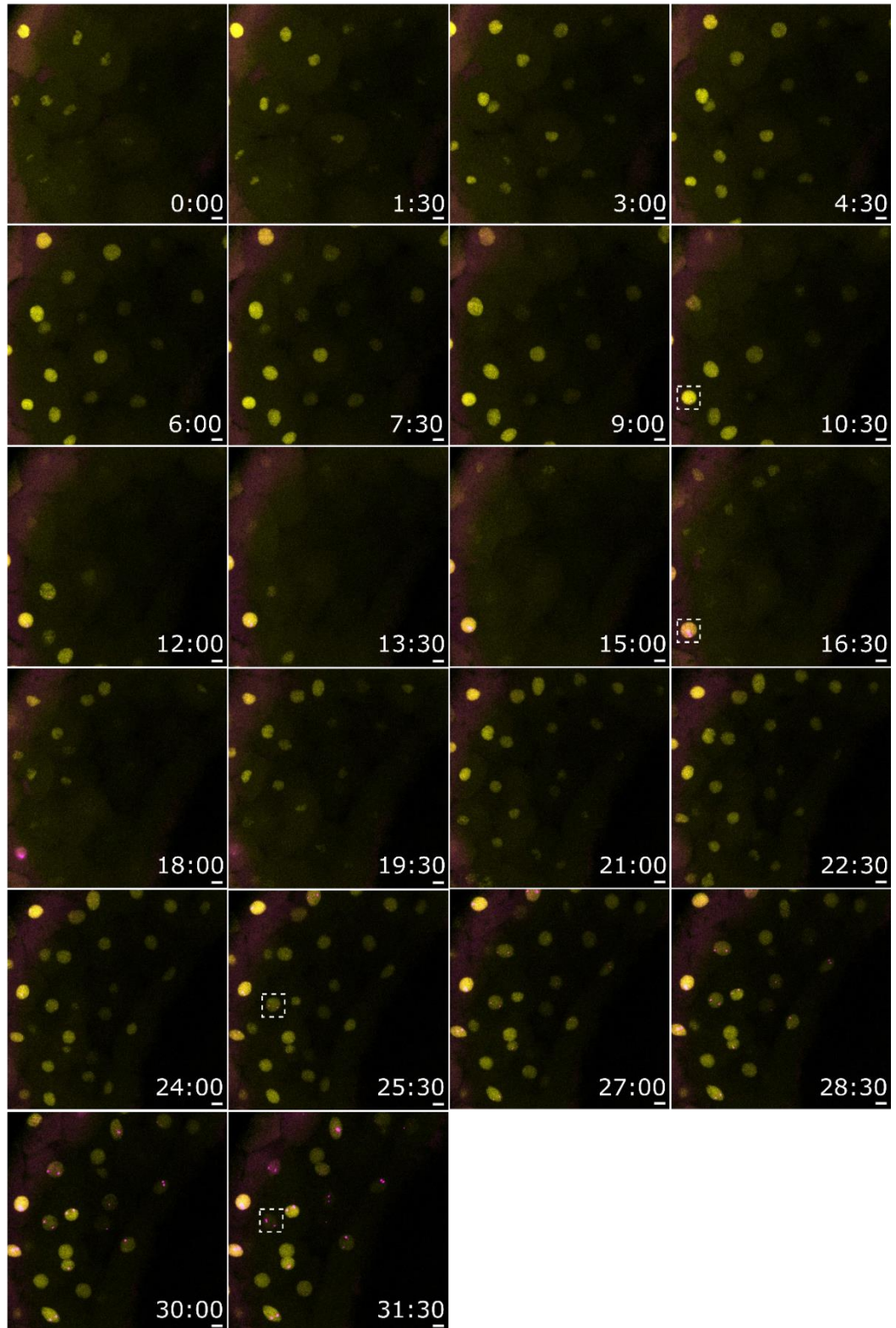
Appendix Figure 7.13 Time-lapse of Nanog-mCitrine foci and miR-430 transcription bodies.

(cont. over page)

*WT embryos were co-injected with Nanog-mCitrine mRNA and Lissamine-tagged miR-430 MO, and a z-stack image was acquired every 90 s during early ZGA (methods 2.4.4). **A)** StDev projections of z-stack images at each time-point, Nanog-mCitrine (N-mCit) and miR-430 intensity channels merged. Magnification of insets in Fig. 5.9.E. Scale bar = 10 µm. B.r. =1.*
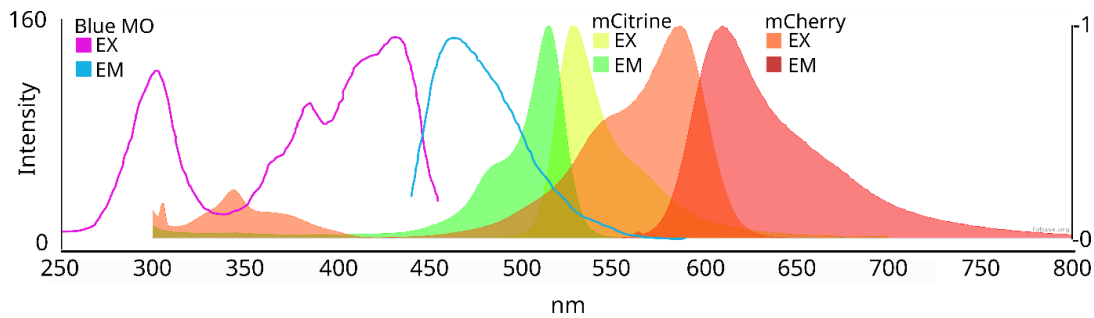
Appendix Figure 7.14 Excitation (EX) and emission (EM) wavelength spectra of GeneTools blue MO, mCitrine, and mCherry fluorophores.

GeneTools Blue MO spectra taken from (GeneTools, 2016), intensities scale from 0-160 (LH axis). mCitrine/mCherry spectra taken from (FPbase, 2023b, FPbase, 2023c), normalised intensities scale from 0-1 (RH axis) .
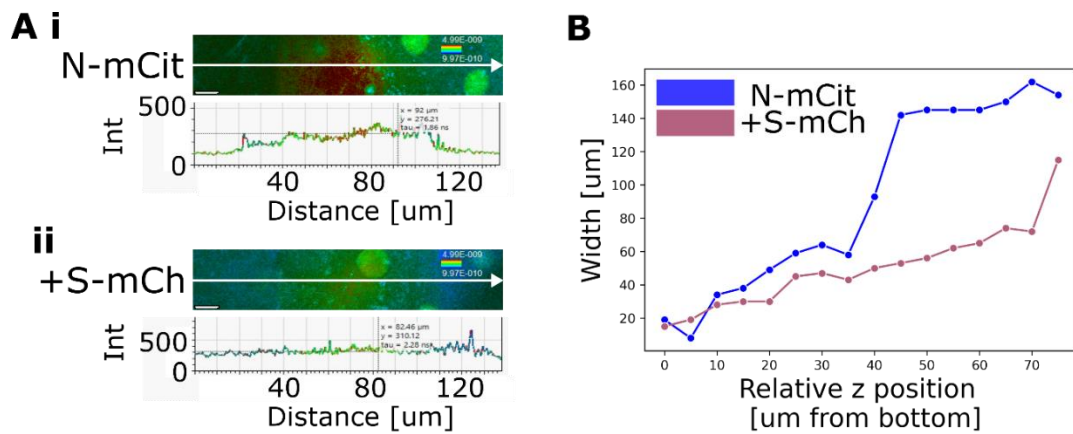
Appendix Figure 7.15 High central AAT pattern.

*WT embryos co-injected with mRNA encoding Nanog-mCitrine (N-mCit) +/- Sox19b-mCherry (S-mCh), and the GeneTools blue miR-430 MO, were deyolked and mounted in optiprep, for image acquisition using setting E1 (methods 2.7.2.4). **A)** Examples of single z-plane AAT images for embryos expressing **i.** Nanog-mCitrine or **ii.** + Sox19b-mCherry, with lineplots of pixel intensity at line draw across image, coloured by AAT (analysis done in LAS-X). **B)** Lineplot of high central AAT area width, measured manually in images across z-planes.*
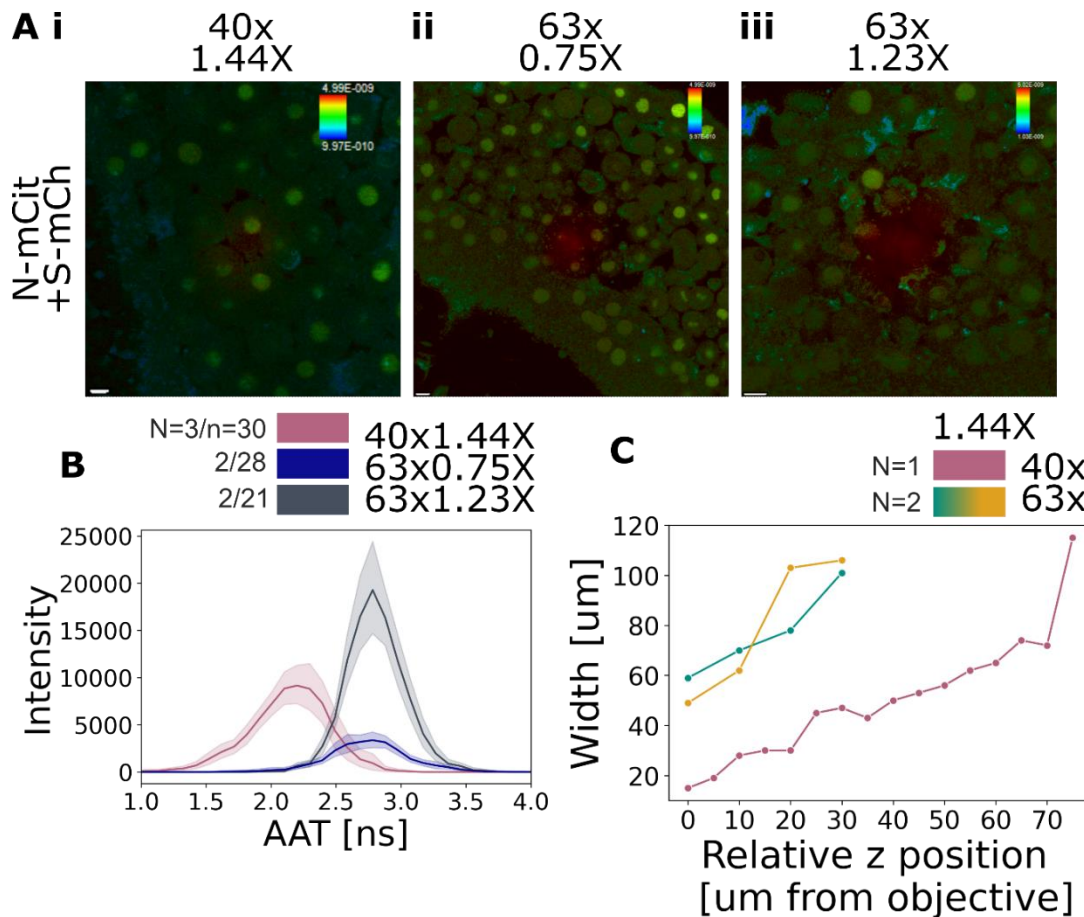
Appendix Figure 7.16 Comparison of 40x and 63x objective for AAT-FRET measurements.

*WT embryos were co-injected with mRNA encoding Nanog-mCitrine (N-mCit) + Sox19b-mCherry (S-mCh), and the GeneTools blue miR430 MO, and mounted in optiprep after deyolking. **A) i-iii** Representative single z-plane AAT images of embryos, taken using setting D (methods 2.7.2.4) with **i.** 1.44X digital magnification on 40x objective **ii.** 0.75X on 63x objective, **iii.** 1.23X on 63x objective. **B)** Non-normalised average nuclear AAT lineplots for each acquisition condition. B.r.=1, N=2-3 embryos, n=21-30 nuclei **C)** WT embryos were co-injected with mRNA encoding Nanog-mCitrine + Sox19b-mCherry, and mounted in optiprep after deyolking. Lineplot of high central AAT area width from images acquired at 1.44x digital magnification, using 40X (setting E2) or 63X (setting E3) objective (methods 2.7.2.4). B.r.=1, N=1-2 embryos.*
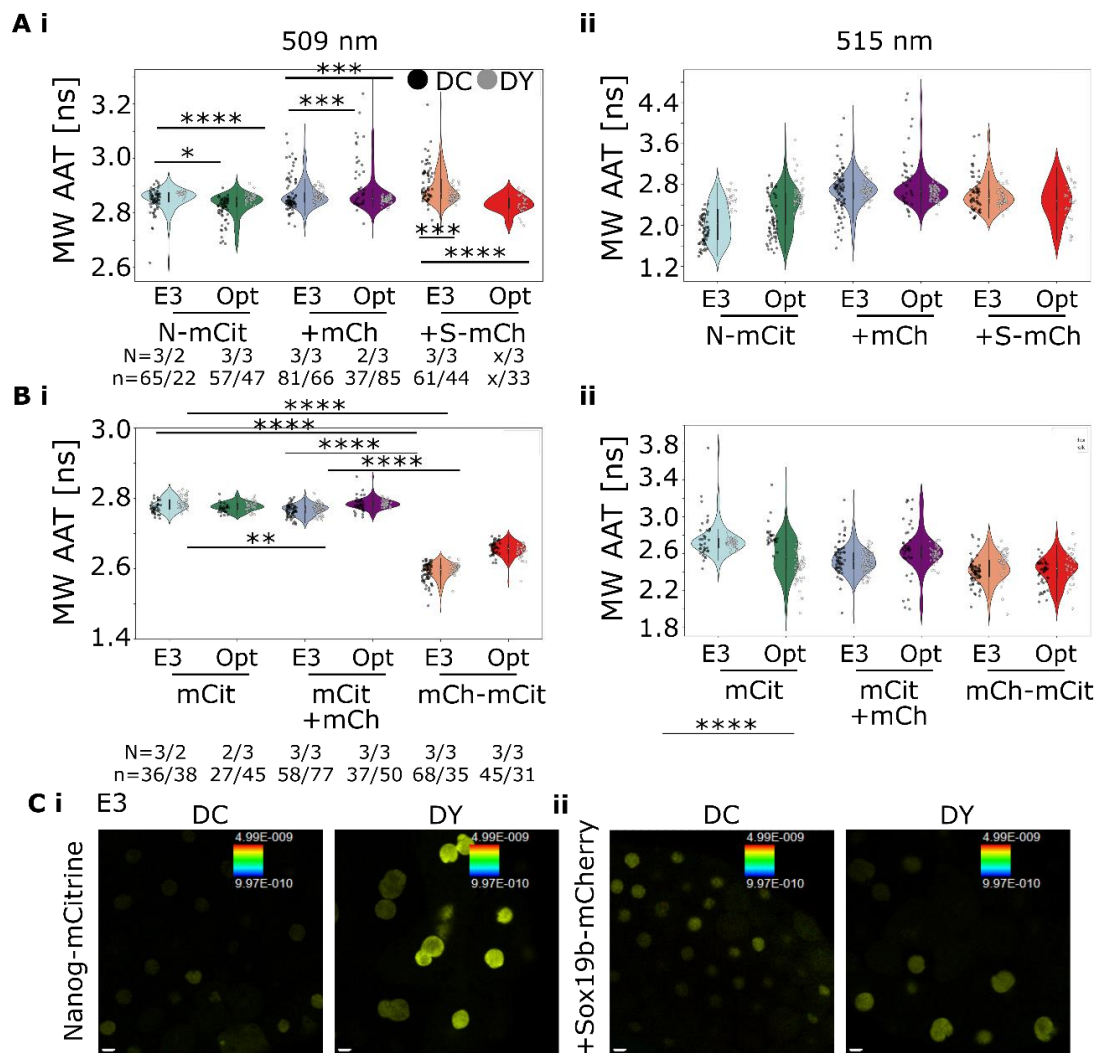
Appendix Figure 7.17 Effect of deyolking and mounting media on control versus biological interactions (accompanies Figure 5.12).

*WT embryos were injected with mRNA encoding control fluorophores (mCitrine, tandem mCherry-mCitrine, or separate mCherry + mCitrine) or SN conditions (Nanog-mCitrine or Nanog-mCitrine + Sox19b-mCherry). Embryos were, deyolked (DY) or dechorionated (DC), and mounted in optiprep (Opt) or E3. Images were acquired using setting F (methods 2.7.2.4) using the 509 nm or 515 nm laser. **A+B)** Violin plots of MW AAT for **A)** control conditions, **B)** SN conditions, using **i.** 509nm laser or **ii.** 515 nm laser. **C)** Representative AAT images of N-S condition embryos mounted in E3, 509 nm laser **i.** Nanog-mCit **ii.** + Sox19b-mCh. Scale bar = 10 µm, AAT range = 0-4 ns. B.r.= 1, N=2-3 embryos, n=22-81 nuclei. Statistics were analysed using linear mixed effect models, and pairwise comparison of means (methods 2.8). n.s. p>0.05, * p≤ 0.05, ** p ≤ 0.01, *** p ≤ 0.001, **** p ≤ 0.0001.*

Appendix Table 7.4 Average MW AAT values for AAT-FRET measurements to compare embryo preparation and laser excitation (Figure 5.12 + Appendix Figure 7.17)

	Prep	DC				DY			
	Medium	E3		Opt		E3		Opt	
	Laser [nm]	**509**	515	**509**	515	**509**	515	**509**	515
Control	mCit	**2.77**	2.78	**2.77**	2.79	**2.79**	2.72	**2.78**	2.44
	mCit+mCh	**2.76**	2.56	**2.78**	2.66	**2.77**	2.50	**2.79**	2.60
	mCh-mCit	**2.59**	2.40	**2.66**	2.39	**2.60**	2.51	**2.65**	2.47
N-S	N-mCit	**2.84**	1.89	**2.81**	2.13	**2.87**	2.53	**2.86**	2.61
	+mCh	**2.87**	2.66	**2.92**	2.93	**2.86**	2.70	**2.85**	2.64
	+S-mCh	**2.91**	2.63			**2.86**	2.55	**2.83**	2.48

Appendix Table 7.5 p-values for Appendix Table 7.4

Comparison			p.val	sign
(mCh-mCit_dc_e3_509)	vs	(mCh-mCit_dc_opt_509)	<.0001	****
(mCh-mCit_dc_e3_509)	vs	(mCh-mCit_dy_e3_509)	0.2051	
(mCh-mCit_dc_e3_509)	vs	(mCh-mCit_dy_opt_509)	<.0001	****
(mCh-mCit_dc_e3_509)	vs	mCit_dc_e3_509	<.0001	****
(mCh-mCit_dc_e3_509)	vs	(mCit+mCh_dc_e3_509)	<.0001	****
(mCh-mCit_dc_opt_509)	vs	(mCh-mCit_dy_e3_509)	<.0001	****
(mCh-mCit_dc_opt_509)	vs	(mCh-mCit_dy_opt_509)	0.106	
(mCh-mCit_dc_opt_509)	vs	mCit_dc_opt_509	<.0001	****
(mCh-mCit_dc_opt_509)	vs	(mCit+mCh_dc_opt_509)	<.0001	****
(mCh-mCit_dy_e3_509)	vs	(mCh-mCit_dy_opt_509)	<.0001	****
(mCh-mCit_dy_e3_509)	vs	mCit_dy_e3_509	<.0001	****
(mCh-mCit_dy_e3_509)	vs	(mCit+mCh_dy_e3_509)	<.0001	****
(mCh-mCit_dy_opt_509)	vs	mCit_dy_opt_509	<.0001	****
(mCh-mCit_dy_opt_509)	vs	(mCit+mCh_dy_opt_509)	<.0001	****
mCit_dc_e3_509	vs	mCit_dc_opt_509	1	
mCit_dc_e3_509	vs	mCit_dy_e3_509	0.0011	**
mCit_dc_e3_509	vs	mCit_dy_opt_509	0.9333	
mCit_dc_e3_509	vs	(mCit+mCh_dc_e3_509)	0.7553	
mCit_dc_opt_509	vs	mCit_dy_e3_509	0.0029	**
mCit_dc_opt_509	vs	mCit_dy_opt_509	0.9897	
mCit_dc_opt_509	vs	(mCit+mCh_dc_opt_509)	0.7904	
mCit_dy_e3_509	vs	mCit_dy_opt_509	0.0884	
mCit_dy_e3_509	vs	(mCit+mCh_dy_e3_509)	0.0045	**
mCit_dy_e3_509	vs	(mCit+mCh_dy_opt_509)	0.9673	

mCit_dy_opt_509	vs	(mCit+mCh_dy_opt_509)	0.927	
(mCit+mCh_dc_e3_509)	vs	(mCit+mCh_dc_opt_509)	<.0001	****
(mCit+mCh_dc_e3_509)	vs	(mCit+mCh_dy_e3_509)	0.7495	
(mCit+mCh_dc_e3_509)	vs	(mCit+mCh_dy_opt_509)	<.0001	****
(mCit+mCh_dc_opt_509)	vs	(mCit+mCh_dy_e3_509)	0.0162	*
(mCit+mCh_dc_opt_509)	vs	(mCit+mCh_dy_opt_509)	1	
(mCit+mCh_dy_e3_509)	vs	(mCit+mCh_dy_opt_509)	0.0002	***
(N-mCit_dc_e3_509)	vs	(N-mCit_dc_opt_509)	0.0182	*
(N-mCit_dc_e3_509)	vs	(N-mCit_dy_e3_509)	0.1722	
(N-mCit_dc_e3_509)	vs	(N-mCit_dy_opt_509)	0.9853	
(N-mCit_dc_e3_509)	vs	(N-mCit+mCh_dc_e3_509)	0.9168	
(N-mCit_dc_e3_509)	vs	(N-mCit+S-mCh_dc_e3_509)	0.0702	
(N-mCit_dc_opt_509)	vs	(N-mCit_dy_e3_509)	<.0001	****
(N-mCit_dc_opt_509)	vs	(N-mCit_dy_opt_509)	0.0008	***
(N-mCit_dc_opt_509)	vs	(N-mCit+mCh_dc_opt_509)	0.0071	**
(N-mCit_dc_opt_509)	vs	(N-mCit+S-mCh_dc_e3_509)	0.0087	**
(N-mCit_dy_e3_509)	vs	(N-mCit+mCh_dy_e3_509)	1	
(N-mCit_dy_e3_509)	vs	(N-mCit+mCh_dy_opt_509)	0.9705	
(N-mCit_dy_e3_509)	vs	(N-mCit+S-mCh_dy_e3_509)	1	
(N-mCit_dy_opt_509)	vs	(N-mCit+mCh_dy_opt_509)	1	
(N-mCit_dy_opt_509)	vs	(N-mCit+S-mCh_dy_opt_509)	0.9958	
(N-mCit+mCh_dc_e3_509)	vs	(N-mCit+mCh_dc_opt_509)	0.0001	***
(N-mCit+mCh_dc_e3_509)	vs	(N-mCit+mCh_dy_e3_509)	1	
(N-mCit+mCh_dc_e3_509)	vs	(N-mCit+mCh_dy_opt_509)	0.7205	
(N-mCit+mCh_dc_e3_509)	vs	(N-mCit+S-mCh_dc_e3_509)	0.3648	
(N-mCit+mCh_dc_opt_509)	vs	(N-mCit+mCh_dy_e3_509)	0.0002	***
(N-mCit+mCh_dc_opt_509)	vs	(N-mCit+mCh_dy_opt_509)	<.0001	****
(N-mCit+mCh_dc_opt_509)	vs	(N-mCit+S-mCh_dy_opt_509)	0.0435	*
(N-mCit+mCh_dy_e3_509)	vs	(N-mCit+mCh_dy_opt_509)	0.8512	
(N-mCit+mCh_dy_e3_509)	vs	(N-mCit+S-mCh_dy_e3_509)	1	
(N-mCit+S-mCh_dc_e3_509)	vs	(N-mCit+S-mCh_dy_e3_509)	0.0002	***
(N-mCit+S-mCh_dc_e3_509)	vs	(N-mCit+S-mCh_dy_opt_509)	<.0001	****
(N-mCit+S-mCh_dy_e3_509)	vs	(N-mCit+S-mCh_dy_opt_509)	0.0853	

8 References

AANES, H., OSTRUP, O., ANDERSEN, I. S., MOEN, L. F., MATHAVAN, S., COLLAS, P. & ALESTROM, P. 2013. Differential transcript isoform usage pre- and post-zygotic genome activation in zebrafish. *BMC Genomics,* 14**,** 331.

AANES, H., WINATA, C. L., LIN, C. H., CHEN, J. P., SRINIVASAN, K. G., LEE, S. G., LIM, A. Y., HAJAN, H. S., COLLAS, P., BOURQUE, G., GONG, Z., KORZH, V., ALESTROM, P. & MATHAVAN, S. 2011. Zebrafish mRNA sequencing deciphers novelties in transcriptome dynamics during maternal to zygotic transition. *Genome Res,* 21**,** 1328-38.

AHMED, K., DEHGHANI, H., RUGG-GUNN, P., FUSSNER, E., ROSSANT, J. & BAZETT-JONES, D. P. 2010. Global chromatin architecture reflects pluripotency and lineage commitment in the early mouse embryo. *PLoS One,* 5**,** e10531.

AKKERS, R. C., VAN HEERINGEN, S. J., JACOBI, U. G., JANSSEN-MEGENS, E. M., FRANCOIJS, K. J., STUNNENBERG, H. G. & VEENSTRA, G. J. 2009. A hierarchy of H3K4me3 and H3K27me3 acquisition in spatial gene regulation in Xenopus embryos. *Dev Cell,* 17**,** 425-34.

AKSOY, I., JAUCH, R., ERAS, V., CHNG, W. B., CHEN, J., DIVAKAR, U., NG, C. K., KOLATKAR, P. R. & STANTON, L. W. 2013. Sox transcription factors require selective interactions with Oct4 and specific transactivation functions to mediate reprogramming. *Stem Cells,* 31**,** 2632-46.

ALJIBOURY, A. A., MUJCIC, A., CAMMERINO, T., RATHBUN, L. I. & HEHNLY, H. 2021. Imaging the early zebrafish embryo centrosomes following injection of small-molecule inhibitors to understand spindle formation. *STAR Protoc,* 2**,** 100293.

ALVAREZ, L., ROBERTI, J., OSSATO, G., LEICA MICROSYSTEMS. 2022. TauInteraction – Studying Molecular Interactions with TauSense. Available: https://www.leica-microsystems.com/science-lab/life-science/tauinteraction-studying-molecular-interactions-with-tausense/ [Accessed 26.08.2022].

AMODEO, A. A., JUKAM, D., STRAIGHT, A. F. & SKOTHEIM, J. M. 2015. Histone titration against the genome sets the DNA-to-cytoplasm threshold for the Xenopus midblastula transition. *Proc Natl Acad Sci U S A,* 112**,** E1086-95.

ANCELIN, K., SYX, L., BORENSZTEIN, M., RANISAVLJEVIC, N., VASSILEV, I., BRISENO-ROA, L., LIU, T., METZGER, E., SERVANT, N., BARILLOT, E., CHEN, C. J., SCHULE, R. & HEARD, E. 2016. Maternal LSD1/KDM1A is an essential regulator of chromatin and transcription landscapes during zygotic genome activation. *Elife,* 5.

ANDERSEN, I. S., REINER, A. H., AANES, H., ALESTROM, P. & COLLAS, P. 2012. Developmental features of DNA methylation during activation of the embryonic zebrafish genome. *Genome Biol,* 13**,** R65.

ART, J. 2006. Photon Detectors for Confocal Microscopy. *In:* PAWLEY, J. B. (ed.) *Handbook Of Biological Confocal Microscopy.* Boston, MA: Springer US.

ATALLAH, J. & LOTT, S. E. 2018. Evolution of maternal and zygotic mRNA complements in the early Drosophila embryo. *PLoS Genet,* 14**,** e1007838.

AUDUGE, N., PADILLA-PARRA, S., TRAMIER, M., BORGHI, N. & COPPEY-MOISAN, M. 2019. Chromatin condensation fluctuations rather than steady-state predict chromatin accessibility. *Nucleic Acids Res,* 47**,** 6184-6194.

AUER, J. M. T., MURPHY, L. C., XIAO, D., LI, D. U. & WHEELER, A. P. 2022. Non-fitting FLIM-FRET facilitates analysis of protein interactions in live zebrafish embryos. *J Microsc*.

AUER, J. M. T., STODDART, J. J., CHRISTODOULOU, I., LIMA, A., SKOULOUDAKI, K., HALL, H. N., VUKOJEVIC, V. & PAPADOPOULOS, D. K. 2020. Of numbers and movement - understanding transcription factor pathogenesis by advanced microscopy. *Dis Model Mech,* 13.

AVILION, A. A., NICOLIS, S. K., PEVNY, L. H., PEREZ, L., VIVIAN, N. & LOVELL-BADGE, R. 2003. Multipotent cell lineages in early mouse development depend on SOX2 function. *Genes Dev,* 17**,** 126-40.

AXELROD, D., KOPPEL, D. E., SCHLESSINGER, J., ELSON, E. & WEBB, W. W. 1976. Mobility measurement by analysis of fluorescence photobleaching recovery kinetics. *Biophys J,* 16**,** 1055-69.

BACIA, K. & SCHWILLE, P. 2007. Practical guidelines for dual-color fluorescence cross-correlation spectroscopy. *Nat Protoc,* 2**,** 2842-56.

BAJAR, B. T., WANG, E. S., ZHANG, S., LIN, M. Z. & CHU, J. 2016. A Guide to Fluorescent Protein FRET Pairs. *Sensors (Basel),* 16.

BANKHEAD, P. 2023. *Microscopes & detectors* [Online]. Available: h[ttps://petebankhead.gitbooks.io/imagej-intro/content/chapters/microscope_types/microscope_types.html](https://petebankhead.gitbooks.io/imagej-intro/content/chapters/microscope_types/microscope_types.html) [Accessed].

BARISIC, D., STADLER, M. B., IURLARO, M. & SCHUBELER, D. 2019. Mammalian ISWI and SWI/SNF selectively mediate binding of distinct transcription factors. *Nature,* 569**,** 136-140.

BARTKOWIAK, B. & GREENLEAF, A. L. 2011. Phosphorylation of RNAPII: To P-TEFb or not to P-TEFb? *Transcription,* 2**,** 115-119.

BASTIAENS, P. I. H., & JOVIN, T. M. 1998. Fluorescence resonance energy transfer microscopy. *In:* CELIS, J. E. (ed.) *Cell Biology: A Laboratory Handbook.* 2 ed. New York: Academic Press.

BAZZINI, A. A., LEE, M. T. & GIRALDEZ, A. J. 2012. Ribosome profiling shows that miR-430 reduces translation before causing mRNA decay in zebrafish. *Science,* 336**,** 233-7.

BECKER, W., SU, B., HOLUB, O. & WEISSHART, K. 2011. FLIM and FCS detection in laser-scanning microscopes: increased efficiency by GaAsP hybrid detectors. *Microsc Res Tech,* 74**,** 804-11.

BENOIT, B., HE, C. H., ZHANG, F., VOTRUBA, S. M., TADROS, W., WESTWOOD, J. T., SMIBERT, C. A., LIPSHITZ, H. D. & THEURKAUF, W. E. 2009. An essential role for the RNA-binding protein Smaug during the Drosophila maternal-to-zygotic transition. *Development,* 136**,** 923-32.

BEREZIN, M. Y. & ACHILEFU, S. 2010. Fluorescence lifetime measurements and biological imaging. *Chem Rev,* 110**,** 2641-84.

BERNSTEIN, B. E., MIKKELSEN, T. S., XIE, X., KAMAL, M., HUEBERT, D. J., CUFF, J., FRY, B., MEISSNER, A., WERNIG, M., PLATH, K., JAENISCH, R., WAGSCHAL, A., FEIL, R., SCHREIBER, S. L. & LANDER, E. S. 2006. A bivalent chromatin structure marks key developmental genes in embryonic stem cells. *Cell,* 125**,** 315-26.

BICKMORE, W. A. 2013. The spatial organization of the human genome. *Annu Rev Genomics Hum Genet,* 14**,** 67-84.

BIDDLE, J. W., NGUYEN, M. & GUNAWARDENA, J. 2019. Negative reciprocity, not ordered assembly, underlies the interaction of Sox2 and Oct4 on DNA. *Elife,* 8.

BILU, Y. & BARKAI, N. 2005. The design of transcription-factor binding sites is affected by combinatorial regulation. *Genome Biol,* 6**,** R103.

BINDELS, D. S., HAARBOSCH, L., VAN WEEREN, L., POSTMA, M., WIESE, K. E., MASTOP, M., AUMONIER, S., GOTTHARD, G., ROYANT, A., HINK, M. A. & GADELLA, T. W., JR.

2017. mScarlet: a bright monomeric red fluorescent protein for cellular imaging. *Nat Methods,* 14**,** 53-56.

BLYTHE, S. A. & WIESCHAUS, E. F. 2016. Establishment and maintenance of heritable chromatin structure during early Drosophila embryogenesis. *Elife,* 5.

BOHMANN, D., BOS, T. J., ADMON, A., NISHIMURA, T., VOGT, P. K. & TJIAN, R. 1987. Human proto-oncogene c-jun encodes a DNA binding protein with structural and functional properties of transcription factor AP-1. *Science,* 238**,** 1386-92.

BOIJA, A., KLEIN, I. A., SABARI, B. R., DALL'AGNESE, A., COFFEY, E. L., ZAMUDIO, A. V., LI, C. H., SHRINIVAS, K., MANTEIGA, J. C., HANNETT, N. M., ABRAHAM, B. J., AFEYAN, L. K., GUO, Y. E., RIMEL, J. K., FANT, C. B., SCHUIJERS, J., LEE, T. I., TAATJES, D. J. & YOUNG, R. A. 2018. Transcription Factors Activate Genes through the Phase-Separation Capacity of Their Activation Domains. *Cell,* 175**,** 1842-1855 e16.

BOOTHE, T., HILBERT, L., HEIDE, M., BERNINGER, L., HUTTNER, W. B., ZABURDAEV, V., VASTENHOUW, N. L., MYERS, E. W., DRECHSEL, D. N. & RINK, J. C. 2017. A tunable refractive index matching medium for live imaging cells, tissues and model organisms. *Elife,* 6.

BOSKOVIC, A., EID, A., PONTABRY, J., ISHIUCHI, T., SPIEGELHALTER, C., RAGHU RAM, E. V., MESHORER, E. & TORRES-PADILLA, M. E. 2014. Higher chromatin mobility supports totipotency and precedes pluripotency in vivo. *Genes Dev,* 28**,** 1042-7.

BOYER, L. A., LEE, T. I., COLE, M. F., JOHNSTONE, S. E., LEVINE, S. S., ZUCKER, J. P., GUENTHER, M. G., KUMAR, R. M., MURRAY, H. L., JENNER, R. G., GIFFORD, D. K., MELTON, D. A., JAENISCH, R. & YOUNG, R. A. 2005. Core transcriptional regulatory circuitry in human embryonic stem cells. *Cell,* 122**,** 947-56.

BOYLE, S., FLYAMER, I. M., WILLIAMSON, I., SENGUPTA, D., BICKMORE, W. A. & ILLINGWORTH, R. S. 2020. A central role for canonical PRC1 in shaping the 3D nuclear landscape. *Genes Dev,* 34**,** 931-949.

BRAHMA, S. & HENIKOFF, S. 2019. RSC-Associated Subnucleosomes Define MNase-Sensitive Promoters in Yeast. *Mol Cell,* 73**,** 238-249 e3.

BRAZDA, P., SZEKERES, T., BRAVICS, B., TOTH, K., VAMOSI, G. & NAGY, L. 2011. Live-cell fluorescence correlation spectroscopy dissects the role of coregulator exchange and chromatin binding in retinoic acid receptor mobility. *J Cell Sci,* 124**,** 3631-42.

BUSHATI, N., STARK, A., BRENNECKE, J. & COHEN, S. M. 2008. Temporal reciprocity of miRNAs and their targets during the maternal-to-zygotic transition in Drosophila. *Curr Biol,* 18**,** 501-6.

CALLEGARI, A., SIEBEN, C., BENKE, A., SUTER, D. M., FIERZ, B., MAZZA, D. & MANLEY, S. 2019. Single-molecule dynamics and genome-wide transcriptomics reveal that NF-kB (p65)-DNA binding times can be decoupled from transcriptional activation. *PLoS Genet,* 15**,** e1007891.

CAO, G., NI, X., JIANG, M., MA, Y., CHENG, H., GUO, L., JI, C., GU, S., XIE, Y. & MAO, Y. 2002. Molecular cloning and characterization of a novel human cAMP response element-binding (CREB) gene (CREB4). *J Hum Genet,* 47**,** 373-6.

CAPOULADE, J., WACHSMUTH, M., HUFNAGEL, L. & KNOP, M. 2011. Quantitative fluorescence imaging of protein diffusion and interaction in living cells. *Nat Biotechnol,* 29**,** 835-9.

CHAMBERS, I., COLBY, D., ROBERTSON, M., NICHOLS, J., LEE, S., TWEEDIE, S. & SMITH, A. 2003. Functional expression cloning of Nanog, a pluripotency sustaining factor in embryonic stem cells. *Cell,* 113**,** 643-55.

CHAN, S. H., TANG, Y., MIAO, L., DARWICH-CODORE, H., VEJNAR, C. E., BEAUDOIN, J. D., MUSAEV, D., FERNANDEZ, J. P., BENITEZ, M. D. J., BAZZINI, A. A., MORENO-

MATEOS, M. A. & GIRALDEZ, A. J. 2019. Brd4 and P300 Confer Transcriptional Competency during Zygotic Genome Activation. *Dev Cell,* 49**,** 867-881 e8.

CHANDRA, V., HUANG, P., HAMURO, Y., RAGHURAM, S., WANG, Y., BURRIS, T. P. & RASTINEJAD, F. 2008. Structure of the intact PPAR-gamma-RXR- nuclear receptor complex on DNA. *Nature,* 456**,** 350-6.

CHEN, J., ZHANG, Z., LI, L., CHEN, B.-C., REVYAKIN, A., HAJJ, B., LEGANT, W., DAHAN, M., LIONNET, T., BETZIG, E., TJIAN, R. & LIU, Z. 2014a. Single-molecule dynamics of enhanceosome assembly in embryonic stem cells. *Cell,* 156**,** 1274-1285.

CHEN, J., ZHANG, Z., LI, L., CHEN, B. C., REVYAKIN, A., HAJJ, B., LEGANT, W., DAHAN, M., LIONNET, T., BETZIG, E., TJIAN, R. & LIU, Z. 2014b. Single-molecule dynamics of enhanceosome assembly in embryonic stem cells. *Cell,* 156**,** 1274-1285.

CHEN, K., JOHNSTON, J., SHAO, W., MEIER, S., STABER, C. & ZEITLINGER, J. 2013. A global change in RNA polymerase II pausing during the Drosophila midblastula transition. *Elife,* 2**,** e00861.

CHEN, X., CHU, M. & GIEDROC, D. P. 1999. MRE-Binding transcription factor-1: weak zinc-binding finger domains 5 and 6 modulate the structure, affinity, and specificity of the metal-response element complex. *Biochemistry,* 38**,** 12915-25.

CHEN, Y., CATTOGLIO, C., DAILEY, G. M., ZHU, Q., TJIAN, R. & DARZACQ, X. 2022. Mechanisms governing target search and binding dynamics of hypoxia-inducible factors. *Elife,* 11.

CHOI, K. J., QUAN, M. D., QI, C., LEE, J. H., TSOI, P. S., ZAHABIYON, M., BAJIC, A., HU, L., PRASAD, B. V. V., LIAO, S. J., LI, W., FERREON, A. C. M. & FERREON, J. C. 2022. NANOG prion-like assembly mediates DNA bridging to facilitate chromatin reorganization and activation of pluripotency. *Nat Cell Biol,* 24**,** 737-747.

CIRILLO, L. A., MCPHERSON, C. E., BOSSARD, P., STEVENS, K., CHERIAN, S., SHIM, E. Y., CLARK, K. L., BURLEY, S. K. & ZARET, K. S. 1998. Binding of the winged-helix transcription factor HNF3 to a linker histone site on the nucleosome. *EMBO J,* 17**,** 244-54.

COLLART, C., ALLEN, G. E., BRADSHAW, C. R., SMITH, J. C. & ZEGERMAN, P. 2013. Titration of four replication factors is essential for the Xenopus laevis midblastula transition. *Science,* 341**,** 893-6.

COLLART, C., OWENS, N. D., BHAW-ROSUN, L., COOPER, B., DE DOMENICO, E., PATRUSHEV, I., SESAY, A. K., SMITH, J. N., SMITH, J. C. & GILCHRIST, M. J. 2014. High-resolution analysis of gene activity during the Xenopus mid-blastula transition. *Development,* 141**,** 1927-39.

COSENTINO, M. S., OSES, C., VAZQUEZ ECHEGARAY, C., SOLARI, C., WAISMAN, A., ALVAREZ, Y., PETRONE, M. V., FRANCIA, M., SCHULTZ, M., SEVLEVER, G., MIRIUKA, S., LEVI, V. & GUBERMAN, A. 2019. Kat6b Modulates Oct4 and Nanog Binding to Chromatin in Embryonic Stem Cells and Is Required for Efficient Neural Differentiation. *J Mol Biol,* 431**,** 1148-1159.

COSTA, A., POWELL, L. M., MALAGUTI, M., SOUFI, A., LOWELL, S. & JARMAN, A. P. 2022. Repurposing the lineage-determining transcription factor Atoh1 without redistributing its genomic binding sites. *Front Cell Dev Biol,* 10**,** 1016367.

COSTANTINI, L. M., BALOBAN, M., MARKWARDT, M. L., RIZZO, M. A., GUO, F., VERKHUSHA, V. V. & SNAPP, E. L. 2015. A palette of fluorescent proteins optimized for diverse cellular environments. *Nat Commun,* 6**,** 7670.

DAHL, J. A., JUNG, I., AANES, H., GREGGAINS, G. D., MANAF, A., LERDRUP, M., LI, G., KUAN, S., LI, B., LEE, A. Y., PREISSL, S., JERMSTAD, I., HAUGEN, M. H., SUGANTHAN, R., BJORAS, M., HANSEN, K., DALEN, K. T., FEDORCSAK, P., REN, B. & KLUNGLAND, A.

2016. Broad histone H3K4me3 domains in mouse oocytes modulate maternal-to-zygotic transition. *Nature,* 537**,** 548-552.

DALLE NOGARE, D. E., PAUERSTEIN, P. T. & LANE, M. E. 2009. G2 acquisition by transcription-independent mechanism at the zebrafish midblastula transition. *Dev Biol,* 326**,** 131-42.

DANG, V. T., KASSAHN, K. S., MARCOS, A. E. & RAGAN, M. A. 2008. Identification of human haploinsufficient genes and their genomic proximity to segmental duplications. *Eur J Hum Genet,* 16**,** 1350-7.

DAS, R. K. & PAPPU, R. V. 2013. Conformations of intrinsically disordered proteins are influenced by linear sequence distributions of oppositely charged residues. *Proc Natl Acad Sci U S A,* 110**,** 13392-7.

DATTA, R., HEASTER, T. M., SHARICK, J. T., GILLETTE, A. A. & SKALA, M. C. 2020. Fluorescence lifetime imaging microscopy: fundamentals and advances in instrumentation, analysis, and applications. *J Biomed Opt,* 25**,** 1-43.

DAVIS, R. L., CHENG, P. F., LASSAR, A. B. & WEINTRAUB, H. 1990. The MyoD DNA binding domain contains a recognition code for muscle-specific gene activation. *Cell,* 60**,** 733-46.

DAVIS, R. L., WEINTRAUB, H. & LASSAR, A. B. 1987. Expression of a single transfected cDNA converts fibroblasts to myoblasts. *Cell,* 51**,** 987-1000.

DE IACO, A., COUDRAY, A., DUC, J. & TRONO, D. 2019. DPPA2 and DPPA4 are necessary to establish a 2C-like state in mouse embryonic stem cells. *EMBO Rep,* 20.

DE IACO, A., PLANET, E., COLUCCIO, A., VERP, S., DUC, J. & TRONO, D. 2017. DUX-family transcription factors regulate zygotic genome activation in placental mammals. *Nat Genet,* 49**,** 941-945.

DE RENZIS, S., ELEMENTO, O., TAVAZOIE, S. & WIESCHAUS, E. F. 2007. Unmasking activation of the zygotic genome using chromosomal deletions in the Drosophila embryo. *PLoS biology,* 5**,** e117-e117.

DENK, W., STRICKLER, J. H. & WEBB, W. W. 1990. Two-photon laser scanning fluorescence microscopy. *Science,* 248**,** 73-6.

DIGMAN, M. A., CAIOLFA, V. R., ZAMAI, M. & GRATTON, E. 2008. The phasor approach to fluorescence lifetime imaging analysis. *Biophys J,* 94**,** L14-6.

DIGMAN, M. A. & GRATTON, E. 2011. Lessons in fluctuation correlation spectroscopy. *Annual review of physical chemistry,* 62**,** 645-668.

DIXON, J. R., SELVARAJ, S., YUE, F., KIM, A., LI, Y., SHEN, Y., HU, M., LIU, J. S. & REN, B. 2012. Topological domains in mammalian genomes identified by analysis of chromatin interactions. *Nature,* 485**,** 376-80.

DODONOVA, S. O., ZHU, F., DIENEMANN, C., TAIPALE, J. & CRAMER, P. 2020. Nucleosome-bound SOX2 and SOX11 structures elucidate pioneer factor function. *Nature,* 580**,** 669-672.

DONOVAN, B. T., CHEN, H., JIPA, C., BAI, L. & POIRIER, M. G. 2019. Dissociation rate compensation mechanism for budding yeast pioneer transcription factors. *Elife,* 8.

DONOVAN, B. T., LUO, Y., MENG, Z. & POIRIER, M. G. 2023. The nucleosome unwrapping free energy landscape defines distinct regions of transcription factor accessibility and kinetics. *Nucleic Acids Res,* 51**,** 1139-1153.

DU, Z., YU, J., LI, F., DENG, L., WU, F., HUANG, X., BERGSTRAND, J., WIDENGREN, J., DONG, C. & REN, J. 2018. In Situ Monitoring of p53 Protein and MDM2 Protein Interaction in Single Living Cells Using Single-Molecule Fluorescence Spectroscopy. *Anal Chem,* 90**,** 6144-6151.

DYSON, H. J. & WRIGHT, P. E. 2016. Role of Intrinsic Protein Disorder in the Function and Interactions of the Transcriptional Coactivators CREB-binding Protein (CBP) and p300. *J Biol Chem,* 291**,** 6714-22.

ECKERSLEY-MASLIN, M., ALDA-CATALINAS, C., BLOTENBURG, M., KREIBICH, E., KRUEGER, C. & REIK, W. 2019. Dppa2 and Dppa4 directly regulate the Dux-driven zygotic transcriptional program. *Genes Dev,* 33**,** 194-208.

EDGAR, B. A. & SCHUBIGER, G. 1986. Parameters controlling transcriptional activation during early Drosophila development. *Cell,* 44**,** 871-7.

EHRENBERG, M. & RIGLER, R. 1974. Rotational brownian motion and fluorescence intensify fluctuations. *Chemical Physics,* 4**,** 390-401.

EICHHORN, S. W., SUBTELNY, A. O., KRONJA, I., KWASNIESKI, J. C., ORR-WEAVER, T. L. & BARTEL, D. P. 2016. mRNA poly(A)-tail changes specified by deadenylation broadly reshape translation in Drosophila oocytes and early embryos. *Elife,* 5.

ELF, J., LI, G. W. & XIE, X. S. 2007. Probing transcription factor dynamics at the single-molecule level in a living cell. *Science,* 316**,** 1191-4.

ELLENBERGER, T. E., BRANDL, C. J., STRUHL, K. & HARRISON, S. C. 1992. The GCN4 basic region leucine zipper binds DNA as a dimer of uninterrupted alpha helices: crystal structure of the protein-DNA complex. *Cell,* 71**,** 1223-37.

ELROD-ERICKSON, M., ROULD, M. A., NEKLUDOVA, L. & PABO, C. O. 1996. Zif268 protein-DNA complex refined at 1.6 A: a model system for understanding zinc finger-DNA interactions. *Structure,* 4**,** 1171-80.

ERSHOV, D., PHAN, M. S., PYLVANAINEN, J. W., RIGAUD, S. U., LE BLANC, L., CHARLES-ORSZAG, A., CONWAY, J. R. W., LAINE, R. F., ROY, N. H., BONAZZI, D., DUMENIL, G., JACQUEMET, G. & TINEVEZ, J. Y. 2022. TrackMate 7: integrating state-of-the-art segmentation algorithms into tracking pipelines. *Nat Methods,* 19**,** 829-832.

FALVO, J. V., THANOS, D. & MANIATIS, T. 1995. Reversal of intrinsic DNA bends in the IFN beta gene enhancer by transcription factors and the architectural protein HMG I(Y). *Cell,* 83**,** 1101-11.

FAN, Y., NIKITINA, T., ZHAO, J., FLEURY, T. J., BHATTACHARYYA, R., BOUHASSIRA, E. E., STEIN, A., WOODCOCK, C. L. & SKOULTCHI, A. I. 2005. Histone H1 depletion in mammals alters global chromatin structure but causes specific changes in gene regulation. *Cell,* 123**,** 1199-212.

FERNANDEZ GARCIA, M., MOORE, C. D., SCHULZ, K. N., ALBERTO, O., DONAGUE, G., HARRISON, M. M., ZHU, H. & ZARET, K. S. 2019. Structural Features of Transcription Factors Associating with Nucleosome Binding. *Mol Cell,* 75**,** 921-932 e6.

FERRIE, J. J., KARR, J. P., TJIAN, R. & DARZACQ, X. 2022. "Structure"-function relationships in eukaryotic transcription factors: The role of intrinsically disordered regions in gene regulation. *Mol Cell,* 82**,** 3970-3984.

FOO, Y. H., NAREDI-RAINER, N., LAMB, D. C., AHMED, S. & WOHLAND, T. 2012. Factors affecting the quantification of biomolecular interactions by fluorescence cross-correlation spectroscopy. *Biophys J,* 102**,** 1174-83.

FORSTER, T. 1946. Energiewanderung und Fluoreszenz. *Naturwissenschaften,* 33**,** 166-175.

FPBASE. 2023a. *Citrine* [Online]. Available: https://www.fpbase.org/protein/VR7EN/ [Accessed 03.03.2023].

FPBASE. 2023b. *mCherry* [Online]. Available: https://www.fpbase.org/protein/ZERB6/ [Accessed 03.03.2023].

FPBASE. 2023c. *mCitrine* [Online]. Available: https://www.fpbase.org/protein/3Q37R/ [Accessed 03.03.2023].

FREDERICK, M. A., WILLIAMSON, K. E., FERNANDEZ GARCIA, M., FERRETTI, M. B., MCCARTHY, R. L., DONAHUE, G., LUZETE MONTEIRO, E., TAKENAKA, N., REYNAGA, J., KADOCH, C. & ZARET, K. S. 2023. A pioneer factor locally opens compacted chromatin to enable targeted ATP-dependent nucleosome remodeling. *Nat Struct Mol Biol,* 30, 31-37.

FRIMAN, E. T., DELUZ, C., MEIRELES-FILHO, A. C., GOVINDAN, S., GARDEUX, V., DEPLANCKE, B. & SUTER, D. M. 2019. Dynamic regulation of chromatin accessibility by pluripotency transcription factors across the cell cycle. *Elife,* 8.

FUNANE, T., HOU, S. S., ZOLTOWSKA, K. M., VAN VELUW, S. J., BEREZOVSKA, O., KUMAR, A. T. N. & BACSKAI, B. J. 2018. Selective plane illumination microscopy (SPIM) with time-domain fluorescence lifetime imaging microscopy (FLIM) for volumetric measurement of cleared mouse brain samples. *Rev Sci Instrum,* 89, 053705.

GADELLA, T. W. J., JR., VAN WEEREN, L., STOUTHAMER, J., HINK, M. A., WOLTERS, A. H. G., GIEPMANS, B. N. G., AUMONIER, S., DUPUY, J. & ROYANT, A. 2023. mScarlet3: a brilliant and fast-maturing red fluorescent protein. *Nat Methods,* 20, 541-545.

GAGLIARDI, A., MULLIN, N. P., YING TAN, Z., COLBY, D., KOUSA, A. I., HALBRITTER, F., WEISS, J. T., FELKER, A., BEZSTAROSTI, K., FAVARO, R., DEMMERS, J., NICOLIS, S. K., TOMLINSON, S. R., POOT, R. A. & CHAMBERS, I. 2013. A direct physical interaction between Nanog and Sox2 regulates embryonic stem cell self-renewal. *EMBO J,* 32, 2231-47.

GAGNON, J. A., OBBAD, K. & SCHIER, A. F. 2018. The primary role of zebrafish nanog is in extra-embryonic tissue. *Development,* 145.

GAO, L., WU, K., LIU, Z., YAO, X., YUAN, S., TAO, W., YI, L., YU, G., HOU, Z., FAN, D., TIAN, Y., LIU, J., CHEN, Z. J. & LIU, J. 2018. Chromatin Accessibility Landscape in Human Early Embryos and Its Association with Evolution. *Cell,* 173, 248-259 e15.

GAO, M., VEIL, M., ROSENBLATT, M., RIESLE, A. J., GEBHARD, A., HASS, H., BURYANOVA, L., YAMPOLSKY, L. Y., GRUNING, B., ULIANOV, S. V., TIMMER, J. & ONICHTCHOUK, D. 2022. Pluripotency factors determine gene expression repertoire at zygotic genome activation. *Nat Commun,* 13, 788.

GARCIA, D. A., FETTWEIS, G., PRESMAN, D. M., PAAKINAHO, V., JARZYNSKI, C., UPADHYAYA, A. & HAGER, G. L. 2021. Power-law behavior of transcription factor dynamics at the single-molecule level implies a continuum affinity model. *Nucleic Acids Res,* 49, 6605-6620.

GASSLER, J., KOBAYASHI, W., GASPAR, I., RUANGROENGKULRITH, S., MOHANAN, A., GOMEZ HERNANDEZ, L., KRAVCHENKO, P., KUMMECKE, M., LALIC, A., RIFEL, N., ASHBURN, R. J., ZACZEK, M., VALLOT, A., CUENCA RICO, L., LADSTATTER, S. & TACHIBANA, K. 2022. Zygotic genome activation by the totipotency pioneer factor Nr5a2. *Science*, eabn7478.

GEBHARDT, J. C., SUTER, D. M., ROY, R., ZHAO, Z. W., CHAPMAN, A. R., BASU, S., MANIATIS, T. & XIE, X. S. 2013. Single-molecule imaging of transcription factor binding to DNA in live mammalian cells. *Nat Methods,* 10, 421-6.

GENETOOLS. 2016. *GTBlue* [Online]. Available: https://www.gene-tools.com/sites/default/files/GTBlue.pdf [Accessed 20.04.23].

GIGUERE, V., ONG, E. S., SEGUI, P. & EVANS, R. M. 1987. Identification of a receptor for the morphogen retinoic acid. *Nature,* 330, 624-9.

GIRALDEZ, A. J., MISHIMA, Y., RIHEL, J., GROCOCK, R. J., VAN DONGEN, S., INOUE, K., ENRIGHT, A. J. & SCHIER, A. F. 2006. Zebrafish MiR-430 promotes deadenylation and clearance of maternal mRNAs. *Science,* 312, 75-9.

GOMEZ-GARCIA, P. A., PORTILLO-LEDESMA, S., NEGUEMBOR, M. V., PESARESI, M., OWEIS, W., ROHRLICH, T., WIESER, S., MESHORER, E., SCHLICK, T., COSMA, M. P. & LAKADAMYALI, M. 2021. Mesoscale Modeling and Single-Nucleosome Tracking Reveal Remodeling of Clutch Folding and Dynamics in Stem Cell Differentiation. *Cell Rep,* 34**,** 108614.

GONZALEZ-SANDOVAL, A. & GASSER, S. M. 2016. On TADs and LADs: Spatial Control Over Gene Expression. *Trends in Genetics,* 32**,** 485-495.

GRAHAM, T. G. W., FERRIE, J. J., DAILEY, G. M., TJIAN, R. & DARZACQ, X. 2022. Detecting molecular interactions in live-cell single-molecule imaging with proximity-assisted photoactivation (PAPA). *Elife,* 11.

GRATTON , E., BREUSEGEM, S., SUTIN, J., D. B., , RUAN, Q. & BARRY, N., P. 2003. Fluorescence lifetime imaging for the two-photon microscope: time-domain and frequency-domain methods. *Journal of Biomedical Optics,* 8**,** 381-390.

GREEN, S., WALTER, P., KUMAR, V., KRUST, A., BORNERT, J. M., ARGOS, P. & CHAMBON, P. 1986. Human oestrogen receptor cDNA: sequence, expression and homology to v-erb-A. *Nature,* 320**,** 134-9.

GREER, E. L. & SHI, Y. 2012. Histone methylation: a dynamic mark in health, disease and inheritance. *Nat Rev Genet,* 13**,** 343-57.

GRIESBECK, O., BAIRD, G. S., CAMPBELL, R. E., ZACHARIAS, D. A. & TSIEN, R. Y. 2001. Reducing the environmental sensitivity of yellow fluorescent protein. Mechanism and applications. *J Biol Chem,* 276**,** 29188-94.

GROSSMAN, S. R., ZHANG, X., WANG, L., ENGREITZ, J., MELNIKOV, A., ROGOV, P., TEWHEY, R., ISAKOVA, A., DEPLANCKE, B., BERNSTEIN, B. E., MIKKELSEN, T. S. & LANDER, E. S. 2017. Systematic dissection of genomic features determining transcription factor binding and enhancer function. *Proc Natl Acad Sci U S A,* 114**,** E1291-E1300.

GRUSCHUS, J. M., TSAO, D. H., WANG, L. H., NIRENBERG, M. & FERRETTI, J. A. 1997. Interactions of the vnd/NK-2 homeodomain with DNA by nuclear magnetic resonance spectroscopy: basis of binding specificity. *Biochemistry,* 36**,** 5372-80.

GUO, F., LI, X., LIANG, D., LI, T., ZHU, P., GUO, H., WU, X., WEN, L., GU, T. P., HU, B., WALSH, C. P., LI, J., TANG, F. & XU, G. L. 2014. Active and passive demethylation of male and female pronuclear DNA in the mammalian zygote. *Cell Stem Cell,* 15**,** 447-459.

GUSS, K. A., NELSON, C. E., HUDSON, A., KRAUS, M. E. & CARROLL, S. B. 2001. Control of a genetic regulatory network by a selector gene. *Science,* 292**,** 1164-7.

GUVEN-OZKAN, T., NISHI, Y., ROBERTSON, S. M. & LIN, R. 2008. Global transcriptional repression in C. elegans germline precursors by regulated sequestration of TAF-4. *Cell,* 135**,** 149-60.

HABERLE, V., LI, N., HADZHIEV, Y., PLESSY, C., PREVITI, C., NEPAL, C., GEHRIG, J., DONG, X., AKALIN, A., SUZUKI, A. M., VAN, I. W. F. J., ARMANT, O., FERG, M., STRAHLE, U., CARNINCI, P., MULLER, F. & LENHARD, B. 2014. Two independent transcription initiation codes overlap on vertebrate core promoters. *Nature,* 507**,** 381-385.

HADZHIEV, Y., QURESHI, H. K., WHEATLEY, L., COOPER, L., JASIULEWICZ, A., VAN NGUYEN, H., WRAGG, J. W., POOVATHUMKADAVIL, D., CONIC, S., BAJAN, S., SIK, A., HUTVAGNER, G., TORA, L., GAMBUS, A., FOSSEY, J. S. & MULLER, F. 2019. A cell cycle-coordinated Polymerase II transcription compartment encompasses gene expression before global genome activation. *Nat Commun,* 10**,** 691.

HADZHIEV, Y., WHEATLEY, L., COOPER, L., ANSALONI, F., WHALLEY, C., CHEN, Z., FINAURINI, S., GUSTINCICH, S., SANGES, R., BURGESS, S., BEGGS, A. & MULLER, F. 2023. The miR-430 locus with extreme promoter density forms a transcription body during the minor wave of zygotic genome activation. *Dev Cell,* 58**,** 155-170 e8.

HALAVATYI, A. & TERJUNG, S. 2017. Measuring Molecular Dynamics and Interactions by Förster Resonance Energy Transfer (FRET). *Standard and Super-Resolution Bioimaging Data Analysis.*

HAMATANI, T., CARTER, M. G., SHAROV, A. A. & KO, M. S. H. 2004. Dynamics of Global Gene Expression Changes during Mouse Preimplantation Development. *Developmental Cell,* 6**,** 117-131.

HANSEN, J. L. & COHEN, B. A. 2022. A quantitative metric of pioneer activity reveals that HNF4A has stronger in vivo pioneer activity than FOXA1. *Genome Biol,* 23**,** 221.

HANSEN, L., MARINO-RAMIREZ, L. & LANDSMAN, D. 2012. Differences in local genomic context of bound and unbound motifs. *Gene,* 506**,** 125-34.

HARRIS, C. R., MILLMAN, K. J., VAN DER WALT, S. J., GOMMERS, R., VIRTANEN, P., COURNAPEAU, D., WIESER, E., TAYLOR, J., BERG, S., SMITH, N. J., KERN, R., PICUS, M., HOYER, S., VAN KERKWIJK, M. H., BRETT, M., HALDANE, A., DEL RÍO, J. F., WIEBE, M., PETERSON, P., GÉRARD-MARCHANT, P., SHEPPARD, K., REDDY, T., WECKESSER, W., ABBASI, H., GOHLKE, C. & OLIPHANT, T. E. 2020. Array programming with NumPy. *Nature,* 585**,** 357-362.

HARRISON, M. M., LI, X. Y., KAPLAN, T., BOTCHAN, M. R. & EISEN, M. B. 2011. Zelda binding in the early Drosophila melanogaster embryo marks regions subsequently activated at the maternal-to-zygotic transition. *PLoS Genet,* 7**,** e1002266.

HARVEY, S. A., SEALY, I., KETTLEBOROUGH, R., FENYES, F., WHITE, R., STEMPLE, D. & SMITH, J. C. 2013. Identification of the zebrafish maternal and paternal transcriptomes. *Development,* 140**,** 2703-10.

HEMMERICH, P., SCHMIEDEBERG, L. & DIEKMANN, S. 2011. Dynamic as well as stable protein interactions contribute to genome function and maintenance. *Chromosome Res,* 19**,** 131-51.

HENDRICKSON, P. G., DORAIS, J. A., GROW, E. J., WHIDDON, J. L., LIM, J. W., WIKE, C. L., WEAVER, B. D., PFLUEGER, C., EMERY, B. R., WILCOX, A. L., NIX, D. A., PETERSON, C. M., TAPSCOTT, S. J., CARRELL, D. T. & CAIRNS, B. R. 2017. Conserved roles of mouse DUX and human DUX4 in activating cleavage-stage genes and MERVL/HERVL retrotransposons. *Nat Genet,* 49**,** 925-934.

HENIKOFF, S. 2008. Nucleosome destabilization in the epigenetic regulation of gene expression. *Nat Rev Genet,* 9**,** 15-26.

HENIKOFF, S. 2009. Labile H3.3+H2A.Z nucleosomes mark 'nucleosome-free regions'. *Nat Genet,* 41**,** 865-6.

HEYN, P., KIRCHER, M., DAHL, A., KELSO, J., TOMANCAK, P., KALINKA, A. T. & NEUGEBAUER, K. M. 2014. The earliest transcribed zygotic genes are short, newly evolved, and different across species. *Cell Rep,* 6**,** 285-92.

HICKEY, G. J., WIKE, C. L., NIE, X., GUO, Y., TAN, M., MURPHY, P. J. & CAIRNS, B. R. 2022. Establishment of developmental gene silencing by ordered polycomb complex recruitment in early zebrafish embryos. *Elife,* 11.

HILBERT, L., SATO, Y., KUZNETSOVA, K., BIANUCCI, T., KIMURA, H., JULICHER, F., HONIGMANN, A., ZABURDAEV, V. & VASTENHOUW, N. L. 2021. Transcription organizes euchromatin via microphase separation. *Nat Commun,* 12**,** 1360.

HINDE, E., CARDARELLI, F., DIGMAN, M. A., KERSHNER, A., KIMBLE, J. & GRATTON, E. 2011. The impact of mitotic versus interphase chromatin architecture on the molecular flow of EGFP by pair correlation analysis. *Biophys J,* 100**,** 1829-36.

HOLLAND, P. W., BOOTH, H. A. & BRUFORD, E. A. 2007. Classification and nomenclature of all human homeobox genes. *BMC Biol,* 5**,** 47.

HOLLENBERG, S. M., WEINBERGER, C., ONG, E. S., CERELLI, G., ORO, A., LEBO, R., THOMPSON, E. B., ROSENFELD, M. G. & EVANS, R. M. 1985. Primary structure and expression of a functional human glucocorticoid receptor cDNA. *Nature,* 318**,** 635-41.

HU, C. D., CHINENOV, Y. & KERPPOLA, T. K. 2002. Visualization of interactions among bZIP and Rel family proteins in living cells using bimolecular fluorescence complementation. *Mol Cell,* 9**,** 789-98.

HU, S., METCALF, E., MAHAT, D. B., CHAN, L., SOHAL, N., CHAKRABORTY, M., HAMILTON, M., SINGH, A., SINGH, A., LEES, J. A., SHARP, P. A. & GARG, S. 2022. Transcription factor antagonism regulates heterogeneity in embryonic stem cell states. *Mol Cell,* 82**,** 4410-4427 e12.

HUG, C. B., GRIMALDI, A. G., KRUSE, K. & VAQUERIZAS, J. M. 2017. Chromatin Architecture Emerges during Zygotic Genome Activation Independent of Transcription. *Cell,* 169**,** 216-228 e19.

HUISKEN, J., SWOGER, J., DEL BENE, F., WITTBRODT, J. & STELZER, E. H. 2004. Optical sectioning deep inside live embryos by selective plane illumination microscopy. *Science,* 305**,** 1007-9.

ILLINGWORTH, R. S. 2019. Chromatin folding and nuclear architecture: PRC1 function in 3D. *Curr Opin Genet Dev,* 55**,** 82-90.

INOUE, A., JIANG, L., LU, F., SUZUKI, T. & ZHANG, Y. 2017. Maternal H3K27me3 controls DNA methylation-independent imprinting. *Nature,* 547**,** 419-424.

IP, Y. T., PARK, R. E., KOSMAN, D., BIER, E. & LEVINE, M. 1992. The dorsal gradient morphogen regulates stripes of rhomboid expression in the presumptive neuroectoderm of the Drosophila embryo. *Genes Dev,* 6**,** 1728-39.

ISBEL, L., GRAND, R. S. & SCHUBELER, D. 2022. Generating specificity in genome regulation through transcription factor sensitivity to chromatin. *Nat Rev Genet,* 23**,** 728-740.

IURLARO, M., STADLER, M. B., MASONI, F., JAGANI, Z., GALLI, G. G. & SCHUBELER, D. 2021. Mammalian SWI/SNF continuously restores local accessibility to chromatin. *Nat Genet,* 53**,** 279-287.

IWAFUCHI-DOI, M., DONAHUE, G., KAKUMANU, A., WATTS, J. A., MAHONY, S., PUGH, B. F., LEE, D., KAESTNER, K. H. & ZARET, K. S. 2016. The Pioneer Transcription Factor FoxA Maintains an Accessible Nucleosome Configuration at Enhancers for Tissue-Specific Gene Activation. *Mol Cell,* 62**,** 79-91.

IZEDDIN, I., RECAMIER, V., BOSANAC, L., CISSE, II, BOUDARENE, L., DUGAST-DARZACQ, C., PROUX, F., BENICHOU, O., VOITURIEZ, R., BENSAUDE, O., DAHAN, M. & DARZACQ, X. 2014. Single-molecule tracking in live cells reveals distinct target-search strategies of transcription factors in the nucleus. *Elife,* 3.

JABLONSKI, A. 1933. Efficiency of Anti-Stokes Fluorescence in Dyes. *Nature,* 131**,** 839-840.

JAMESON, D. M., GRATTON, E. & HALL, R.D. 1984. The Measurement and Analysis of Heterogeneous Emissions by Multifrequency Phase and Modulation Fluorometry. *Appl Spectrosc Rev,* 20: 55–106.

JANG, M. K., MOCHIZUKI, K., ZHOU, M., JEONG, H. S., BRADY, J. N. & OZATO, K. 2005. The bromodomain protein Brd4 is a positive regulatory component of P-TEFb and stimulates RNA polymerase II-dependent transcription. *Mol Cell,* 19**,** 523-34.

JARES-ERIJMAN, E. A. & JOVIN, T. M. 2003. FRET imaging. *Nat Biotechnol,* 21**,** 1387-95.

JEVTIC, P. & LEVY, D. L. 2015. Nuclear size scaling during Xenopus early development contributes to midblastula transition timing. *Curr Biol,* 25**,** 45-52.

JEVTIC, P. & LEVY, D. L. 2017. Both Nuclear Size and DNA Amount Contribute to Midblastula Transition Timing in Xenopus laevis. *Sci Rep,* 7**,** 7908.

JING, D., HUANG, Y., LIU, X., SIA, K. C. S., ZHANG, J. C., TAI, X., WANG, M., TOSCAN, C. E., MCCALMONT, H., EVANS, K., MAYOH, C., POULOS, R. C., SPAN, M., MI, J., ZHANG, C., WONG, J. W. H., BECK, D., PIMANDA, J. E. & LOCK, R. B. 2018. Lymphocyte-Specific Chromatin Accessibility Pre-determines Glucocorticoid Resistance in Acute Lymphoblastic Leukemia. *Cancer Cell,* 34**,** 906-921 e8.

JOSEPH, S. R., PÁLFY, M., HILBERT, L., KUMAR, M., KARSCHAU, J., ZABURDAEV, V., SHEVCHENKO, A. & VASTENHOUW, N. L. 2017. Competition between histone and transcription factor binding regulates the onset of transcription in zebrafish embryos. *eLife,* 6**,** e23326.

JUKAM, D., SHARIATI, S. A. M. & SKOTHEIM, J. M. 2017. Zygotic Genome Activation in Vertebrates. *Developmental Cell,* 42**,** 316-332.

KAAIJ, L. J., MOKRY, M., ZHOU, M., MUSHEEV, M., GEEVEN, G., MELQUIOND, A. S., DE JESUS DOMINGUES, A. M., DE LAAT, W., NIEHRS, C., SMITH, A. D. & KETTING, R. F. 2016. Enhancers reside in a unique epigenetic environment during early zebrafish development. *Genome Biol,* 17**,** 146.

KAAIJ, L. J. T., VAN DER WEIDE, R. H., KETTING, R. F. & DE WIT, E. 2018. Systemic Loss and Gain of Chromatin Architecture throughout Zebrafish Development. *Cell Rep,* 24**,** 1-10 e4.

KAMACHI, Y., UCHIKAWA, M., TANOUCHI, A., SEKIDO, R. & KONDOH, H. 2001. Pax6 and SOX2 form a co-DNA-binding partner complex that regulates initiation of lens development. *Genes Dev,* 15**,** 1272-86.

KANE, L., WILLIAMSON, I., FLYAMER, I. M., KUMAR, Y., HILL, R. E., LETTICE, L. A. & BICKMORE, W. A. 2022. Cohesin is required for long-range enhancer action at the Shh locus. *Nat Struct Mol Biol,* 29**,** 891-897.

KAUR, G., COSTA, M. W., NEFZGER, C. M., SILVA, J., FIERRO-GONZALEZ, J. C., POLO, J. M., BELL, T. D. & PLACHTA, N. 2013. Probing transcription factor diffusion dynamics in the living mammalian embryo with photoactivatable fluorescence correlation spectroscopy. *Nat Commun,* 4**,** 1637.

KELLER, A. D. & MANIATIS, T. 1992. Only two of the five zinc fingers of the eukaryotic transcriptional repressor PRDI-BF1 are required for sequence-specific DNA binding. *Mol Cell Biol,* 12**,** 1940-9.

KIEFFER-KWON, K. R., NIMURA, K., RAO, S. S. P., XU, J., JUNG, S., PEKOWSKA, A., DOSE, M., STEVENS, E., MATHE, E., DONG, P., HUANG, S. C., RICCI, M. A., BARANELLO, L., ZHENG, Y., TOMASSONI ARDORI, F., RESCH, W., STAVREVA, D., NELSON, S., MCANDREW, M., CASELLAS, A., FINN, E., GREGORY, C., ST HILAIRE, B. G., JOHNSON, S. M., DUBOIS, W., COSMA, M. P., BATCHELOR, E., LEVENS, D., PHAIR, R. D., MISTELI, T., TESSAROLLO, L., HAGER, G., LAKADAMYALI, M., LIU, Z., FLOER, M., SHROFF, H., AIDEN, E. L. & CASELLAS, R. 2017. Myc Regulates Chromatin Decompaction and Nuclear Architecture during B Cell Activation. *Mol Cell,* 67**,** 566-578 e10.

KIMMEL, C. B., BALLARD, W. W., KIMMEL, S. R., ULLMANN, B. & SCHILLING, T. F. 1995. Stages of embryonic development of the zebrafish. *Developmental Dynamics,* 203**,** 253-310.

KING, H. W. & KLOSE, R. J. 2017. The pioneer factor OCT4 requires the chromatin remodeller BRG1 to support gene regulatory element function in mouse embryonic stem cells. *Elife,* 6.

KISSINGER, C. R., LIU, B. S., MARTIN-BLANCO, E., KORNBERG, T. B. & PABO, C. O. 1990. Crystal structure of an engrailed homeodomain-DNA complex at 2.8 A resolution: a framework for understanding homeodomain-DNA interactions. *Cell,* 63**,** 579-90.

KLEMM, S. L., SHIPONY, Z. & GREENLEAF, W. J. 2019. Chromatin accessibility and the regulatory epigenome. *Nat Rev Genet,* 20**,** 207-220.

KLOSIN, A., OLTSCH, F., HARMON, T., HONIGMANN, A., JULICHER, F., HYMAN, A. A. & ZECHNER, C. 2020. Phase separation provides a mechanism to reduce noise in cells. *Science,* 367**,** 464-468.

KLUG, A. 1999. Zinc finger peptides for the regulation of gene expression. *J Mol Biol,* 293**,** 215-8.

KNOX, R. S. & VAN AMERONGEN, H. 2002. Refractive Index Dependence of the Förster Resonance Excitation Transfer Rate. *The Journal of Physical Chemistry B,* 106**,** 5289-5293.

KRAUSE, M., FIRE, A., HARRISON, S. W., PRIESS, J. & WEINTRAUB, H. 1990. CeMyoD accumulation defines the body wall muscle cell fate during C. elegans embryogenesis. *Cell,* 63**,** 907-19.

KREMERS, G. J., GOEDHART, J., VAN MUNSTER, E. B. & GADELLA, T. W., JR. 2006. Cyan and yellow super fluorescent proteins with improved brightness, protein folding, and FRET Forster radius. *Biochemistry,* 45**,** 6570-80.

KRIEGER, J., TÓTH, K. & LANGOWSKI., J. 2014. Practical Course Biophysics: Fluorescence Correlation Spectroscopy. Heidelberg: DKFZ.

KRMPOT, A. J., NIKOLIC, S. N., OASA, S., PAPADOPOULOS, D. K., VITALI, M., OURA, M., MIKUNI, S., THYBERG, P., TISA, S., KINJO, M., NILSSON, L., TERENIUS, L., RIGLER, R. & VUKOJEVIC, V. 2019. Functional Fluorescence Microscopy Imaging: Quantitative Scanning-Free Confocal Fluorescence Microscopy for the Characterization of Fast Dynamic Processes in Live Cells. *Anal Chem,* 91**,** 11129-11137.

KRONJA, I., YUAN, B., EICHHORN, S. W., DZEYK, K., KRIJGSVELD, J., BARTEL, D. P. & ORR-WEAVER, T. L. 2014. Widespread changes in the posttranscriptional landscape at the Drosophila oocyte-to-embryo transition. *Cell Rep,* 7**,** 1495-1508.

KUBIK, S., BRUZZONE, M. J., JACQUET, P., FALCONE, J. L., ROUGEMONT, J. & SHORE, D. 2015. Nucleosome Stability Distinguishes Two Different Promoter Types at All Protein-Coding Genes in Yeast. *Mol Cell,* 60**,** 422-34.

KULIC, I. M. & SCHIESSEL, H. 2008. Opening and closing DNA: theories on the nucleosome. *DNA Interactions with Polymers and Surfactants. RS Dias and B. Lindman, editors. Wiley, London, UK***,** 173-208.

KUZNETSOVA, K., CHABOT, N. M., UGOLINI, M., WU, E., LALIT, M., ODA, H., SATO, Y., KIMURA, H., JUG, F. & VASTENHOUW, N. L. 2023. Nanog organizes transcription bodies. *Curr Biol,* 33**,** 164-173 e5.

LADSTATTER, S. & TACHIBANA, K. 2019. Genomic insights into chromatin reprogramming to totipotency in embryos. *J Cell Biol,* 218**,** 70-82.

LAM, A. J., ST-PIERRE, F., GONG, Y., MARSHALL, J. D., CRANFILL, P. J., BAIRD, M. A., MCKEOWN, M. R., WIEDENMANN, J., DAVIDSON, M. W., SCHNITZER, M. J., TSIEN, R. Y. & LIN, M. Z. 2012a. Improving FRET dynamic range with bright green and red fluorescent proteins. *Nat Methods,* 9**,** 1005-12.

LAM, C. S., MISTRI, T. K., FOO, Y. H., SUDHAHARAN, T., GAN, H. T., RODDA, D., LIM, L. H., CHOU, C., ROBSON, P., WOHLAND, T. & AHMED, S. 2012b. DNA-dependent Oct4-Sox2 interaction and diffusion properties characteristic of the pluripotent cell state revealed by fluorescence spectroscopy. *Biochem J,* 448**,** 21-33.

LANCASTER, A. K., NUTTER-UPHAM, A., LINDQUIST, S. & KING, O. D. 2014. PLAAC: a web and command-line application to identify proteins with prion-like amino acid composition. *Bioinformatics,* 30**,** 2501-2.

LANDGRAF, D., OKUMUS, B., CHIEN, P., BAKER, T. A. & PAULSSON, J. 2012. Segregation of molecules at cell division reveals native protein localization. *Nat Methods,* 9**,** 480-2.

LANDRY, J. J., PYL, P. T., RAUSCH, T., ZICHNER, T., TEKKEDIL, M. M., STUTZ, A. M., JAUCH, A., AIYAR, R. S., PAU, G., DELHOMME, N., GAGNEUR, J., KORBEL, J. O., HUBER, W. & STEINMETZ, L. M. 2013. The genomic and transcriptomic landscape of a HeLa cell line. *G3 (Bethesda),* 3**,** 1213-24.

LANDSCHULZ, W. H., JOHNSON, P. F. & MCKNIGHT, S. L. 1988. The leucine zipper: a hypothetical structure common to a new class of DNA binding proteins. *Science,* 240**,** 1759-64.

LARSON, E. D., KOMORI, H., GIBSON, T. J., OSTGAARD, C. M., HAMM, D. C., SCHNELL, J. M., LEE, C. Y. & HARRISON, M. M. 2021. Cell-type-specific chromatin occupancy by the pioneer factor Zelda drives key developmental transitions in Drosophila. *Nat Commun,* 12**,** 7153.

LAUE, K., RAJSHEKAR, S., COURTNEY, A. J., LEWIS, Z. A. & GOLL, M. G. 2019. The maternal to zygotic transition regulates genome-wide heterochromatin establishment in the zebrafish embryo. *Nat Commun,* 10**,** 1551.

LEE, D. Y., HAYES, J. J., PRUSS, D. & WOLFFE, A. P. 1993. A positive role for histone acetylation in transcription factor access to nucleosomal DNA. *Cell,* 72**,** 73-84.

LEE, H. H. & FRASCH, M. 2005. Nuclear integration of positive Dpp signals, antagonistic Wg inputs and mesodermal competence factors during Drosophila visceral mesoderm induction. *Development,* 132**,** 1429-42.

LEE, J., LIU, Z., SUZUKI, P. H., AHRENS, J. F., LAI, S., LU, X., GUAN, S. & ST-PIERRE, F. 2020. Versatile phenotype-activated cell sorting. *Sci Adv,* 6.

LEE, M. T., BONNEAU, A. R., TAKACS, C. M., BAZZINI, A. A., DIVITO, K. R., FLEMING, E. S. & GIRALDEZ, A. J. 2013. Nanog, Pou5f1 and SoxB1 activate zygotic gene expression during the maternal-to-zygotic transition. *Nature,* 503**,** 360-364.

LEICHSENRING, M., MAES, J., MÖSSNER, R., DRIEVER, W. & ONICHTCHOUK, D. 2013. Pou5f1 Transcription Factor Controls Zygotic Gene Activation In Vertebrates. *Science,* 341**,** 1005-1009.

LERAY, A., SPRIET, C., TRINEL, D., USSON, Y. & HELIOT, L. 2012. Generalization of the polar representation in time domain fluorescence lifetime imaging microscopy for biological applications: practical implementation. *J Microsc,* 248**,** 66-76.

LETTICE, L. A., WILLIAMSON, I., WILTSHIRE, J. H., PELUSO, S., DEVENNEY, P. S., HILL, A. E., ESSAFI, A., HAGMAN, J., MORT, R., GRIMES, G., DEANGELIS, C. L. & HILL, R. E. 2012. Opposing functions of the ETS factor family define Shh spatial expression in limb buds and underlie polydactyly. *Dev Cell,* 22**,** 459-67.

LEVINE, M. 2010. Transcriptional enhancers in animal development and evolution. *Curr Biol,* 20**,** R754-63.

LI, D. D., AMEER-BEG, S., ARLT, J., TYNDALL, D., WALKER, R., MATTHEWS, D. R., VISITKUL, V., RICHARDSON, J. & HENDERSON, R. K. 2012. Time-domain fluorescence lifetime imaging techniques suitable for solid-state imaging sensor arrays. *Sensors (Basel),* 12**,** 5650-69.

LI, D. U., RAE, B., ANDREWS, R., ARLT, J. & HENDERSON, R. 2010. Hardware implementation algorithm and error analysis of high-speed fluorescence lifetime sensing systems using center-of-mass method. *J Biomed Opt,* 15**,** 017006.

LI, G., LEVITUS, M., BUSTAMANTE, C. & WIDOM, J. 2005. Rapid spontaneous accessibility of nucleosomal DNA. *Nat Struct Mol Biol,* 12**,** 46-53.

LI, G. & WIDOM, J. 2004. Nucleosomes facilitate their own invasion. *Nat Struct Mol Biol,* 11**,** 763-9.

LI, L., GUO, F., GAO, Y., REN, Y., YUAN, P., YAN, L., LI, R., LIAN, Y., LI, J., HU, B., GAO, J., WEN, L., TANG, F. & QIAO, J. 2018. Single-cell multi-omics sequencing of human early embryos. *Nat Cell Biol,* 20**,** 847-858.

LI, S., ZHENG, E. B., ZHAO, L. & LIU, S. 2019. Nonreciprocal and Conditional Cooperativity Directs the Pioneer Activity of Pluripotency Transcription Factors. *Cell Rep,* 28**,** 2689-2703 e4.

LIANG, H. L., NIEN, C. Y., LIU, H. Y., METZSTEIN, M. M., KIROV, N. & RUSHLOW, C. 2008. The zinc-finger protein Zelda is a key activator of the early zygotic genome in Drosophila. *Nature,* 456**,** 400-3.

LIBER, D., DOMASCHENZ, R., HOLMQVIST, P. H., MAZZARELLA, L., GEORGIOU, A., LELEU, M., FISHER, A. G., LABOSKY, P. A. & DILLON, N. 2010. Epigenetic priming of a pre-B cell-specific enhancer through binding of Sox2 and Foxd3 at the ESC stage. *Cell Stem Cell,* 7**,** 114-26.

LIPPMAN, M. E., HALTERMAN, R. H., LEVENTHAL, B. G., PERRY, S. & THOMPSON, E. B. 1973. Glucocorticoid-binding proteins in human acute lymphoblastic leukemic blast cells. *J Clin Invest,* 52**,** 1715-25.

LIU, B., MAVROVA, S. N., VAN DEN BERG, J., KRISTENSEN, S. K., MANTOVANELLI, L., VEENHOFF, L. M., POOLMAN, B. & BOERSMA, A. J. 2018a. Influence of Fluorescent Protein Maturation on FRET Measurements in Living Cells. *ACS Sens,* 3**,** 1735-1742.

LIU, G., WANG, W., HU, S., WANG, X. & ZHANG, Y. 2018b. Inherited DNA methylation primes the establishment of accessible chromatin during genome activation. *Genome Res,* 28**,** 998-1007.

LIU, S., ZIBETTI, C., WAN, J., WANG, G., BLACKSHAW, S. & QIAN, J. 2017. Assessing the model transferability for prediction of transcription factor binding sites based on chromatin accessibility. *BMC Bioinformatics,* 18**,** 355.

LIU, X., WANG, C., LIU, W., LI, J., LI, C., KOU, X., CHEN, J., ZHAO, Y., GAO, H., WANG, H., ZHANG, Y., GAO, Y. & GAO, S. 2016. Distinct features of H3K4me3 and H3K27me3 chromatin domains in pre-implantation embryos. *Nature,* 537**,** 558-562.

LIU, Z., LEGANT, W. R., CHEN, B.-C., LI, L., GRIMM, J. B., LAVIS, L. D., BETZIG, E. & TJIAN, R. 2014a. 3D imaging of Sox2 enhancer clusters in embryonic stem cells. *eLife,* 3**,** e04236-e04236.

LIU, Z., LEGANT, W. R., CHEN, B. C., LI, L., GRIMM, J. B., LAVIS, L. D., BETZIG, E. & TJIAN, R. 2014b. 3D imaging of Sox2 enhancer clusters in embryonic stem cells. *Elife,* 3**,** e04236.

LIU, Z. & TJIAN, R. 2018. Visualizing transcription factor dynamics in living cells. *The Journal of Cell Biology,* 217**,** 1181-1191.

LORD, S. J., LEE, H. L. & MOERNER, W. E. 2010. Single-molecule spectroscopy and imaging of biomolecules in living cells. *Anal Chem,* 82**,** 2192-203.

LOTT, S. E., VILLALTA, J. E., SCHROTH, G. P., LUO, S., TONKIN, L. A. & EISEN, M. B. 2011. Noncanonical compensation of zygotic X transcription in early Drosophila melanogaster development revealed through single-embryo RNA-seq. *PLoS Biol,* 9**,** e1000590.

LU, F., LIU, Y., INOUE, A., SUZUKI, T., ZHAO, K. & ZHANG, Y. 2016. Establishing Chromatin Regulatory Landscape during Mouse Preimplantation Development. *Cell,* 165**,** 1375-1388.

LUISI, B. F., XU, W. X., OTWINOWSKI, Z., FREEDMAN, L. P., YAMAMOTO, K. R. & SIGLER, P. B. 1991. Crystallographic analysis of the interaction of the glucocorticoid receptor with DNA. *Nature,* 352**,** 497-505.

LUKINAVIČIUS, G., BLAUKOPF, C., PERSHAGEN, E., SCHENA, A., REYMOND, L., DERIVERY, E., GONZALEZ-GAITAN, M., D'ESTE, E., HELL, S. W., WOLFRAM GERLICH, D. & JOHNSSON, K. 2015. SiR–Hoechst is a far-red DNA stain for live-cell nanoscopy. *Nature Communications,* 6**,** 8497.

LUND, E., LIU, M., HARTLEY, R. S., SHEETS, M. D. & DAHLBERG, J. E. 2009. Deadenylation of maternal mRNAs mediated by miR-427 in Xenopus laevis embryos. *RNA,* 15**,** 2351-63.

LUNDE, K., BELTING, H. G. & DRIEVER, W. 2004. Zebrafish pou5f1/pou2, homolog of mammalian Oct4, functions in the endoderm specification cascade. *Curr Biol,* 14**,** 48-55.

LUO, H., LI, X., CLAYCOMB, J. M. & LIPSHITZ, H. D. 2016. The Smaug RNA-Binding Protein Is Essential for microRNA Synthesis During the Drosophila Maternal-to-Zygotic Transition. *G3 (Bethesda),* 6**,** 3541-3551.

LUZETE-MONTEIRO, E. & ZARET, K. S. 2022. Structures and consequences of pioneer factor binding to nucleosomes. *Curr Opin Struct Biol,* 75**,** 102425.

MACQUARRIE, K. L., FONG, A. P., MORSE, R. H. & TAPSCOTT, S. J. 2011. Genome-wide transcription factor binding: beyond direct target regulation. *Trends Genet,* 27**,** 141-8.

MAEKAWA, T., SAKURA, H., SUDO, T. & ISHII, S. 1989. Putative metal finger structure of the human immunodeficiency virus type 1 enhancer binding protein HIV-EP1. *J Biol Chem,* 264**,** 14591-3.

MAGDE, D., ELSON, E. & WEBB, W. W. 1972. Thermodynamic Fluctuations in a Reacting System---Measurement by Fluorescence Correlation Spectroscopy. *Physical Review Letters,* 29**,** 705-708.

MANGELSDORF, D. J., ONG, E. S., DYCK, J. A. & EVANS, R. M. 1990. Nuclear receptor that identifies a novel retinoic acid response pathway. *Nature,* 345**,** 224-9.

MANSISIDOR, A. R. & RISCA, V. I. 2022. Chromatin accessibility: methods, mechanisms, and biological insights. *Nucleus,* 13**,** 236-276.

MATHAVAN, S., LEE, S. G., MAK, A., MILLER, L. D., MURTHY, K. R., GOVINDARAJAN, K. R., TONG, Y., WU, Y. L., LAM, S. H., YANG, H., RUAN, Y., KORZH, V., GONG, Z., LIU, E. T. & LUFKIN, T. 2005. Transcriptome analysis of zebrafish embryogenesis using microarrays. *PLoS Genet,* 1**,** 260-76.

MATSUMOTO, S., CAVADINI, S., BUNKER, R. D., GRAND, R. S., POTENZA, A., RABL, J., YAMAMOTO, J., SCHENK, A. D., SCHUBELER, D., IWAI, S., SUGASAWA, K., KURUMIZAKA, H. & THOMA, N. H. 2019. DNA damage detection in nucleosomes involves DNA register shifting. *Nature,* 571**,** 79-84.

MAZZA, D., ABERNATHY, A., GOLOB, N., MORISAKI, T. & MCNALLY, J. G. 2012. A benchmark for chromatin binding measurements in live cells. *Nucleic Acids Res,* 40**,** e119.

MCCLELAND, M. L. & O'FARRELL, P. H. 2008. RNAi of mitotic cyclins in Drosophila uncouples the nuclear and centrosome cycle. *Curr Biol,* 18**,** 245-54.

MCCULLOCK, T. W., MACLEAN, D. M. & KAMMERMEIER, P. J. 2020. Comparing the performance of mScarlet-I, mRuby3, and mCherry as FRET acceptors for mNeonGreen. *PLoS One,* 15**,** e0219886.

MCDANIEL, S. L., GIBSON, T. J., SCHULZ, K. N., FERNANDEZ GARCIA, M., NEVIL, M., JAIN, S. U., LEWIS, P. W., ZARET, K. S. & HARRISON, M. M. 2019. Continued Activity of the Pioneer Factor Zelda Is Required to Drive Zygotic Genome Activation. *Molecular Cell,* 74**,** 185-195.e4.

MCKINNEY, W. Data Structures for Statistical Computing in Python. *In:* VAN DER WALT, S., MILLMAN, JARROD, ed. 9th Python in Science Conference, 2010. 56-61.

MCLAUGHLIN, K., FLYAMER, I. M., THOMSON, J. P., MJOSENG, H. K., SHUKLA, R., WILLIAMSON, I., GRIMES, G. R., ILLINGWORTH, R. S., ADAMS, I. R., PENNINGS, S., MEEHAN, R. R. & BICKMORE, W. A. 2019. DNA Methylation Directs Polycomb-Dependent 3D Genome Re-organization in Naive Pluripotency. *Cell Rep,* 29**,** 1974-1985 e6.

MEIER, M., GRANT, J., DOWDLE, A., THOMAS, A., GERTON, J., COLLAS, P., O'SULLIVAN, J. M. & HORSFIELD, J. A. 2018. Cohesin facilitates zygotic genome activation in zebrafish. *Development,* 145.

MEREDITH, A. & JOHNSON, J. E. 2000. Negative autoregulation of Mash1 expression in CNS development. *Dev Biol,* 222**,** 336-46.

MERIKA, M., WILLIAMS, A. J., CHEN, G., COLLINS, T. & THANOS, D. 1998. Recruitment of CBP/p300 by the IFN beta enhanceosome is required for synergistic activation of transcription. *Mol Cell,* 1**,** 277-87.

MIAO, L., TANG, Y., BONNEAU, A. R., CHAN, S. H., KOJIMA, M. L., POWNALL, M. E., VEJNAR, C. E., GAO, F., KRISHNASWAMY, S., HENDRY, C. E. & GIRALDEZ, A. J. 2022. The landscape of pioneer factor activity reveals the mechanisms of chromatin reprogramming and genome activation. *Mol Cell,* 82**,** 986-1002 e9.

MICHAEL, A. K., GRAND, R. S., ISBEL, L., CAVADINI, S., KOZICKA, Z., KEMPF, G., BUNKER, R. D., SCHENK, A. D., GRAFF-MEYER, A., PATHARE, G. R., WEISS, J., MATSUMOTO, S., BURGER, L., SCHUBELER, D. & THOMA, N. H. 2020. Mechanisms of OCT4-SOX2 motif readout on nucleosomes. *Science,* 368**,** 1460-1465.

MICHAEL, A. K. & THOMA, N. H. 2021. Reading the chromatinized genome. *Cell,* 184**,** 3599-3611.

MICHELMAN-RIBEIRO, A., MAZZA, D., ROSALES, T., STASEVICH, T. J., BOUKARI, H., RISHI, V., VINSON, C., KNUTSON, J. R. & MCNALLY, J. G. 2009. Direct measurement of association and dissociation rates of DNA binding in live cells by fluorescence correlation spectroscopy. *Biophys J,* 97**,** 337-46.

MIECZKOWSKI, J., COOK, A., BOWMAN, S. K., MUELLER, B., ALVER, B. H., KUNDU, S., DEATON, A. M., URBAN, J. A., LARSCHAN, E., PARK, P. J., KINGSTON, R. E. & TOLSTORUKOV, M. Y. 2016. MNase titration reveals differences between nucleosome occupancy and chromatin accessibility. *Nat Commun,* 7**,** 11485.

MIESFELD, R., RUSCONI, S., GODOWSKI, P. J., MALER, B. A., OKRET, S., WIKSTROM, A. C., GUSTAFSSON, J. A. & YAMAMOTO, K. R. 1986. Genetic complementation of a glucocorticoid receptor deficiency by expression of cloned receptor cDNA. *Cell,* 46**,** 389-99.

MILLAN-ZAMBRANO, G., BURTON, A., BANNISTER, A. J. & SCHNEIDER, R. 2022. Histone post-translational modifications - cause and consequence of genome function. *Nat Rev Genet,* 23**,** 563-580.

MILLER, J. A. & WIDOM, J. 2003. Collaborative competition mechanism for gene activation in vivo. *Mol Cell Biol,* 23**,** 1623-32.

MINDERJAHN, J., SCHMIDT, A., FUCHS, A., SCHILL, R., RAITHEL, J., BABINA, M., SCHMIDL, C., GEBHARD, C., SCHMIDHOFER, S., MENDES, K., RATERMANN, A., GLATZ, D., NUTZEL, M., EDINGER, M., HOFFMANN, P., SPANG, R., LANGST, G., IMHOF, A. & REHLI, M. 2020. Mechanisms governing the pioneering and redistribution capabilities of the non-classical pioneer PU.1. *Nat Commun,* 11**,** 402.

MINSKY, M. 1988. Memoir on inventing the confocal scanning microscope. *Scanning,* 10**,** 128-138.

MIR, M., REIMER, A., HAINES, J. E., LI, X. Y., STADLER, M., GARCIA, H., EISEN, M. B. & DARZACQ, X. 2017. Dense Bicoid hubs accentuate binding along the morphogen gradient. *Genes Dev,* 31**,** 1784-1794.

MISHIMA, Y. & TOMARI, Y. 2016. Codon Usage and 3' UTR Length Determine Maternal mRNA Stability in Zebrafish. *Mol Cell,* 61**,** 874-85.

MISTRI, T. K., KELLY, D., MAK, J., COLBY, D., MULLIN, N. & CHAMBERS, I. 2022. Analysis of pluripotency transcription factor interactions reveals preferential binding of NANOG to SOX2 rather than NANOG or OCT4. *bioRxiv***,** 2020.06.24.169185.

MIVELAZ, M., CAO, A. M., KUBIK, S., ZENCIR, S., HOVIUS, R., BOICHENKO, I., STACHOWICZ, A. M., KURAT, C. F., SHORE, D. & FIERZ, B. 2020. Chromatin Fiber Invasion and Nucleosome Displacement by the Rap1 Transcription Factor. *Mol Cell,* 77**,** 488-500 e9.

MIZIANTY, M. J., STACH, W., CHEN, K., KEDARISETTI, K. D., DISFANI, F. M. & KURGAN, L. 2010. Improved sequence-based prediction of disordered regions with multilayer fusion of multiple information sources. *Bioinformatics,* 26**,** i489-96.

MONDAL, A., MISHRA, S. K. & BHATTACHERJEE, A. 2022. Nucleosome breathing facilitates cooperative binding of pluripotency factors Sox2 and Oct4 to DNA. *Biophys J,* 121**,** 4526-4542.

MOREY, C., KRESS, C. & BICKMORE, W. A. 2009. Lack of bystander activation shows that localization exterior to chromosome territories is not sufficient to up-regulate gene expression. *Genome Res,* 19**,** 1184-94.

MUELLER, B., MIECZKOWSKI, J., KUNDU, S., WANG, P., SADREYEV, R., TOLSTORUKOV, M. Y. & KINGSTON, R. E. 2017. Widespread changes in nucleosome accessibility without changes in nucleosome occupancy during a rapid transcriptional induction. *Genes Dev,* 31**,** 451-462.

MUELLER, F., STASEVICH, T. J., MAZZA, D. & MCNALLY, J. G. 2013. Quantifying transcription factor kinetics: at work or at play? *Crit Rev Biochem Mol Biol,* 48**,** 492-514.

MUKHERJEE, S., LUEDEKE, D. M., MCCOY, L., IWAFUCHI, M. & ZORN, A. M. 2022a. SOX transcription factors direct TCF-independent WNT/beta-catenin responsive transcription to govern cell fate in human pluripotent stem cells. *Cell Rep,* 40**,** 111247.

MUKHERJEE, S., MANNA, P., HUNG, S.-T., VIETMEYER, F., FRIIS, P., PALMER, A. E. & JIMENEZ, R. 2022b. Directed Evolution of a Bright Variant of mCherry: Suppression of Nonradiative Decay by Fluorescence Lifetime Selections. *The Journal of Physical Chemistry B,* 126**,** 4659-4668.

MULLEN, A. C., ORLANDO, D. A., NEWMAN, J. J., LOVEN, J., KUMAR, R. M., BILODEAU, S., REDDY, J., GUENTHER, M. G., DEKOTER, R. P. & YOUNG, R. A. 2011. Master transcription factors determine cell-type-specific responses to TGF-beta signaling. *Cell,* 147**,** 565-76.

MULLIN, N. P., GAGLIARDI, A., KHOA, L. T. P., COLBY, D., HALL-PONSELE, E., ROWE, A. J. & CHAMBERS, I. 2017. Distinct Contributions of Tryptophan Residues within the Dimerization Domain to Nanog Function. *J Mol Biol,* 429**,** 1544-1553.

MURRE, C., MCCAW, P. S. & BALTIMORE, D. 1989. A new DNA binding and dimerization motif in immunoglobulin enhancer binding, daughterless, MyoD, and myc proteins. *Cell,* 56**,** 777-83.

NAJAFABADI, H. S., MNAIMNEH, S., SCHMITGES, F. W., GARTON, M., LAM, K. N., YANG, A., ALBU, M., WEIRAUCH, M. T., RADOVANI, E., KIM, P. M., GREENBLATT, J., FREY, B. J. & HUGHES, T. R. 2015. C2H2 zinc finger proteins greatly expand the human regulatory lexicon. *Nat Biotechnol,* 33**,** 555-62.

NECCI, M., PIOVESAN, D., DOSZTANYI, Z. & TOSATTO, S. C. E. 2017. MobiDB-lite: fast and highly specific consensus prediction of intrinsic disorder in proteins. *Bioinformatics,* 33**,** 1402-1404.

NG, X. W., SAMPATH, K. & WOHLAND, T. 2018. Fluorescence Correlation and Cross-Correlation Spectroscopy in Zebrafish. *Methods Mol Biol,* 1863**,** 67-105.

NIEN, C. Y., LIANG, H. L., BUTCHER, S., SUN, Y., FU, S., GOCHA, T., KIROV, N., MANAK, J. R. & RUSHLOW, C. 2011. Temporal coordination of gene networks by Zelda in the early Drosophila embryo. *PLoS Genet,* 7**,** e1002339.

NISHIMURA, M., ARIMURA, Y., NOZAWA, K. & KURUMIZAKA, H. 2020. Linker DNA and histone contributions in nucleosome binding by p53. *J Biochem,* 168**,** 669-675.

O'SHAUGHNESSY, E. C., STONE, O. J., LAFOSSE, P. K., AZOITEI, M. L., TSYGANKOV, D., HEDDLESTON, J. M., LEGANT, W. R., WITTCHEN, E. S., BURRIDGE, K., ELSTON, T. C., BETZIG, E., CHEW, T. L., ADALSTEINSSON, D. & HAHN, K. M. 2019. Software for lattice light-sheet imaging of FRET biosensors, illustrated with a new Rap1 biosensor. *J Cell Biol,* 218**,** 3153-3160.

O'SHEA, E. K., KLEMM, J. D., KIM, P. S. & ALBER, T. 1991. X-ray structure of the GCN4 leucine zipper, a two-stranded, parallel coiled coil. *Science,* 254**,** 539-44.

OASA, S., KRMPOT, A. J., NIKOLIC, S. N., CLAYTON, A. H. A., TSIGELNY, I. F., CHANGEUX, J. P., TERENIUS, L., RIGLER, R. & VUKOJEVIC, V. 2021. Dynamic Cellular Cartography: Mapping the Local Determinants of Oligodendrocyte Transcription Factor 2 (OLIG2) Function in Live Cells Using Massively Parallel Fluorescence Correlation Spectroscopy Integrated with Fluorescence Lifetime Imaging Microscopy (mpFCS/FLIM). *Anal Chem,* 93**,** 12011-12021.

OASA, S., VUKOJEVIC, V., RIGLER, R., TSIGELNY, I. F., CHANGEUX, J. P. & TERENIUS, L. 2020. A strategy for designing allosteric modulators of transcription factor dimerization. *Proc Natl Acad Sci U S A,* 117**,** 2683-2686.

OLLION, J., COCHENNEC, J., LOLL, F., ESCUDÉ, C. & BOUDIER, T. 2013. TANGO: a generic tool for high-throughput 3D image analysis for studying nuclear organization. *Bioinformatics,* 29**,** 1840-1.

ONICHTCHOUK, D. & DRIEVER, W. 2016. Chapter Fifteen - Zygotic Genome Activators, Developmental Timing, and Pluripotency. *In:* WASSARMAN, P. M. (ed.) *Current Topics in Developmental Biology.* Academic Press.

ONICHTCHOUK, D., GEIER, F., POLOK, B., MESSERSCHMIDT, D. M., MÖSSNER, R., WENDIK, B., SONG, S., TAYLOR, V., TIMMER, J. & DRIEVER, W. 2010. Zebrafish Pou5f1-dependent transcriptional networks in temporal control of early development. *Molecular systems biology,* 6**,** 354-354.

OYAKE, T., ITOH, K., MOTOHASHI, H., HAYASHI, N., HOSHINO, H., NISHIZAWA, M., YAMAMOTO, M. & IGARASHI, K. 1996. Bach proteins belong to a novel family of BTB-basic leucine zipper transcription factors that interact with MafK and regulate transcription through the NF-E2 site. *Mol Cell Biol,* 16**,** 6083-95.

OZAWA, T. & UMEZAWA, Y. 2002. Peptide Assemblies in Living Cells. Methods for Detecting Protein-Protein Interactions†. *Supramolecular Chemistry,* 14**,** 271-280.

PADILLA-PARRA, S., AUDUGE, N., COPPEY-MOISAN, M. & TRAMIER, M. 2008. Quantitative FRET analysis by fast acquisition time domain FLIM at high spatial resolution in living cells. *Biophys J,* 95**,** 2976-88.

PADILLA-PARRA, S., AUDUGE, N., COPPEY-MOISAN, M. & TRAMIER, M. 2011. Non fitting based FRET-FLIM analysis approaches applied to quantify protein-protein interactions in live cells. *Biophys Rev,* 3**,** 63-70.

PADILLA-PARRA, S., AUDUGE, N., LALUCQUE, H., MEVEL, J. C., COPPEY-MOISAN, M. & TRAMIER, M. 2009. Quantitative comparison of different fluorescent protein couples for fast FRET-FLIM acquisition. *Biophys J,* 97**,** 2368-76.

PALFY, M., JOSEPH, S. R. & VASTENHOUW, N. L. 2017. The timing of zygotic genome activation. *Curr Opin Genet Dev,* 43**,** 53-60.

PALFY, M., SCHULZE, G., VALEN, E. & VASTENHOUW, N. L. 2020. Chromatin accessibility established by Pou5f3, Sox19b and Nanog primes genes for activity during zebrafish genome activation. *PLoS Genet,* 16**,** e1008546.

PASINI, D. & DI CROCE, L. 2016. Emerging roles for Polycomb proteins in cancer. *Curr Opin Genet Dev,* 36**,** 50-8.

PAVLETICH, N. P. & PABO, C. O. 1991. Zinc finger-DNA recognition: crystal structure of a Zif268-DNA complex at 2.1 A. *Science,* 252**,** 809-17.

PAVLETICH, N. P. & PABO, C. O. 1993. Crystal structure of a five-finger GLI-DNA complex: new perspectives on zinc fingers. *Science,* 261**,** 1701-7.

PEAT, J. R., DEAN, W., CLARK, S. J., KRUEGER, F., SMALLWOOD, S. A., FICZ, G., KIM, J. K., MARIONI, J. C., HORE, T. A. & REIK, W. 2014. Genome-wide bisulfite sequencing in zygotes identifies demethylation targets and maps the contribution of TET3 oxidation. *Cell Rep,* 9**,** 1990-2000.

PEREZ-CAMPS, M., TIAN, J., CHNG, S. C., SEM, K. P., SUDHAHARAN, T., TEH, C., WACHSMUTH, M., KORZH, V., AHMED, S. & REVERSADE, B. 2016. Quantitative imaging reveals real-time Pou5f3-Nanog complexes driving dorsoventral mesendoderm patterning in zebrafish. *Elife,* 5.

PEREZ-MONTERO, S., CARBONELL, A., MORAN, T., VAQUERO, A. & AZORIN, F. 2013. The embryonic linker histone H1 variant of Drosophila, dBigH1, regulates zygotic genome activation. *Dev Cell,* 26**,** 578-90.

PERNUS, A. & LANGOWSKI, J. 2015. Imaging Fos-Jun transcription factor mobility and interaction in live cells by single plane illumination-fluorescence cross correlation spectroscopy. *PLoS One,* 10**,** e0123070.

PETERSEN, N. O., JOHNSON, D. C. & SCHLESINGER, M. J. 1986. Scanning fluorescence correlation spectroscopy. II. Application to virus glycoprotein aggregation. *Biophys J,* 49**,** 817-20.

PETKOVICH, M., BRAND, N. J., KRUST, A. & CHAMBON, P. 1987. A human retinoic acid receptor which belongs to the family of nuclear receptors. *Nature,* 330**,** 444-50.

PETRÁŇ, M., HADRAVSKÝ, M., EGGER, M. D. & GALAMBOS, R. 1968. Tandem-Scanning Reflected-Light Microscope*. *Journal of the Optical Society of America,* 58**,** 661-664.

PETROVICK, M. S., HIEBERT, S. W., FRIEDMAN, A. D., HETHERINGTON, C. J., TENEN, D. G. & ZHANG, D. E. 1998. Multiple functional domains of AML1: PU.1 and C/EBPalpha synergize with different regions of AML1. *Mol Cell Biol,* 18**,** 3915-25.

PICOQUANT. 2023. *Photon Counting Detectors* [Online]. Available: https://www.picoquant.com/products/category/photon-counting-detectors [Accessed].

PLUTA, R., ARAGON, E., PRESCOTT, N. A., RUIZ, L., MEES, R. A., BAGINSKI, B., FLOOD, J. R., MARTIN-MALPARTIDA, P., MASSAGUE, J., DAVID, Y. & MACIAS, M. J. 2022. Molecular basis for DNA recognition by the maternal pioneer transcription factor FoxH1. *Nat Commun,* 13, 7279.

POLACH, K. J. & WIDOM, J. 1995. Mechanism of protein access to specific DNA sequences in chromatin: a dynamic equilibrium model for gene regulation. *J Mol Biol,* 254, 130-49.

POLAND, S. P., KRSTAJIC, N., COELHO, S., TYNDALL, D., WALKER, R. J., DEVAUGES, V., MORTON, P. E., NICHOLAS, N. S., RICHARDSON, J., LI, D. D., SUHLING, K., WELLS, C. M., PARSONS, M., HENDERSON, R. K. & AMEER-BEG, S. M. 2014. Time-resolved multifocal multiphoton microscope for high speed FRET imaging in vivo. *Opt Lett,* 39**,** 6013-6.

POTOK, M. E., NIX, D. A., PARNELL, T. J. & CAIRNS, B. R. 2013. Reprogramming the maternal zebrafish genome after fertilization to match the paternal methylation pattern. *Cell,* 153**,** 759-72.

PRADEEPA, M. M., GRIMES, G. R., KUMAR, Y., OLLEY, G., TAYLOR, G. C., SCHNEIDER, R. & BICKMORE, W. A. 2016. Histone H3 globular domain acetylation identifies a new class of enhancers. *Nat Genet,* 48**,** 681-6.

PRIEST, D. G., BERNARDINI, A., LOU, J., MANTOVANI, R. & HINDE, E. 2021. Live cell dynamics of the NF-Y transcription factor. *Sci Rep,* 11**,** 10992.

PRIEST, D. G., SOLANO, A., LOU, J. & HINDE, E. 2019. Fluorescence fluctuation spectroscopy: an invaluable microscopy tool for uncovering the biophysical rules for navigating the nuclear landscape. *Biochem Soc Trans,* 47**,** 1117-1129.

PRITCHARD, D. K. & SCHUBIGER, G. 1996. Activation of transcription in Drosophila embryos is a gradual process mediated by the nucleocytoplasmic ratio. *Genes Dev,* 10**,** 1131-42.

QIAN, Y. Q., OTTING, G., BILLETER, M., MULLER, M., GEHRING, W. & WUTHRICH, K. 1993. Nuclear magnetic resonance spectroscopy of a DNA complex with the uniformly 13C-labeled Antennapedia homeodomain and structure determination of the DNA-bound homeodomain. *J Mol Biol,* 234**,** 1070-83.

RACCAUD, M., FRIMAN, E. T., ALBER, A. B., AGARWAL, H., DELUZ, C., KUHN, T., GEBHARDT, J. C. M. & SUTER, D. M. 2019. Mitotic chromosome binding predicts transcription factor properties in interphase. *Nat Commun,* 10**,** 487.

RADTKE, F., HEUCHEL, R., GEORGIEV, O., HERGERSBERG, M., GARIGLIO, M., DEMBIC, Z. & SCHAFFNER, W. 1993. Cloned transcription factor MTF-1 activates the mouse metallothionein I promoter. *EMBO J,* 12**,** 1355-62.

RAO, S. S. P., HUANG, S. C., GLENN ST HILAIRE, B., ENGREITZ, J. M., PEREZ, E. M., KIEFFER-KWON, K. R., SANBORN, A. L., JOHNSTONE, S. E., BASCOM, G. D., BOCHKOV, I. D., HUANG, X., SHAMIM, M. S., SHIN, J., TURNER, D., YE, Z., OMER, A. D., ROBINSON, J. T., SCHLICK, T., BERNSTEIN, B. E., CASELLAS, R., LANDER, E. S. & AIDEN, E. L. 2017. Cohesin Loss Eliminates All Loop Domains. *Cell,* 171**,** 305-320 e24.

RAVASI, T., SUZUKI, H., CANNISTRACI, C. V., KATAYAMA, S., BAJIC, V. B., TAN, K., AKALIN, A., SCHMEIER, S., KANAMORI-KATAYAMA, M., BERTIN, N., CARNINCI, P., DAUB, C. O., FORREST, A. R., GOUGH, J., GRIMMOND, S., HAN, J. H., HASHIMOTO, T., HIDE, W., HOFMANN, O., KAMBUROV, A., KAUR, M., KAWAJI, H., KUBOSAKI, A., LASSMANN, T., VAN NIMWEGEN, E., MACPHERSON, C. R., OGAWA, C., RADOVANOVIC, A., SCHWARTZ, A., TEASDALE, R. D., TEGNER, J., LENHARD, B., TEICHMANN, S. A., ARAKAWA, T., NINOMIYA, N., MURAKAMI, K., TAGAMI, M., FUKUDA, S., IMAMURA, K., KAI, C., ISHIHARA, R., KITAZUME, Y., KAWAI, J., HUME, D. A., IDEKER, T. & HAYASHIZAKI, Y. 2010. An atlas of combinatorial transcriptional regulation in mouse and man. *Cell,* 140**,** 744-52.

REHO, B., LAU, L., MOCSAR, G., MULLER, G., FADEL, L., BRAZDA, P., NAGY, L., TOTH, K. & VAMOSI, G. 2020. Simultaneous Mapping of Molecular Proximity and Comobility Reveals Agonist-Enhanced Dimerization and DNA Binding of Nuclear Receptors. *Anal Chem,* 92**,** 2207-2215.

REIM, G. & BRAND, M. 2006. Maternal control of vertebrate dorsoventral axis formation and epiboly by the POU domain protein Spg/Pou2/Oct4. *Development,* 133**,** 2757-70.

REISSER, M., PALMER, A., POPP, A. P., JAHN, C., WEIDINGER, G. & GEBHARDT, J. C. M. 2018. Single-molecule imaging correlates decreasing nuclear volume with increasing TF-chromatin associations during zebrafish development. *Nat Commun,* 9**,** 5218.

ROBERTI, M. J., LOPEZ, L. O., OSSATO, G., STEINMETZ, I., HAAS, P, HECHT, F. & ALVAREZ, L. A. J. 2020. Application Notes: TauSense: a fluorescence lifetime-based tool set for everyday imaging.

ROBERTS, G. A., OZKAN, B., GACHULINCOVA, I., O'DWYER, M. R., HALL-PONSELE, E., SAXENA, M., ROBINSON, P. J. & SOUFI, A. 2021. Dissecting OCT4 defines the role of nucleosome binding in pluripotency. *Nat Cell Biol,* 23**,** 834-845.

ROHS, R., JIN, X., WEST, S. M., JOSHI, R., HONIG, B. & MANN, R. S. 2010. Origins of specificity in protein-DNA recognition. *Annu Rev Biochem,* 79**,** 233-69.

ROMERO, J. J., DE ROSSI, M. C., OSES, C., ECHEGARAY, C. V., VERNERI, P., FRANCIA, M., GUBERMAN, A. & LEVI, V. 2022. Nucleus-cytoskeleton communication impacts on OCT4-chromatin interactions in embryonic stem cells. *BMC Biol,* 20**,** 6.

ROMERO, P., OBRADOVIC, Z. & DUNKER, A. K. 2004. Natively disordered proteins: functions and predictions. *Appl Bioinformatics,* 3**,** 105-13.

ROST, F. W. D. 1991. *Quantitative Fluorescence Microscopy*, Cambridge University Press.

ROTHE, M., PEHL, M., TAUBERT, H. & JACKLE, H. 1992. Loss of gene function through rapid mitotic cycles in the Drosophila embryo. *Nature,* 359**,** 156-9.

SABARI, B. R., DALL'AGNESE, A., BOIJA, A., KLEIN, I. A., COFFEY, E. L., SHRINIVAS, K., ABRAHAM, B. J., HANNETT, N. M., ZAMUDIO, A. V., MANTEIGA, J. C., LI, C. H., GUO, Y. E., DAY, D. S., SCHUIJERS, J., VASILE, E., MALIK, S., HNISZ, D., LEE, T. I., CISSE, II, ROEDER, R. G., SHARP, P. A., CHAKRABORTY, A. K. & YOUNG, R. A. 2018a. Coactivator condensation at super-enhancers links phase separation and gene control. *Science,* 361.

SABARI, B. R., DALL'AGNESE, A., BOIJA, A., KLEIN, I. A., COFFEY, E. L., SHRINIVAS, K., ABRAHAM, B. J., HANNETT, N. M., ZAMUDIO, A. V., MANTEIGA, J. C., LI, C. H., GUO, Y. E., DAY, D. S., SCHUIJERS, J., VASILE, E., MALIK, S., HNISZ, D., LEE, T. I., CISSE, I. I., ROEDER, R. G., SHARP, P. A., CHAKRABORTY, A. K. & YOUNG, R. A. 2018b. Coactivator condensation at super-enhancers links phase separation and gene control. *Science,* 361**,** eaar3958.

SADAMOTO, H., SAITO, K., MUTO, H., KINJO, M. & ITO, E. 2011. Direct observation of dimerization between different CREB1 isoforms in a living cell. *PLoS One,* 6**,** e20285.

SAEKI, H., OHSUMI, K., AIHARA, H., ITO, T., HIROSE, S., URA, K. & KANEDA, Y. 2005. Linker histone variants control chromatin dynamics during early embryogenesis. *Proc Natl Acad Sci U S A,* 102**,** 5697-702.

SASSONE-CORSI, P., RANSONE, L. J., LAMPH, W. W. & VERMA, I. M. 1988. Direct interaction between fos and jun nuclear oncoproteins: role of the 'leucine zipper' domain. *Nature,* 336**,** 692-5.

SATO, Y., HILBERT, L., ODA, H., WAN, Y., HEDDLESTON, J. M., CHEW, T. L., ZABURDAEV, V., KELLER, P., LIONNET, T., VASTENHOUW, N. & KIMURA, H. 2019. Histone H3K27 acetylation precedes active transcription during zebrafish zygotic genome activation as revealed by live-cell analysis. *Development,* 146.

SCHAUER, A., PINHEIRO, D., HAUSCHILD, R. & HEISENBERG, C. P. 2020. Zebrafish embryonic explants undergo genetically encoded self-assembly. *Elife,* 9.

SCHICK, S., GROSCHE, S., KOHL, K. E., DRPIC, D., JAEGER, M. G., MARELLA, N. C., IMRICHOVA, H., LIN, J. G., HOFSTATTER, G., SCHUSTER, M., RENDEIRO, A. F., KOREN, A., PETRONCZKI, M., BOCK, C., MULLER, A. C., WINTER, G. E. & KUBICEK, S. 2021. Acute BAF perturbation causes immediate changes in chromatin accessibility. *Nat Genet,* 53**,** 269-278.

SCHINDELIN, J., ARGANDA-CARRERAS, I., FRISE, E., KAYNIG, V., LONGAIR, M., PIETZSCH, T., PREIBISCH, S., RUEDEN, C., SAALFELD, S., SCHMID, B., TINEVEZ, J. Y., WHITE, D. J., HARTENSTEIN, V., ELICEIRI, K., TOMANCAK, P. & CARDONA, A. 2012. Fiji: an open-source platform for biological-image analysis. *Nat Methods,* 9**,** 676-82.

SCHMIDT, U., WEIGERT, M., BROADDUS, C. & MYERS, G. Cell Detection with Star-Convex Polygons. *In:* FRANGI, A. F., SCHNABEL, J. A., DAVATZIKOS, C., ALBEROLA-LÓPEZ, C. & FICHTINGER, G., eds. Medical Image Computing and Computer Assisted Intervention – MICCAI 2018, 2018// 2018 Cham. Springer International Publishing, 265-273.

SCHOENFELDER, S., SEXTON, T., CHAKALOVA, L., COPE, N. F., HORTON, A., ANDREWS, S., KURUKUTI, S., MITCHELL, J. A., UMLAUF, D., DIMITROVA, D. S., ESKIW, C. H., LUO, Y., WEI, C. L., RUAN, Y., BIEKER, J. J. & FRASER, P. 2010. Preferential associations between co-regulated genes reveal a transcriptional interactome in erythroid cells. *Nat Genet,* 42**,** 53-61.

SCHUFF, M., SIEGEL, D., PHILIPP, M., BUNDSCHU, K., HEYMANN, N., DONOW, C. & KNOCHEL, W. 2012. Characterization of Danio rerio Nanog and functional comparison to Xenopus Vents. *Stem Cells Dev,* 21**,** 1225-38.

SCHULZ, K. N. & HARRISON, M. M. 2019. Mechanisms regulating zygotic genome activation. *Nat Rev Genet,* 20**,** 221-234.

SCHWEIKHARD, V., ALVAREZ, LUIS A.J., ROBERTI, M. J., BIRK, HOLGER, GISKE, ARNOLD, LEICA MICROSYSTEMS. 2020. Application Note: The Power HyD family of detectors for confocal microscopy.

SCHWILLE, P. & HAUSTEIN, E. Fluorescence Correlation Spectroscopy An Introduction to its Concepts and Applications. 2002.

SCOTT, B. L. & HOPPE, A. D. 2015. Optimizing fluorescent protein trios for 3-Way FRET imaging of protein interactions in living cells. *Sci Rep,* 5**,** 10270.

SEYDOUX, G. & DUNN, M. A. 1997. Transcriptionally repressed germ cells lack a subpopulation of phosphorylated RNA polymerase II in early embryos of Caenorhabditis elegans and Drosophila melanogaster. *Development,* 124**,** 2191-201.

SHANER, N. C., CAMPBELL, R. E., STEINBACH, P. A., GIEPMANS, B. N., PALMER, A. E. & TSIEN, R. Y. 2004. Improved monomeric red, orange and yellow fluorescent proteins derived from Discosoma sp. red fluorescent protein. *Nat Biotechnol,* 22**,** 1567-72.

SHANER, N. C., LAMBERT, G. G., CHAMMAS, A., NI, Y., CRANFILL, P. J., BAIRD, M. A., SELL, B. R., ALLEN, J. R., DAY, R. N., ISRAELSSON, M., DAVIDSON, M. W. & WANG, J. 2013. A bright monomeric green fluorescent protein derived from Branchiostoma lanceolatum. *Nat Methods,* 10**,** 407-9.

SHEN, X., LIU, Y., HSU, Y. J., FUJIWARA, Y., KIM, J., MAO, X., YUAN, G. C. & ORKIN, S. H. 2008. EZH1 mediates methylation on histone H3 lysine 27 and complements EZH2 in maintaining stem cell identity and executing pluripotency. *Mol Cell,* 32**,** 491-502.

SHI, X., FOO, Y. H., SUDHAHARAN, T., CHONG, S. W., KORZH, V., AHMED, S. & WOHLAND, T. 2009. Determination of dissociation constants in living zebrafish embryos with single wavelength fluorescence cross-correlation spectroscopy. *Biophys J,* 97**,** 678-86.

SHINDO, Y. & AMODEO, A. A. 2019. Dynamics of Free and Chromatin-Bound Histone H3 during Early Embryogenesis. *Curr Biol,* 29**,** 359-366 e4.

SHU, X., SHANER, N. C., YARBROUGH, C. A., TSIEN, R. Y. & REMINGTON, S. J. 2006. Novel chromophores and buried charges control color in mFruits. *Biochemistry,* 45**,** 9639-47.

SIEGEL, A. P., HAYS, N. M. & DAY, R. N. 2013. Unraveling transcription factor interactions with heterochromatin protein 1 using fluorescence lifetime imaging microscopy and fluorescence correlation spectroscopy. *J Biomed Opt,* 18**,** 25002.

SIMICEVIC, J., SCHMID, A. W., GILARDONI, P. A., ZOLLER, B., RAGHAV, S. K., KRIER, I., GUBELMANN, C., LISACEK, F., NAEF, F., MONIATTE, M. & DEPLANCKE, B. 2013. Absolute quantification of transcription factors during cellular differentiation using multiplexed targeted proteomics. *Nat Methods,* 10**,** 570-6.

SIMON, J. A. & KINGSTON, R. E. 2013. Occupying chromatin: Polycomb mechanisms for getting to genomic targets, stopping transcriptional traffic, and staying put. *Mol Cell,* 49**,** 808-24.

SLATTERY, M., RILEY, T., LIU, P., ABE, N., GOMEZ-ALCALA, P., DROR, I., ZHOU, T., ROHS, R., HONIG, B., BUSSEMAKER, H. J. & MANN, R. S. 2011. Cofactor binding evokes latent differences in DNA binding specificity between Hox proteins. *Cell,* 147**,** 1270-82.

SLATTERY, M., ZHOU, T., YANG, L., DANTAS MACHADO, A. C., GORDAN, R. & ROHS, R. 2014. Absence of a simple code: how transcription factors read the genome. *Trends Biochem Sci,* 39**,** 381-99.

SLUTSKY, M. & MIRNY, L. A. 2004. Kinetics of protein-DNA interaction: facilitated target location in sequence-dependent potential. *Biophys J,* 87**,** 4021-35.

SODERBERG, O., LEUCHOWIUS, K. J., GULLBERG, M., JARVIUS, M., WEIBRECHT, I., LARSSON, L. G. & LANDEGREN, U. 2008. Characterizing proteins and their interactions in cells and tissues using the in situ proximity ligation assay. *Methods,* 45**,** 227-32.

SOUFI, A., DONAHUE, G. & ZARET, K. S. 2012. Facilitators and impediments of the pluripotency reprogramming factors' initial engagement with the genome. *Cell,* 151**,** 994-1004.

SOUFI, A., GARCIA, M. F., JAROSZEWICZ, A., OSMAN, N., PELLEGRINI, M. & ZARET, K. S. 2015. Pioneer transcription factors target partial DNA motifs on nucleosomes to initiate reprogramming. *Cell,* 161**,** 555-568.

SPITZ, F. & FURLONG, E. E. 2012. Transcription factors: from enhancer binding to developmental control. *Nat Rev Genet,* 13**,** 613-26.

SPRING, K. E., FELLERS, T.J., DAVIDSON, M.W. 2023. *Introduction to Charge-Coupled Devices (CCDs)* [Online]. MicroscopyU: MicroscopyU. Available: https://www.microscopyu.com/digital-imaging/introduction-to-charge-coupled-devices-ccds [Accessed].

SRIVASTAVA, M. & PETERSEN, N. O. 1996. Image cross-correlation spectroscopy: a new experimental biophysical approach to measurement of slow diffusion of fluorescent molecules. *Methods in cell science,* 18**,** 47-54.

STANOJEVIC, D., SMALL, S. & LEVINE, M. 1991. Regulation of a segmentation stripe by overlapping activators and repressors in the Drosophila embryo. *Science,* 254**,** 1385-7.

STAPEL, L. C., ZECHNER, C. & VASTENHOUW, N. L. 2017. Uniform gene expression in embryos is achieved by temporal averaging of transcription noise. *Genes Dev,* 31**,** 1635-1640.

STASEVICH, T. J., MUELLER, F., MICHELMAN-RIBEIRO, A., ROSALES, T., KNUTSON, J. R. & MCNALLY, J. G. 2010. Cross-validating FRAP and FCS to quantify the impact of photobleaching on in vivo binding estimates. *Biophys J,* 99**,** 3093-101.

STOKES, G. G. 1852. XXX. On the change of refrangibility of light. *Philosophical Transactions of the Royal Society of London,* 142**,** 463-562.

STORMBERG, T., FILLIAUX, S., BAUGHMAN, H. E. R., KOMIVES, E. A. & LYUBCHENKO, Y. L. 2021. Transcription factor NF-kappaB unravels nucleosomes. *Biochim Biophys Acta Gen Subj,* 1865**,** 129934.

STORTZ, M., ANGIOLINI, J., MOCSKOS, E., WOLOSIUK, A., PECCI, A. & LEVI, V. 2018. Mapping the dynamical organization of the cell nucleus through fluorescence correlation spectroscopy. *Methods,* 140-141**,** 10-22.

STREBINGER, D., DELUZ, C., FRIMAN, E. T., GOVINDAN, S., ALBER, A. B. & SUTER, D. M. 2019. Endogenous fluctuations of OCT4 and SOX2 bias pluripotent cell fate decisions. *Mol Syst Biol,* 15**,** e9002.

STROM, A. R., BIGGS, R. J., BANIGAN, E. J., WANG, X., CHIU, K., HERMAN, C., COLLADO, J., YUE, F., RITLAND POLITZ, J. C., TAIT, L. J., SCALZO, D., TELLING, A., GROUDINE, M., BRANGWYNNE, C. P., MARKO, J. F. & STEPHENS, A. D. 2021. HP1alpha is a chromatin crosslinker that controls nuclear and mitotic chromosome mechanics. *Elife,* 10.

STRYER, L. & HAUGLAND, R. P. 1967. Energy transfer: a spectroscopic ruler. *Proc Natl Acad Sci U S A,* 58**,** 719-26.

SUBTELNY, A. O., EICHHORN, S. W., CHEN, G. R., SIVE, H. & BARTEL, D. P. 2014. Poly(A)-tail profiling reveals an embryonic switch in translational control. *Nature,* 508**,** 66-71.

SUN, X. H. & BALTIMORE, D. 1991. An inhibitory domain of E12 transcription factor prevents DNA binding in E12 homodimers but not in E12 heterodimers. *Cell,* 64**,** 459-70.

SUTHERLAND, H. & BICKMORE, W. A. 2009. Transcription factories: gene expression in unions? *Nat Rev Genet,* 10**,** 457-66.

SZALOKI, N., KRIEGER, J. W., KOMAROMI, I., TOTH, K. & VAMOSI, G. 2015. Evidence for Homodimerization of the c-Fos Transcription Factor in Live Cells Revealed by Fluorescence Microscopy and Computer Modeling. *Mol Cell Biol,* 35**,** 3785-98.

TADROS, W., GOLDMAN, A. L., BABAK, T., MENZIES, F., VARDY, L., ORR-WEAVER, T., HUGHES, T. R., WESTWOOD, J. T., SMIBERT, C. A. & LIPSHITZ, H. D. 2007. SMAUG is a major regulator of maternal mRNA destabilization in Drosophila and its translation is activated by the PAN GU kinase. *Dev Cell,* 12**,** 143-55.

TADROS, W. & LIPSHITZ, H. D. 2009. The maternal-to-zygotic transition: a play in two acts. *Development,* 136**,** 3033-3042.

TAKAHASHI, K. & YAMANAKA, S. 2006. Induction of pluripotent stem cells from mouse embryonic and adult fibroblast cultures by defined factors. *Cell,* 126**,** 663-76.

TAN, C. & TAKADA, S. 2020. Nucleosome allostery in pioneer transcription factor binding. *Proc Natl Acad Sci U S A,* 117**,** 20586-20596.

TAN, M. H., AU, K. F., YABLONOVITCH, A. L., WILLS, A. E., CHUANG, J., BAKER, J. C., WONG, W. H. & LI, J. B. 2013. RNA sequencing reveals a diverse and dynamic repertoire of the Xenopus tropicalis transcriptome over development. *Genome Res,* 23**,** 201-16.

TANG, X., LI, T., LIU, S., WISNIEWSKI, J., ZHENG, Q., RONG, Y., LAVIS, L. D. & WU, C. 2022. Kinetic principles underlying pioneer function of GAGA transcription factor in live cells. *Nat Struct Mol Biol,* 29**,** 665-676.

TEH, C., SUN, G., SHEN, H., KORZH, V. & WOHLAND, T. 2015. Modulating the expression level of secreted Wnt3 influences cerebellum development in zebrafish transgenics. *Development,* 142**,** 3721-33.

TEVES, S. S., AN, L., HANSEN, A. S., XIE, L., DARZACQ, X. & TJIAN, R. 2016. A dynamic mode of mitotic bookmarking by transcription factors. *eLife,* 5**,** e22280.

THEUNISSEN, T. W., COSTA, Y., RADZISHEUSKAYA, A., VAN OOSTEN, A. L., LAVIAL, F., PAIN, B., CASTRO, L. F. & SILVA, J. C. 2011. Reprogramming capacity of Nanog is functionally conserved in vertebrates and resides in a unique homeodomain. *Development,* 138**,** 4853-65.

THOMSEN, S., ANDERS, S., JANGA, S. C., HUBER, W. & ALONSO, C. R. 2010. Genome-wide analysis of mRNA decay patterns during early Drosophila development. *Genome Biol,* 11**,** R93.

TIMS, H. S., GURUNATHAN, K., LEVITUS, M. & WIDOM, J. 2011. Dynamics of nucleosome invasion by DNA binding proteins. *J Mol Biol,* 411**,** 430-48.

TIWARI, M. & KINJO, M. 2015. Determination of the dissociation constant of the NFkappaB p50/p65 heterodimer in living cells using fluorescence cross-correlation spectroscopy. *Methods Mol Biol,* 1228**,** 173-86.

TRAMIER, M., ZAHID, M., MEVEL, J. C., MASSE, M. J. & COPPEY-MOISAN, M. 2006. Sensitivity of CFP/YFP and GFP/mCherry pairs to donor photobleaching on FRET determination by fluorescence lifetime imaging microscopy in living cells. *Microsc Res Tech,* 69**,** 933-9.

TROJANOWSKI, J., FRANK, L., RADEMACHER, A., MUCKE, N., GRIGAITIS, P. & RIPPE, K. 2022. Transcription activation is enhanced by multivalent interactions independent of phase separation. *Mol Cell,* 82**,** 1878-1893 e10.

TSUTSUMI, M., MUTO, H., MYOBA, S., KIMOTO, M., KITAMURA, A., KAMIYA, M., KIKUKAWA, T., TAKIYA, S., DEMURA, M., KAWANO, K., KINJO, M. & AIZAWA, T. 2016. In vivo fluorescence correlation spectroscopy analyses of FMBP-1, a silkworm transcription factor. *FEBS open bio,* 6**,** 106-125.

TURRO, N. J. 1991. *Modern Molecular Photochemistry*, University Science Books.

VAMOSI, G., BAUDENDISTEL, N., VON DER LIETH, C. W., SZALOKI, N., MOCSAR, G., MULLER, G., BRAZDA, P., WALDECK, W., DAMJANOVICH, S., LANGOWSKI, J. & TOTH, K. 2008. Conformation of the c-Fos/c-Jun complex in vivo: a combined FRET, FCCS, and MD-modeling study. *Biophys J,* 94**,** 2859-68.

VAN ROSSUM, G. 1995. Python reference manual. CWI.

VARDY, L. & ORR-WEAVER, T. L. 2007. The Drosophila PNG kinase complex regulates the translation of cyclin B. *Dev Cell,* 12**,** 157-66.

VASTENHOUW, N. L., CAO, W. X. & LIPSHITZ, H. D. 2019. The maternal-to-zygotic transition revisited. *Development,* 146.

VASTENHOUW, N. L., ZHANG, Y., WOODS, I. G., IMAM, F., REGEV, A., LIU, X. S., RINN, J. & SCHIER, A. F. 2010. Chromatin signature of embryonic pluripotency is established during genome activation. *Nature,* 464**,** 922-6.

VEENSTRA, G. J., DESTREE, O. H. & WOLFFE, A. P. 1999. Translation of maternal TATA-binding protein mRNA potentiates basal but not activated transcription in Xenopus embryos at the midblastula transition. *Mol Cell Biol,* 19**,** 7972-82.

VEIL, M., SCHAECHTLE, M. A., GAO, M., KIRNER, V., BURYANOVA, L., GRETHEN, R. & ONICHTCHOUK, D. 2018. Maternal Nanog is required for zebrafish embryo architecture and for cell viability during gastrulation. *Development,* 145.

VEIL, M., YAMPOLSKY, L. Y., GRÜNING, B. & ONICHTCHOUK, D. 2019. Pou5f3, SoxB1, and Nanog remodel chromatin on high nucleosome affinity regions at zygotic genome activation. *Genome Research,* 29**,** 383-395.

VERBOOGEN, D. R. J., GONZALEZ MANCHA, N., TER BEEST, M. & VAN DEN BOGAART, G. 2017. Fluorescence Lifetime Imaging Microscopy reveals rerouting of SNARE trafficking driving dendritic cell activation. *Elife,* 6.

VERNERI, P., VAZQUEZ ECHEGARAY, C., OSES, C., STORTZ, M., GUBERMAN, A. & LEVI, V. 2020. Dynamical reorganization of the pluripotency transcription factors Oct4 and Sox2 during early differentiation of embryonic stem cells. *Sci Rep,* 10**,** 5195.

VOSS, T. C., SCHILTZ, R. L., SUNG, M.-H., YEN, P. M., STAMATOYANNOPOULOS, J. A., BIDDIE, S. C., JOHNSON, T. A., MIRANDA, T. B., JOHN, S. & HAGER, G. L. 2011. Dynamic exchange at regulatory elements during chromatin remodeling underlies assisted loading mechanism. *Cell,* 146**,** 544-554.

VUKOJEVIC, V., PAPADOPOULOS, D. K., TERENIUS, L., GEHRING, W. J. & RIGLER, R. 2010. Quantitative study of synthetic Hox transcription factor-DNA interactions in live cells. *Proceedings of the National Academy of Sciences of the United States of America,* 107**,** 4093-4098.

WACHSMUTH, M., KNOCH, T. A. & RIPPE, K. 2016. Dynamic properties of independent chromatin domains measured by correlation spectroscopy in living cells. *Epigenetics Chromatin,* 9**,** 57.

WADDINGTON, C. H. 1942. Canalization of development and the inheritance of acquired characters. *Nature,* 150**,** 563-565.

WALLKAMM, V., DORLICH, R., RAHM, K., KLESSING, T., NIENHAUS, G. U., WEDLICH, D. & GRADL, D. 2014. Live imaging of Xwnt5A-ROR2 complexes. *PLoS One,* 9**,** e109428.

WASKOM, M. L. 2021. seaborn: statistical data visualization. *The Journal of Open Source Software,* 6.

WHITE, M. D., ANGIOLINI, J. F., ALVAREZ, Y. D., KAUR, G., ZHAO, Z. W., MOCSKOS, E., BRUNO, L., BISSIERE, S., LEVI, V. & PLACHTA, N. 2016. Long-Lived Binding of Sox2 to DNA Predicts Cell Fate in the Four-Cell Mouse Embryo. *Cell,* 165**,** 75-87.

WHYTE, W. A., ORLANDO, D. A., HNISZ, D., ABRAHAM, B. J., LIN, C. Y., KAGEY, M. H., RAHL, P. B., LEE, T. I. & YOUNG, R. A. 2013. Master transcription factors and mediator establish super-enhancers at key cell identity genes. *Cell,* 153**,** 307-19.

WILLIAMSON, I., ESKELAND, R., LETTICE, L. A., HILL, A. E., BOYLE, S., GRIMES, G. R., HILL, R. E. & BICKMORE, W. A. 2012. Anterior-posterior differences in HoxD chromatin topology in limb development. *Development,* 139**,** 3157-67.

WINATA, C. L., LAPINSKI, M., PRYSZCZ, L., VAZ, C., BIN ISMAIL, M. H., NAMA, S., HAJAN, H. S., LEE, S. G. P., KORZH, V., SAMPATH, P., TANAVDE, V. & MATHAVAN, S. 2018. Cytoplasmic polyadenylation-mediated translational control of maternal mRNAs directs maternal-to-zygotic transition. *Development,* 145.

WOHLAND, T., SHI, X., SANKARAN, J. & STELZER, E. H. 2010. Single plane illumination fluorescence correlation spectroscopy (SPIM-FCS) probes inhomogeneous three-dimensional environments. *Opt Express,* 18**,** 10627-41.

WRIGGERS, W., CHAKRAVARTY, S. & JENNINGS, P. A. 2005. Control of protein functional dynamics by peptide linkers. *Biopolymers,* 80**,** 736-46.

WU, E. & VASTENHOUW, N. L. 2020. From mother to embryo: A molecular perspective on zygotic genome activation. *Curr Top Dev Biol,* 140**,** 209-254.

WU, J., HUANG, B., CHEN, H., YIN, Q., LIU, Y., XIANG, Y., ZHANG, B., LIU, B., WANG, Q., XIA, W., LI, W., LI, Y., MA, J., PENG, X., ZHENG, H., MING, J., ZHANG, W., ZHANG, J., TIAN,

G., XU, F., CHANG, Z., NA, J., YANG, X. & XIE, W. 2016. The landscape of accessible chromatin in mammalian preimplantation embryos. *Nature,* 534**,** 652-7.

XI, Y., YAO, J., CHEN, R., LI, W. & HE, X. 2011. Nucleosome fragility reveals novel functional states of chromatin and poises genes for activation. *Genome Res,* 21**,** 718-24.

XIA, W., XU, J., YU, G., YAO, G., XU, K., MA, X., ZHANG, N., LIU, B., LI, T., LIN, Z., CHEN, X., LI, L., WANG, Q., SHI, D., SHI, S., ZHANG, Y., SONG, W., JIN, H., HU, L., BU, Z., WANG, Y., NA, J., XIE, W. & SUN, Y. P. 2019. Resetting histone modifications during human parental-to-zygotic transition. *Science,* 365**,** 353-360.

XIAO, D., SAPERMSAP, N., SAFAR, M., CUNNINGHAM, M. R., CHEN, Y. & LI, D. D. 2021. On Synthetic Instrument Response Functions of Time-Correlated Single-Photon Counting Based Fluorescence Lifetime Imaging Analysis. *Front. Phys.,* 9:635645.

XU, J., WATTS, J. A., POPE, S. D., GADUE, P., KAMPS, M., PLATH, K., ZARET, K. S. & SMALE, S. T. 2009. Transcriptional competence and the active marking of tissue-specific enhancers by defined transcription factors in embryonic and induced pluripotent stem cells. *Genes Dev,* 23**,** 2824-38.

XU, X., YIN, Z., HUDSON, J. B., FERGUSON, E. L. & FRASCH, M. 1998. Smad proteins act in combination with synergistic and antagonistic regulators to target Dpp responses to the Drosophila mesoderm. *Genes Dev,* 12**,** 2354-70.

YANG, Y., ZHOU, C., WANG, Y., LIU, W., LIU, C., WANG, L., LIU, Y., SHANG, Y., LI, M., ZHOU, S., WANG, Y., ZENG, W., ZHOU, J., HUO, R. & LI, W. 2017. The E3 ubiquitin ligase RNF114 and TAB1 degradation are required for maternal-to-zygotic transition. *EMBO Rep,* 18**,** 205-216.

YAO, J., MUNSON, K. M., WEBB, W. W. & LIS, J. T. 2006. Dynamics of heat shock factor association with native gene loci in living cells. *Nature,* 442**,** 1050-3.

YU, X. & BUCK, M. J. 2019. Defining TP53 pioneering capabilities with competitive nucleosome binding assays. *Genome Res,* 29**,** 107-115.

ZANG, Z., XIAO, D., WANG, Q., LI, Z., XIE, W., CHEN, Y & LI, D. D. 2022. Fast fluorescence lifetime imaging analysis via extreme learning machine. *arXiv*.

ZARET, K. S. 2020. Pioneer Transcription Factors Initiating Gene Network Changes. *Annu Rev Genet,* 54**,** 367-385.

ZEITLINGER, J., STARK, A., KELLIS, M., HONG, J. W., NECHAEV, S., ADELMAN, K., LEVINE, M. & YOUNG, R. A. 2007. RNA polymerase stalling at developmental control genes in the Drosophila melanogaster embryo. *Nat Genet,* 39**,** 1512-6.

ZENK, F., LOESER, E., SCHIAVO, R., KILPERT, F., BOGDANOVIC, O. & IOVINO, N. 2017. Germ line-inherited H3K27me3 restricts enhancer function during maternal-to-zygotic transition. *Science,* 357**,** 212-216.

ZHANG, B., WU, X., ZHANG, W., SHEN, W., SUN, Q., LIU, K., ZHANG, Y., WANG, Q., LI, Y., MENG, A. & XIE, W. 2018. Widespread Enhancer Dememorization and Promoter Priming during Parental-to-Zygotic Transition. *Mol Cell,* 72**,** 673-686 e6.

ZHANG, B., ZHENG, H., HUANG, B., LI, W., XIANG, Y., PENG, X., MING, J., WU, X., ZHANG, Y., XU, Q., LIU, W., KOU, X., ZHAO, Y., HE, W., LI, C., CHEN, B., LI, Y., WANG, Q., MA, J., YIN, Q., KEE, K., MENG, A., GAO, S., XU, F., NA, J. & XIE, W. 2016. Allelic reprogramming of the histone modification H3K4me3 in early mammalian development. *Nature,* 537**,** 553-557.

ZHANG, M., KOTHARI, P., MULLINS, M. & LAMPSON, M. A. 2014a. Regulation of zygotic genome activation and DNA damage checkpoint acquisition at the mid-blastula transition. *Cell Cycle,* 13**,** 3828-38.

ZHANG, Y., VASTENHOUW, N. L., FENG, J., FU, K., WANG, C., GE, Y., PAULI, A., VAN HUMMELEN, P., SCHIER, A. F. & LIU, X. S. 2014b. Canonical nucleosome organization at promoters forms during genome activation. *Genome Res,* 24**,** 260-6.

ZHU, F., FARNUNG, L., KAASINEN, E., SAHU, B., YIN, Y., WEI, B., DODONOVA, S. O., NITTA, K. R., MORGUNOVA, E., TAIPALE, M., CRAMER, P. & TAIPALE, J. 2018. The interaction landscape between transcription factors and the nucleosome. *Nature,* 562**,** 76-81.

ZHU, W., XU, X., WANG, X. & LIU, J. 2019. Reprogramming histone modification patterns to coordinate gene expression in early zebrafish embryos. *BMC Genomics,* 20**,** 248.

ZHUO, X. & KNOX, B. E. 2022. Interaction of human CRX and NRL in live HEK293T cells measured using fluorescence resonance energy transfer (FRET). *Sci Rep,* 12**,** 6937.

ZILBERMAN, D., COLEMAN-DERR, D., BALLINGER, T. & HENIKOFF, S. 2008. Histone H2A.Z and DNA methylation are mutually antagonistic chromatin marks. *Nature,* 456**,** 125-9.